Luca Pivano

Thrust Estimation and Control of Marine Propellers in Four-Quadrant Operations

Thesis for the degree of philosophiae doctor

Trondheim, April 2008

Norwegian University of
Science and Technology
Faculty of Information Technology, Mathematics, and Electrical Engineering
Department of Engineering Cybernetics

NTNU
Norwegian University of
Science and Technology

NTNU
Norwegian University of Science and Technology

Thesis for the degree of philosophiae doctor

Faculty of Information Technology, Mathematics, and Electrical Engineering
Department of Engineering Cybernetics

ISBN 978-82-471-6258-3 (printed ver.)
ISBN 978-82-471-6261-3 (electronic ver.)
ISSN 1503-8181

ITK report 2008:3-W

Theses at NTNU, 2008:20

Printed by Tapir Uttrykk

Summary

Speed and position control systems for marine vehicles have been subject to an increased focus with respect to performance and safety. An example is represented by drilling operations performed with semi submersible rigs where the control of position and heading requires high accuracy. Drifting from the well position could cause severe damage to equipment and environment. Also, the use of underwater vehicles for deep ocean survey, exploration, bathymetric mapping and reconnaissance missions, has become lately more widespread. The employment of such vehicles in complex missions requires high precision and maneuverability.

This thesis focuses on thrust estimation and control of marine propellers with particular attention to four-quadrant operations, in which the propeller shaft speed and the propeller inflow velocity (advance speed) assume values in the whole plane. In the overall control system, propellers play a fundamental role since they are the main force producing devices. The primary objective of the thruster controller is to obtain the desired thrust from the propeller regardless the environmental state. During operations, propellers are often affected by thrust losses due to e.g. changes in the in-line water velocity, cross flows, ventilation, in-and-out of water effects, wave-induced water velocities, interaction between the vessel hull and the propeller and between propellers. Propellers may thus work far from ideal conditions. Therefore, the knowledge of the propeller thrust and torque, together with forces induced by the interaction between the vehicle and propellers and between propellers, is fundamental to achieve high control performance. Unfortunately a propeller system is usually not equipped with thrust and torque sensors, therefore thrust losses are not directly measured.

Motivated by this, a new four-quadrant thrust estimation scheme is presented, extending previous results valid for propeller operating in two quadrants. Based on shaft speed and motor torque measurements, the scheme involves a nonlinear observer for the propeller torque that shows

stability and robustness for bounded modeling and measurement errors. The propeller thrust is computed as a static function of the propeller torque. The performance is demonstrated in experimental tests, showing improved accuracy in the thrust reproduction with respect to the direct use of the four-quadrant propeller characteristics.

A nonlinear observer for the torque loss estimation, similar to the one implemented in the thrust estimation scheme, is included in a new four-quadrant nonlinear thrust controller, designed for calm and moderate sea conditions. The control strategy is based on a shaft speed controller where the desired velocity is computed from the desired propeller thrust and on the torque losses. Experimental results are provided, demonstrating the effectiveness of the new controller with respect to the conventional shaft speed and torque controllers.

The thrust controller, designed for calm and moderate sea conditions, is subsequently improved by including an anti-spin strategy to reduce power peaks and wear-and-tear in extreme sea conditions. The anti-spin strategy is derived from previous works that were designed for Dynamics Positioning (DP) operations. The presented controller can operate also for maneuvering and transit operations, where the vehicle speed is larger than in DP operations. The performance of the controller is validated by experimental tests.

Motivated by environmental issues and the need of reduced fuel consumption and CO_2 emissions, a novel control scheme for improving, in moderate sea, the propulsion efficiency with respect to conventional propeller controllers is presented. The main idea is to exploit the variation in the advance speed due to waves to increase the average propulsion efficiency without reducing the vessel speed. A nonlinear controller is proposed showing that, theoretically, is possible to increase the propulsion efficiency. Model tests determine dynamic characteristics of propellers in waves and a simulation is employed to validate the novel control scheme.

Acknowledgments

This thesis is the result of my doctoral studies, primarily carried out at the Norwegian University of Technology and Science (NTNU) and partly at Johns Hopkins University in Baltimore within the period August 2004 - August 2007. The research has been performed within the project Computational Methods in Nonlinear Motion Control sponsored by the Research Council of Norway (NFR).

Most of all, I would like to thank my supervisor, Professor Tor Arne Johansen at the Department of Engineering Cybernetics at NTNU, which has given me the opportunity to undertake the doctoral study in Norway and to participate to a very interesting project. He has been supporting me during all the research period through his great knowledge in control systems, with his ideas and also with his efficiency in solving practical issues.

I am also thankful to my co-supervisor, Professor Thor Inge Fossen, for many ideas, suggestions, and for his enthusiasm and optimism. Furthermore, I would like to thank Professor Louis L. Whitcomb for inviting me at the Department of Mechanical Engineering at Johns Hopkins University in Baltimore. I have greatly benefited from valuable discussions and advices. I am also grateful to Professor Mogens Blanke for sharing his ideas and for involving me on a challenging project on the optimization of the propulsion efficiency. Professor Sverre Steen is thanked for sharing his knowledge of marine propellers.

I deeply appreciated the discussions with Dr Øyvind Smogeli, for his help on the experimental setup at the laboratory, his new ideas and inspirations that resulted in many jointed publications. The collaboration with Jostein Bakkeheim and Even Børhaug has also been highly appreciated. I would also like to thank my colleagues at the Department of Engineering Cybernetics for making the working environment a great place to work, for their friendship and patience with my poor Norwegian language. In particular, I am thankful to Aksel Transeth, whom I shared the office with and

Johannes Tjønnås for many interesting and philosophical discussion about science, control systems and football. Matthias Schellhase is gratefully acknowledged for the help given during the experimental tests.

Without the help of Knut Arne Hegstad, Torgeir Wahl at Marintek and Stefano Bertelli, Terje Haugen, and Hans Jørgen Berntsen at the Department of Engineering Cybernetics, it would have been impossible to perform experiments. Also, the administrative staff at the Department of Engineering Cybernetics should be thanked for their efficiency and patience.

Finally, I would like to express my gratitude to my girlfriend, Ilaria, for her love and support, and my parents that always supported my choices, even if that kept me far from home.

Trondheim, Norway
January 2008 Luca Pivano

Contents

Chapter 1

Introduction

The topic of this thesis is thrust estimation and control of marine propellers in four-quadrant operations. This chapter will introduce briefly the structure of a typical motion control system of a marine vehicle and will describe the propulsion systems adopted nowadays, giving emphasis to the *low-level thruster control* and explaining the motivation for carrying out this work. Further, the contribution of this thesis will be presented.

1.1 Background and motivation

1.1.1 Structure of a marine vehicle motion control system

The typical structure of the real-time control system of a marine vehicle is usually divided into three levels (Balchen *et al.* (1976), Healey and Marco (1992*a*), Healey and Marco (1992*b*), Sørensen *et al.* (1996), Strand (1999), Fossen (2002), Bray (2003)):

- *Guidance and navigation system*
- *High-level motion control*
- *Low-level thruster control*

A sketch of the control system is shown in Figure 1.1. The block diagram shows signals which are relevant from the control point of view, even though other signals are usually interfaced between the various subsystems, e.g. status signals. The guidance and navigation system is usually employed to generate a reference trajectory or setpoints. This is based on the input reference, which can be previously generated (e.g. contained in a script)

or defined by the operator through a user interface (joystick, keyboard, etc.), and the mission or operation that the vehicle has to perform. The reference trajectory or setpoints are generally computed in combination with reference models, desired degree of precision for the mission, filtered measurements from sensors and other available data, e.g. earth topographical information. This could also involve anti-collision and anti-grounding functions. The guidance and navigation system may include, for example, setpoint chasing, trajectory tracking, and weather-vaning functions.

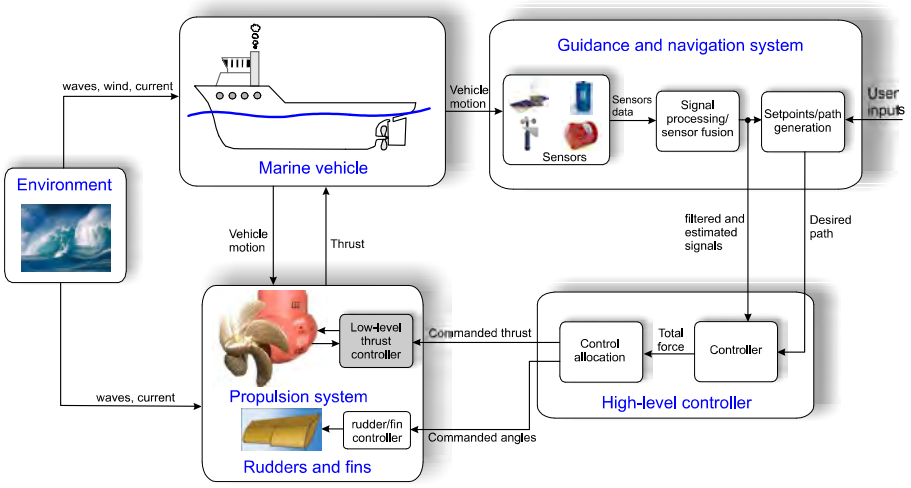

Figure 1.1: Sketch of a marine vehicle control system.

The high-level motion control computes the commanded forces and moments for tracking the desired path defined by the guidance and navigation system. Traditionally, model based PID controllers are employed, where an integral action is commonly used to counteract slow varying environmental loads and unmodeled dynamics. For surface vessels equipped with dynamic positioning (DP) systems or thruster assisted position mooring (PM) systems, a feedforward action is usually adopted in the control law to directly counteract for wind forces. The integral action compensates for drift forces due to waves and ocean currents (see for example Sørensen *et al.* (1996), Strand (1999), Fossen (2002), Bray (2003) and references therein). Similarly for underwater vehicles, which are not affected by wind and waves, ocean currents are not directly compensated by feedforward terms since they are not usually measured. Also in this case, integral action is usually adopted in the control laws (see Fossen (1991), Healey and Lienard

(1993), Fossen and Fjellstad (1995), Encarnação *et al.* (2000), Alonge *et al.* (2001), Smallwood and Whitcomb (2004), Børhaug and Pettersen (2005), Refsnes *et al.* (2007) and reference therein). More recently, nonlinear observers for the estimation of the ocean current were developed since its direct compensation may result in better control performance (Refsnes *et al.* (2006), Børhaug *et al.* (2007)). The high-level plant control includes also the control allocation algorithm and the power management system (not always present on underwater vehicles). The control allocation algorithm computes, from the total force and moment, the required force from each actuator: thrusters, rudders, control surfaces and stabilizing fins. This is usually performed according to optimization criteria, for example, minimization of the fuel consumption (or power consumption), drag, the mechanical wear-and-tear of the propulsion systems and others, e.g. actuator position limitations (see for example Lindfors (1993), Sørdalen (1997), Berge and Fossen (1997), Fossen (2002), Lindegaard and Fossen (2003), Johansen *et al.* (2004), Johansen *et al.* (2008) and Tjønnås and Johansen (2007)).

The thrust command is sent to the low-level thruster control which controls the thrusters in order to obtain the required force. It is also often possible to command the thrusters manually, sending the command directly to the low-level thruster control by using handles on the operator station. A brief description of different propulsion systems is given in the next section.

1.1.2 Propulsion and thruster systems

Different propulsion and thruster systems are nowadays employed on marine vehicles. Typically, a propulsion system should be defined as the equipment employed during transit while a thruster system should describe the equipment used for low-speed and DP. In this work, they will be treated as equivalent. Generally, surface vessels can be equipped with tunnel thrusters, azimuth thrusters, podded propulsion units and main propellers positioned aft of the hull. Tunnel thrusters are primarily used for docking, slow speed maneuvering, emergency steering and station keeping. They are installed athwartship or in the stern of the vessel in a tunnel positioned in the lower part of the hull. The usually employ fixed pitch propellers (FPP), i.e. the blade angle is fixed. Azimuth thrusters can direct the thrust in any direction by rotating along a vertical axis. They are used for both main propulsion and steering. They are employed when enhanced maneuverability is required in applications such as dynamic positioning, ship escort and ship docking services. Both tunnel and azimuth

thrusters can be driven by electric motors, diesel engines and hydraulic systems. Both fixed pitch and controllable pitch propellers (CPP), in the configuration with or without a duct surrounding the propeller, are used. Podded propulsion units are similar to azimuth thrusters because they can also rotate and can be used for main propulsion. They are usually driven by an electric motor which is placed in the pod external to the hull and they mainly employ FPP. The propellers positioned aft of the hull are used to generate the main thrust for propulsion. They can be connected directly to diesel engines through a shaft and gear-box or driven by electric motors or hydraulic system. Both FPP and CPP are employed for the main propulsion. Other type of propulsion systems are: water jets, Gill jets and Voith Schneider propellers.

As well as surface vessel, underwater vehicles can present different thruster configurations due to the type of operations that they are used for. Remotely operated vehicles (ROVs) are usually equipped with five or six fixed pitch propellers in order to guarantee high degree of maneuverability (Smallwood and Whitcomb (2003), Fossen (2002)). Others, like slender autonomous underwater vehicles (AUV) may be fitted with just one or two main propellers, tunnel thrusters for station keeping and low speed maneuvering and use fins for steering and for controlling the vehicle depth (Kristensen and Vestgard (1998), Stokey *et al.* (2005), Pascoal *et al.* (1997)). In some cases, vehicles are equipped with thrusters that can rotate, so that they can be used to push the vehicle forward/backward or to produce thrust in the vertical direction to control the depth (Martin *et al.* (2006)). Both electrically driven propellers and hydraulic thrusters, with and without duct, are commonly employed. Further information about thruster configurations can be found for example in Bray (2003), Carlton (1994), and in the web-pages of propulsion system vendors (ABB, Converteam, Fincantieri, Lips, Rolls-Royce, Schottel, Siemens, Thrustmaster, Wärtsilä, etc.).

This thesis will focus on thrusters equipped with fixed pitch propellers disregarding other types of propulsion systems.

1.1.3 Low-level thruster control

A block diagram of the propulsion system, including the low-level thruster control, is depicted in Figure 1.2. The primary objective of the low-level thruster controller is to obtain the desired thrust from the propeller regardless of the environmental state and vessel motion. The thrust tracking capability is one of the performance criteria considered in a thruster con-

troller. It is also very important to take into account the power consumption as well as the power fluctuations and the mechanical wear-and-tear of the propulsion system.

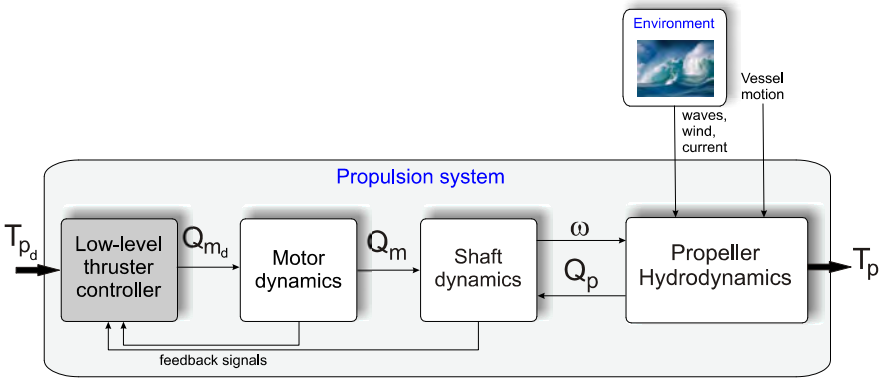

Figure 1.2: Block diagram of the propulsion system.

When a marine vehicle performs an operation, propellers are often affected by thrust losses due to the influence of the environment, vehicle motion, and the interaction between the vehicle and propellers and between propellers. Propellers may thus work far from ideal conditions therefore, knowledge of the propeller thrust and torque is fundamental to achieve high vehicle control performance. As reported in Smogeli *et al.* (2005), today's industrial standard for fixed pitch propellers is shaft speed control where the desired shaft speed is computed from the desired thrust through a static mapping. Conventionally, also torque and power control are employed for propellers (see for example Smogeli *et al.* (2005), Sørensen *et al.* (1997) and Blanke and Nielsen (1990)). In general, these controller schemes do not employ the actual value of the propeller thrust since it is not usually measured. Therefore, when large thrust losses occur, the performance of the low-level thruster control may be reduced, possibly leading to unsatisfactory vehicle behaviour.

Compared to the high-level vehicle motion control, the low-level thruster control has been subject to less focus in the scientific community but, in the last years, modeling and control of propellers has become a topic of growing interest. Much research has been carried out on the identification of the dynamics of propellers for underwater vehicles (Yoerger *et al.* (1990), Healey *et al.* (1995), Blanke *et al.* (2000), Bachmayer *et al.* (2000), Kim and Chung (2006), Pivano *et al.* (2006*c*)). The incorporation of precise

models in the low-level thruster controller may improve the overall vehicle performance (Fossen and Blanke (2000), Guibert *et al.* (2005), Kim *et al.* (n.d.), Pivano *et al.* (2007*a*)).

Due to the increased use of electrically driven propellers, in addition to the classical propeller shaft speed controller (Blanke and Nielsen (1990)), new controller designs and monitoring schemes have been presented for surface ship (Sørensen *et al.* (1997), Blanke *et al.* (1998), Strand (1999), Smogeli *et al.* (2004*a*), Smogeli *et al.* (2005), Smogeli (2006), Pivano *et al.* (2006*b*), Pivano *et al.* (2006*a*), Pivano *et al.* (2007*b*), Blanke *et al.* (2007)).

Particular attention has been also given to the thruster control for extreme sea conditions, where, due to the motion of the vessel in waves, propellers are often subject to ventilation and in-and-out of water effect that cause large thrust and torque losses (see for example Shiba (1953), Minsaas *et al.* (1987), Smogeli *et al.* (2003), Koushan (2004), Koushan (2006*b*), Koushan (2007)). Ventilation occurs when surface air or exhaust gases are drawn into the propeller blades due to a decrease of pressure. This phenomenon is particularly common for heavily loaded propellers that operate close to the water surface. The effect of the ventilation can result in thrust loss up to 80%. Moreover, there have been cases of mechanical failures of power transmission components which were related to ventilation. Control designs for extreme sea conditions aim to limit fluctuations of the consumed power and reduce the mechanical wear-and-tear (Smogeli *et al.* (2003), Smogeli *et al.* (2004*b*), Bakkeheim *et al.* (2006), Smogeli (2006), Bakkeheim *et al.* (2007), Pivano *et al.* (2008*a*)).

Since propellers are the main force producing devices of a marine vehicle, it is clear that the low-level thruster control is of vital importance in the overall control system. The understanding of the propeller dynamics and the interaction between the propeller, the surrounding flows and the vehicle is essential for obtaining a more accurate control of thrust forces and, in consequence, improved vehicle performance with respect to position and speed control. Monitoring of the propeller performance is also important. Knowledge of the actual thrust value may improve fault detection and thrust allocation in different propeller working conditions. This could be achieved with the employment of accurate thrust estimations schemes since marine vehicles are not usually equipped with thrust sensors.

1.2 Contribution and scope of the thesis

The main motivation for the development of thrust estimation schemes and new strategies for the low-level thruster control presented in this thesis was the improvement of the thrust control performance with respect to the conventional thruster controllers. The accuracy in the thrust control was one of the performance criteria adopted, but also the mechanical wear-and-tear, the power consumption and the efficiency of the propulsion system have been considered, especially for moderate and rough sea conditions. In this work, applicable to fixed pitch propeller, particular attention was given to four-quadrant operations, where the propeller shaft speed and the propeller inflow velocity (advance speed) assume values in the whole plane. For example, in station-keeping operations and low speed maneuvering, propellers mainly work in the first and the third quadrant but it is also important to obtain accurate performance in the second and fourth quadrant since they are also explored. For transit operations, however, only the first quadrant is usually explored therefore the accuracy required in the other quadrants is not particularly high. Except for some few exceptions, only positive shaft speed and advance speed were traditionally considered in the literature. The contribution of this thesis can be summarized as follow:

- Chapter 3: A model of the propeller dynamics in four-quadrant operations is derived from experimental data obtained in a towing tank. The model includes the dynamics of the axial flow velocity, measured with an acoustic Doppler velocimeter (ADV), and the shaft speed. This model is compared to the four-quadrant propeller characteristics in terms of thrust and torque reproduction. The results have been published in Pivano *et al.* (2006*c*).

- Chapter 4: A new four-quadrant thrust estimation scheme is presented, extending previous results valid for propeller operating in two quadrants, see Smogeli (2006). Based on shaft speed and motor torque measurements, the scheme involves a nonlinear observer for the propeller torque that shows stability and robustness for bounded modeling and measurement errors. The propeller thrust is computed as a static function of the propeller torque. The performance has been demonstrated in experimental tests. The results of this work have been published in Pivano *et al.* (2006*b*) and Pivano *et al.* (2006*a*). In addition, the article Pivano *et al.* (2008*b*) has been accepted for publication.

- Chapter 5: A four-quadrant nonlinear thrust controller, designed for calm and moderate sea conditions, is presented. It is based on a shaft speed controller where the desired velocity is computed from the desired propeller thrust and the torque loss, estimated with a nonlinear observer. Experimental results are provided to demonstrate the effectiveness of the controller with respect to conventional control strategies. The main contributions of this chapter have been published Pivano *et al.* (2007*b*).

- Chapter 6: The four-quadrant nonlinear thrust controller presented in Chapter 5 is applied to the velocity control of an underwater vehicle. A simulation study is performed in order to compare the performance of the underwater vehicle when employing the new thrust controller with respect to the use of the conventional shaft speed and torque propeller controllers. The result of this work has been published in Pivano *et al.* (2007*a*).

- Chapter 7: The thrust controller, designed for calm and moderate sea conditions, is improved by including an anti-spin strategy to reduce power peaks and wear-and-tear in extreme sea conditions. The anti-spin algorithm is derived from Smogeli *et al.* (2004*b*) and Smogeli (2006), where the anti-spin controllers were designed for DP operations. The presented controller can operate also for maneuvering and transit operations, where the vehicle speed is larger than in DP operations. The performance of the controller is validated by experimental tests. The developed anti-spin algorithm has been published in Bakkeheim *et al.* (2007) and will also appear in Pivano *et al.* (2008*a*).

- Chapter 8: A novel control scheme for improving the propulsion efficiency in moderate sea, with respect to conventional propeller controllers, is presented. The main idea is to exploit the variation in the advance speed due to waves to increase the average propulsion efficiency without reducing the vessel speed. A nonlinear controller is proposed showing that, theoretically, is possible to increase the propulsion efficiency. Model tests are carried out to determine dynamic characteristics of propellers in waves and a simulation is employed to validate the novel control scheme. The results have been presented in Blanke *et al.* (2007).

Figure 1.3: Photograph of a main propeller (www.wartsila.com)

1.3 List of publications

The following is the list of the author's publications related to the work presented in the thesis.

- L. Pivano, T.A. Johansen and Ø.N. Smogeli - A Four-Quadrant Thrust Controller for Marine Propellers with Loss Estimation and Anti-Spin: Theory and Experiments - *Submitted to Automatica*

- L. Pivano, J. Bakkeheim, T.A. Johansen and Ø.N. Smogeli - A Four-Quadrant Thrust Controller for Marine Propellers with Loss Estimation and Anti-Spin - *To appear at the IFAC World Congress 2008*, 6-11 July, 2008, Seoul, Korea

- L. Pivano, Ø.N. Smogeli and T.A. Johansen - A Four-Quadrant Thrust Estimation Scheme for Marine Propellers: Theory and Experiments - *To appear, as a brief paper, in IEEE Transaction on Control System Technology.*

- L. Pivano, L. L. Whitcomb, T.A. Johansen and T.I. Fossen - Preliminary Simulation Studies of a New Four-Quadrant Propeller Thrust Controller Applied to Underwater Vehicles - *IFAC Conference on Control Applications in Marine Systems (CAMS'2007)*, 19-21 September, Bol, Croatia

- M. Blanke, L. Pivano and T.A. Johansen - An Efficiency Optimizing Propeller Speed Control for Ships in Moderate Seas - Model Experiments and Simulation - *IFAC Conference on Control Applications in Marine Systems (CAMS'2007)*, 19-21 September, Bol, Croatia

- J. Bakkeheim, L. Pivano, T.A. Johansen and Ø.N. Smogeli - Integrator Reset Anti-spin for Marine Thrusters Operating in Four-Quadrants and Extreme Sea Conditions - *IFAC Conference on Control Applications in Marine Systems (CAMS'2007)*, 19-21 September, Bol, Croatia

- E. Børhaug, L. Pivano, K. Y. Pettersen and T.A. Johansen - A Model-Based Ocean Current Observer for 6DOF Underwater Vehicles - *IFAC Conference on Control Applications in Marine Systems (CAMS'2007)*, 19-21 September, Bol, Croatia

- L. Pivano, T.A. Johansen, Ø.N. Smogeli and T.I. Fossen - Nonlinear Thrust Controller for Marine Propellers in Four-Quadrant Operations - 2007 American Control Conference (ACC2007), July 11-13, 2007, New York, USA

- L. Pivano, Ø.N. Smogeli, T.I. Fossen and T.A. Johansen - Experimental Validation of a Marine Propeller Thrust Estimation Scheme - 7th Conference on Manoeuvring and Control of Marine Craft (MCMC'2006), Lisbon, Portugal

- L. Pivano, Ø.N. Smogeli, T.A. Johansen and T.I. Fossen - Marine Propeller Thrust Estimation in Four-Quadrant Operations - *45th IEEE Conference on Decision and Control (CDC'2006)*, San Diego, US

- L. Pivano, T.I. Fossen and T.A. Johansen - Nonlinear Model Identification of a Marine Propeller over Four-Quadrant Operations -*14th IFAC Symposium on System Identification, SYSID-2006* , Newcastle, Australia

Chapter 2

Experimental setup: Marine Cybernetics Laboratory

The tests presented in this thesis were performed on model scale propellers and carried out at the Marine Cybernetics Laboratory[1] (MCLab), an experimental laboratory located at NTNU in Trondheim (see Appendix A.5 for scaling factors). The basin, 6.45 m wide, 40 m long and 1.5 m deep, is equipped with a 6 DOF towing carriage that can reach a maximum speed of 2 m/s, and a wave generator able to generate waves up to 30 cm. A picture of the towing carriage is presented in Figure 2.1.

A three phase brushless motor was employed in combination with a drive equipped with a built-in torque controller and a built-in shaft speed controller. In this way we could choose to control the motor torque or the shaft speed. The built-in torque controller furnished the desired motor torque practically instantaneously due to the dynamics of the electrical part of the system (frequency converter, stator and rotor) being much faster than the shaft dynamics. The motor was connected to the propeller shaft through a gear-box with ratio 1:1.

Electrically driven propellers (diesel-electric propulsion systems) are often employed on ships nowadays. Contrary to the conventional arrangement where the prime mover diesel engine provides propulsion power and the auxiliary engines provide electricity, the diesel-electric propulsion system provides electricity (with a generator) for both propulsion and energy needs of the ship. A frequency converter is disposed between the power bus and the motor which is usually coupled to the propeller shaft through a gearbox.

[1] (http://www.itk.ntnu.no/marinkyb/MCLab/)

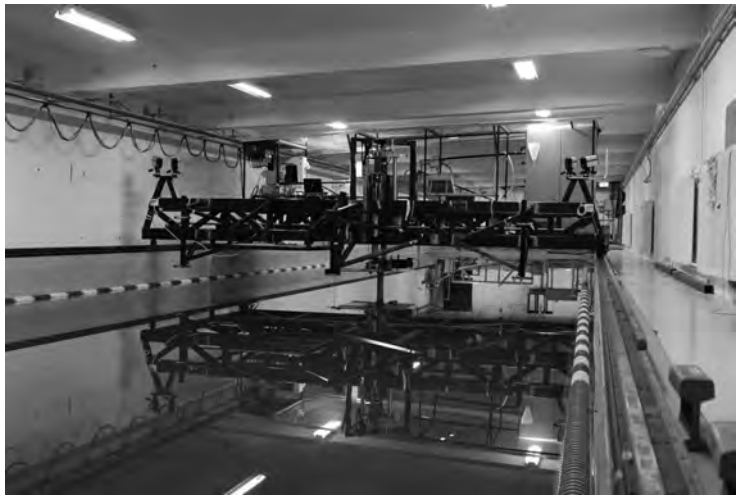

Figure 2.1: Picture of the towing carriage.

The rig with motor, underwater housing, shaft and propeller was attached to the towing carriage in order to move the propeller through the water. The towing carriage allowed also the rotation of the propeller housing about its vertical axis and to change the propeller submergence. These two DOF have been exploited to simulate turns of a vehicle and the vertical motion that propeller may experience in extreme sea conditions due to the wave induced motion of the vessel. A PC onboard the carriage was used to control the motor drive and to acquire the signals from the sensors. The code was written in the Matlab/Simulink® environment, employing the real-time system Opal RT-Lab®. A sketch of the propeller system is shown in Figure 2.2.

Different fixed pitch propellers, with geometrical characteristics given in Tables 2.1, 2.2 and 2.3, have been employed during the experiments. Tests have been mainly conducted on unducted propellers (P1362 and P1020) and few times on a propeller with an accelerating duct (P1009). Figures 2.3 and 2.4 show the propellers P1009 and P1020, respectively.

Some experiments have been carried out with a wake screen, shown in Figure 2.5, placed upstream the propeller. The wake screen reduced uniformly the water velocity into the propeller disc at forward towing carriage speed. It was employed in order to simulate one of the effects of the hull on the propeller inflow.

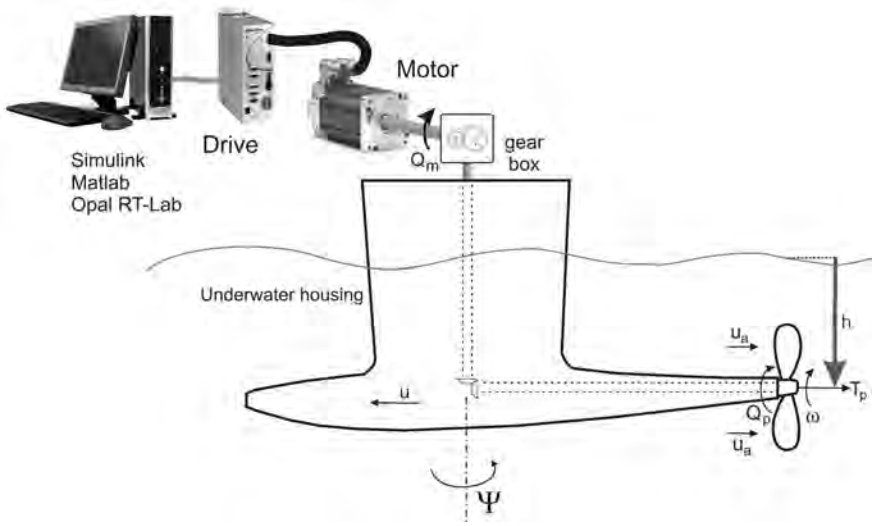

Figure 2.2: Sketch of the experimental setup.

Table 2.1: Geometrical parameters of the propeller P1362.

Parameter	Value	Description
D	0.25 m	Propeller diameter
Z	4	Number of blades
P/D	1	Pitch ratio P/D
A_e/A_0	0.58	Expanded blade area ratio

2.1 Instrumentation

The signals measured in the experiments are listed below. Beside that, we logged also some other useful parameters and state variables, e.g. shaft speed reference when testing the shaft speed control law.

- The *propeller shaft speed*, defined by ω, was measured on the motor shaft with a tachometer dynamo. Figure 2.6 shows an example of a raw and a filtered version of the shaft speed measurement.

- The *propeller thrust and torque*, denoted T_p and Q_p, were measured with an inductive transducer and a strain gauge transducer placed on the propeller shaft, respectively. Both signals were quite noisy due to the nature of the sensors and vibrations of the propeller shaft.

Table 2.2: Geometrical parameters of the propeller P1020.

Parameter	Value	Description
D	0.25 m	Propeller diameter
Z	4	Number of blades
P/D	1	Pitch ratio P/D
A_e/A_0	0.55	Expanded blade area ratio

Table 2.3: Geometrical parameters of the propeller P1009.

Parameter	Value	Description
D	0.24 m	Propeller diameter
Z	4	Number of blades
P/D	1	Pitch ratio P/D
A_e/A_0	0.47	Expanded blade area ratio

Figures 2.7 shows an example of thrust and torque measurements.

- The *duct thrust* was measured with a strain gauge placed in the duct support structure. The signal, shown in Figure 2.8, presents high frequency noise, probably due to vibrations of the duct.

- The *motor torque* signal Q_m was furnished by the motor drive. This signal, shown in Figure 2.9, was also heavily corrupted by noise.

- The *propeller submergence* h, defined equal to zero when the center of the propeller was at the water level and positive when the propeller was submerged, was measured with a water level probe. At large towing carriage speed, the measurement was affected by high frequency noise due to probe vibrations. A sample of this signal is shown in Figure 2.10.

- The *propeller axial flow velocity* u_p, defined as the speed of the water at the propeller disc measured at some convenient radial position, was acquired with a Sontek 10 MHz 3D Acoustic Doppler Velocimeter (ADV). The ADV uses acoustic Doppler technology to measure 3D flow in a small sampling volume (0.25 cm^3) located at a fixed distance (10 cm) from the probe. Data were acquired with a sampling rate of 25 Hz. With no zero offset, the ADV can measure flow velocities from less than 1 mm/s to 3 m/s. Figure 2.11 shows an example of the axial flow velocity measurement obtained 7 cm downstream the propeller

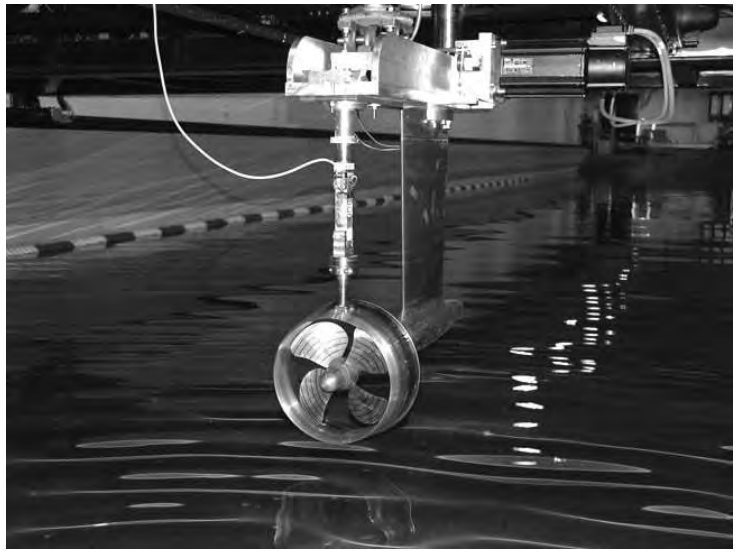

Figure 2.3: Picture of the ducted propeller P1009.

at radial position $0.7R$, where R is the propeller radius. Figure 2.12 shows how the ADV probe was mounted in our system.

- The *towing carriage position* TC_{pos}, shown in Fig 2.13, was provided by the towing carriage speed control system. Due to the low noise level of this measurement, the computed towing carriage speed u was accurate.

- The *propeller housing yaw angle* Ψ, measured about the vertical axis of the housing, was also provided by the towing carriage speed control system. A sample of data is presented in Figure 2.14.

All the signals were acquired at the frequency of 200Hz. The ADV measurement, originally with a sampling frequency of 25 Hz, was oversampled.

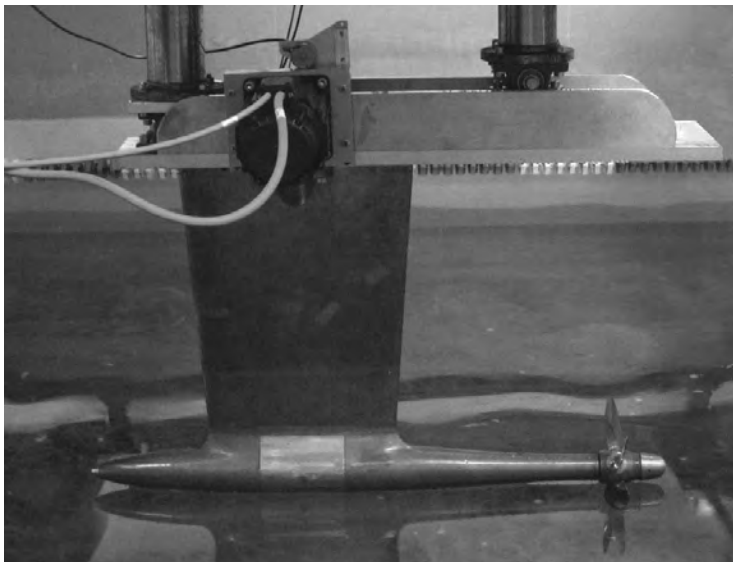

Figure 2.4: Picture of the unducted propeller P1020.

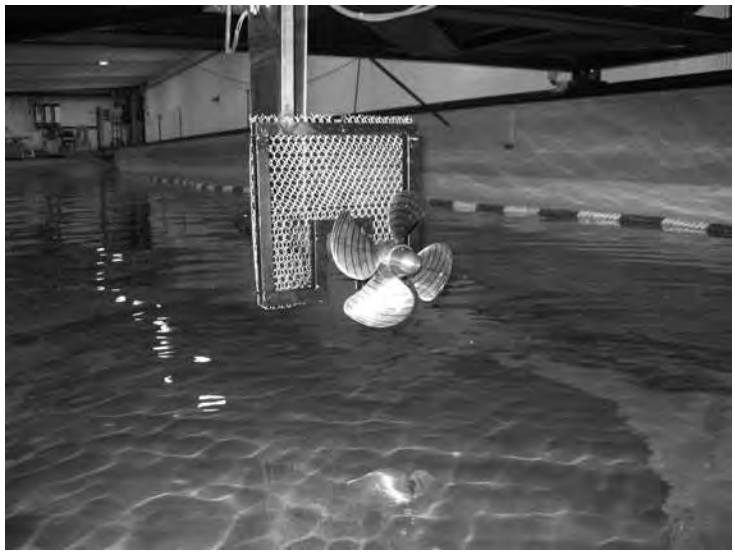

Figure 2.5: Picture of the propeller P1362 with the wake screen.

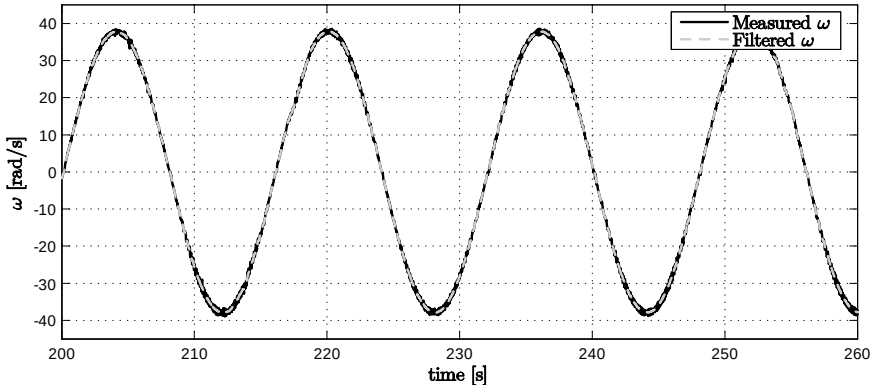

Figure 2.6: Measured and filtered shaft speed signal.

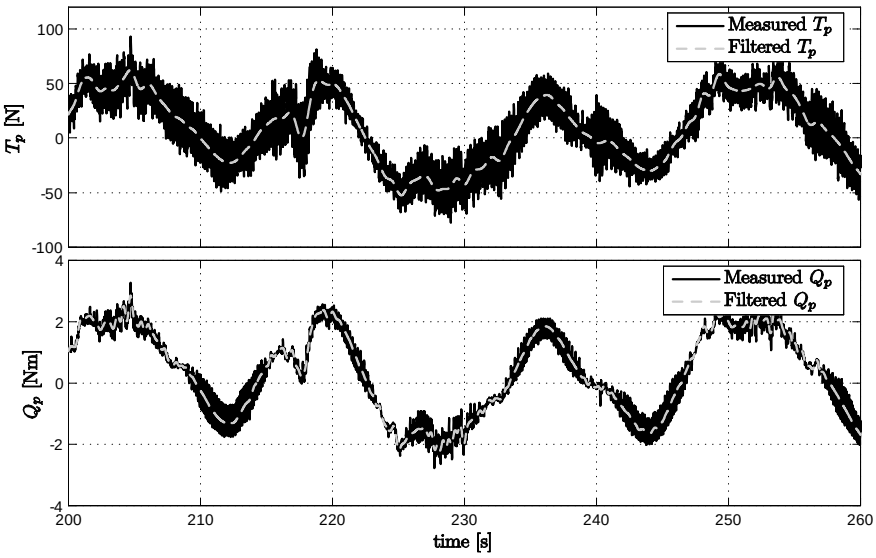

Figure 2.7: Measured and filtered propeller thrust and torque signals.

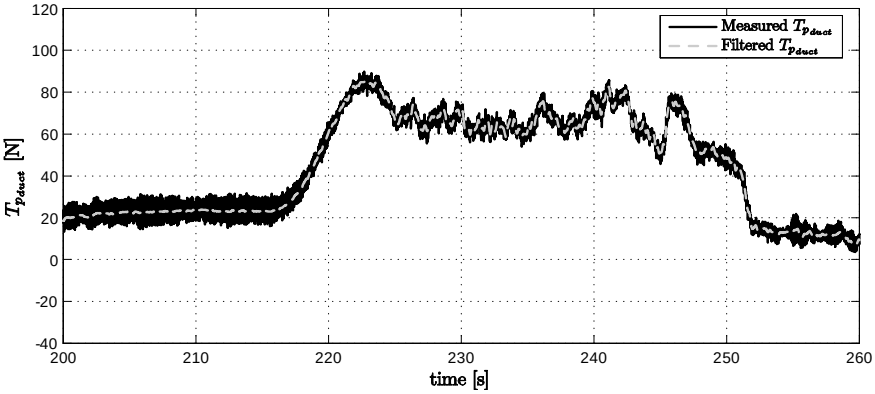

Figure 2.8: Measured and filtered duct thrust signal.

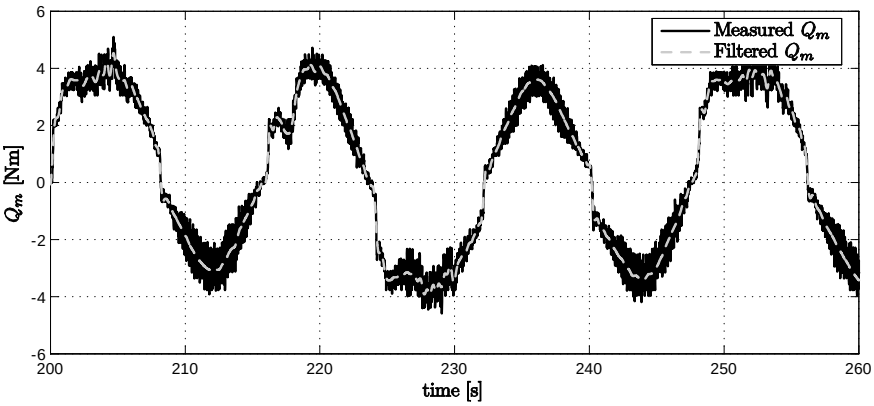

Figure 2.9: Measured and filtered motor torque signal.

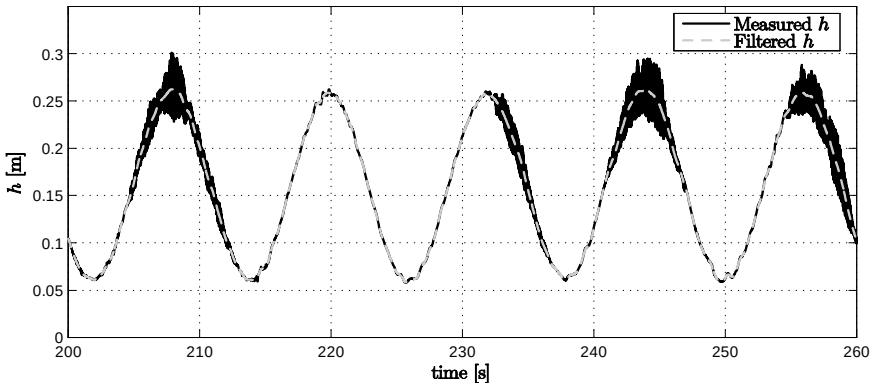

Figure 2.10: Measured and filtered propeller submergence signal.

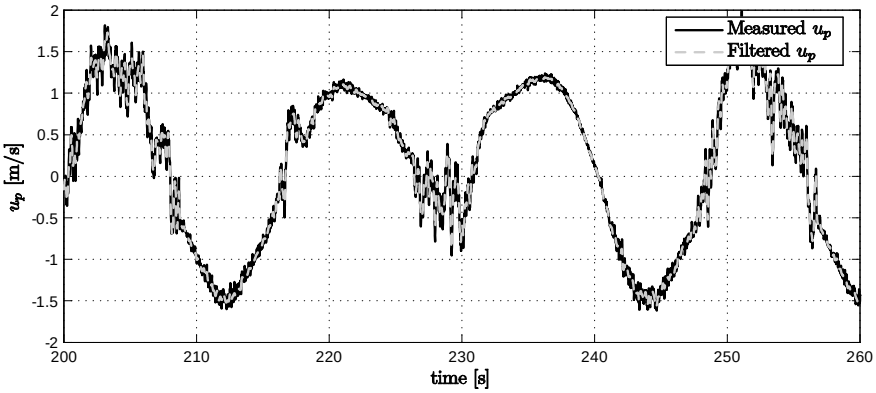

Figure 2.11: Measured and filtered axial flow velocity signal.

Figure 2.12: Picture of the ADV probe.

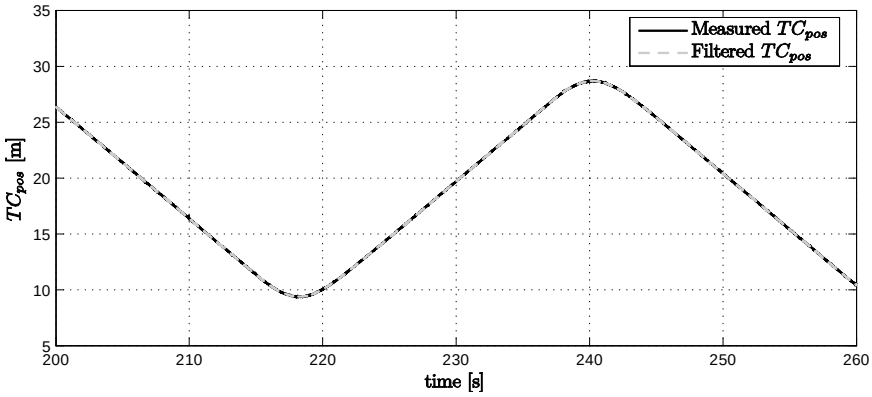

Figure 2.13: Measured and filtered towing carriage position signal.

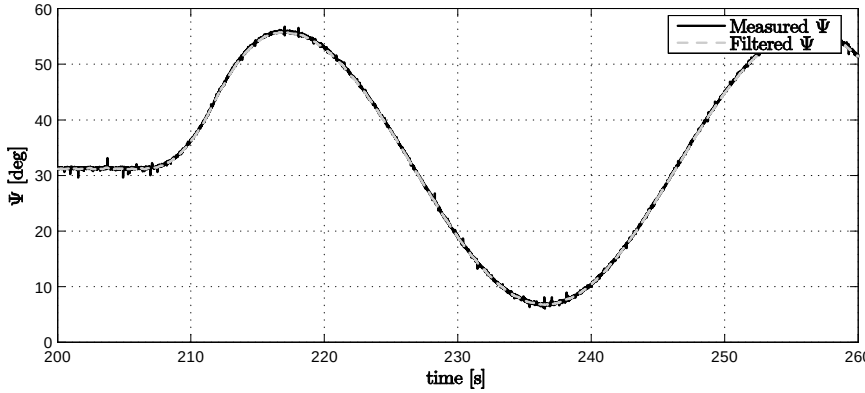

Figure 2.14: Measured and filtered propeller housing yaw angle.

Chapter 3

Propeller modeling

When designing a marine vehicle control system, the main difficulties in achieving high vehicle performance lie in the modeling of the dynamics of the vehicle and propellers and in the problem of measuring the environmental state. Since propellers are the main force producing devices of a marine vehicle, the vehicle control performance would benefit from accurate propeller modeling. The latter has been the focus of many works in the last years. See for example Blanke (1981), Healey *et al.* (1995), Bachmayer *et al.* (2000), Blanke *et al.* (2000), Kim and Chung (2006) and the references therein. Difficulties in the prediction of the produced thrust, generally not measured, arise because propellers are often affected by thrust losses due to changes in the in-line water velocity, cross flows, ventilation, in-and-out of water effects, wave-induced water velocities, interaction between the vessel hull and propellers and between propellers. Propeller losses are treated, for example, in Lehn (1992), Sørensen *et al.* (1997) and in Smogeli (2006). Propeller models are usually chosen based upon the propeller application. For ship in transit, for example, modeling should particularly focus in obtaining accurate thrust and torque values for positive shaft speed and advance speed. For dynamic positioning systems, more importance should be given to low advance speed regimes, considering that propellers may operate in all the four quadrants of the plane composed by the shaft speed and the advance speed.

This chapter is organized as follows. The propeller system is described in Section 3.1. The propeller shaft dynamics and the motor dynamics are presented in Sections 3.2 and 3.3, respectively. The open-water propeller characteristics are described in Section 3.4. The effects of the flow dynamics on the propeller thrust and torque are illustrated in Section 3.5. Simplified

torque models are given in Section 3.6.

3.1 Description of the propeller system

We consider a propulsion system composed by a fixed pitch propeller driven either by an electric motor or a diesel engine through a shaft and a gear box. A block diagram that represents the system is shown in Figure 3.1.

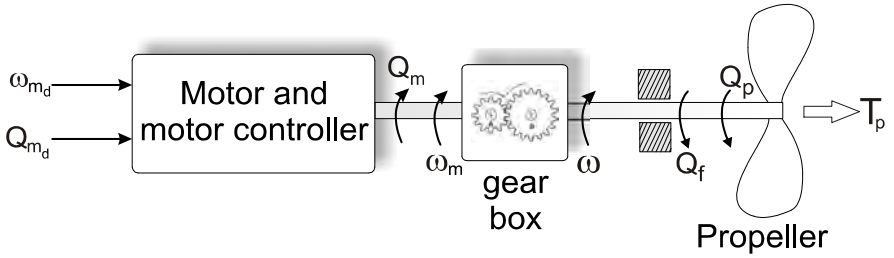

Figure 3.1: Block diagram of the propeller system.

Referring to the block diagram of Figure 3.1, the motor torque applied to the shaft is defined by Q_m. The gear ratio is defined by $R_{gb} = \omega_m/\omega$, where ω_m is the motor shaft angular speed and ω is the propeller angular speed. The value of ω is particularly influenced by the load, represented by the propeller torque Q_p, due to the rotation of the blades in the water. The shaft friction torque is denoted Q_f. The output of the system is the thrust T_p produced by the propeller. The desired motor torque and motor shaft speed are defined by Q_{m_d} and ω_{m_d}, respectively. Usually, the motor controller can regulate either the shaft speed or the motor torque. In some cases both controllers are available.

3.2 Propeller shaft dynamics

The shaft dynamics is derived by considering the motor connected to the propeller through a rigid shaft and a gear-box with gear ratio R_{gb}, as shown in the block diagram of Figure 3.1. The shaft is considered affected by a friction torque denoted $Q_f(\omega)$, which is assumed to depend only upon the shaft speed. The shaft dynamics can be written as

$$J_m\dot{\omega} = R_{gb}Q_m - Q_p - Q_f(\omega), \tag{3.1}$$

where J_m is the total moment of inertia including the shaft, the gear box and the propeller. The shaft moment of inertia should, in general, include the effect of the hydrodynamic added mass proportional to $\dot{\omega}$, which result in a time varying moment of inertia. The added mass has been treated in Parsons and Vorus (1981) and Wereldsma (1965) in the context of propeller vibrations. Experiments presented in Parsons and Vorus (1981) showed the dependence of the added mass from the advance speed. It is natural to assume that the propeller submergence may also affect the added mass. When the propeller rotates close to the water surface, the volume of water surrounding the propeller is much smaller than for deeply submerged propeller. In the presented work, the added mass has been neglected due to the fact that its effect appeared to be not very significant and quite difficult to model.

Motivated by experiments carried out in the laboratory, the friction torque has been modeled as

$$Q_f(\omega) = k_{f_1} \arctan\left(\frac{\omega}{\epsilon}\right) + k_{f_2}\omega + k_{f_3} \arctan(k_{f_4}\omega), \tag{3.2}$$

where the Coulomb effect, usually written as a $\text{sign}(\omega)$, has been replaced by the function $\frac{2}{\pi}\arctan(\frac{\omega}{\epsilon})$ with a small positive ϵ in order to avoid the discontinuity for $\omega = 0$. The remaining terms in (3.2) represent a linear and a nonlinear viscous effect. All the coefficients k_{f_i} are constant and positive. The static friction model in (3.2) is able to approximate the friction torques experienced in practice; see Bachmayer *et al.* (2000), Kim and Chung (2006) and Pivano *et al.* (2006*a*). More complex static and dynamics models (LuGre models, Karnopp's model, etc.) may be used, but they are not considered in the current work.

3.2.1 Shaft moment of inertia and friction torque identification: experimental results

To identify the friction torque and the shaft moment of inertia, tests were performed with different motor torque profiles and various towing carriage speeds. The desired motor torque was obtained by employing the built-in torque controller in the motor drive. From the measurement of the propeller angular speed, the motor torque and the propeller torque, and computing the derivative of ω with the necessary filtering, we identified the parameters k_{f_i} of the friction torque model in (3.2) and the shaft moment of inertia J_m. The parameters k_{f_i} and J_m can be grouped in the vector

$$\theta = \begin{bmatrix} k_{f_1} & k_{f_2} & k_{f_3} & k_{f_4} & J_m \end{bmatrix}^T. \tag{3.3}$$

With $R_{gb} = 1$ and defining $z = Q_m - Q_p$, θ was computed over a time-series of N samples as

$$\theta = \arg\min_{\theta} \sum_{i=1}^{N} \left| z_i - Q_f(\omega_i, \theta_1, \theta_2, \theta_3, \theta_4) - \theta_5 \dot{\omega}_i \right|^2 , \tag{3.4}$$

where the subscript i indicates the i-th sample. See for examples Gill *et al.* (1981). The parameters obtained with the propeller P1362 are shown in Table 3.1.

Table 3.1: Friction model parameters and shaft moment of inertia.

Parameter	Value	Parameter	Value
J_m	$6.07 \cdot 10^{-3}$	k_{f_3}	$6.61 \cdot 10^{-3}$
k_{f_1}	$3.97 \cdot 10^{-1}$	k_{f_4}	$8.94 \cdot 10^{-2}$
k_{f_2}	$9.28 \cdot 10^{-3}$	ϵ	$1 \cdot 10^{-3}$

Figure 3.2 shows the friction torque computed from measurements and the identified model. The friction exhibited a nonlinear behavior and was affected by the temperature in the gears, bearings and oil. It presented also a hysteresis effect, but its influence was not very significant and it has been neglected. Also, the friction torque in the tested system was quite large. Losses due to the friction torque are generally more significant for small propeller systems, e.g. for underwater vehicles and for model scale tests, than for full scale propellers for ships.

Remark 3.1 *For full scale ships, where the propeller torque measurement is usually not available, z can be obtained from the motor torque measurement by performing tests with the propeller in air, where the propeller load torque is negligible.*

3.3 Motor dynamics

3.3.1 Electric motors

In electric motors, the motor torque is controlled by means of motor currents, voltages and motor fluxes (depending on the type of motor). The dynamics of the electrical part of the system (frequency converter, stator and rotor) is usually much faster than the propeller shaft dynamics and can be often neglected. However, for small propellers, the time constants of the

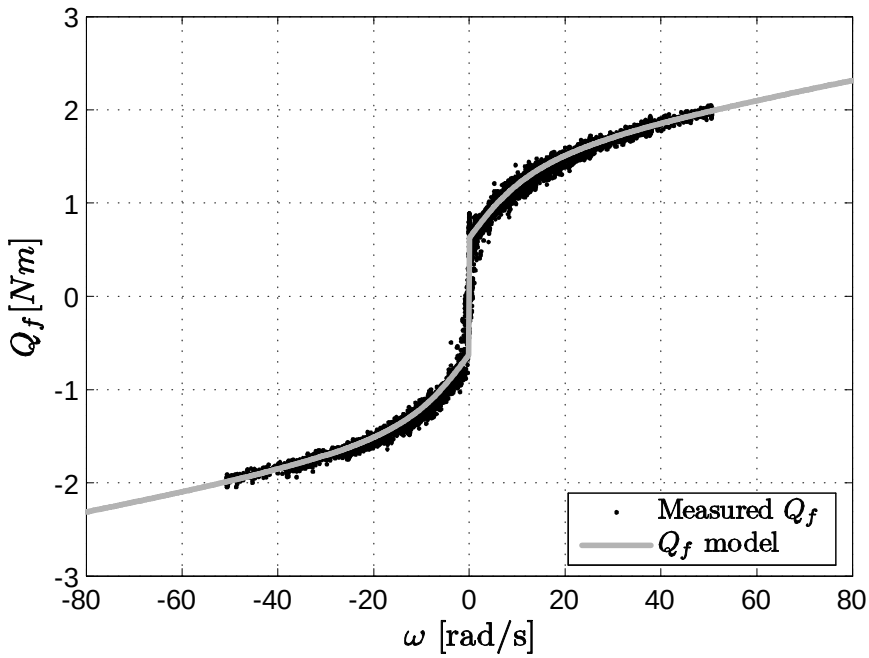

Figure 3.2: Friction torque: computed from measurements and the identified nonlinear static model.

electrical and the mechanical system may be comparable. In this case the motor dynamics should be considered. According to Leonard (2001), the motor torque dynamics can be described by the first order filter

$$Q_m = \frac{1}{T_m}\left(Q_{m_d} - Q_m\right), \tag{3.5}$$

where the time constant T_m needs to be identified. In our setup, the torque controller was sufficiently fast; therefore the motor dynamics has been neglected, i.e. $Q_{m_d} = Q_m$. As shown in Figure 3.3, the measured motor torque signal is almost indistinguishable from the desired one.

3.3.2 Diesel engines

The dynamics of diesel engines is quite complex and, generally, it is slower than the dynamics of electric motors. See Makartchouk (2002) and Xiros (2002). For control purposes, simple models are usually employed. For

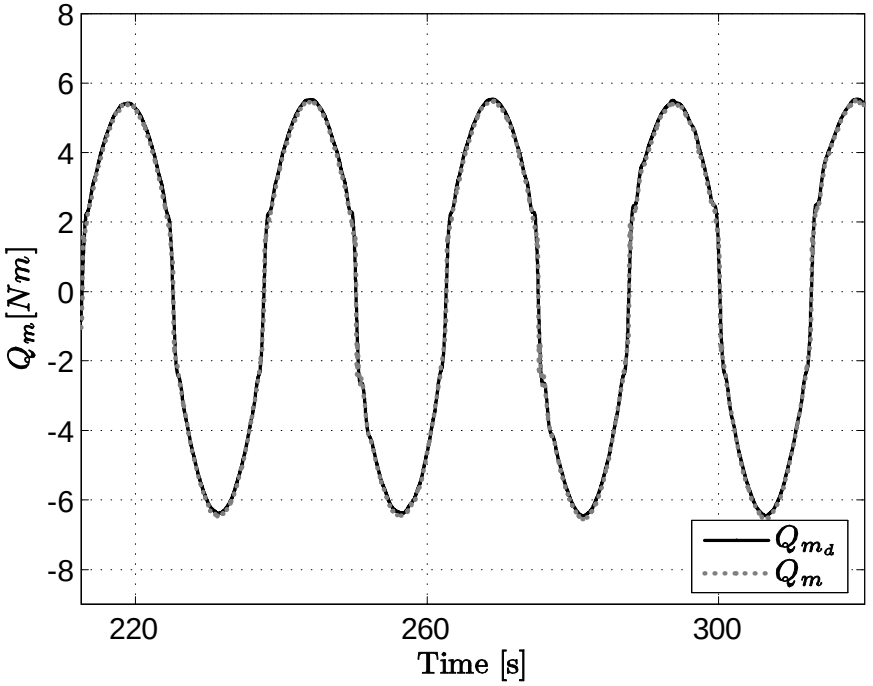

Figure 3.3: Desired and measured motor torque.

example, according to Andersen (1974) and Blanke (1981), the motor dynamics can be approximated by a transfer function that accounts for the gradual build up of cylinder pressure and the discrete nature of cylinder firings. The model, in the Laplace domain, is given by

$$Q_m(s) = e^{-s\tau_m} \frac{K_y}{1 + sT_m} Y(s), \tag{3.6}$$

where τ_m is a time delay, T_m a time constant, K_y a motor torque constant and $Y(s)$ is the fuel index. The desired motor torque is given by

$$Q_{m_d}(t) = K_y y(t). \tag{3.7}$$

Other models can be found, for instance, in Rajamani (2006), Jung and Glover (2006) and the references therein.

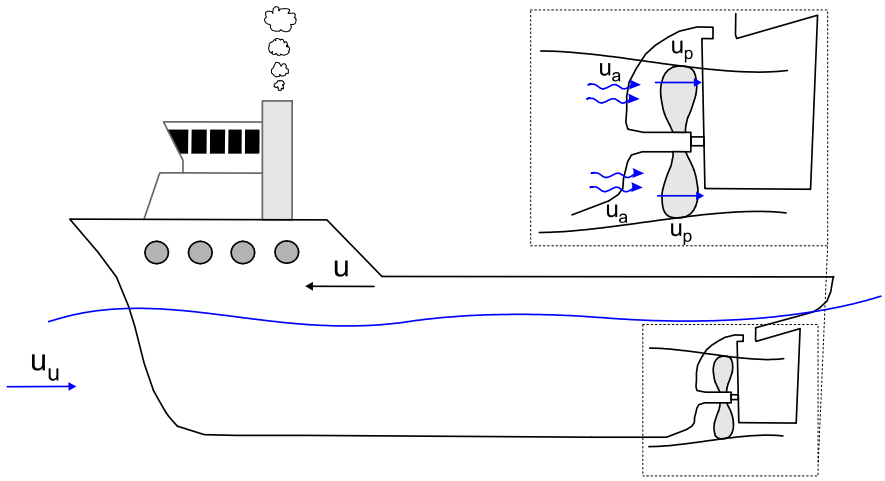

Figure 3.4: Definition of the advance speed u_a, axial flow velocity u_p, vessel speed u and the undisturbed flow velocity u_u.

3.4 Open-water propeller characteristics

Modeling of the thrust and torque produced by a propeller is a complicated task, since it is difficult to develop a finite-dimensional analytical model from the laws of physics. This is mainly due to the difficulty in modeling the flow dynamics, especially when the flow is not uniform. See, for example, Breslin and Andersen (1994), Healey *et al.* (1995), Bachmayer *et al.* (2000), Blanke *et al.* (2000), Kim and Chung (2006) and Pivano *et al.* (2006*c*). The thrust and torque depend also upon the propeller geometrical parameters (i.e. propeller diameter, pitch angle, etc.), the non-dimensional parameters advance number J and Reynolds number, the propeller submergence and environmental state (waves, currents, etc.). As stated before, for control design purposes, the common practice is the use of simplified models which are chosen based on the propeller application. See, for example, Fossen and Blanke (2000), Pivano *et al.* (2007*b*) and Smogeli *et al.* (2004*a*) and the references therein.

Neglecting the effect of waves and ocean currents, and assuming a deeply submerged fixed pitch propeller, the thrust and torque are usually represented in nondimensional form. They can be described by the standard open-water coefficients K_T and K_Q, given as functions of the advance number J. The term open-water refers to the case where the propeller is tested

without the presence of a vessel hull. The coefficients K_T and K_Q are defined in Carlton (1994) as

$$K_T = T_p \frac{4\pi^2}{\rho \left|\omega\right| \omega D^4}, \tag{3.8}$$

$$K_Q = Q_p \frac{4\pi^2}{\rho \left|\omega\right| \omega D^5}, \tag{3.9}$$

where ρ is the density of the water and D is the propeller diameter. The advance number is computed as

$$J = \frac{2\pi u_a}{\omega D}, \tag{3.10}$$

where u_a is the advance speed, i.e. the water inflow velocity to the propeller. The K_T and K_Q curves are measured for a range of propeller advance numbers J, usually in a cavitation tunnel or a towing tank. The guidelines for such tests are reported in the manual ITTC (2002*b*).

When the propeller works in water that has been disturbed by the passage of the hull, it is no longer advancing relatively to the water at the speed of the ship u, but at some different speed u_a (Lewis, 1988). The advance speed is very difficult to measure and an estimate of u_a is usually computed using the steady-state relation

$$u_a = (1 - w_f)u, \tag{3.11}$$

where w_f is the *wake fraction number,* often identified from experimental tests. See, e.g., Lewis (1988) and ITTC (2002*b*). The relation (3.11) is valid in steady-state conditions, for advance speed and shaft speed with the same sign, but fails when the propeller operates at off-design conditions, e.g. in crashback and crashahead manoeuvres. Figure 3.4 shows a sketch of a vessel with the velocities involved. The surge vessel speed-over-ground is defined by u, u_a is the advance speed relative to the propeller disc and u_p is defined as the axial flow velocity at the propeller disc. The undisturbed water velocity u_u has the same magnitude as the vessel speed but with opposite direction.

A measure of the propeller performance is the open-water efficiency η_o, which is defined as the ratio of the produced to the consumed power by the propeller. The open-water efficiency is usually plotted for positive values of J and is computed from (3.8), (3.9) and (3.10) as

$$\eta_o = \frac{u_a T_p}{\omega Q_p} = \frac{u_a K_T}{\omega D K_Q} = \frac{J K_T}{2\pi K_Q}. \tag{3.12}$$

The presence of the hull influences also the total propulsion efficiency which will differ from the one computed from open-water tests. Behind the hull, for the same values of advance speed, thrust and shaft speed obtained in open-water conditions, the propeller torque will be different. The ratio between the open-water torque and the one obtained behind a hull, defined with Q_{p_b}, is called relative rotative efficiency η_R. This difference in torque is mainly due to two reasons. First, the propeller inflow behind the hull is heterogenous and the flow conditions over a given blade section differ greatly from the open-water conditions, where the flow is uniform. This results in a different efficiency of any particular blade element. Second, the amount of laminar and turbulent flow on the propeller blades may be different in the two cases. The turbulence in the water behind the hull is usually greater than in open-water case.

In addition, a propeller increases the hull resistance. For main propellers, for example, this is due to the pressure reduction over the stern (Lewis, 1988). This is caused by the action of the propeller in accelerating the water flowing into it, leading to an increased thrust necessary to propel the ship. The increase of the hull resistance is usually accounted for by the *thrust deduction factor* $(1-t_d)$, where t_d is positive and rarely exceeds 0.4. Given the hull resistance R_v, measured at speed u without the propeller, the thrust necessary to overcome the hull residence, when the propeller works behind the hull, at the same speed u is equal to

$$T_p = \frac{R_v}{(1-t_d)}. \tag{3.13}$$

The total propulsion efficiency η_p is defined by the work done by the propeller in overcoming the vessel resistance R_v at speed u divided by the work done to produce the propeller torque. The total propulsion efficiency is usually computed neglecting the shaft moment of inertia and is given by

$$\begin{aligned} \eta_p &= \frac{R_v u}{\omega \frac{Q_{p_b}}{\eta_m}} \\ &= \frac{T_p(1-t_d)u_a}{\omega Q_p(1-w_f)}\eta_m\eta_R \\ &= \eta_o\eta_R\eta_m\eta_H \end{aligned} \tag{3.14}$$

where η_m is the mechanical efficiency that represents losses in gears and bearings and η_H is defined as the hull efficiency:

$$\eta_H = \frac{(1-t_d)}{(1-w_f)}. \tag{3.15}$$

Remark 3.2 *The total propulsion efficiency η_p is sometimes written considering also the shaft friction torque Q_f such that*

$$\eta_p = \frac{T_p(1-t_d)u_a}{\omega\left(Q_p+Q_f\right)(1-w_f)}\eta_m\eta_R. \tag{3.16}$$

Both the open-water propeller efficiency and the total propulsion efficiency are important for vessels in transit. In bollard pull conditions, where the propeller is kept at rest, the efficiency does not represent a useful datum since $\eta_p \approx 0$ due to $\eta_o \approx 0$. In this case a different definition of the efficiency is employed as documented in Smogeli (2006).

The curves K_T and K_Q are usually employed in the first and in third quadrant of the plane composed by u_a and ω, and they are not defined for $\omega = 0$. For propellers operating in the whole plane (u_a,ω), the four-quadrant open-water coefficients C_T and C_Q are normally utilized (Carlton, 1994). The quadrants in which the propeller operates, described in Table 3.2, are often defined by the advance angle β, which is computed with the four-quadrant inverse tangent function as

$$\beta = \arctan2\left(u_a, 0.7R\omega\right), \tag{3.17}$$

where R is the propeller disc radius. The four-quadrant coefficients, usually plotted as a function of β, are defined in Carlton (1994) as

$$C_T = \frac{T_p}{\frac{1}{2}\rho V_r^2 A_0}, \tag{3.18}$$

$$C_Q = \frac{Q_p}{\frac{1}{2}\rho V_r^2 A_0 D}, \tag{3.19}$$

where A_0 is the propeller disc area and V_r is the relative advance velocity:

$$V_r^2 = u_a^2 + (0.7R\omega)^2. \tag{3.20}$$

Both the standard and four-quadrant propeller characteristics describe the thrust and torque in steady-state conditions and are valid for deeply submerged propellers. When a propeller is subject to cross-flows or is not deeply submerged, for example, the degradation of the propeller performance is accounted for by employing thrust and torque loss functions (Lehn,

Quadrant	ω	$u_{\mathbf{a}}$	β
1^{st}	≥ 0	≥ 0	$0 \leq \beta \leq 90$ deg
2^{nd}	< 0	≥ 0	$90 < \beta \leq 180$ deg
3^{rd}	< 0	≤ 0	$180 < \beta \leq 270$ deg
4^{th}	> 0	< 0	$270 < \beta < 360$ deg

Table 3.2: Definition of four quadrants

1992). In that case, additional measurements of the cross flow velocity and the propeller submergence are needed.

In Chapter 4, it will be shown that the thrust and torque obtained by employing the propeller characteristics do not reproduce accurately the measurements when the propeller operates in the second and fourth quadrant.

Measured open-water characteristics

At the Marine Cybernetics Laboratory, the tank dimensions may appear too small for accurate open-water tests due to the influence of previous motions, presence of walls and free surface motion. The variance of the obtained results was found, however, sufficiently small. To measure the open-water propeller characteristics, tests were performed at different constant values of the advance number J. To obtain the desired shaft speed ω, the built-in speed controller of the motor drive was used. In our setup, the housing that contains gear and measurement devices did not create a significant wake and the advance speed u_a has been considered equal to the towing carriage speed u. This resulted in a wake fraction number w_f equal to zero. The standard propeller characteristics for the unducted propeller P1362 and for the ducted one P1009 are plotted in Figures 3.5 and 3.6, respectively. The curves are the result of the average of three tests. For each test, the coefficients were obtained employing the average values of thrust and torque computed over a 5 s window. In order to obtain more accurate results, these tests are usually carried out in longer towing tanks.

For both propellers, the efficiency was larger at positive shaft speeds since they were designed to work mainly at forward vessel speed. Moreover, ducted propellers present, in general, better efficiency for small values of J. This can be seen by comparing the propeller characteristics in Figures 3.5 and 3.6; the efficiency of the ducted propeller has its maximum at lower values of J.

Figure 3.7 shows a sample of filtered data used to derive the K_T and

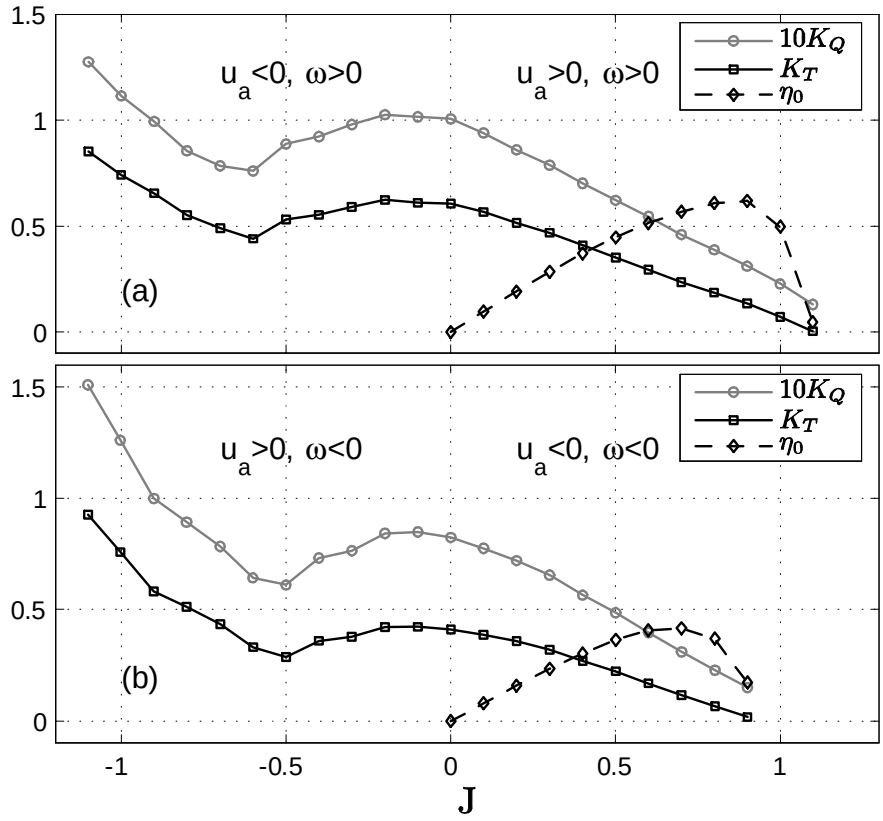

Figure 3.5: Measured standard propeller characteristics for the unducted propeller P1362: positive ω (a) and negative ω (b).

K_Q curves for the propeller P1362. The values of K_T and K_Q, computed for negative J, presented large variance due to large oscillations in the propeller thrust and torque. When J is negative, the propeller tries to reverse the inlet flow and a recirculation zone, often called a ring vortex, occurs; see Vysohlid and Mahesh (2004) and Jessup *et al.* (2004). This is due to the interaction between the inlet flow and the reversed flow. The flow then becomes unsteady and causes oscillations in the propeller thrust and torque. For positive u_a and ω, the inflow to the propeller is uniform and the thrust and torque are sufficiently steady.

The four-quadrant propeller characteristics were obtained from tests carried out at different constant values of β. Figure 3.8 shows the four-

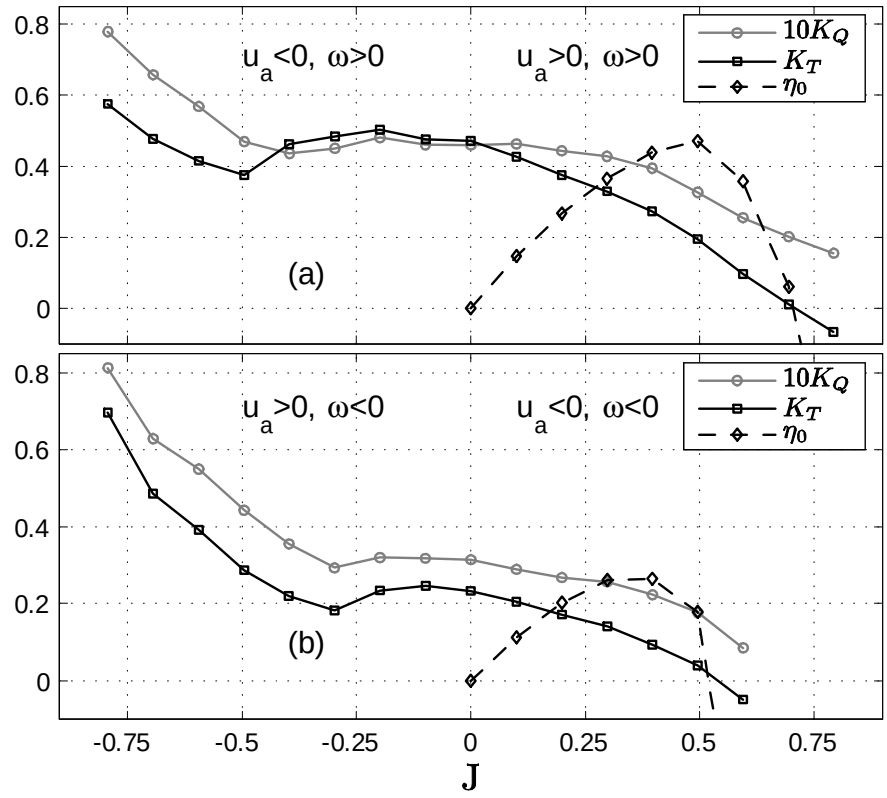

Figure 3.6: Measured standard propeller characteristics for the ducted propeller P1009: positive ω (a) and negative ω (b).

quadrant propeller characteristics obtained computing the average of three tests and an approximation computed with a 25^{th} order Fourier series, commonly adopted for the C_T and C_Q curves; see Carlton (1994).

3.5 Flow dynamics effects

The effects of the propeller flow dynamics and its implication in the thrust control were investigated in many works, especially in the context of underwater vehicles. See, for example, Yoerger *et al.* (1990), Healey *et al.* (1995), Whitcomb and Yoerger (1999), Bachmayer *et al.* (2000) and Kim and Chung (2006). This was motivated by experiments that showed that the propeller thrust and torque obtained from the propeller characteristics

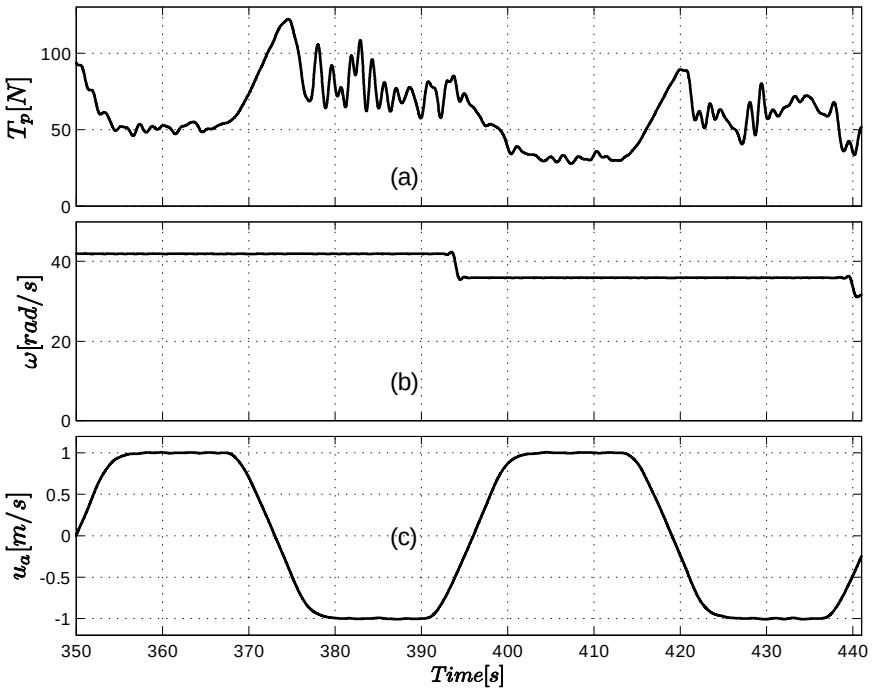

Figure 3.7: Sample of measured data used to compute the propeller characteristics.

could not reproduce accurately the measurements during fast shaft speed transients. These works focused on the development of finite-dimensional lumped-parameter dynamical systems able to better approximate the transient dynamics of thrusters.

In particular, in Healey *et al.* (1995), the authors presented a nonlinear model, based on the motor electromechanical dynamics and thin-foil propeller hydrodynamics, able to improve the thrust prediction compared to the one-state model introduced in Yoerger *et al.* (1990). In order to reproduce the thrust overshoots observed in the experiments, the authors included the axial flow velocity state u_p, i.e. the speed of the water at the propeller disc measured at some convenient radial position (usually $0.7R$). Propeller and fluid dynamics were approximated by a two-dimensional second-order nonlinear dynamical system with axial fluid velocity and propeller rotational velocity as state variables. The model, obtained by modeling a control volume of water around the propeller as a mass-damper system,

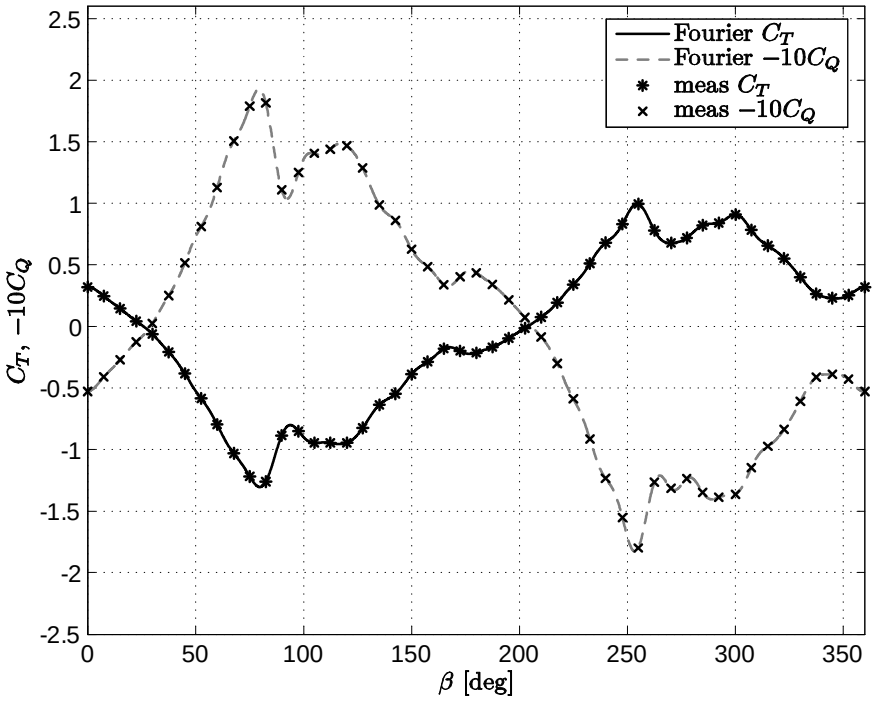

Figure 3.8: Measured propeller four-quadrant open-water characteristics for the propeller P1362.

was given by

$$\begin{aligned} J_m\dot{\omega} &= Q_m - Q_p - Q_f(\omega), \\ m_f\dot{u}_p + d_f(u_p - u)\,|u_p - u| &= T_p, \\ T_p &= T_p(\omega, u_p), \\ Q_p &= Q_p(\omega, u_p), \end{aligned} \tag{3.21}$$

where m_f was defined as the mass of the water in the control volume (equivalent water inertia) and d_f as the quadratic damping coefficient. The thrust and torque were related to the lift and drag produced by the propeller blade according to sinusoidal lift/drag curves. In Whitcomb and Yoerger (1999), the authors reported experiments, conducted at bollard-pool conditions (in absence of currents and with $u_a = 0$) that demonstrated the utility of the axial flow model, but also identified discrepancies between the thruster's

transient response and the model predictions. The cause of these discrepancies was scrutinized in Bachmayer *et al.* (2000). The authors demonstrated that accurate thrust predictions could be obtained by using the model in Healey *et al.* (1995), but with the use of nonsinusoidal lift/drag curves. They also concluded that the inclusion of the rotational flow velocity dynamics did not improve significantly the model performance. The latter model showed high accuracy in reproducing thrust and propeller shaft speed, but it was identified from data acquired during bollard-pull tests; therefore it could only be employed for limited range of advance speeds. To overcome this limitation, in Blanke *et al.* (2000), a model of the flow dynamics, valid also for positive advance speeds, was proposed. In the thrust/torque mapping from the axial flow velocity and the shaft speed, a linear approximation of the open-water standard propeller characteristics was utilized. Hence, they could not guarantee accurate results in the full four-quadrant range of the propeller shaft speed and the advance speed. To obtain a mapping valid also for four-quadrant operations, we carried out a series of tests at MCLab employing an ADV probe to measure the speed of the water downstream the propeller. The results of this study are reported in the next section.

3.5.1 Four-quadrant propeller model

The model is composed by the propeller shaft dynamics, the axial flow dynamics and a mapping to compute thrust and torque, as shown in the block diagram in Figure 3.9.

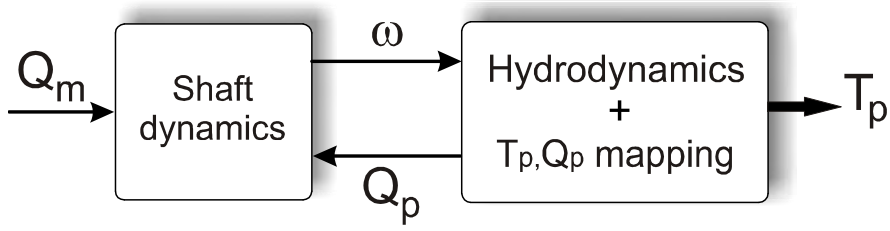

Figure 3.9: Block diagram of the propeller model.

Hydrodynamic model

To derive the axial flow dynamics we firstly built a model for zero advance speed (bollard pull model). Secondly, we modified the equation obtained

at the first step considering the case when the propeller moved through the water (maneuvering model).

Bollard pull model ($u_a = 0$) Considering the propeller as an infinitely thin disc of area A_0 in the mid-section of a cylinder of water of length l and mass m_f (Bernoulli tube), we can apply the momentum theory (Lewis, 1988) relating the axial thrust to the rate of change of momentum through the control volume:

$$T_p = m_f \dot{u}_p + \rho A_0 K_f \left|u_p\right| u_p, \tag{3.22}$$

where T_p is the propeller thrust, ρ is the water density and K_f is the axial flow form factor, which has to be identified. By defining $d_{f_1} = \rho A_0 K_f$, (3.22) can be rewritten as:

$$m_f \dot{u}_p = -d_{f_1} \left|u_p\right| u_p + T_p, \tag{3.23}$$

where the positive nonlinear damping coefficient d_{f_1} and the equivalent water inertia m_f have to be identified.

Maneuvering model ($u_a \neq 0$) The dynamics of the axial flow velocity is influenced by the advance speed. By considering positive flow velocities, indicated in Figure 3.10, we can write the dynamics of the mass of water in the Bernoulli tube as in Blanke *et al.* (2000):

$$m_f \dot{u}_p = T_p + \frac{1}{2}\rho A_0 (u_a^2 - u_w^2), \tag{3.24}$$

where u_w is defined as the wake velocity.

When the blades rotate in order to accelerate the incoming water flow of speed u_a, the axial flow velocity u_p at the propeller disc section will be greater than u_a because the fluid acquires some speed before it reaches the disc, as it results from momentum theory. This allows us to write:

$$u_p = a u_w + (1 - a) u_a, \tag{3.25}$$

where $0 < a < 1$ is constant. Solving (3.25) for u_w and substituting the expression of u_w in (3.24) we can derive the dynamics of the axial flow velocity at the propeller disc:

$$m_f \dot{u}_p = -d_{f_1} u_p^2 + d_{f_2} u_p u_a + d_{f_3} u_a^2 + T_p, \tag{3.26}$$

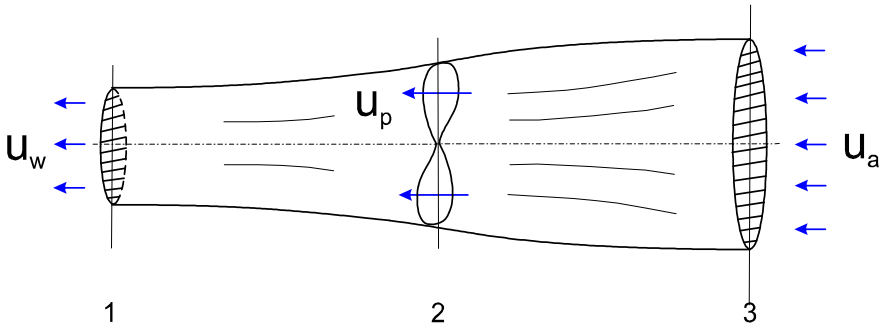

Figure 3.10: Flow velocities: advance speed u_a (cross-section 3), axial flow velocity u_p at the propeller disc (cross-section 2) and wake speed u_w (cross-section 1).

where $d_{f_1} = \frac{1}{2a^2}\rho A_0$, $d_{f2} = \frac{1-a}{a^2}\rho A_0$ and $d_{f3} = \frac{2a-1}{2a^2}\rho A_0$. To take into account negative velocities, i.e. to extend the model validity to the third quadrant, (3.26) must be rewritten as

$$m_f \dot{u}_p = -d_{f_1} |u_p| u_p + d_{f_2} |u_p| u_a + d_{f_3} |u_a| u_a + T_p, \tag{3.27}$$

where d_{f_1}, d_{f_2}, d_{f_3} are constant and positive.

When the propeller rotates to push the water in the opposite direction with respect to the direction of the inlet flow (crashback and crashahead), the axial flow velocity becomes unsteady; see, e.g., Vysohlid and Mahesh (2004) and Jessup *et al.* (2004). In the region close to the blades (region of reversed flow), a recirculation zone is observable. In this particular case the momentum theory is not valid due to the presence of unsteady flows and the model (3.27) may give inaccurate results.

Taking the average of the measured axial flow velocity, we found that the model of (3.27) was still valid, as long the magnitude of axial flow velocity u_p, induced by the propeller, was greater than the magnitude of the inlet water flow u_a. Vice versa, when the propeller rotates with a speed under certain values (depending on the vehicle velocity), it was not able to reverse the incoming flow and the model (3.27) was not accurate. The propeller behaved as a brake and it reduced the speed of the inlet flow. This can be represented by a second dynamical model that was experimentally derived:

$$m_f \dot{u}_p = -d_{f_4} u_p + d_{f_5} u_a + d_{f_6} |u_a| u_a + T_p, \tag{3.28}$$

where d_{f_4}, d_{f_5}, d_{f_6} are constant and positive.

Four-quadrant propeller thrust and torque mapping

To improve the thrust and torque prediction compared to the use of the four-quadrant open-water propeller characteristics, we identified the difference between the measured thrust and torque, $T_{P_{meas}}$ and $Q_{P_{meas}}$, and the ones computed with the open-water characteristics (3.17)-(3.20), $T_{P_{CT}}$ and $Q_{P_{CQ}}$, as a function of the angle β defined in (3.17) and the axial flow velocity u_p. This approach is not directly related to the actual angle of attack of the blades and lift/drag curves. The identification of a mapping involving lift/drag curves as functions of three variables, u_a, u_p and ω, appeared quite complex. This could be addressed in future works.

To relate the thrust and torque differences

$$T_{P_D} = T_{P_{meas}} - T_{P_{CT}}, \tag{3.29}$$
$$Q_{P_D} = Q_{P_{meas}} - Q_{P_{CQ}}, \tag{3.30}$$

to the axial flow velocity u_p, two new coefficients were derived. Similarly to the four-quadrant open-water coefficients, the new coefficients were computed as

$$C_{T|u_p} = \frac{T_{P_D}}{\frac{1}{2}\rho A_0 u_p |u_p|}, \tag{3.31}$$
$$C_{Q|u_p} = \frac{Q_{P_D}}{\frac{1}{2}\rho A_0 u_p |u_p| D}. \tag{3.32}$$

System identification procedure and experimental validation

To identify the hydrodynamic model and the thrust/torque mapping, we run some tests with the propeller P1020 employing the Sontek 10 MHz 3D Acoustic Doppler Velocimeter (ADV) to measure the flow velocity. The probe was vertically mounted as close as possible to the propeller disc. It was places 7 cm downstream the propeller with its x axis aligned to the propeller shaft. The distance between the sampling volume and the center of the propeller shaft was set equal to $0.7R$, where R is the radius of the propeller disc. This radial distance is usually chosen because the axial flow velocity presents its maximum at that point (Rhee and Joshi, 2005).

Bollard-pull model To identify the parameters in (3.23), we considered first a steady-state condition. Applying steps of motor torque of different amplitudes, we measured the steady-state values of the axial flow velocity. We obtained the curve shown in Figure 3.11 that proves the quadratic dependence of the propeller thrust with respect to u_p.

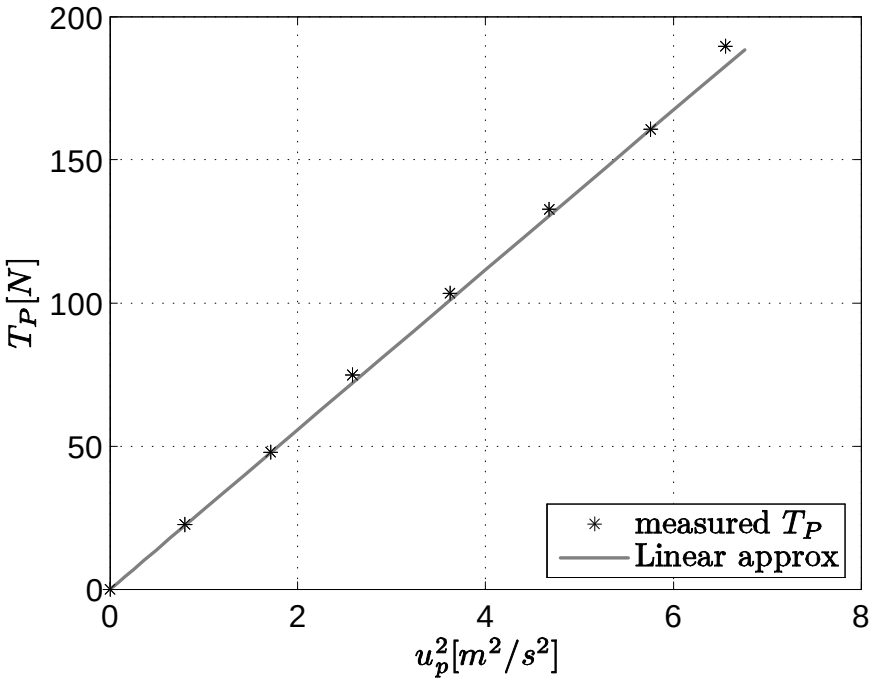

Figure 3.11: Steady-state relation between axial flow velocity and propeller thrust for zero advance speed.

The plot includes only positive values of thrust and velocity since the probe for measuring the flow speed was placed downstream the propeller. We have assumed that (3.23) was valid also for negative u_p. The value of d_{f_1} was estimated using the least squares method applied to the steady-state characteristic of Figure 3.11. To identify the value of m_f the least squares method has been applied to (3.23) employing data obtained in transient conditions. The identified values are shown in Table 3.3.

Maneuvering model To identify the parameters in (3.27) and (3.28), we performed tests with different velocity profiles of the towing carriage and

motor torque. Due to the fact that in our setup the wake fraction number was zero, the advance speed was equal to the towing carriage speed. The overall axial flow dynamics model is written in compact form as

$$m_f \dot{u}_p = \begin{cases} -d_{f_4} u_p + d_{f_5} u_a + d_{f_6} |u_a| \, u_a + T_p & \text{if } \operatorname{sgn}(u_a) = -\operatorname{sgn}(\omega), |u_p| < |u_a| \\ -d_{f_1} |u_p| \, u_p + d_{f_2} |u_p| \, u_a + d_{f_3} |u_a| \, u_a + T_p & \text{else} \end{cases} \tag{3.33}$$

The coefficients df_2, df_3, df_4, df_5, df_6, shown in Table 3.3, were estimated in order to fit the steady-state values of the measured propeller thrust using the least squares method.

Table 3.3: Experimentally identified parameters of the hydrodynamic model.

Parameter	Value	Parameter	Value
m_f $[kg]$	8.62	d_{f_4} $[kg/s]$	41.13
d_{f_1} $[kg/m]$	27.89	d_{f_5} $[kg/s]$	20.39
d_{f_2} $[kg/m]$	7.66	d_{f_6} $[kg/m]$	39.39
d_{f_3} $[kg/m]$	18.37		

The model (3.33), driven by the measured propeller thrust, was validated for different motor torques and advance speed profiles. These simulations were carried out with data that were not used for the model identification. The results of two different simulations are depicted in Figures 3.12 and 3.13.

Figure 3.12 shows data from an experiment with positive sinusoidal shaft speed and with trapezoidal advance speed profile. The axial flow obtained from the model reproduced accurately the measurements when the advance speed and the shaft speed had the same sign. For negative values of the advance speed, the flow was unsteady and the model was only able to reproduce the trend of the measurements. Data from a different test are presented in Figure 3.13. In this experiment a triangular profile for advance speed was employed. Similarly to the previous test, the model could not reproduce the fast variations in the flow velocity.

Four-quadrant thrust and torque mapping The new coefficients, introduced in (3.31) and (3.32), were obtained by performing some tests with different constant towing carriage speeds and with different constant shaft speeds. To identify the mapping, the axial flow measurement was not used

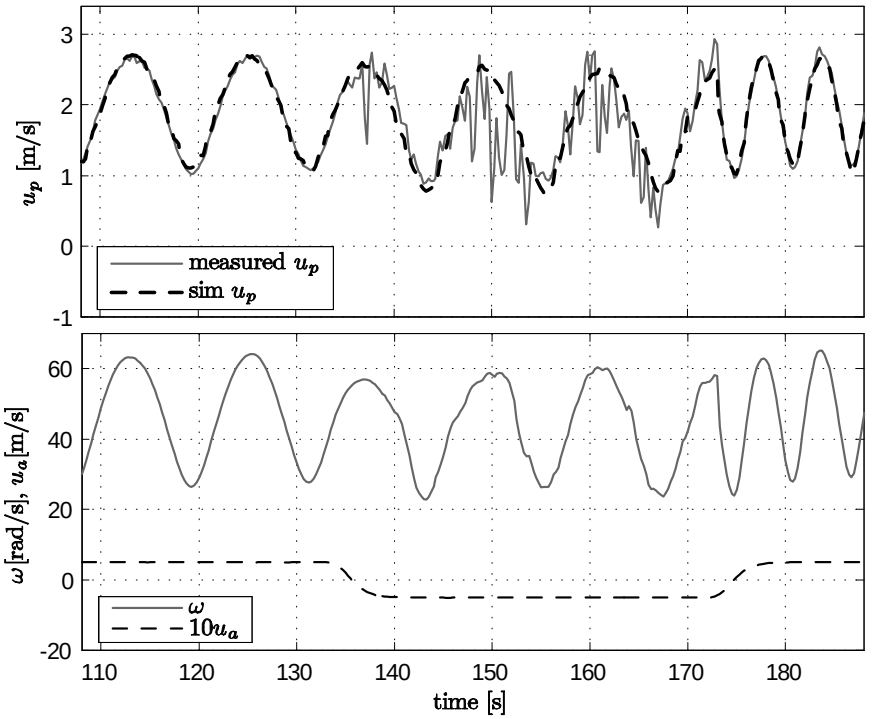

Figure 3.12: Axial flow model simulation with sinusoidal motor torque and trapezoidal carriage speed.

directly for the following reason. When the flow was unsteady (second and fourth quadrant) the axial flow velocity measurement exhibited large oscillations, as shown in Fig 3.12. The correlation between these oscillations and the thrust and torque oscillations was found to be poor. This was maybe caused by the fact that the probe measures the flow velocity in a small sample volume which does not describe entirely the flow behaviour around the propeller. In order to obtain a smoother version of u_p, we simulated the model (3.33) employing the measured thrust. The obtained $C_{T|u_p}$ and $C_{Q|u_p}$ coefficients, plotted as a function of the advance angle β, are shown in Figure 3.14. The graph that was obtained had data quite scattered, but it was possible to deduce the trend, plotted in Figure 3.14.

The overall propeller model, including the shaft dynamics, was not simulated because in these experiments the friction torque presented abrupt variations. This was due to the malfunction of a watertight support of the

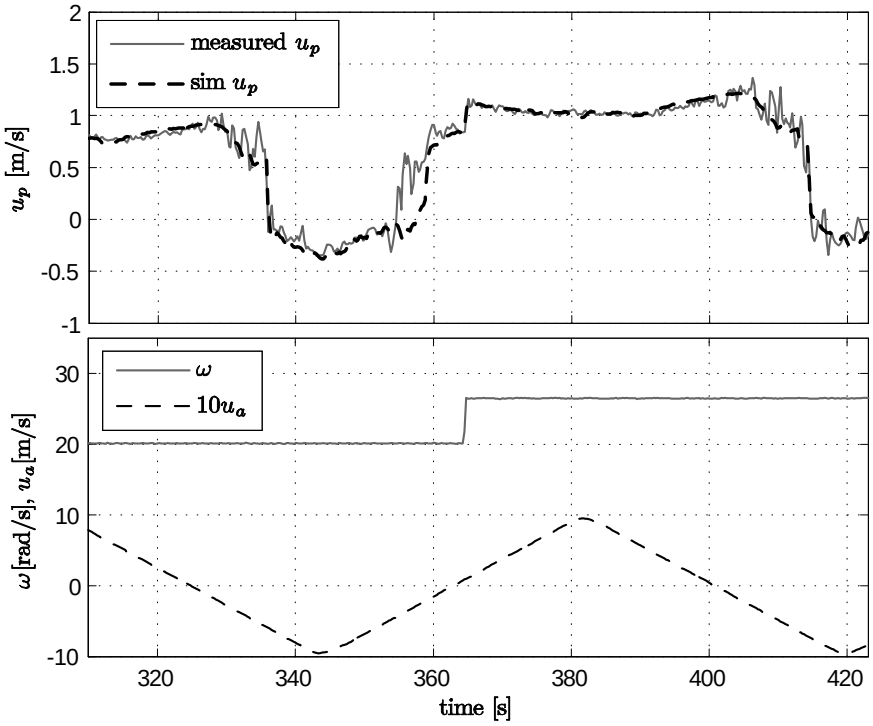

Figure 3.13: Axial flow model simulation with square motor torque and triangular carriage speed.

propeller shaft. This problem was resolved later. To validate the identified mapping, we employed the shaft speed measurement, which is usually available in a propulsion system. The identified mapping was tested over a large number of different shaft speeds, employing triangular, square and sinusoidal waves with various amplitudes and frequencies, and with different carriage speed profiles. In all cases the model developed here improved the accuracy of the thrust prediction compared to the use of the four-quadrant open-water propeller characteristics (3.17)-(3.20). Figure 3.15 compares the propeller thrust and torque measurements with the ones obtained from the four-quadrant characteristics and the model that employs the axial flow dynamics. To validate the mapping in all four quadrants, indicated in Figure 3.15 (d), the advance speed and the shaft speed assumed both positive and negative values. The thrust and torque, obtained from the model, reproduced well the measurements in the first and third quadrant. However,

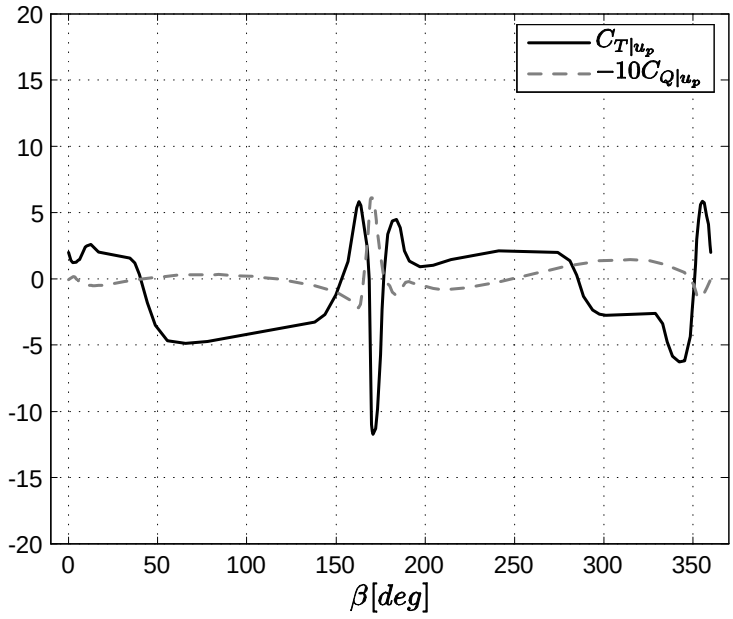

Figure 3.14: Experimentally derived $C_{T|u_p}$ and $C_{Q|u_p}$.

due to the impossibility to reproduce the axial flow velocity in regime of unsteady flows, the model did not reproduce the thrust and torque oscillations that occurred in the second and fourth quadrant.

Discussion Previous work (Bachmayer *et al.*, 2000) demonstrated that, in bollard pool conditions, the inclusion of the axial flow dynamics in the propeller model leads to improved accuracy in thrust prediction compared to the use of the open-water propeller characteristics. This was also confirmed by the experimental results presented here conducted at nonzero advance speed. However, the identified mapping was not able to predict the thrust and torque variations in presence of unsteady flows (described often as *off-design condition*). This was due to the fact that, as mentioned previously, measuring the flow velocity in a small sample volume is not sufficient to describe the flow behaviour around the propeller. In the last years, particle image velocimeters (PIVs) and laser Doppler velocimeters (LDVs) have become the most common instruments for measuring the flows around the propeller. See, for example, Jessup *et al.* (2004), Joon *et al.* (2004), Stella *et al.* (2000) and the references therein. By employing

lasers and underwater cameras, it is possible to measure the speed of the water over a quite large plane allowing better understanding of the flow dynamics. However, such measurement devices are not recommended for their use in propulsion systems due to their fragility. Such tests are mainly carried out to validate more complex models obtained with computational fluid dynamics (CFD) techniques. These models are able to reproduce the thrust and torque also in off-design conditions and they are often employed in the propeller design stage. These models allow obtaining accurate simulation of various propeller operating conditions reducing drastically the number of experimental tests.

For the reasons described above, the use of complex models that involves the flow dynamics appeared to be difficult for the control point of view. A common practice is to use the open-water propeller characteristics that yet require the knowledge of the advance speed, generally not measured. This was one of the motivation for developing a thrust estimation scheme.

3.6 Simplified torque models for state observers

To estimate the propeller torque and the torque loss with observers, we employed two torque models that do not have a structure related to the propeller hydrodynamics and geometry, but they are often used for the estimation of unknown variables.

3.6.1 Model A

In the first model the propeller torque Q_p is treated as a time-varying parameter and modeled, as in Smogeli *et al.* (2004*b*), as a first order Markov-like process with a positive time constant τ_1, driven by a bounded noise w_1:

$$\dot{Q}_p = -\frac{1}{\tau_1} Q_p + w_1. \tag{3.34}$$

3.6.2 Model B

In the second model, the propeller load torque Q_p is represented by the torque produced at zero advance speed, assuming that the propeller is deeply submerged and not subject to losses, plus a term Δ_q that represents torque losses (Pivano *et al.*, 2007*b*):

$$Q_p = \begin{cases} G_{Q_p} |\omega| \omega + \Delta_q & \omega \geq 0 \\ G_{Q_n} |\omega| \omega + \Delta_q & \omega < 0. \end{cases} \tag{3.35}$$

The constants $G_{Q_p}$and G_{Q_n} are the gains from the shaft speed to the propeller torque at zero advance speed, usually of different magnitudes due to the propeller asymmetry. In compact form, the propeller torque can be written as

$$Q_p = G_{Q_{p,n}} |\omega| \omega + \Delta_q, \tag{3.36}$$

where the constant $G_{Q_{p,n}}$ is defined by

$$G_{Q_{p,n}} = \begin{cases} G_{Q_p}, & \omega \geq 0 \\ G_{Q_n}, & \omega < 0. \end{cases} \tag{3.37}$$

The term Δ_q is considered as a time-varying parameter represented by a Markov-like process with positive time constant τ_2 driven by a bounded noise signal w_2:

$$\dot{\Delta}_q = -\frac{1}{\tau_2}\Delta_q + w_2. \tag{3.38}$$

The noise w_2 represents the contribution of all the phenomena that can generate torque losses.

Remark 3.3 *These two models need to be combined with the shaft speed dynamics in order to be used in observers since w_1 and w_2 are not measured.*

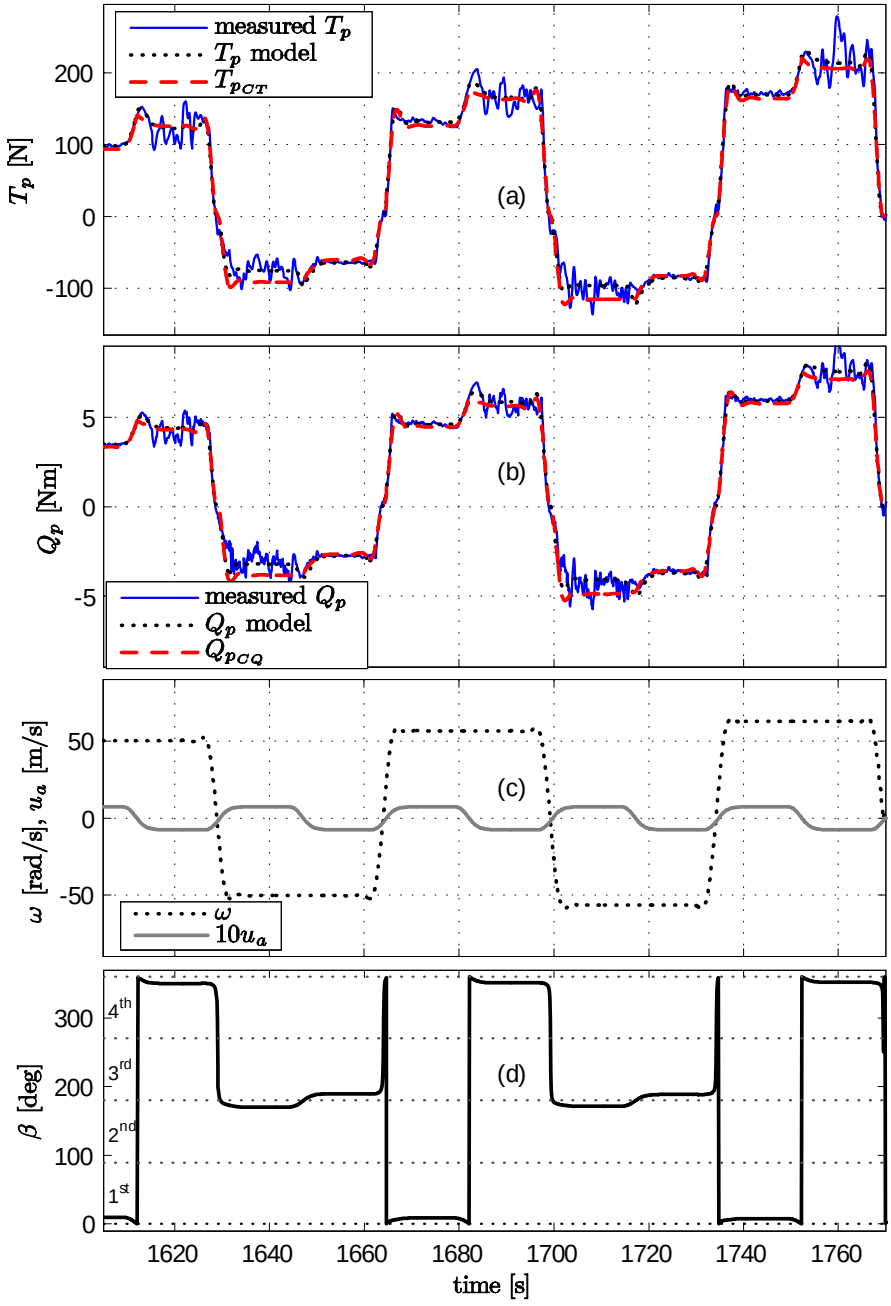

Figure 3.15: Validation of the propeller model.

Chapter 4

Thrust and torque estimation

As explained in Chapter 3, the propeller operational condition can change quickly and since propellers are often affected by thrust and torque losses, they may work far from ideal conditions. Therefore, knowledge of the actual propeller thrust and torque is fundamental to achieve high vessel control performance. Monitoring of the propeller performance is also important for improving fault detection and thrust allocation in different propeller working conditions. Moreover, thrust and torque estimates could also be employed in controller for reducing power fluctuations and wear-and-tear in high sea state (Smogeli, 2006) and for optimizing the propeller efficiency (Blanke *et al.*, 2007).

These considerations motivate the development of schemes to estimate the propeller thrust and torque because, in general, their measurements are not available. Such estimation schemes could be applied to underwater vehicles, where accurate thrust estimates could improve, for example, the performance of observers for the ocean current or be employed in adaptive schemes for the identification of the vehicle hydrodynamic drag; see Fossen (2002), Smallwood and Whitcomb (2004) and Børhaug *et al.* (2007).

Recently, observers for monitoring the propeller performance have been developed and included in new control designs for electrically driven propellers; see Blanke *et al.* (1998), Lootsma (2001), Guibert *et al.* (2005), Smogeli *et al.* (2004*a*), Smogeli (2006), and Pivano *et al.* (2007*b*).

The problem of propeller thrust estimation has been treated in Zhinkin (1989), where full-scale experimental results were provided in steady-state conditions, in waves, and for slanted inflow. The estimation was based

on the propeller torque measurement and a linear relation between thrust and torque. Experimental results were presented only for positive shaft speed and vessel speed. Steady-state thrust estimates can also be obtained from thrust and torque identity techniques, see Carlton (1994), where the propeller torque, assumed to be known, is used to compute an equivalent open-water advance number. This is combined with the open-water propeller characteristics, corrected for scale effects, to obtain the thrust estimate. Thrust estimation has been also treated in Guibert *et al.* (2005), where the estimate was computed from the propeller torque obtained with a Kalman filter employing a linear shaft friction torque model. The relation between thrust and torque involved an axial flow velocity model and required the knowledge of the advance speed. The scheme was highly sensitive to hydrodynamic and mechanical modeling errors. The performance was validated by simulations.

An adaptive observer for variable pitch propellers was designed in Blanke *et al.* (1998) and Lootsma (2001) to estimate shaft speed and thrust. The observer was used for the fault detection in the shaft speed control loop. A linear approximation of the propeller standard characteristics was utilized; therefore, this approach could not guarantee accurate results in all four-quadrants of plane composed by the advance speed and the propeller shaft speed. Moreover, the observer employed the vessel speed measurement.

In this chapter, a four-quadrant thrust estimation scheme is developed. The strength of the presented approach is that only measurements of the propeller shaft speed and the motor torque, normally available on ships, are utilized. Differently from Guibert *et al.* (2005), the advance speed, which is very difficult to measure in real vessels, is assumed to be unknown.

This chapter is organized as follows. The thrust estimation scheme is presented in Section 4.1. Experimental results are described in Section 4.2 and a discussion is given in Section 4.3.

4.1 Thrust estimation scheme

The thrust estimation scheme, described by the block diagram in Figure 4.1, includes a nonlinear observer that computes the estimate $\hat{Q}_p$ of the propeller load torque and the estimate $\hat{\omega}$ of the shaft speed. An estimate $\hat{T}_p$ of the propeller thrust is computed using the observer estimates $\hat{Q}_p$ and $\hat{\omega}$ through a mapping f. This mapping, derived from the standard open-water propeller characteristics introduced in Chapter 3, involves the estimation of the advance number J. In order to analyze the effect of the measurement

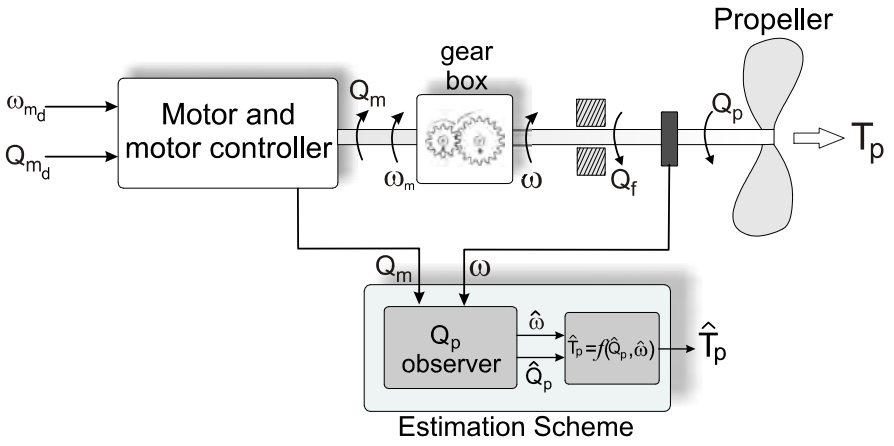

Figure 4.1: Block diagram of the propeller system and the thrust estimation scheme.

and friction modeling errors on the observer estimates, a Lyapunov based robustness analysis has been performed.

4.1.1 Propeller torque observer

The observer is based on the shaft dynamics and the simplified torque model described in Section 3.6.1. The motor torque Q_m and the shaft speed ω are assumed to be measurable. For electric motors, the motor torque can be computed quite accurately from the motor current and voltage. In our setup, its measurement was furnished by the motor drive. For diesel engines, the motor torque can be measured with strain gauges on the motor shaft or by measuring the fuel index. See, for example, Blanke (1981) and Blanke *et al.* (1998). The signal obtained from the fuel index may be less precise and influence the accuracy of the estimates.

The overall propeller dynamics is written from the shaft dynamics (3.1), the friction model (3.2) and the propeller torque model (3.34). By adding measurement and modeling errors we obtain

$$\begin{aligned} J_m\dot{\omega} = \quad & R_{gb}Q_m - Q_p + \Delta_f - k_{f_1}\arctan\left(\tfrac{\omega}{\epsilon}\right) - k_{f_2}\omega \\ & -k_{f_3}\arctan(k_{f_4}\omega), \\ \dot{Q}_p = \quad & -\tfrac{1}{\tau_1}Q_p + w_1. \end{aligned} \tag{4.1}$$

The output of the system is represented by

$$y = \omega + v. \tag{4.2}$$

where v is a bounded measurement error. The friction torque modeling error and the measurement error on Q_m are accounted for by Δ_f, assumed to be bounded. Defining with $\hat{y} = \hat{\omega}$ the estimate of the angular shaft speed and with $\hat{Q}_p$ the estimate of the propeller torque, the following observer with gains l_1 and l_2 is proposed:

$$\begin{aligned} J_m\dot{\hat{\omega}} = \quad & R_{gb}Q_m - \hat{Q}_p - k_{f_1}\arctan(\tfrac{\hat{\omega}}{\epsilon}) - k_{f_2}\hat{\omega} \\ & -k_{f_3}\arctan(k_{f_4}\hat{\omega}) + l_1(y - \hat{y}), \\ \dot{\hat{Q}}_p = \quad & -\tfrac{1}{\tau_1}\hat{Q}_p - l_2(y - \hat{y}). \end{aligned} \tag{4.3}$$

The observer is derived from the one introduced in Smogeli *et al.* (2004*a*), where the friction torque was modeled as a linear viscous effect. By adding the Coulomb and the nonlinear viscous effect, we are able to represent with more accuracy the friction torque that is usually experienced in practice.

The noise and errors can be treated as inputs, grouped in the vector δ:

$$\delta \quad = [u_1 \quad u_2 \quad u_3]^T = [\Delta_f \quad v \quad w_1]^T. \tag{4.4}$$

With $\tilde{e}_1 = \omega - \hat{\omega}$ and $\tilde{e}_2 = Q_p - \hat{Q}_p$, the observer error dynamics can be written as:

$$\begin{aligned} \dot{\tilde{e}}_1 = \quad & \tfrac{1}{J_m}\left[-\tilde{e}_2 - k_{f_1}\left(\arctan\left(\tfrac{\omega}{\epsilon}\right) - \arctan\left(\tfrac{\hat{\omega}}{\epsilon}\right)\right)\right] \\ & -\tfrac{k_{f_3}}{J_m}\left[\arctan\left(k_{f_4}\omega\right) - \arctan\left(k_{f_4}\hat{\omega}\right)\right] \\ & +\tfrac{1}{J_m}\left[-k_{f_2}\tilde{e}_1 - l_1\tilde{e}_1 + u_1 - l_1u_2\right], \\ \dot{\tilde{e}}_2 = \quad & -\tfrac{1}{\tau_1}\tilde{e}_2 + l_2\tilde{e}_1 + l_2u_2 + u_3. \end{aligned} \tag{4.5}$$

Substituting $\omega = \tilde{e}_1 + \hat{\omega}$ in (4.5), we can group the nonlinearities in the following function:

$$\begin{aligned} \psi(\tilde{e}_1, \hat{\omega}) = \quad & +\tfrac{k_{f_1}}{J_m}\left(\arctan\left(\tfrac{\tilde{e}_1 + \hat{\omega}}{\epsilon}\right) - \arctan\left(\tfrac{\hat{\omega}}{\epsilon}\right)\right) \\ & +\tfrac{k_{f_3}}{J_m}\left(\arctan\left(k_{f_4}\left(\tilde{e}_1 + \hat{\omega}\right)\right) - \arctan\left(k_{f_4}\hat{\omega}\right)\right), \end{aligned} \tag{4.6}$$

where $\psi(\tilde{e}_1, \hat{\omega})$ has the property that $\forall\tilde{e}_1, \forall\hat{\omega}$, $\tilde{e}_1\psi(\tilde{e}_1, \hat{\omega}) \geq 0$. With $\tilde{e} = [\tilde{e}_1 \; \tilde{e}_2]^T$ and using (4.6), we can rewrite the observer error dynamics (4.5) as

$$\dot{\tilde{e}} = \quad -A_1\tilde{e} - F_1(\tilde{e}_1, \hat{\omega}) + B_1\delta \quad , \tag{4.7}$$

where

$$A_1 = \begin{bmatrix} \frac{1}{J_m}(k_{f_2} + l_1) & \frac{1}{J_m} \\ -l_2 & \frac{1}{\tau_1} \end{bmatrix}, \tag{4.8}$$

$$F_1(\tilde{e}_1, \hat{\omega}) = \begin{bmatrix} \psi(\tilde{e}_1, \hat{\omega}) \\ 0 \end{bmatrix}, \tag{4.9}$$

$$B_1 = \begin{bmatrix} \frac{1}{J_m} & -\frac{l_1}{J_m} & 0 \\ 0 & l_2 & 1 \end{bmatrix}. \tag{4.10}$$

Proposition 4.1 *If the parameters α, μ, k, and the observer gains l_1, l_2 are chosen such that*

A1 $\alpha > 0$ such that $\forall \tilde{e}_1$, $\forall \hat{\omega}$: $|\psi(\tilde{e}_1, \hat{\omega})| \leq \alpha |\tilde{e}_1|$,
A2 $0 < \mu < \frac{2}{J_m}$,
A3 $\kappa > 0$,
A4 $0 < l_2 < \alpha^4 \kappa^2 J_m$,
A5 $l_1 > -k_{f_2} + \frac{l_2}{\alpha^2 \kappa} + \frac{1}{2\mu\kappa}$,
then the system (4.5) is input-to-state stable (ISS).

Proof. The proof is given in Appendix A.1. ■

Remark 4.1 *For the observer considered, there always exist parameter and gain values that can be chosen according to the above criteria.*

The ISS property of the observer error dynamics provides the robustness of the observer against noise and modeling errors. The observer errors, and thus the torque and shaft speed estimates, remain bounded for any initial conditions regardless of the values of the measurement errors, the noise w_1 in the propeller torque model and the friction torque modeling errors. In particular, the observer robustness against friction torque modeling errors is very important. The shaft friction torque may depend upon variables which are not directly accounted for in the model, like temperature and bearing lubrication.

4.1.2 Thrust and torque relationship

As stated in Chapter 3, it is difficult to predict accurately the thrust and torque, especially when the inflow to the propeller is not uniform. Thrust and torque are produced by the same physical phenomenon and are closely related. It is not wrong to think that in the value of propeller torque, some variables that influence the behavior of the propeller, like the axial flow

velocity for example, are implicitly hidden within. For this reason, it is possible to compute an estimate of the propeller thrust from the propeller torque and the shaft speed.

The mapping to compute the propeller thrust from the torque utilizes the standard propeller characteristics, presented in Chapter 3. Even though the propeller characteristics are measured in steady-state conditions, we are able to achieve quite accurate results in all four quadrants due to the close relationship between thrust and torque. An example of the procedure to derive the thrust/torque mapping is given considering the propeller P1362 with geometrical parameters given in Table 2.1 and open-water characteristics plotted in Figure 3.5.

Considering the standard propeller characteristics and taking the ratio of the K_T and K_Q coefficients, defined in (3.8) and (3.9), the steady-state propeller thrust can be expressed as

$$T_p = Q_p G_{QT}(J), \tag{4.11}$$

where

$$G_{QT}(J) = \frac{K_T}{K_Q D}, \tag{4.12}$$

is defined as the steady-state gain from the propeller torque to the thrust. This gain depends on the propeller working conditions and can be expressed as a function of the advance number J. Since the advance speed is not measured, the value of J is estimated in order to compute the value of $G_{QT}(J)$. The estimation of J is performed using the estimates $\hat{Q}_p$ and $\hat{\omega}$. From (3.9), we can compute $\hat{K}_Q$, an estimate of K_Q as

$$\hat{K}_Q = \hat{Q}_p \frac{4\pi^2}{\rho \left|\hat{\omega}\right| \hat{\omega} D^5}, \quad \hat{\omega} \neq 0. \tag{4.13}$$

Considering the K_Q characteristics, shown in Figures 4.2 and 4.3, the value of $\hat{K}_Q$ has been limited by the upper bound $K_Q(J_{\min})$ and lower bound $K_Q(J_{\max})$, where $[J_{\min}, J_{\max}]$ is the considered range of J. A propeller does not usually work at values of J greater than about 1 (depending on the propeller), where the produced thrust is negative, and for J smaller than -1.5. Therefore we can limit our analysis in a confined range of values of J. However, when the shaft speed is reversed, the propeller works for a short time outside the considered range of J. In this condition, both thrust and torque are small, since the shaft speed is small, and the error introduced in the approximation of $G_{QT}(J)$ does not affect the estimation significantly. This is shown in the experimental results reported in Section

4.2. The use of the the standard open-water propeller characteristics, which are not defined for $\omega = 0$, does not represent a problem in this case since J is limited in the interval $[J_{\min}, J_{\max}]$.

An estimate $\hat{J}$ of the advance number can be derived by inverting the K_Q curve and using the value of $\hat{K}_Q$ computed with (4.13). It can be noticed, in part (a) of Figures 4.2 and 4.3, that the K_Q curve is not invertible in the whole range of J considered. For this reason, the J axis has been divided in three zones. In zone 1 and 3 the K_Q curve is invertible and an accurate estimate of J can be computed. In zone 2, $\hat{J}$ has been approximated with zero to ensure correct thrust estimation when the advance speed is zero, i.e. the vessel is at rest and not subjected to current. This approximation introduces an error on the estimate which is computed as

$$\hat{T}_p = \begin{cases} \hat{Q}_p G_{QT}(\hat{J})|_{\hat{\omega}\geq 0} & \hat{\omega} \geq 0 \\ \hat{Q}_p G_{QT}(\hat{J})|_{\hat{\omega}<0} & \hat{\omega} < 0. \end{cases} \tag{4.14}$$

Plots of the gains $G_{QT}(J)$ and $G_{QT}(\hat{J})$ for positive and negative values of ω are shown in Figures 4.2 and 4.3. If $\hat{Q}_p$ and $\hat{\omega}$ are accurate, outside zone 2, $G_{QT}(\hat{J})$ approximates accurately $G_{QT}(J)$ and the estimated thrust is precise. In zone 2, $G_{QT}(\hat{J})$ is equal to $G_{QT}(0)$ and, due to the propeller characteristics, the difference between $G_{QT}(\hat{J})$ and $G_{QT}(J)$ is not of significant magnitude. In the border of zone 2, $G_{QT}(\hat{J})$ has been joined smoothly with $G_{QT}(0)$ to avoid sharp variation on the thrust estimate. For the particular example with the propeller P1362, the value of J was limited to the range [-1.5,1.1] for $\omega \geq 0$ and to the range [-1.5,0.9] for $\omega < 0$. The maximum relative error between $G_{QT}(\hat{J})$ and $G_{QT}(J)$ was about 8% for $\omega \geq 0$ and 13% for $\omega < 0$.

A block diagram that represents the thrust estimation procedure is shown in Figure 4.4.

Remark 4.2 *On full scale vessels, the open-water characteristics obtained in a model scale are expected to be corrected for scale effects and for the effects due to the interaction between the vehicle and the propeller (see Appendix A.5).*

Remark 4.3 *If the open-water propeller characteristics are not available, Computational Fluid Dynamics (CFD) techniques can help to derive it from the 3D drawing of the propeller, see for example Martínez-Calle* et al. *(2002) and references therein.*

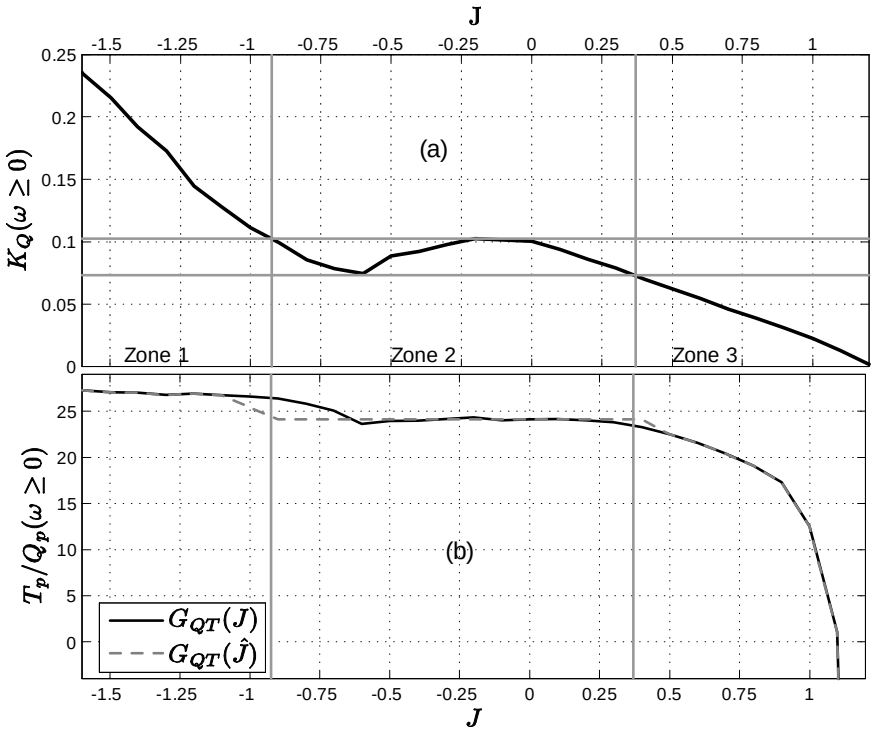

Figure 4.2: Part (a): K_Q characteristic plotted for positive ω. Part (b): the ratio $G_{QT}(J)$ between thrust and torque computed from the propeller characteristics and its approximation $G_{QT}(\hat{J})$ plotted for positive ω.

Remark 4.4 *The thrust and torque relationship is not derived from the four-quadrant propeller characteristics (see Chapter 3) because it is not possible to estimate the advance angle β from only $\hat{Q}_p$ and $\hat{\omega}$, due to the fact that we cannot compute the coefficient C_Q without knowing u_a. This makes this parametrization difficult to use while in the presented approach we can obtain a satisfactory approximation of J from K_Q, which is computed using $\hat{\omega}$ and $\hat{Q}_p$.*

Remark 4.5 *For ducted propellers, the steady-state thrust/torque gain $G_{QT}(J)$ looks slightly different with respect to unducted propellers. This is due to different K_T and K_Q curves, as shown in Section 3.4.*

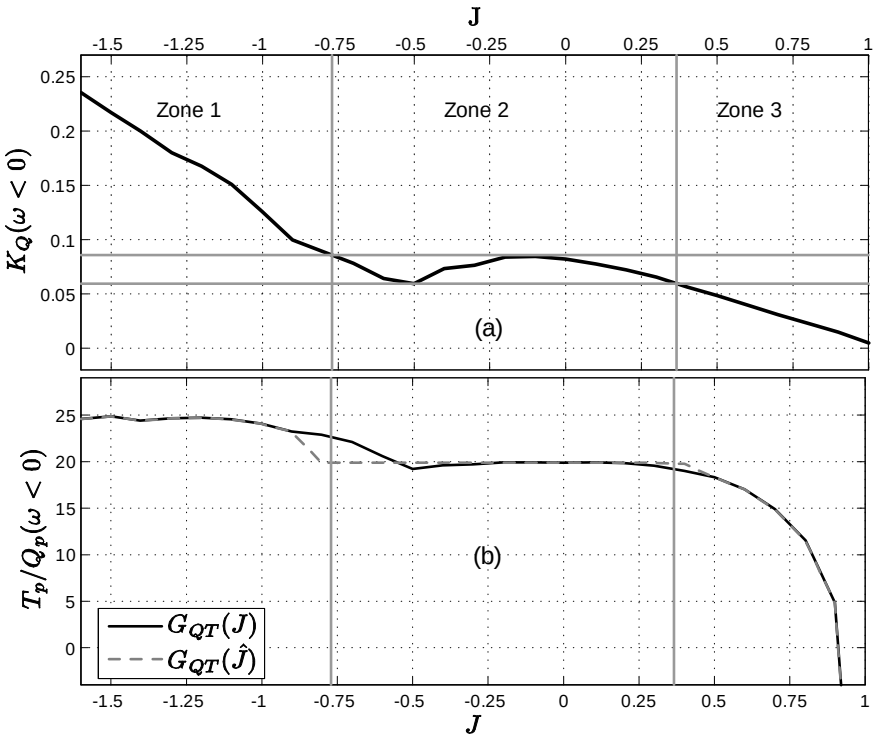

Figure 4.3: Part (a): K_Q characteristic plotted for negative ω. Part (b): the ratio $G_{QT}(J)$ between thrust and torque computed from the propeller characteristics and its approximation $G_{QT}(\hat{J})$ plotted for negative ω.

4.2 Experimental results

The performance of the proposed scheme was demonstrated by extensive experiments carried out at MCLab. The performed tests are summarized in the following:

- Tests in close to open-water conditions. We could not reproduce entirely the open-water conditions due to the influence of previous motions, presence of walls and free surface motion. The results were, however, accurate.

- Tests with a wake screen, described in Chapter 2, placed upstream the propeller. This device scaled the local flow down in order to simulate

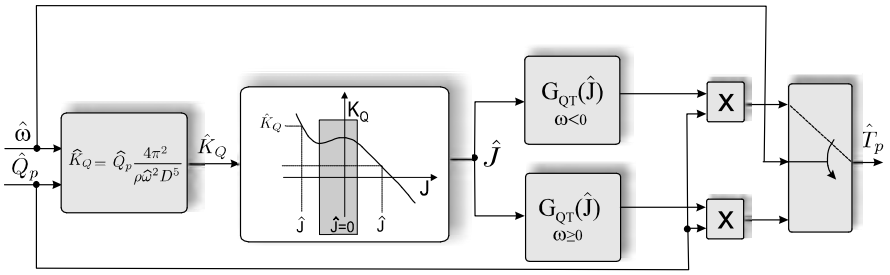

Figure 4.4: Block diagram of the procedure to compute the propeller thrust from the estimated torque and shaft speed.

one of the effects of the interaction between the propeller and the vessel hull.

- Tests with yawed flows. We carried out some experiments by running the towing carriage at constant speed and rotating the propeller housing along its vertical axis, influencing the propeller inflow with varying cross flows.

- Tests in small amplitude waves

- Tests with large thrust loss. These tests were conducted in order to reproduce the main effects that occur when propellers operate in extreme sea conditions.

The described results were obtained with the propeller P1362.

4.2.1 Observer tuning

The gains l_1, l_2 and the time constant τ_1 for the torque observer in (4.3) were chosen as follows. The condition A1 of proposition 4.1 in Section 4.1 was satisfied with $\alpha = 1.7 \cdot 10^5$. This value was quite large due to the *arctan* function that represents the Coulomb friction, which presents a steep slope for values of ω close to zero due to the small value of ϵ. The conditions A2-A5 were satisfied with $\mu = 1$, $\kappa = 10$, and with

$$\begin{aligned} l_1 &> 4.1 \cdot 10^{-2} + 3.5 \cdot 10^{-12} l_2, \\ 0 &< l_2 < 5 \cdot 10^{20}, \end{aligned}$$

which practically allowed us to choose l_1 and l_2 freely. The gains l_1 and l_2 were chosen as a trade-off between the two opposite requirements: the need of having the observer dynamics faster than the system dynamics and noise free estimates.

The time constant was obtained from a sensitivity analysis on the observer estimation errors with respect to τ_1. Running the observer with $l_1 = 3$, $l_2 = 80$, on data acquired over more than 1 h of tests carried out at different advance speeds and shaft speeds, we derived the plot of Figure 4.5. The graph shows the root mean square error (RMSE) between the observer estimates and the measurements. The value of the time constant has been varied between 0.01 and 100. For $\tau_1 \geq 1$, the accuracy of the estimates was practically the same, while for smaller values the estimates were less precise. For small values of τ_1, a decrease of the shaft speed estimation error corresponded to a decrease of the torque estimation error. This allows choosing the time constant based on the measured speed error, since the torque measurements is not available in real cases. The observer parameters used in the experiments are $l_1 = 3$, $l_2 = 80$ and $\tau_1 = 10$.

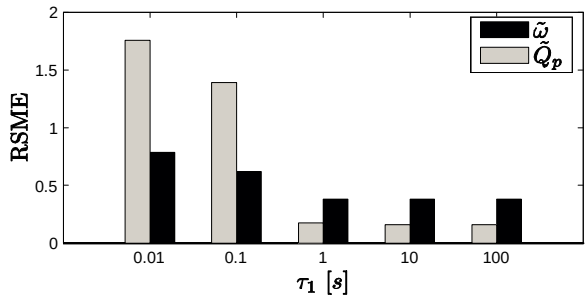

Figure 4.5: Observer estimation errors for different values of τ_1.

4.2.2 Open-water tests

When performing the open-water tests, in order to avoid losses due to ventilation, the relative propeller submergence was chosen equal to $h/R = 4$, where h is the propeller submergence. Figures 4.6 and 4.7 show data from an experiment where both the advance speed and the shaft speed had a trapezoidal form. Figures 4.8 and 4.9 show data obtained with sinusoidal advance and shaft speed.

The shaft speed and propeller torque estimates are plotted in part (a) and (b) of Figures 4.6 and 4.8 respectively. Both estimates are accurate

and almost indistinguishable from the measurements. Part (c) and (f) of the same figures show the torque estimation errors and the advance speed.

Figures 4.7 and 4.9 show the measured and estimated thrust from the same tests. The estimated $\hat{T}_p$ obtained with the proposed method, shown in part (a), reproduced quite well the measurements in all the quadrants, indicated, together with the advance angle β, in part (e) of the same figures. The estimate $\hat{T}_p$ is compared with the estimate $\hat{T}_{p_{C_T}}$, shown in part (c), computed using the measured four-quadrant propeller characteristics C_T, introduced in Section 3.4. The estimates obtained from the propeller characteristic were not very accurate, especially in the second and fourth quadrant where the inflow to the propeller was irregular. Similar results, in terms of accuracy, were obtained with the torque estimates $\hat{Q}_{p_{C_Q}}$ computed employing the four-quadrant propeller characteristic C_Q, shown in part (d) of figures 4.6 and 4.8. The proposed scheme furnished a more accurate thrust estimate since it can sense the effect of the advance speed variation through the propeller torque estimate.

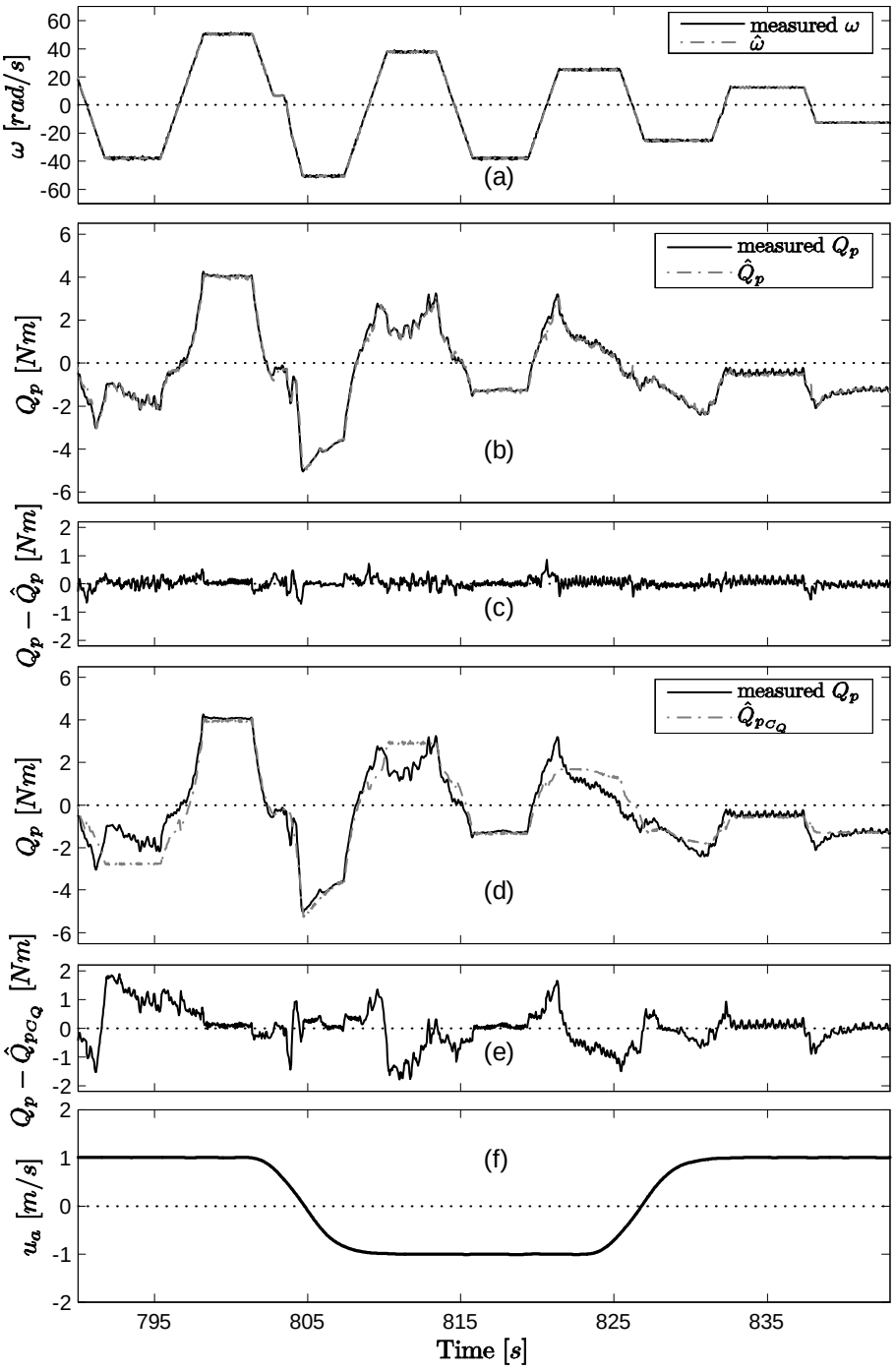

Figure 4.6: Data from the first open-water test.

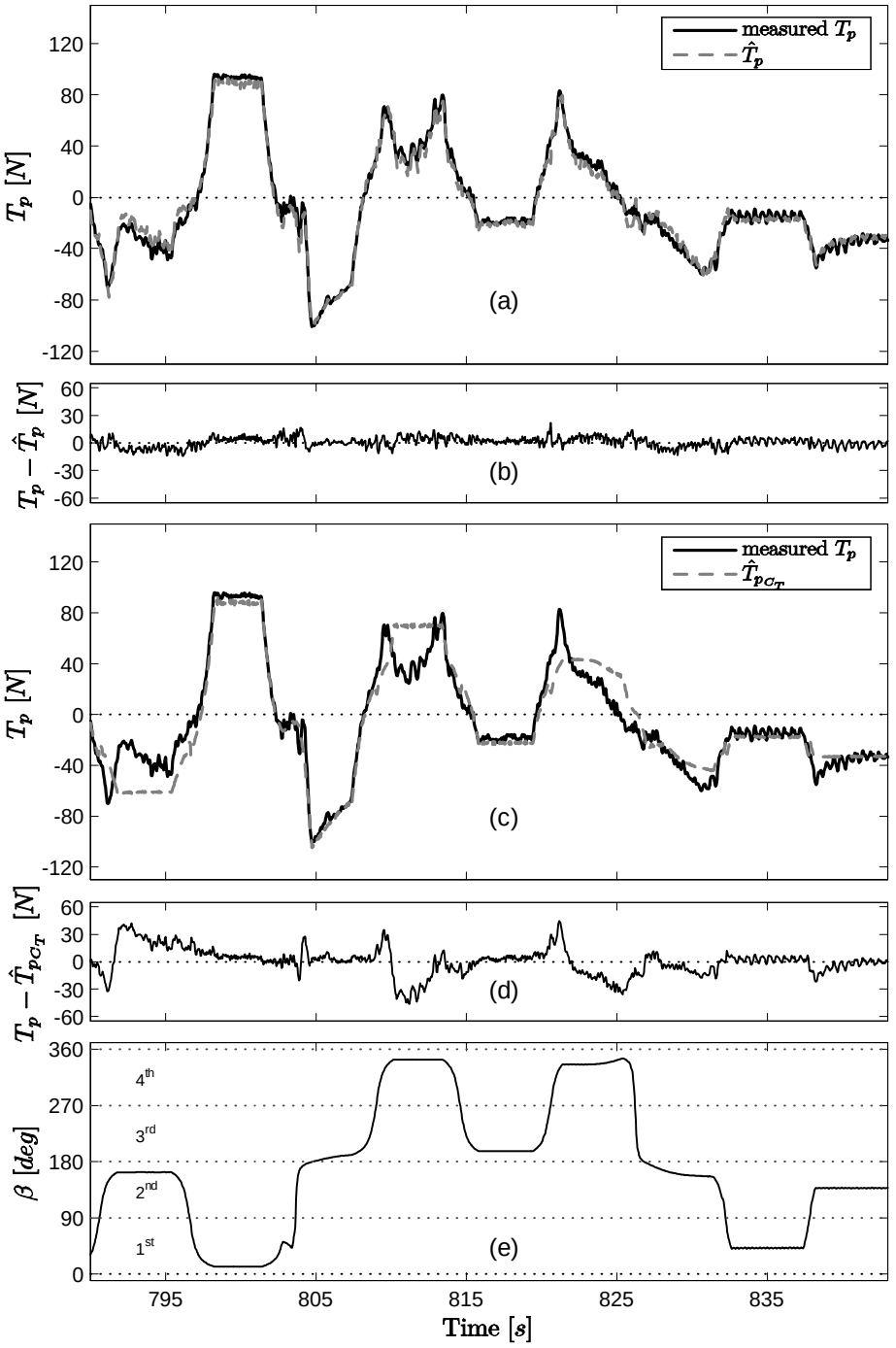

Figure 4.7: Data from the first open-water test.

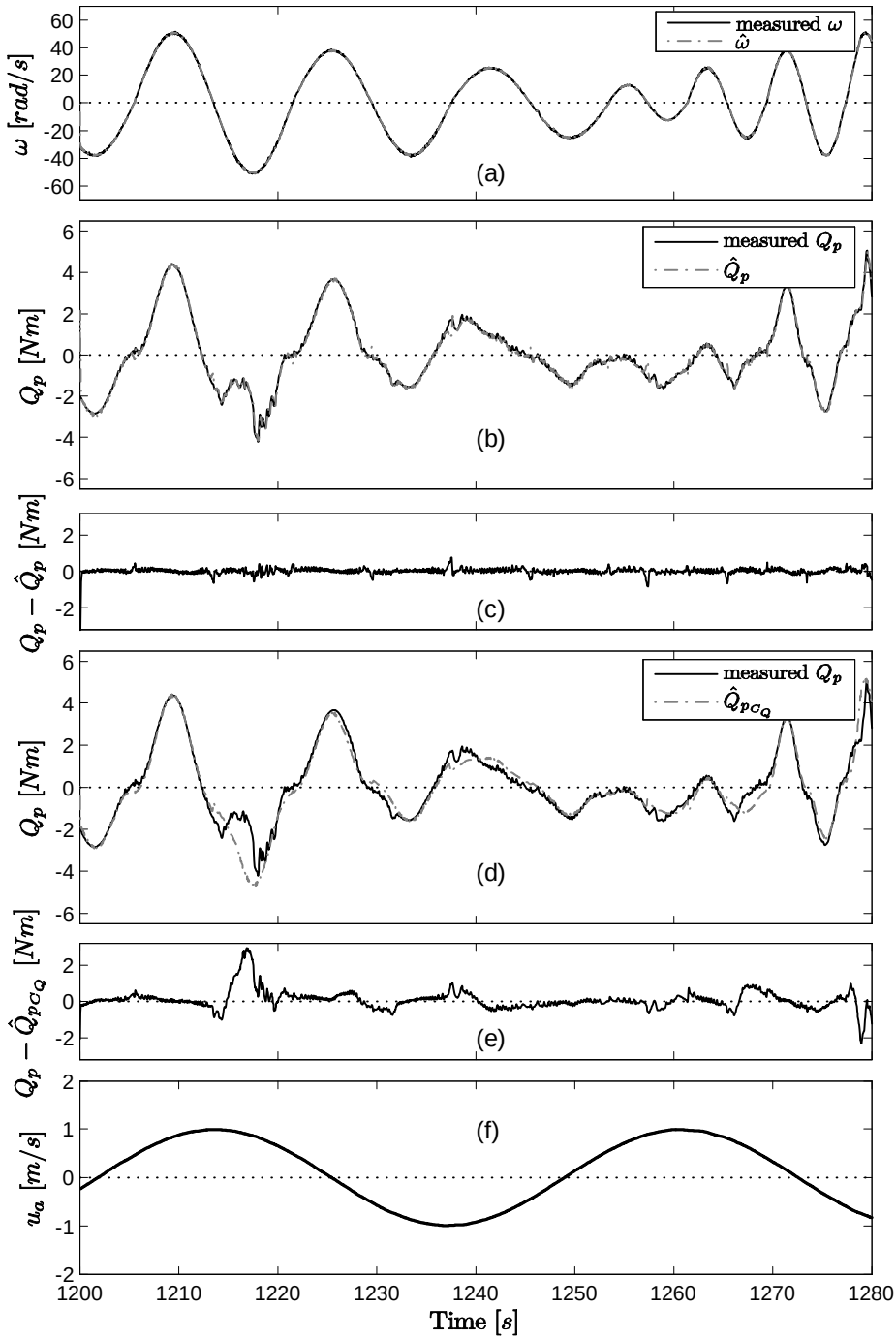

Figure 4.8: Data from the second open-water test.

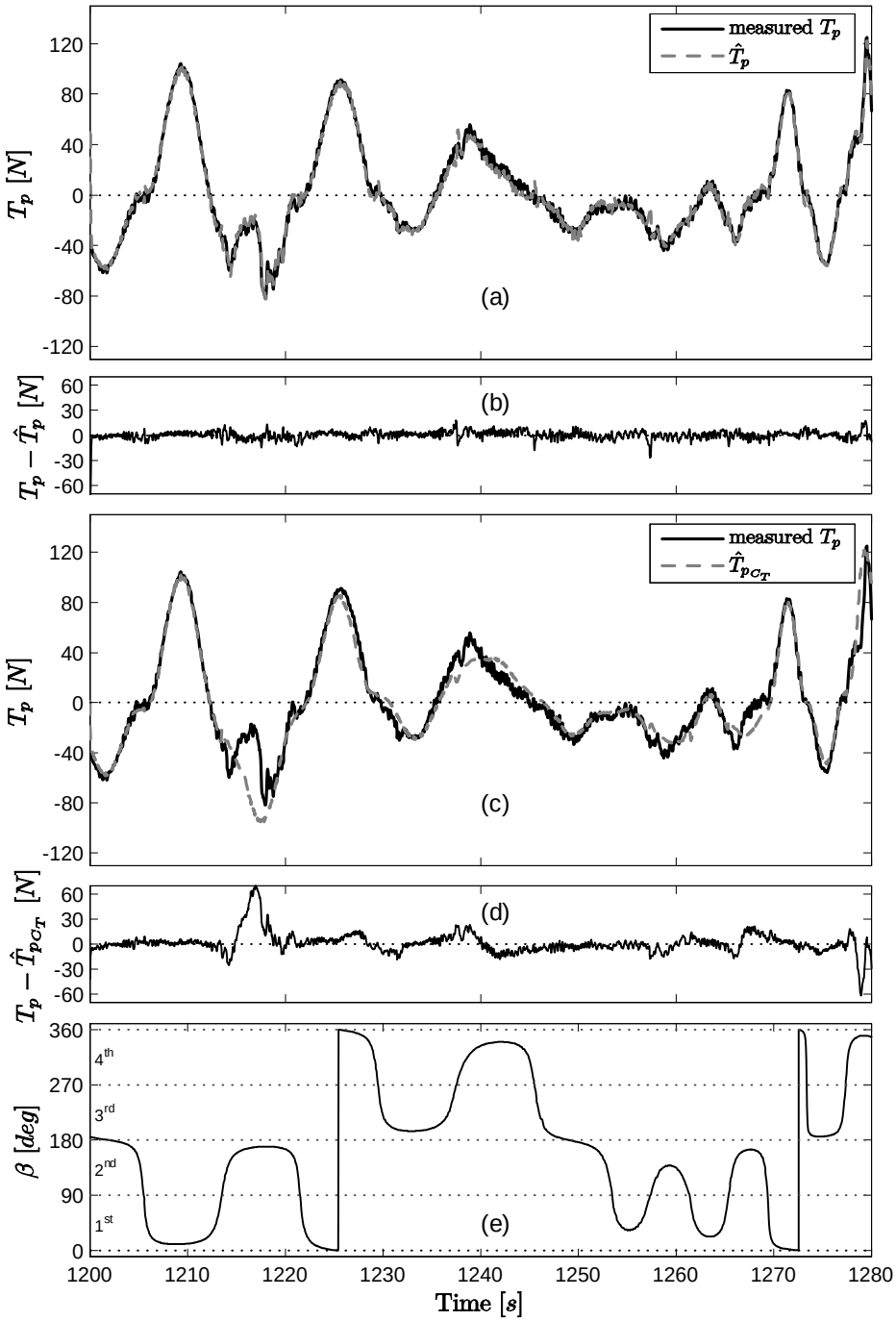

Figure 4.9: Data from the second open-water test.

4.2.3 Wake screen tests

Tests with a wake screen, shown in Figure 2.5, were performed to simulate one of the effects of the hull on the propeller inflow. The wake screen creates a uniform loss of the speed of the inflow to the propeller. This does not represent entirely the effect of the hull because the propeller inflow is not usually uniform. However, this test represents a more realistic scenario with respect to the open-water conditions. The relative propeller submergence was equal to $h/R = 4$.

Figures 4.10 and 4.11 show the results from a test where both the advance speed and the shaft speed had a trapezoidal shape. As for the open-water experiments, the estimates provided by the observer, shown in part (a) and (b) of Figure 4.10, were very accurate.

In parts (a) and (c) of Figure 4.11, the estimate $\hat{T}_p$ obtained with the proposed method is compared with the estimate $\hat{T}_{p_{C_T}}$, computed using the four-quadrant propeller characteristic C_T. The advance speed u_a, employed with the C_T characteristic, was computed with (3.11), where the value of the wake fraction w_f was identified from tests performed in steady-state conditions. For positive towing carriage speed u, shown in part(f) of Figure 4.10, the experimentally found value was $w_f = 0.3$. For negative towing carriage speed, the inlet water flow to the propeller was not affected by the grid, placed upstream of the propeller, and the wake fraction number was zero. The estimate $\hat{T}_p$ was quite accurate also in this experiment while the estimate $\hat{T}_{p_{C_T}}$, as for the open-water tests, was accurate only in the first and third quadrant. The same results were obtained when comparing the torque estimates.

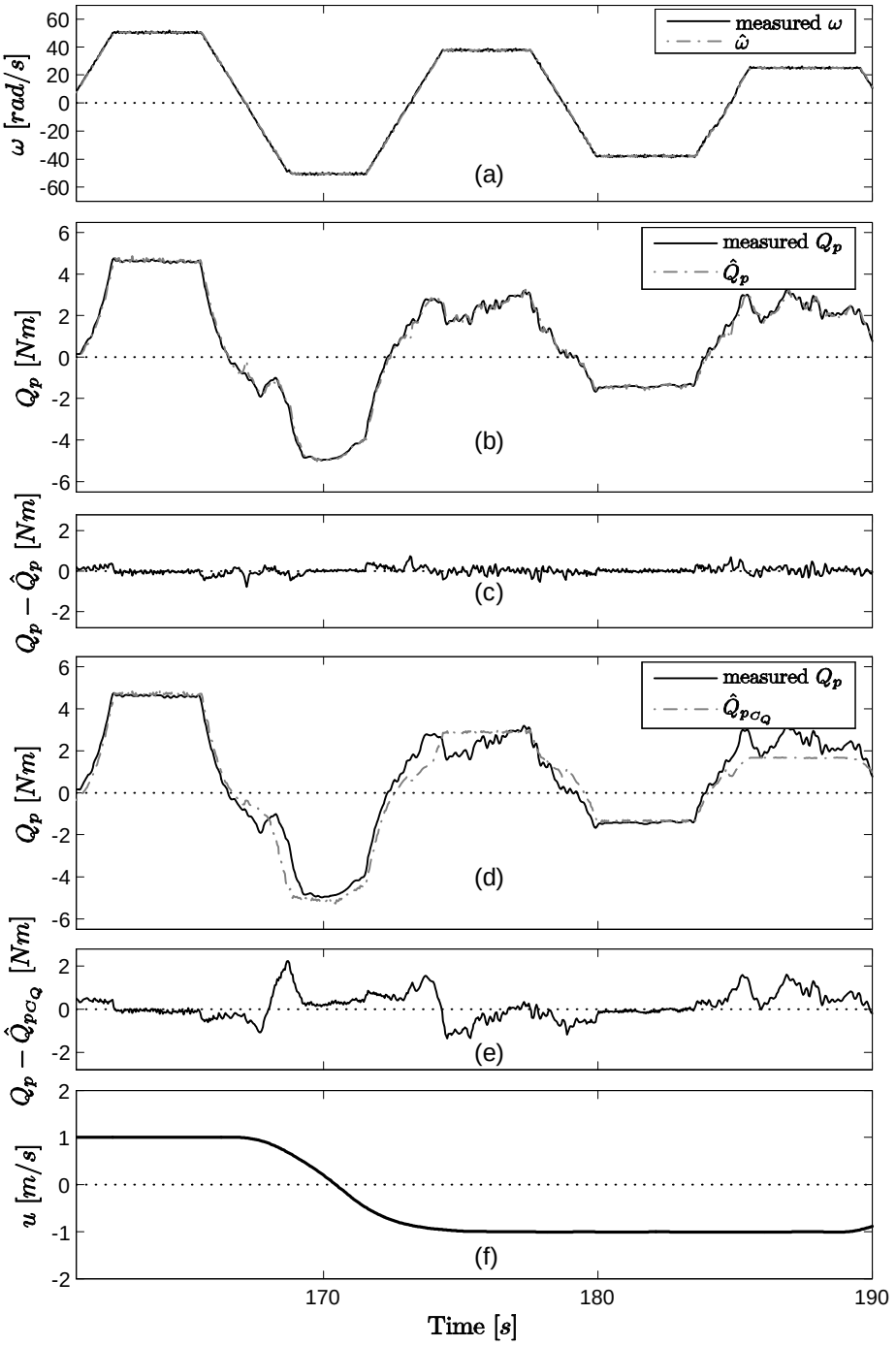

Figure 4.10: Data from the wake screen experiment.

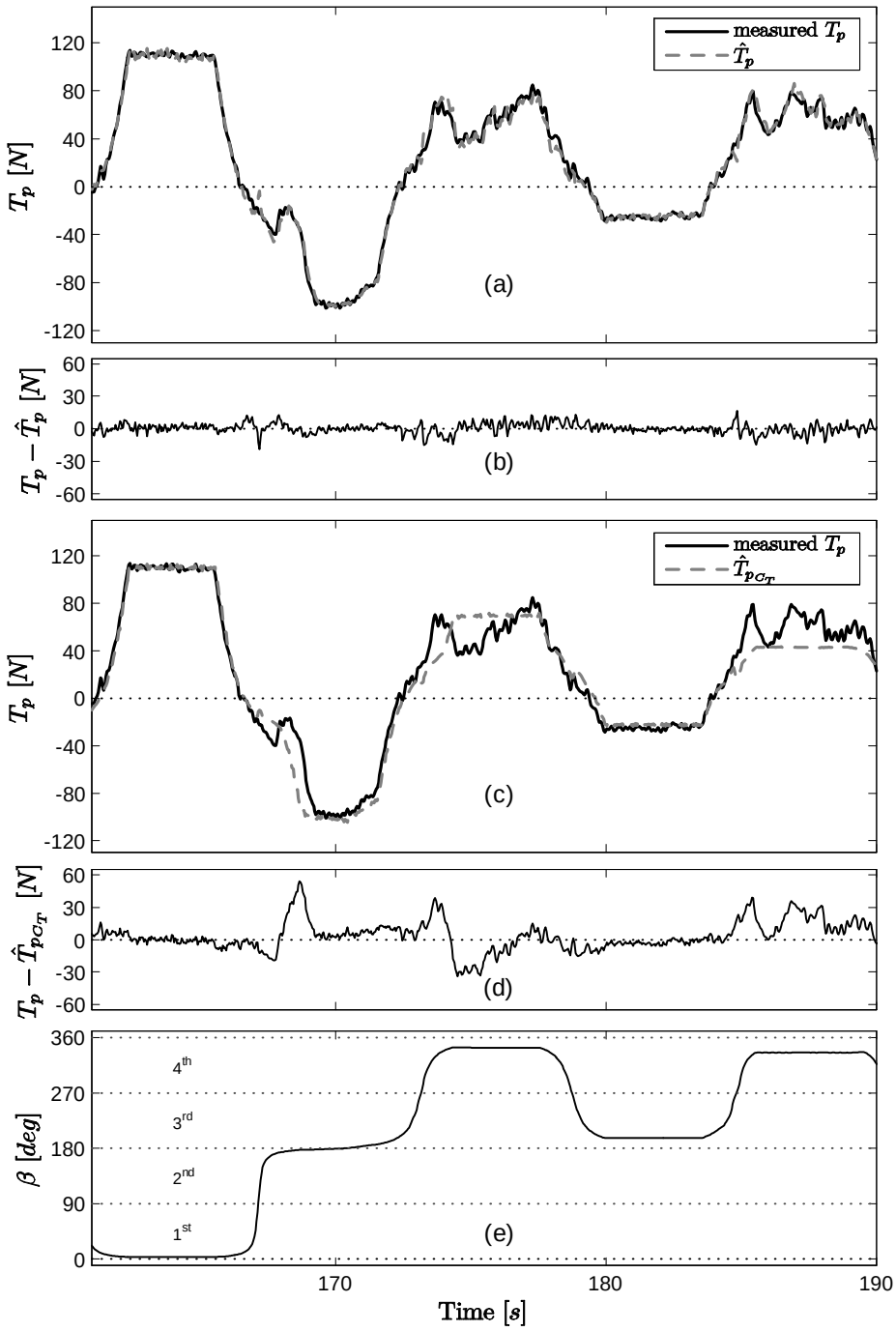

Figure 4.11: Data from the wake screen experiment.

4.2.4 Yawed flow tests

These tests were carried out to validate the estimation scheme in presence of varying yawed flows. Propellers are subject to yawed flows when vehicles turn, in presence of ocean currents or when the propeller is subject to other propeller wakes. These tests were performed by rotating the propeller housing along its vertical axis, as explained in Chapter 2. Figures 4.12 and 4.13 show data from a test where the propeller housing yaw angle ψ varied from -25 deg to $+25$ deg ($\psi = 0$ was the usual propeller position). The shaft speed, depicted in part (a) of Figure 4.12, presented oscillations because the motor was operating in torque control mode. The estimates obtained with our scheme were more accurate than the one obtained from the four-quadrant propeller characteristics. Even the thrust/torque mapping did not include the contribution of the yaw rate, the estimate were quite accurate due to the close relationship between thrust and torque. The thrust and torque obtained using the four-quadrant propeller characteristics resulted less accurate, especially in the fourth quadrant, due to the use of the towing carriage speed u instead of the unknown actual advance speed u_a for the computation of the advance angle β.

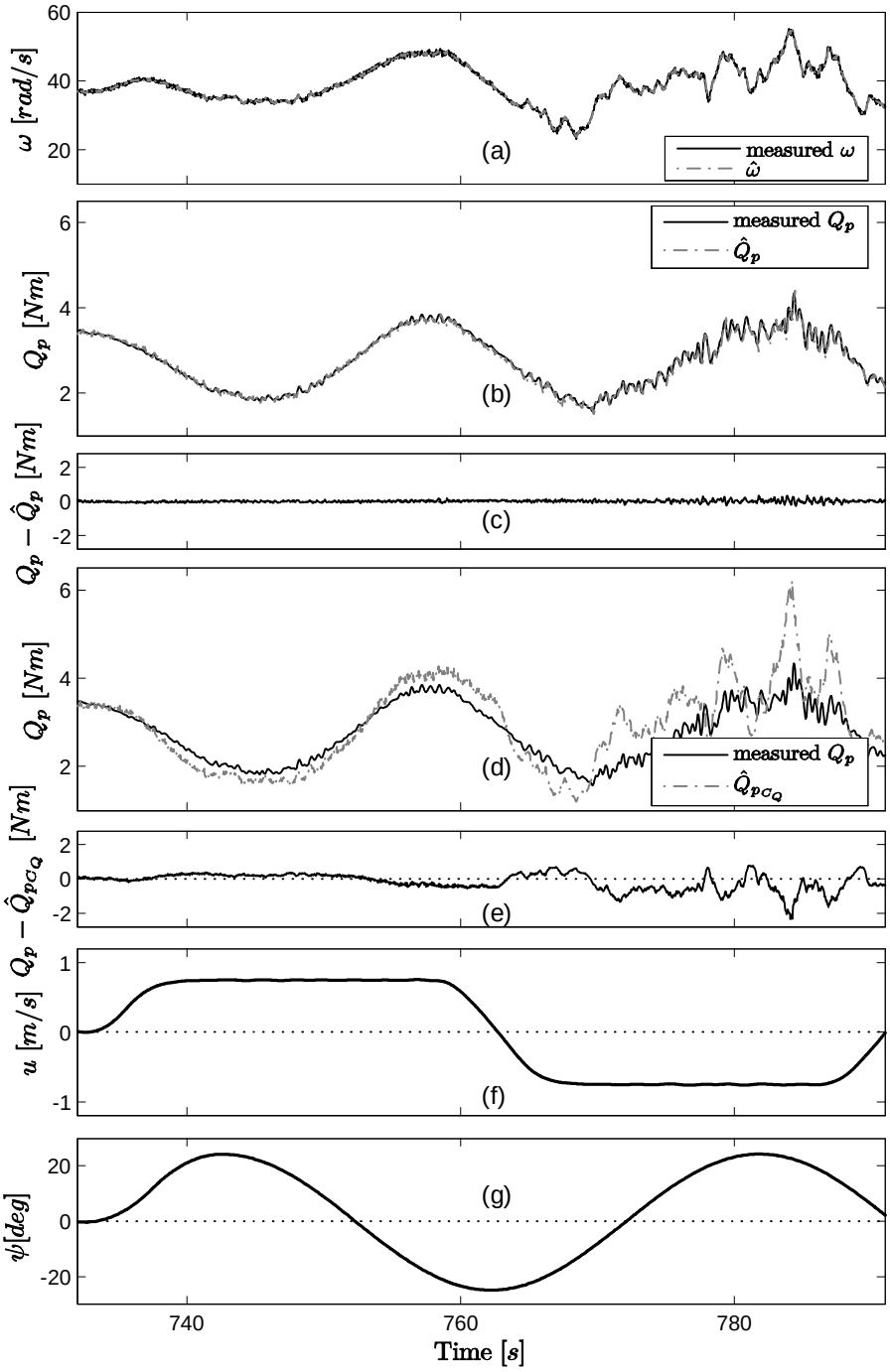

Figure 4.12: Data from the yawed flow test.

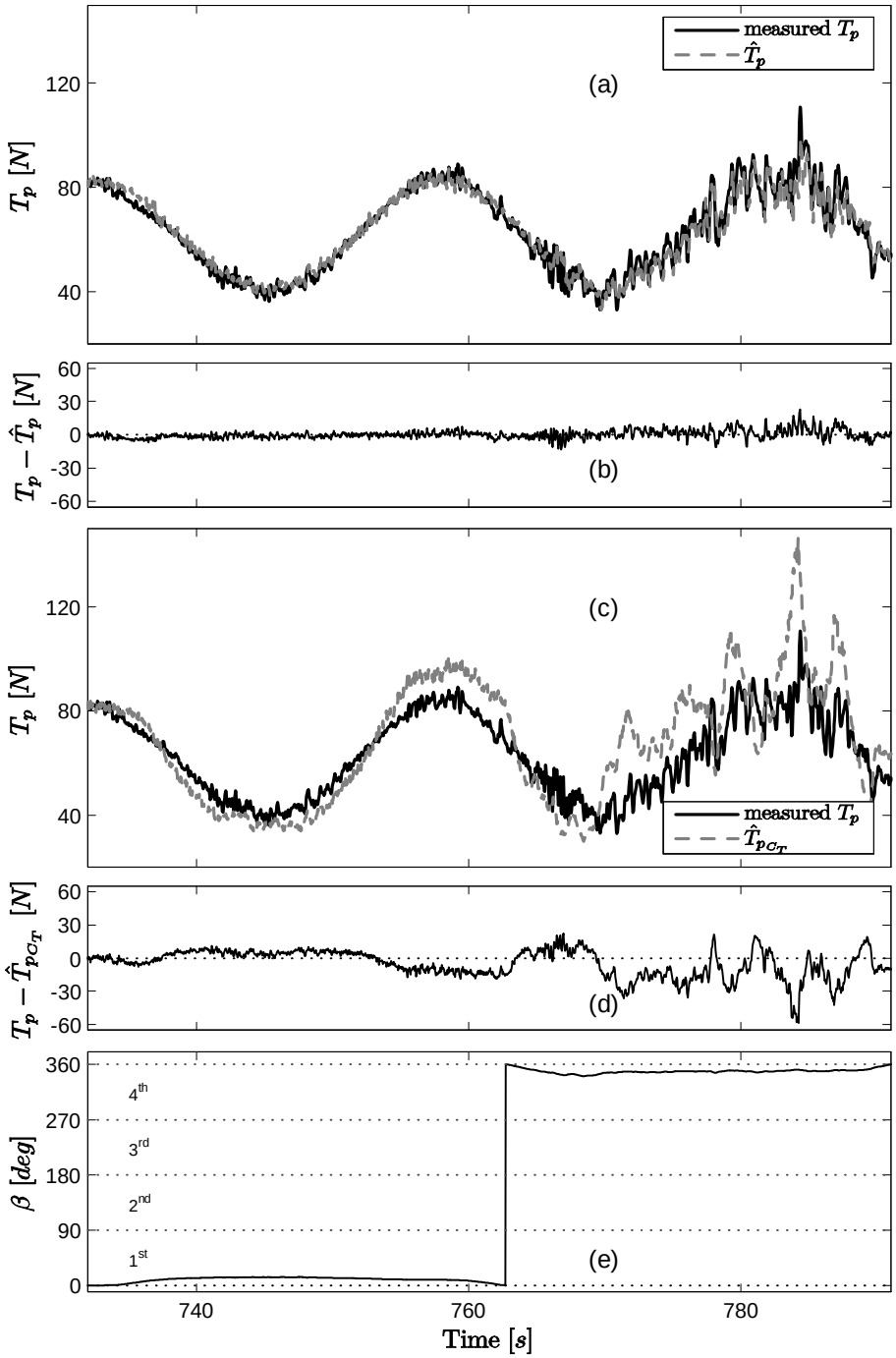

Figure 4.13: Data from the yawed flow test.

4.2.5 Tests with small amplitude waves

The tests with small amplitude regular waves were carried out to reproduce the typical situation that occurs when ships travel in moderate sea conditions. For ships on passage, waves create load fluctuations in the propeller shaft due to variations of the propeller inflow velocity. At constant speed, for example, variations in inflow velocity gives rise to variations of the advance number J and hence in the propeller efficiency, as known from the open-water propeller characteristics. The estimation of the load variations, therefore the propeller operational condition, may be exploited in controllers for increasing the total propulsion efficiency. This will be treated in Chapter 8.

The results of this test are presented in Figures 4.14 and 4.15. We employed waves with 10 cm peak-to-trough amplitude and 2.5 s period. Even at constant shaft speed and towing carriage speed, thrust and torque presented fluctuations due to waves that created a periodic additional axial velocity that varies with depth and time across the propeller plane. These oscillations were accurately reproduced by the torque and thrust estimates, plotted in part (b) and (a) of Figures 4.14 and 4.15, respectively. The thrust and torque obtained from the propeller characteristics, depicted in part (d) and (c) of the same plots, did not exhibit the measured oscillations, vice versa constant values were obtained. This is due to the use of the towing carriage speed u instead of the actual advance speed u_a. It is interesting to note the correlation between the thrust, torque and the propeller submergence h, plotted in part (g) of Figure 4.14. The magnitude of thrust and torque was smaller when the propeller was closer to the water surface. This is due to the horizontal water speed induced by the waves that, according to the classical wave theory, is greater close to the surface, causing smaller values of thrust and torque. Vice versa, for greater values of the propeller submergence, the advance speed was smaller producing larger thrust and torque values.

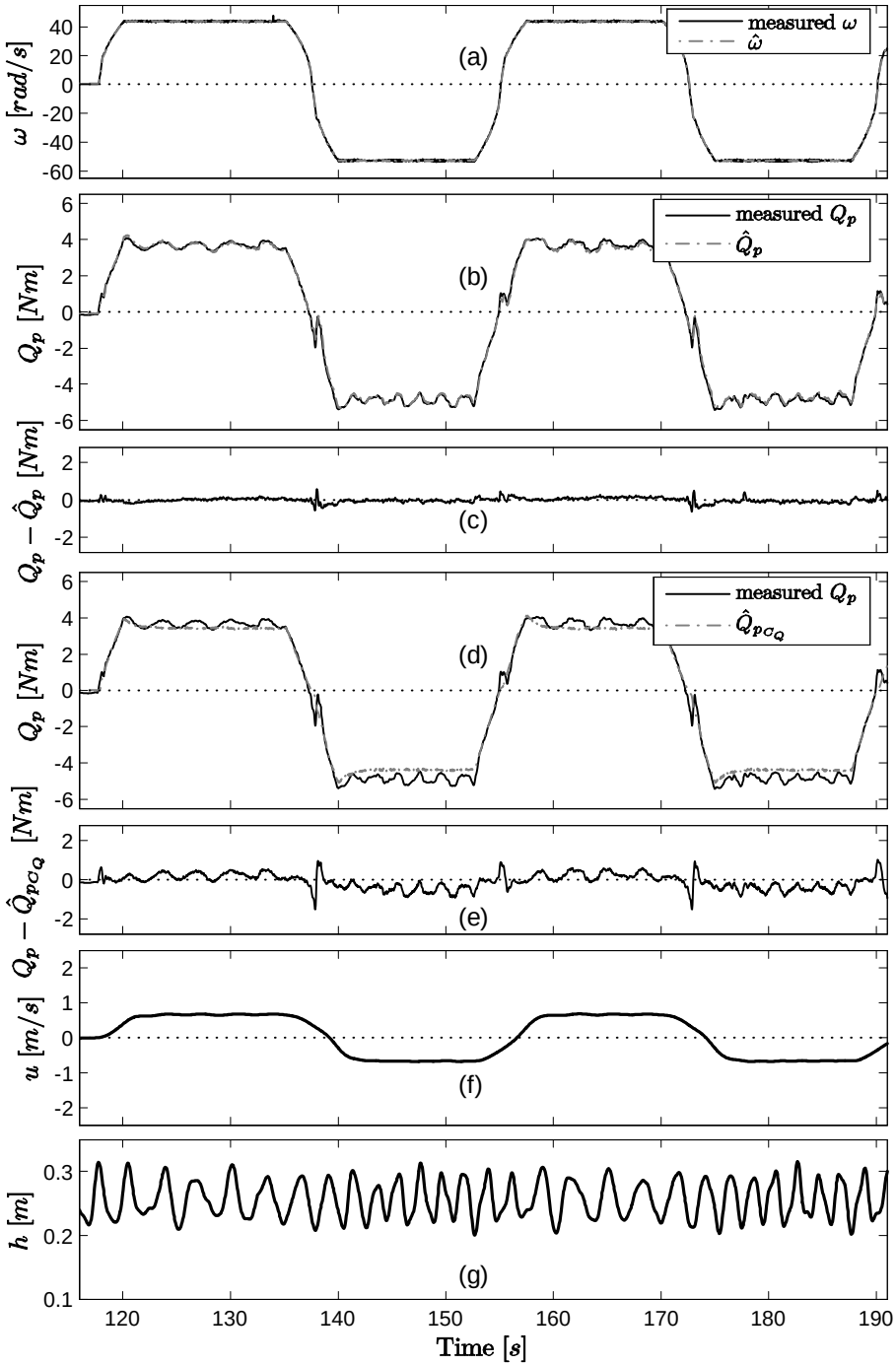

Figure 4.14: Data from the experiment with small amplitude waves.

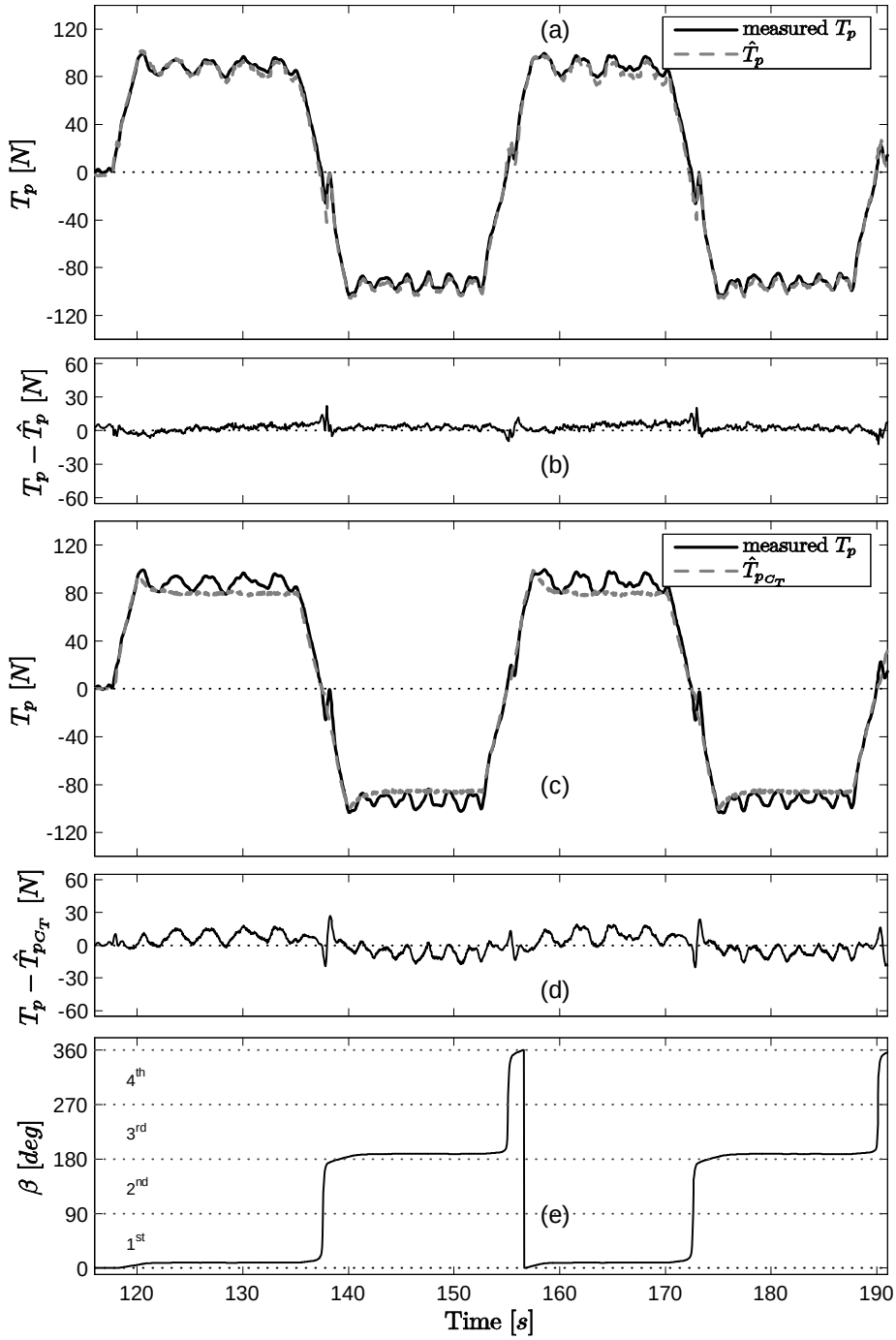

Figure 4.15: Data from the experiment with small amplitude waves.

4.2.6 Large thrust loss tests

In this section, the results of two tests performed with induced large thrust losses are presented. Large thrust losses are usually experienced in rough sea conditions where, due to the vessel motion induced by waves, propellers can operate close to the water surface or even partially in air. Losses are due to two main causes, in-and-out of water effect and ventilation (air suction). More information about these phenomena and how they influence the propeller behaviour are given in Chapter 7.

To induce large propeller losses, tests were conducted by moving the propeller along its vertical axis with a sinusoidal motion. This test, obviously, did not reproduce entirely rough sea conditions, but it was a valid indication of the performance of the proposed method when propellers operate in off-design conditions.

The first test was performed at zero towing carriage speed ($u = 0$) and with regular waves with peak-to-trough amplitude of 10 cm and 1.45 s period. The results are plotted in Figures 4.16 and 4.17. The propeller shaft speed, depicted in part (a) of Figure 4.16, was kept constant at 38 rad/s. Part (g) of the same plot shows the propeller vertical displacement d, measured from the water surface to the propeller shaft. A drop of thrust and torque occurred when the propeller rotated close to the water surface and partially in air, where the load decreased due to ventilation and loss of effective disc area. The small oscillations of thrust and torque were caused by waves that created a periodic additional axial velocity. Both phenomena were well reproduced by the torque estimate, as shown in part (b) of Figure 4.16. The thrust estimate $\hat{T}_p$ obtained from the proposed method, depicted in part (a) of Figure 4.17, is compared with $\hat{T}_{p_{C_T}}$, obtained from the C_T characteristic, showed in part (c) of the same plot. The proposed method produced a satisfactory estimate and both the oscillations and the drop of thrust were properly captured. The estimates obtained from the four-quadrant characteristics were computed assuming $u_a = 0$, the best guess we could make since $u = 0$. As mentioned earlier, the actual advance speed was non zero since waves created an inflow to the propeller. With constant shaft speed and $u_a = 0$, both the estimate $\hat{T}_{p_{C_T}}$ and $\hat{Q}_{p_{C_Q}}$ were constant and could not capture the oscillations and the drops of thrust.

The second test was performed at nonzero towing carriage speed. In order to simulate a real scenario, the towing carriage was moved according to a surge vehicle dynamics combined with the measured thrust produced by the propeller. The towing carriage speed reference was computed from

$$m\dot{u} = R(u) + (1 - t_d)\, T_p, \tag{4.15}$$

where $(1 - t_d)$ is the thrust deduction factor introduced in Chapter 3. The hull resistance $R(u)$ included a linear and quadratic drag term and was computed from

$$R(u) = -d_l u - d_q u\,|u|\,. \tag{4.16}$$

The vessel dynamics was simulated with $m = 200\ kg$, $d_l = 30$ and $d_q = 20$. The measured propeller thrust was fed into the model (4.15) and the resulting vehicle speed was used as a reference for the towing carriage velocity control system. The results of this test, which was performed without waves, are reported in Figures 4.18 and 4.19. As shown in part (g) of Figure 4.18, the propeller submergence h varied from 24 cm to the extreme value of 0 cm, where the propeller rotated with half diameter out of the water. Due to ventilation and in-and-out of water effect, the largest thrust and torque losses were measured in correspondence of the minimum submergence. According to the vessel dynamics (4.16), the towing carriage speed decreased after the drops in the propeller thrust, and accelerated when the thrust increased. The towing carriage speed is plotted in part (f) of Figure 4.18.

The torque estimate, shown in part (b) of Figure 4.18, was quite accurate. The small discrepancies between the estimate and the measurement were probably due to variations in the friction torque. The accuracy of thrust estimates, plotted in part (a) of Figure 4.19, was acceptable but there were some discrepancies between the estimates and the measurements, especially in correspondence of the drops of thrust. The reason for this is that the thrust/torque mapping accounts only for the variations in the advance speed. The gain between torque and thrust, when the propeller pierces the water, can be quite different from the case where the propeller is deeply submerged. Nevertheless, the results obtained employing the presented scheme were more precise than the one obtained from the propeller characteristics, shown in part (d) and part (c) of Figures 4.18 and 4.19, respectively.

It is interesting to notice the behaviour of the thrust and torque estimates obtained with the open-water propeller characteristics when the drops of thrust occurred. Since the advance speed u_a was assumed to be equal to the towing carriage speed u, when the towing velocity decreased, due to loss of thrust, the estimates increased. This is due to the fact that, according to the propeller characteristics, a reduction of the advance speed, at constant shaft speed, gives rise to an increase of the propeller thrust. Therefore, the drops of thrust were not captured at all.

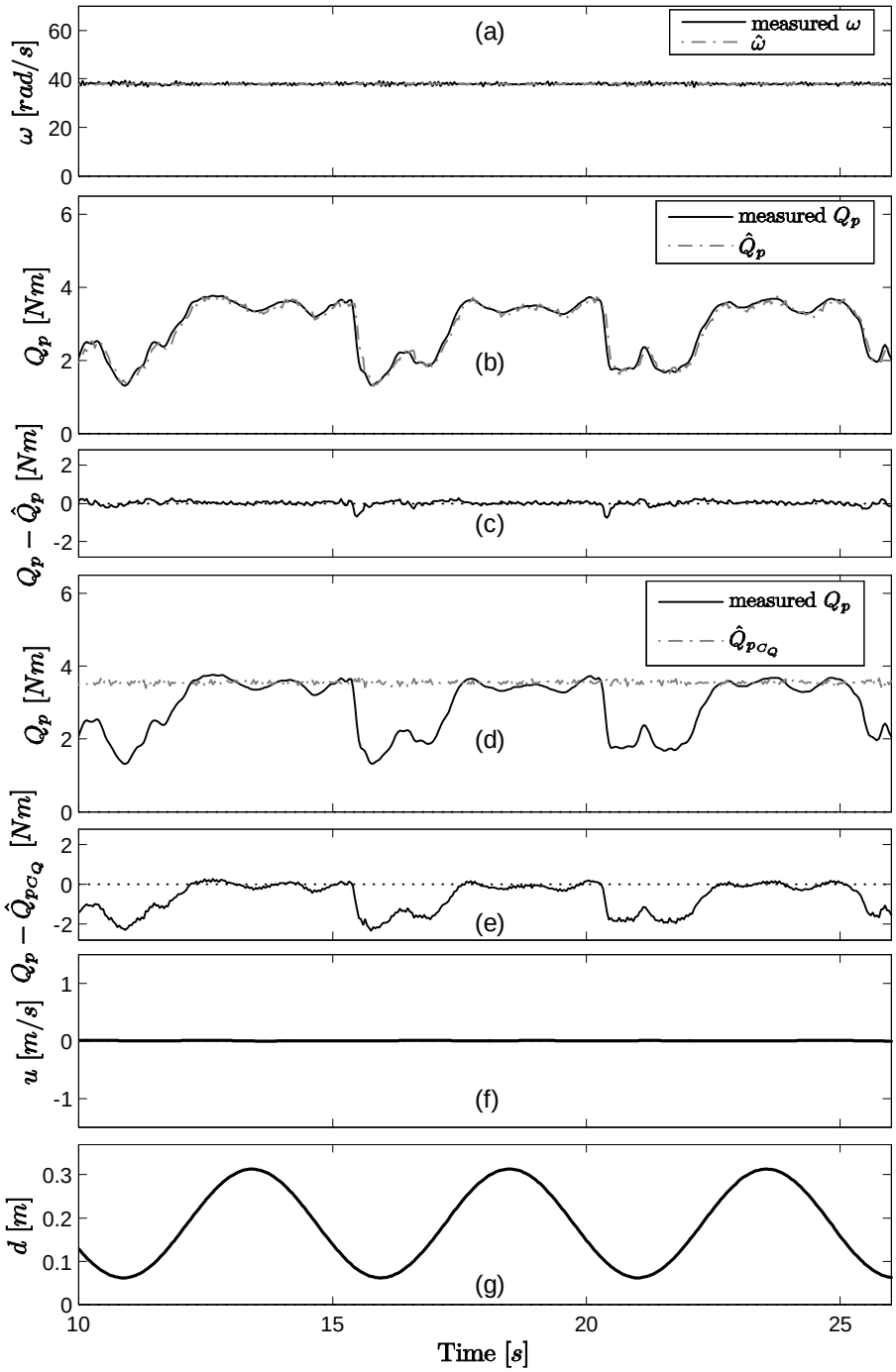

Figure 4.16: Data from the experiment with large thrust loss and $u = 0$.

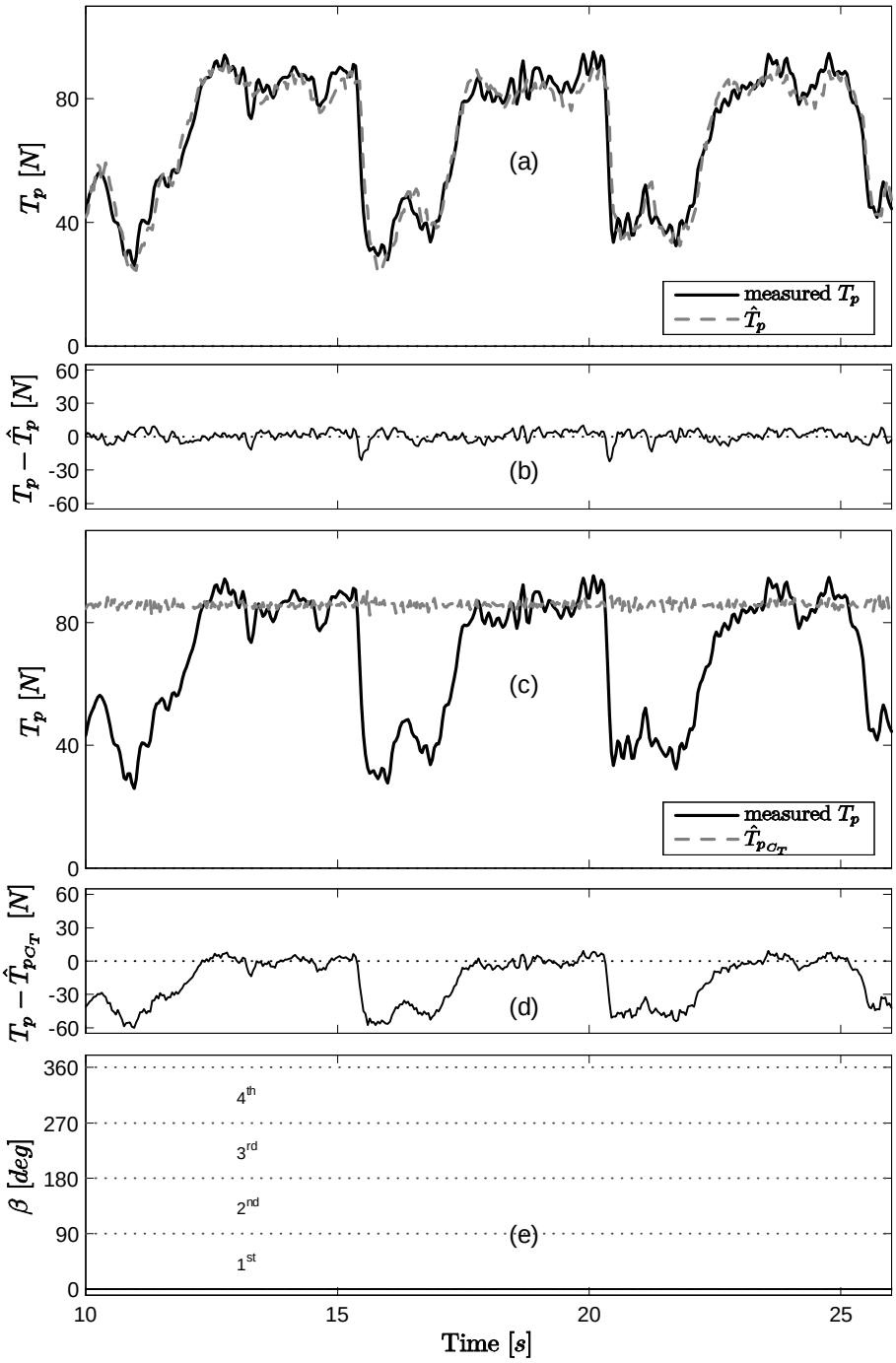

Figure 4.17: Data from the experiment with large thrust loss and $u = 0$.

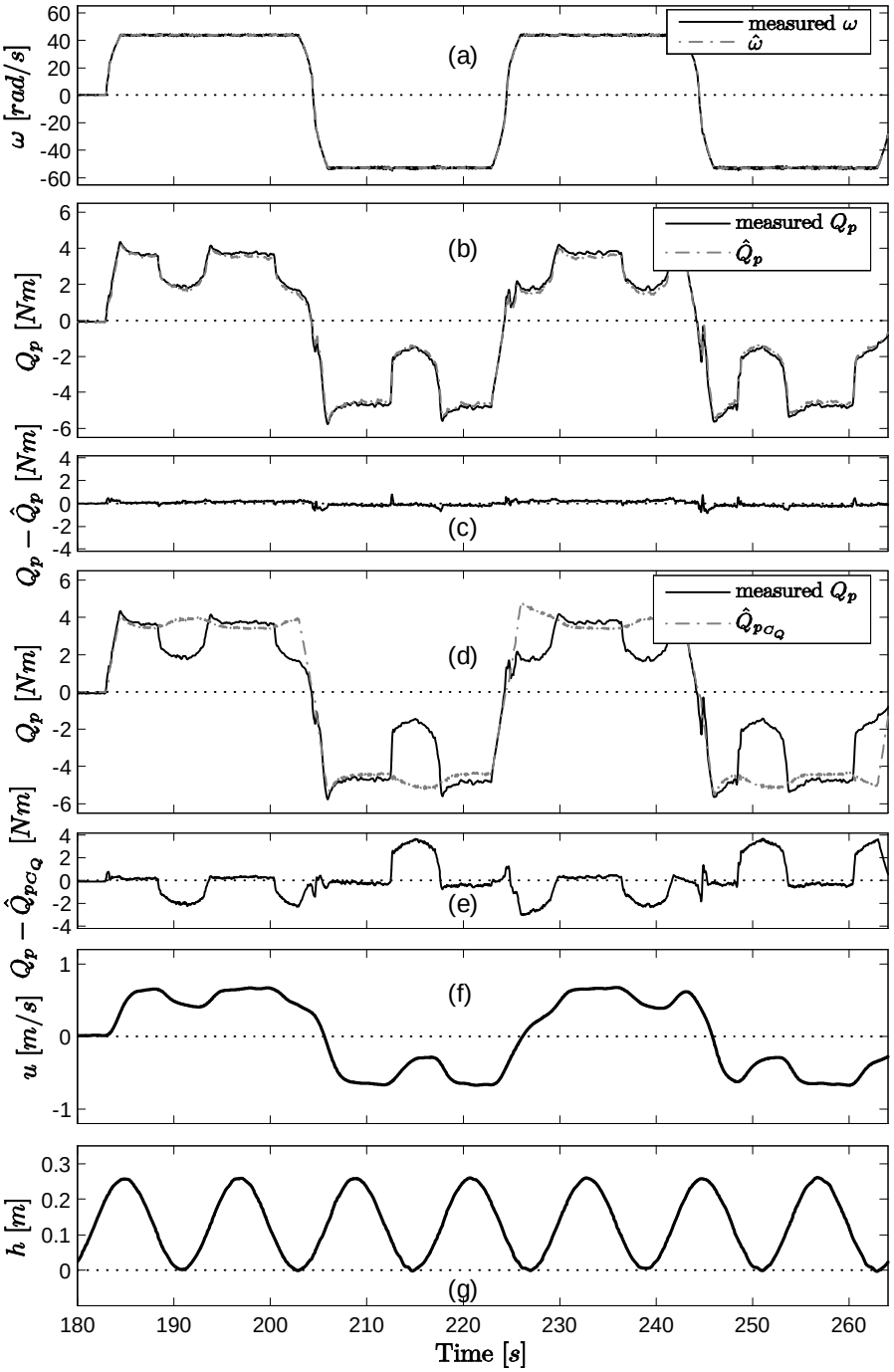

Figure 4.18: Data from the experiment with large thrust loss and $u \neq 0$.

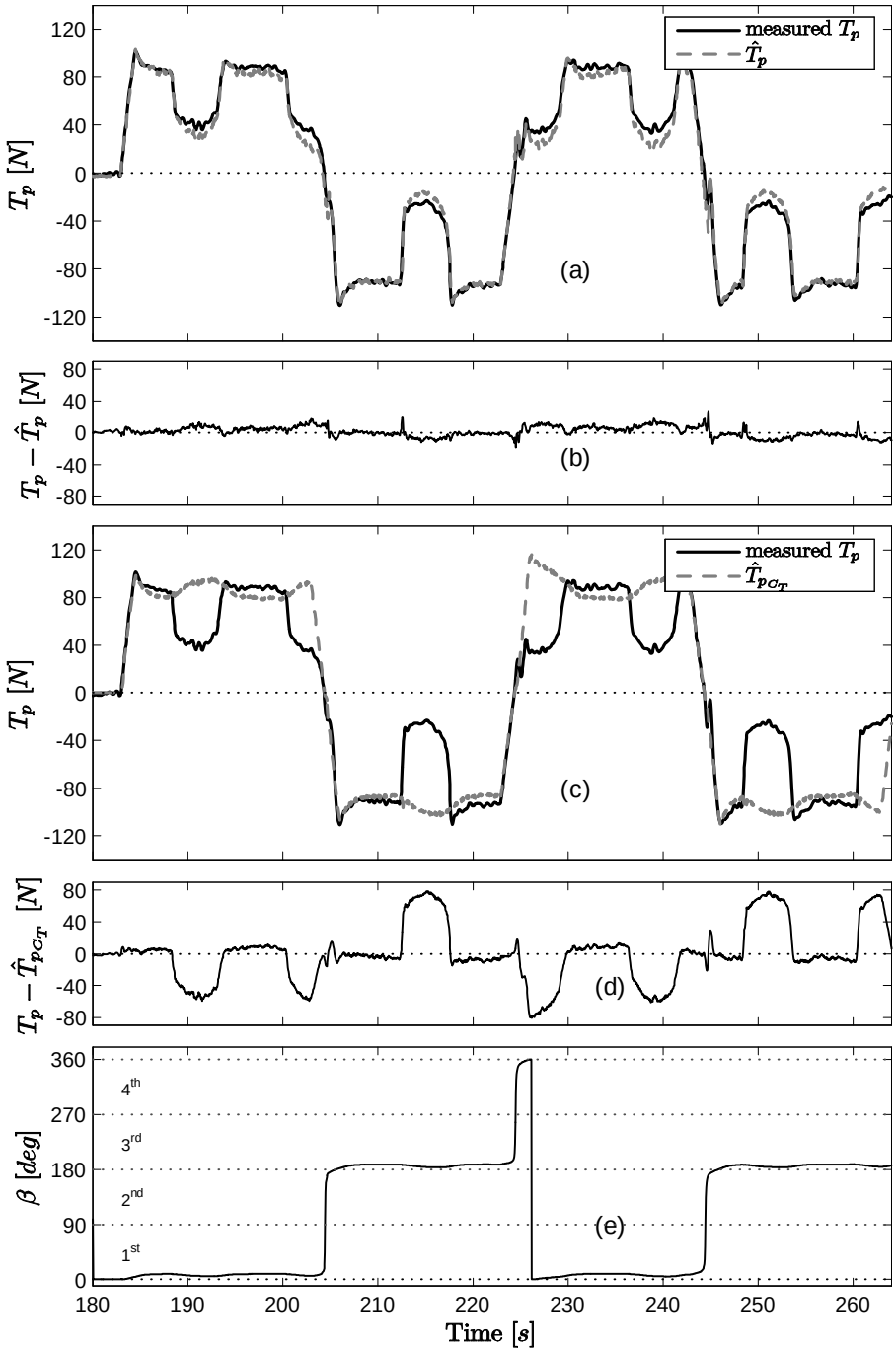

Figure 4.19: Data from the experiment with large thrust loss and $u \neq 0$.

4.3 Discussion

The presented estimation scheme furnished good estimates in all the tested cases and, when compared to the use of the four-quadrant propeller characteristics, it showed improved performance in terms of accuracy. The strength of this approach lies in the use of only the shaft speed and the motor torque measurements, usually available on propulsion systems. The thrust estimation scheme can be implemented both for unducted and ducted propellers and, although the presented results concern tests carried out on an electrically driven propeller, the scheme could be applied also to propellers driven by diesel engines.

The accuracy of the estimates depends highly on the quality of the measurements and the identified friction torque and shaft moment of inertia. This is due to the fact that the torque model used in the observer is not derived from the physics of the system, but it represents a time-varying parameter. If the shaft speed measurement is heavily corrupted by noise, the observer gains will be small and the delay between the estimates and the actual values could be significant. In our setup, the motor torque signal was quite noisy, but the shaft speed, used in the output injection terms in the observer, was of good quality. Therefore, the delay between the estimates and the measurement was not significant. A small delay can be observed in Figures 4.16 and 4.17, where the time scale is smaller then in the other plots. The observer gains influence also the filtering property of the observer. Therefore, a trade-off should be found between the needs of noise free estimates (small gains) and contained delays between the estimates and the actual values (high gains). Moreover, to obtain accurate results, the open-water propeller characteristics need to be precise. For full-scale vessels, if the propeller characteristics are obtained from model scale tests, it must be corrected for scale effects.

An alternative way to obtain the thrust and torque estimates would be to employ an observer that uses the simplified torque model of Section 3.6.2 instead of using the one adopted here. In that way we could estimate the torque loss and compute the torque estimate from (3.36) and (3.37). This approach has been tested and the results were practically equivalent, in terms of accuracy, to the ones obtained with scheme presented in this chapter. For this reason they have not been reported.

Chapter 5

Thrust controller for calm and moderate sea conditions

Speed and positioning control systems for marine vehicles are subject to an increased focus with respect to performance and safety. An example is represented by drilling operations performed with semi submersible rigs where the control of position and heading requires high accuracy. Drifting from the drilling position could cause severe damage to equipment and environment. Also, the use of underwater vehicles for deep ocean survey, exploration, bathymetric mapping and reconnaissance missions, has become more widespread. The employment of such vehicles in complex missions requires high precision and maneuverability, therefore, demanding accurate thrust control.

In the overall vehicle control system, propellers play a fundamental role since they are the main force producing devices. The primary objective of the low-level thruster controller is to obtain the desired thrust from the propeller regardless of the environmental state. The thrust tracking capability is one of the performance criteria considered in a thruster control system. It is also very important to take into account the power consumption and the mechanical wear-and-tear of the propulsion system. In general, for surface vessels, it is fundamental to avoid large power peaks and overload of the power generators that may result in power blackout, compromising the results of the operations. For underwater vehicles, due to the limited battery life, high propulsion efficiency is essential to ensure the accomplishment of the missions. The mechanical wear-and-tear of the propulsion system is certainly a more important matter for surface vessels than underwater vehicles. The operational conditions of propellers on sur-

face vessels are highly influenced by waves, ocean currents and the vessel motion due to the environmental forces; therefore, propeller are subject to more load variations than on underwater vehicles. These load variations can produce oscillations in the motor and propeller torque and lead to increased mechanical wear-and-tear, as investigated in Domachowski *et al.* (1997). The propellers on underwater vehicles, since they usually operate far from the surface, are not influenced by waves and the propeller inflow is, in general, more uniform than for surface vessels. In this case, the load variations due to the environment are less significant.

As reported in Smogeli *et al.* (2005), today's industrial standard for fixed pitch propellers is shaft speed control, where the desired shaft speed is computed from the desired thrust through a static mapping. Conventionally, also torque and power control are employed for propellers; see for example Smogeli *et al.* (2005), Sørensen *et al.* (1997) and Blanke and Nielsen (1990). Experiments presented in Smogeli *et al.* (2005) and Pivano *et al.* (2007*b*), show that, in terms of produced thrust, the conventional shaft speed controller is the most sensitive to variations in the advance speed, followed by the power and the conventional torque controller. The power controller presents the smallest variations in the consumed power and it is usually employed if the power generators do not allow large power fluctuations. The conventional shaft speed controller gives generally the best results in terms of wear-and-tear of the mechanical parts. All the mentioned controllers do not use any information about the propeller working condition; therefore, when thrust losses occur, the degradation of the propeller performance may lead to unsatisfactory vehicle behaviour. This represented the main motivation for designing a propeller controller for calm and moderate sea conditions with improved thrust tracking capability with respect to the conventional propeller controllers.

The key element of the proposed controller is the estimation of the propeller torque losses, that allows deriving the propeller working condition. The strength of the proposed approach lies also in the fact that only the motor torque and the propeller shaft speed measurement, usually available on ships, are needed. The idea is to control the propeller shaft speed, where the speed reference is computed from the demanded thrust to the propeller and an estimate of the torque loss. The latter is obtained with a nonlinear observer similar to the one presented in Chapter 4.

A similar approach was presented in Guibert *et al.* (2005), where a thrust estimate, computed from the propeller torque obtained with a Kalman filter, was used in a feedback loop in order to obtain the demanded thrust.

The relation between thrust and torque involved an axial flow velocity model and required the knowledge of the advance speed, which is not necessary in the current work. The scheme was also highly sensitive to hydrodynamic and mechanical modeling errors. The performance was validated by simulations.

A propeller thrust controller for underwater vehicles was presented in Fossen and Blanke (2000). They focused on the design of a propeller shaft speed controller with feedback from an estimate of the propeller axial flow velocity. The motivation for that work was the compensation of thrust losses due to variations in the magnitude of the propeller axial flow velocity, coupled to the vehicle surge dynamics. A linear approximation of the standard propeller characteristics was utilized. Hence, they could not guarantee accurate results in the full four-quadrant range of the propeller shaft speed and the vehicle speed. In the present work, the proposed controller is able to operate in all four quadrants, and does not need the vehicle speed measurement.

A nonlinear model based open loop controller that involved the axial flow velocity was also reported in Bachmayer and Whitcomb (2001). The focus was put into the design of a thrust tracking controller exploiting the nonlinear dynamic model previously introduced in Bachmayer *et al.* (2000). The controller was designed only for a limited range of the advance speed. Moreover, the model used lift/drag coefficients identified from the axial flow velocity, conventionally not measured on propellers. The controller was validated by simulations.

This chapter is organized as follows. The thrust controller scheme is presented in Section 5.1. The observer for the torque loss estimation is developed in Section 5.2. The shaft speed reference generator is described in Section 5.3 and the control law presented in Section 5.4. The experimental results are illustrated in Section 5.5. Alternative thrust control schemes are presented in Section 5.6 and a discussion is given in Section 5.7.

5.1 Structure of the thrust controller

A sketch of the overall control system is depicted in Figure 5.1. The main idea is to compensate for the thrust losses due to changes in the advance speed by varying the shaft speed to fulfill the demanded thrust. First, the desired propeller torque Q_{p_d} is computed from the desired thrust T_{p_d} using the standard propeller characteristics in combination with an estimate of the advance number J; second, the desired shaft speed is computed from

Q_{p_d} and the estimated torque loss $\hat{\Delta}_q$. The torque loss $\hat{\Delta}_q$ is estimated with an observer based on the simplified torque model (3.38) and the shaft speed dynamics (3.1).

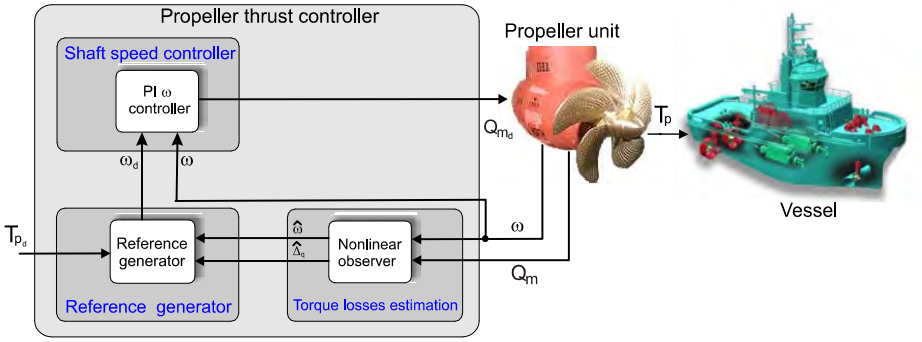

Figure 5.1: Thrust control scheme for calm and moderate sea conditions.

5.2 Observer for torque loss estimation

Grouping the nonlinearities in the function $\psi(\omega)$, the shaft dynamics (3.1) can be rewritten as:

$$J_m\dot{\omega} = R_{gb}Q_m - \psi(\omega) - k_{f_2}\omega - \Delta_q \tag{5.1}$$

where Δ_q is given by (3.38), recalled here for convenience of the reader:

$$\dot{\Delta}_q = -\frac{1}{\tau_2}\Delta_q + w_2. \tag{5.2}$$

The nonlinearity $\psi(\omega)$ includes the nonlinear friction terms and the term of the torque model (3.36) with a quadratic dependence from the shaft speed:

$$\psi(\omega) = G_{Q_{p,n}}\,|\omega|\,\omega + k_{f_1}\frac{2}{\pi}\arctan\left(\frac{\omega}{\epsilon}\right) + k_{f_3}\arctan(k_{f_4}\omega), \tag{5.3}$$

A nonlinear observer with gain l_1 and l_2 is designed to estimate the torque loss $\hat{\Delta}_q$ and the shaft speed $\hat{\omega} = \hat{y}$:

$$\begin{aligned} J_m\dot{\hat{\omega}} &= R_{gb}Q_m - \psi(\hat{\omega}) - k_{f_2}\hat{\omega} - \hat{\Delta}_q + l_1(y-\hat{y}) \\ \dot{\hat{\Delta}}_q &= -\tfrac{1}{\tau_2}\hat{\Delta}_q - l_2(y-\hat{y}) \\ y &= \omega. \end{aligned} \tag{5.4}$$

As for the torque observer presented in Section 4.1.1, the motor torque Q_m and the shaft speed ω are assumed to be measurable. Defining the observer error variables as $\tilde{\omega} = \omega - \hat{\omega}$ and $\tilde{\Delta}_q = \Delta_q - \hat{\Delta}_q$, from the model in (5.1)-(5.3) and the observer in (5.4), the observer error dynamics becomes:

$$\begin{array}{ll} J_m\dot{\tilde{\omega}} & = -\left(\psi(\omega) - \psi(\hat{\omega})\right) - l_1\tilde{\omega} - k_{f_2}\tilde{\omega} - \tilde{\Delta}_q \\ \dot{\tilde{\Delta}}_q & = -\frac{1}{\tau_2}\tilde{\Delta}_q + l_2\tilde{\omega} + w_2. \end{array} \tag{5.5}$$

Proposition 5.1 *If there exist two constants* a_{11}, $a_{22}>0$ *and the gains* l_1 *and* l_2 *are chosen such that*

A1 $l_1 > -k_{f_2}$,

A2 $\left|\frac{a_{11}}{J_m} + a_{22}l_2\right| < 2\sqrt{a_{11}a_{22}\left(\frac{k_{f_2}+l_1}{\tau J_m}\right)}$,

then the error dynamics (5.5) is uniformly globally exponentially stable (UGES) when $w_2 = 0\ \forall t$, *and input-to-state stable (ISS) with respect to* w_2.

Proof. The proof is given in Appendix A.2. ■

The estimates $\hat{\omega}$ and $\hat{\Delta}_q$ can be used to compute an estimate of the propeller torque from (3.36) as

$$\hat{Q}_p = G_{Q_{p,n}}\,|\hat{\omega}|\,\hat{\omega} + \hat{\Delta}_q. \tag{5.6}$$

5.3 Shaft speed reference generator

In order to compute the reference shaft speed, an intermediate step is necessary. This consists of the computation of the desired propeller torque Q_{p_d}, which is performed combining the desired thrust T_{p_d} with the thrust/torque relationship $G_{QT}(J)$, introduced in Section 4.1.2. Based on the argument presented in Section 4.1.2, the thrust to torque gain is derived by estimating the advance number J. The desired torque is computed as

$$Q_{p_d} = \frac{1}{G_{QT}(\hat{J})}T_{p_d}. \tag{5.7}$$

Two versions of the shaft speed reference generator were developed. In the first version, the gain $G_{QT}(\hat{J})$ was derived for the thrust estimation scheme; see Section 4.1.2. For the propeller P1362, described in Chapter 2, the gain $G_{QT}(\hat{J})$ is shown in Figures 4.2 and 4.3. As described in the experimental results presented in the previous chapters, at negative values of J, unsteady flows can cause quick variations of the propeller load and

consequently oscillations of K_Q and $\hat{K}_Q$. This, in turn, leads to oscillations on $G_{QT}(\hat{J})$ and even constant values of the desired thrust could result in quick variations on Q_{p_d}. This may cause high control activity, as presented in Pivano *et al.* (2007*b*), that may increase the mechanical wear-and-tear of the system. To avoid this, in the second version of the reference generator, $G_{QT}(J)$ was approximated with $G_{QT}(0)$ also in zone 1, as shown in Figures 5.2 and 5.3. This value was chosen in order to ensure a correct value of Q_{p_d} for zero advance speed ($J = 0$). This approximation did not influence significantly the propeller control performances because propellers operate rarely for J smaller than -0.5. For the propeller P1362, for example, the value of J was limited to the range where the propeller usually works, i.e. $-1.5 \leq J \leq 1$ for $\omega \geq 0$ and $-1.5 \leq J \leq 0.9$ for $\omega < 0$. The value of $\hat{J}$ was also limited in the same range. This is necessary to avoid the singularity of Q_{p_d} when $G_{QT}(\hat{J})$ crosses zero.

In order to track the desired propeller torque Q_{p_d}, a shaft speed controller is designed. Given the desired propeller torque Q_{p_d}, the desired shaft speed $\bar{\omega}_d$ is computed by inverting (3.36), employing the estimated torque loss $\hat{\Delta}_q$:

$$\bar{\omega}_d = \sqrt{\frac{\left|Q_{p_d} - \hat{\Delta}_q\right|}{G_{Q_{p,n}}}} \operatorname{sign}(Q_{p_d} - \hat{\Delta}_q). \tag{5.8}$$

To generate a smooth reference signal ω_d and $\dot{\omega}_d$, the second order low pass filter with cutoff frequency equal to ω_c and relative damping factor ξ is employed:

$$\ddot{\omega}_d + 2\omega_c \xi \dot{\omega}_d + \omega_c^2 \omega_d = \omega_c^2 \bar{\omega}_d. \tag{5.9}$$

The filter is also needed because the time derivative of $\bar{\omega}_d$, used in the feed-forward term of the controller, is infinity when $Q_{p_d} - \hat{\Delta}_q = 0$.

5.4 Control law

To track the desired shaft speed ω_d, the following control law, which includes a feed-forward part, a proportional action and an integral action to ensure convergence in the presence of constant disturbances, is designed:

$$\begin{aligned} Q_{m_d} = \quad & \tfrac{1}{R_{gb}} \Big(J_m \dot{\omega}_d + \hat{\Delta}_q + \psi(-\gamma e_1 + \omega_d) + k_{f_2} \omega_d \\ & - (k_I + \gamma k_P)\, e_1 - k_P e_2 \Big) . \end{aligned} \tag{5.10}$$

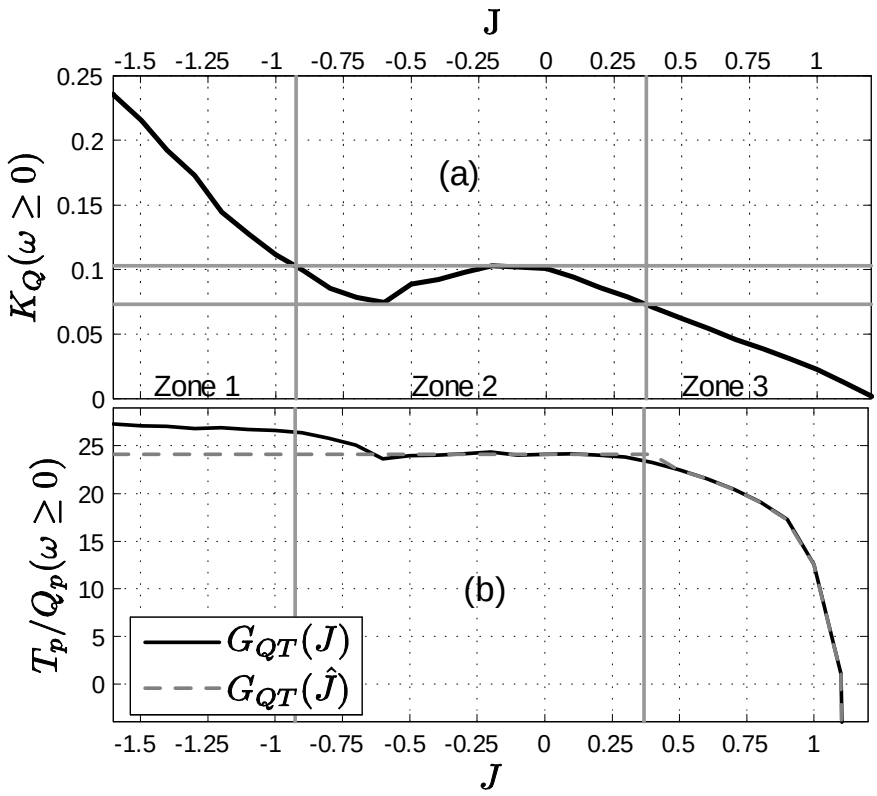

Figure 5.2: K_Q characteristic and the ratio between thrust and torque for $\omega \geq 0$.

Neglecting the motor dynamics, much faster than the propeller dynamics, the desired motor torque Q_{m_d} is considered equal to the actual motor torque Q_m. Defining the control error $e_1 = \int_0^t (\omega(\tau) - \omega_d(\tau))d\tau$ and $e_2 = \omega - \omega_d$, and inserting the control law (5.10) in (5.1)-(5.3), the control error dynamics is written as

$$\begin{aligned} \dot{e}_1 &= e_2 \\ \dot{e}_2 &= -\frac{k_{f_2}}{J_m} e_2 - \frac{1}{J_m}\left[\psi(\omega) - \psi(-\gamma e_1 + \omega_d)\right] - \frac{k_P}{J_m} e_2 \\ &\quad -\frac{1}{J_m}\left(k_I + \gamma k_P\right) e_1 - \frac{1}{J_m}\tilde{\Delta}_q. \end{aligned} \tag{5.11}$$

Proposition 5.2 *If the gains γ, k_I and k_P are chosen such that*

B1 $\gamma > 0$,

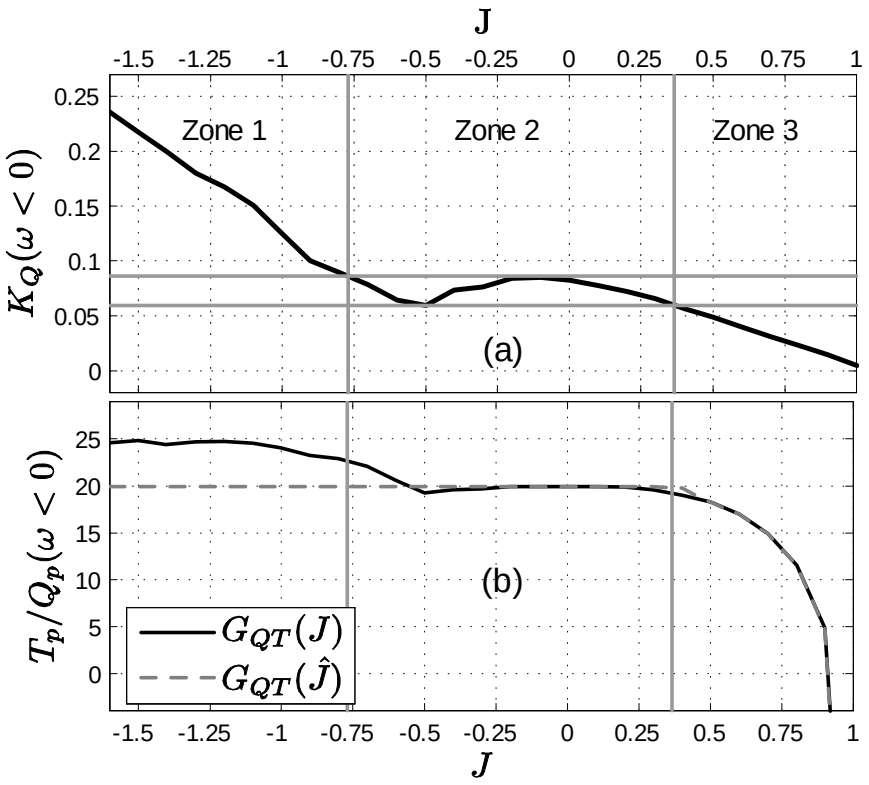

Figure 5.3: K_Q characteristic and the ratio between thrust and torque for $\omega < 0$.

B2 $k_P > 0$, $k_P > \gamma J_m - k_{f_2}$,

B3 $k_I > 0$, $k_I > -J_m\gamma^2 + \gamma k_{f_2}$,

then the origin of the overall error dynamics (observer + controller) is ISS with respect to w_2.

Proof. The proof is given in Appendix A.3. ■

Furthermore the bound of the control error decreases when increasing the control gains, since it results in an increase of the value of $\lambda_{\min}\{Q_2\}$ in (A.38).

5.5 Experimental results

This section presents experimental results of tests carried out in order to compare the performance of the proposed control scheme with the conventional shaft speed and torque controllers. These tests were performed in undisturbed water in order to reproduce calm sea state. The proposed controller was also tested with varying yawed flows and in small amplitude waves. The presented results were obtained with the propeller P1362.

5.5.1 Observer and controller tuning

The first experiments were carried out to tune the observer and controller gains. The observer gains l_1 and l_2, were chosen in order to obtain the observer dynamics faster than the system dynamics and, at the same time, to obtain low noise estimates. A good compromise was achieved with $l_1 = 3$ and $l_2 = 85$. Estimates with high frequency content could have produced noisy Q_{p_d} and $\hat{\Delta}_q$, therefore a noisy shaft speed reference signal leading to shaft speed oscillations. The time constant in (5.2) was obtained from a sensitivity analysis on the observer estimation errors with respect to τ_2. Running the observer with the gains $l_1 = 3$ and $l_2 = 85$ on data acquired at different advance and shaft speeds, we derived the bar plot of Figure 5.4. The graph shows the root mean square error (RMSE) between the observer estimates and the measurements. The value of the time constant has been varied between 0.002 and 100. The accuracy of the estimates increased by increasing τ_2 and, practically, it did not change for value of τ_2 greater than 1. The torque estimation error reflected the trend of the shaft speed estimation error. On real vehicles, this allows us to choose the time constant based on the speed error, since the torque estimation error is not available. The time constant was chosen equal to 10. With the chosen observer gains and time constant, the inequalities of Proposition 5.1 were satisfied with $a_{11} = 1$ and $a_{22} = 2$.

The shaft speed controller gains k_p, k_I and γ were initially chosen quite small. This was done to avoid the small oscillations of the shaft speed that were experienced for values of T_{p_d} and ω close to zero. The oscillations may have been caused by the Coulomb effect in the shaft friction torque that presented a steep slope at $\omega = 0$. The variation in the friction torque influenced the torque loss estimate and for small values of T_{p_d}, where also the value of Q_{p_d} was small, we observed oscillations of the torque loss estimate inducing oscillations in the desired shaft speed. This problem was solved by multiplying the controller gains k_p and k_I by a bell function

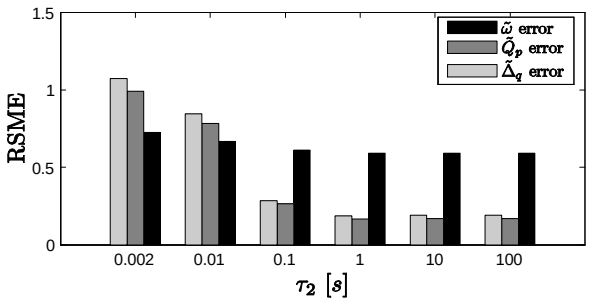

Figure 5.4: Observer estimation errors for different values of τ_2.

to reduce the gains for small value of ω. This allowed us to increase the controller gains to obtain a precise tracking of the shaft speed reference. The bell function was implemented with the constant parameters k, p and b as

$$\alpha(\omega) = 1 - (1 - b)e^{-|k\omega|^p}.$$

The observer and controller parameters are reported in Table 5.1.

Table 5.1: Observer and controller parameters.

Parameter	Value	Parameter	Value	Parameter	Value
l_1	3	k_I	0.2	k	0.1
l_2	85	γ	1.1	b	0.1
$\tau_2[s]$	10	ω_c [rad/s]	31	p	10
k_p	0.09	ξ	1		

5.5.2 Comparison of different propeller controllers in open-water conditions

The proposed controller, defined as the thrust controller, was compared with the conventional shaft speed and torque controllers in terms of thrust tracking performance. These tests were performed in open-water conditions with varying advance speeds. In order to avoid losses due to ventilation, the propeller was submerged at $h/R = 4$, where h is the propeller submergence. To simulate a realistic scenario the towing carriage speed was first positive when the thrust was positive and then became negative when the thrust

was reversed. The shaft speed reference generator was employed with the thrust/torque mapping presented in Figures 5.2 and 5.3 .

According to Sørensen *et al.* (1997) and Smogeli *et al.* (2005), both conventional controllers use the nominal values of the propeller characteristics for $J = 0$. For the conventional shaft speed controller, the demanded shaft speed $\bar{\omega}_d$ is calculated as

$$\bar{\omega}_d = \sqrt{\frac{4\pi^2 \left|T_{p_d}\right|}{\rho D^4 K_T|_{J=0}}} \operatorname{sign}\left(T_{p_d}\right). \tag{5.12}$$

To control the shaft speed, the control law (5.10) and the reference filter in (5.9) were employed. For a torque controller with friction compensation, the demanded motor torque is computed as

$$Q_{m_d} = \frac{1}{G_{QT}(0)} T_{p_d} + Q_f(\omega). \tag{5.13}$$

A comprehensive analysis of the thrust sensitivity with respect to changes in the advance speed is presented in Smogeli (2006), where the conventional shaft speed, torque, power controllers and combinations of those were considered.

Figures 5.5 and 5.6 show data from an experiment employing the thrust controller where the demanded thrust T_{p_d} was a trapezoidal signal with ± 80 N amplitude. The advance speed u_a, shown in part (e) of Figure 5.6, varied from 0 to ± 1 m/s. The results obtained with the conventional torque and shaft speed controller in a similar experiment are reported in Figures 5.7, 5.8, 5.9 and 5.10.

The thrust T_p obtained with the proposed controller tracked the desired one more precisely than the thrusts produced when using the conventional torque and shaft speed controllers. The propeller torque and its estimate, computed with (5.6), are plotted in part (b) of Figure 5.6 showing good agreement. Where the shaft speed crossed zero, the torque estimation error presented some spikes. This was due to modeling errors in the shaft friction torque.

When employing the thrust and the conventional shaft speed controllers, the propeller shaft speed tracked the reference precisely, proving the effectiveness of the control law (5.10). The advance angle β, showing the quadrant where the propeller operated, is reported in part (c) of Figures 5.5, 5.7 and 5.9.

The thrust controller, through the loss estimation, was able to counteract the effect of the changes in the advance speed. The conventional torque

controller produced the required torque, but it did not compensate for the variations in the thrust/torque gain $G_{QT}(J)$ due to changes in the advance speed and for the shaft moment of inertia. If the inertia is significant, the term $J_m\dot{\omega}$ (with the necessary filtering) could be added to the desired motor torque in (5.13). The conventional shaft speed furnished the worst results in terms of thrust production because the shaft speed reference does not account for the variations of the propeller load for varying advance speed.

Similar results were obtained when comparing the three controllers with a desired thrust of ± 45 N amplitude. The data obtained with the thrust controller are plotted in Figures 5.11 and 5.12. The propeller was moved through the water at the same advance speed of the previous test. This would correspond to a vehicle with less hydrodynamic drag since the thrust was almost halved compared to the first test. In this case the propeller operated at larger values of the advance number J, where losses due to the advance speed are greater. For this reason the thrust controller, compared to the torque and shaft speed controllers, performs even better than in the first test. The results obtained with the conventional controllers are plotted in Figures 5.13, 5.14, 5.15 and 5.16.

It is possible to notice, especially for this second test, that the thrust produced when employing the thrust controller presented a small drop just after the point where the desired thrust reaches ± 45 N. In that region, the advance number J increases, moving the working point from zone 2 to zone 3 of Figures 5.2 and 5.3. The drop is due to the approximation adopted for $G_{QT}(J)$ in the crossing between the two zones.

When employing the thrust controller, the largest thrust tracking errors occurred when the propeller operated in the second and fourth quadrants where, due to unsteady flows, it is difficult to counteract quick load variations.

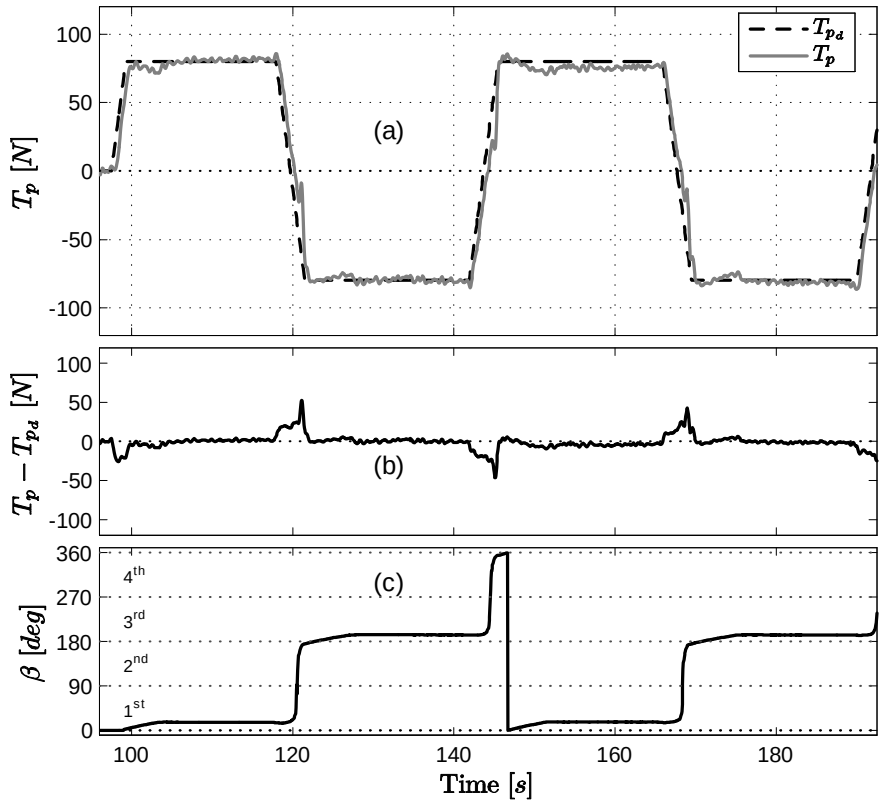

Figure 5.5: Performance of the thrust controller in open-water conditions with $T_d = \pm 80N$.

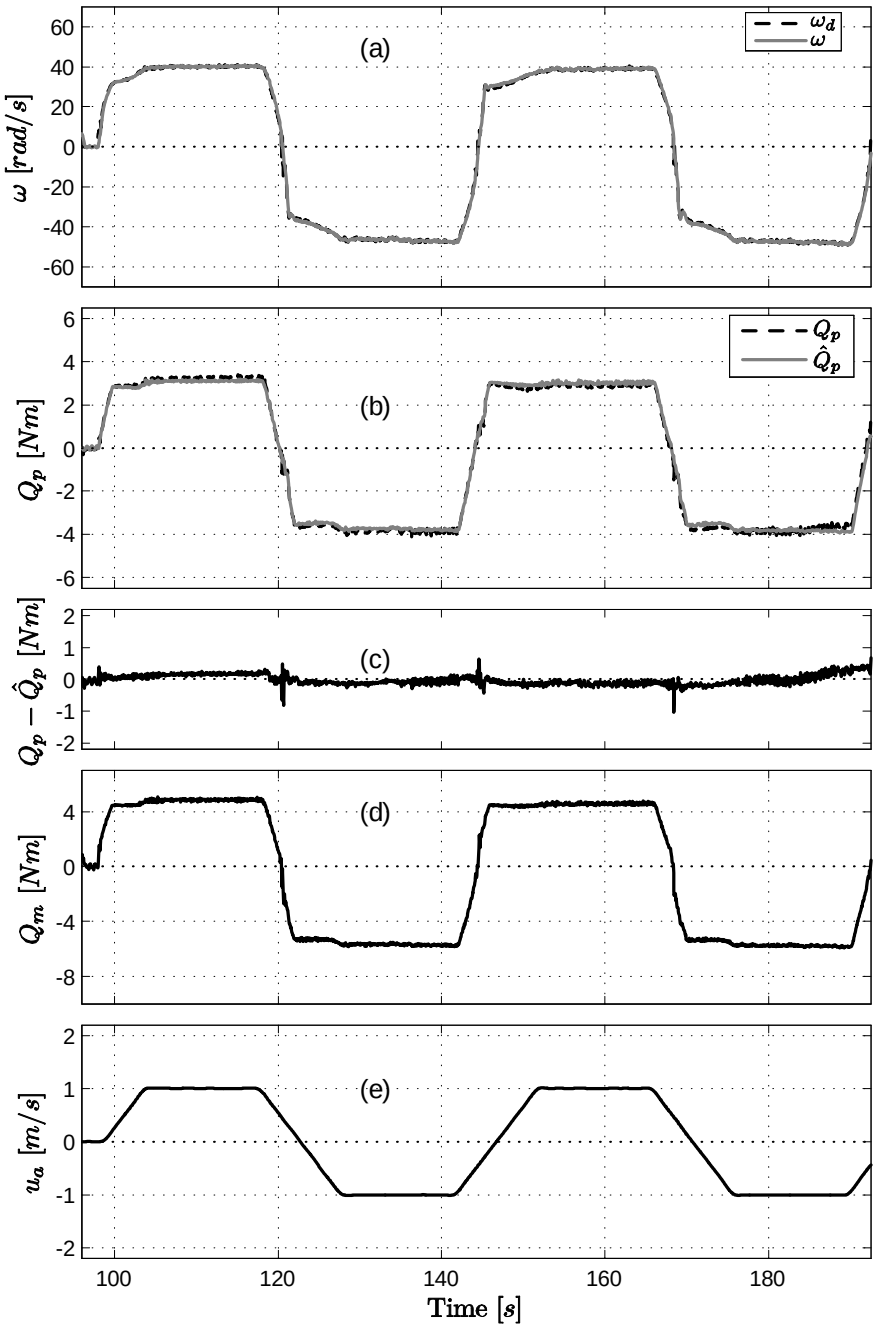

Figure 5.6: Performance of the thrust controller in open-water conditions with $T_d = \pm 80N$.

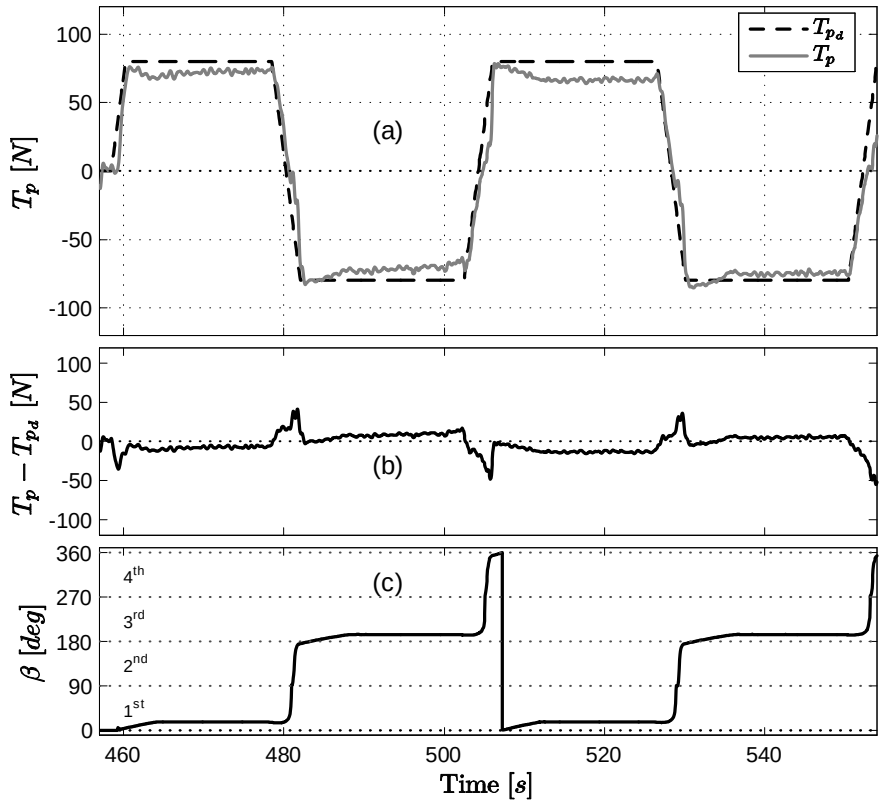

Figure 5.7: Performance of the conventional torque controller in open-water conditions with $T_d = \pm 80N$.

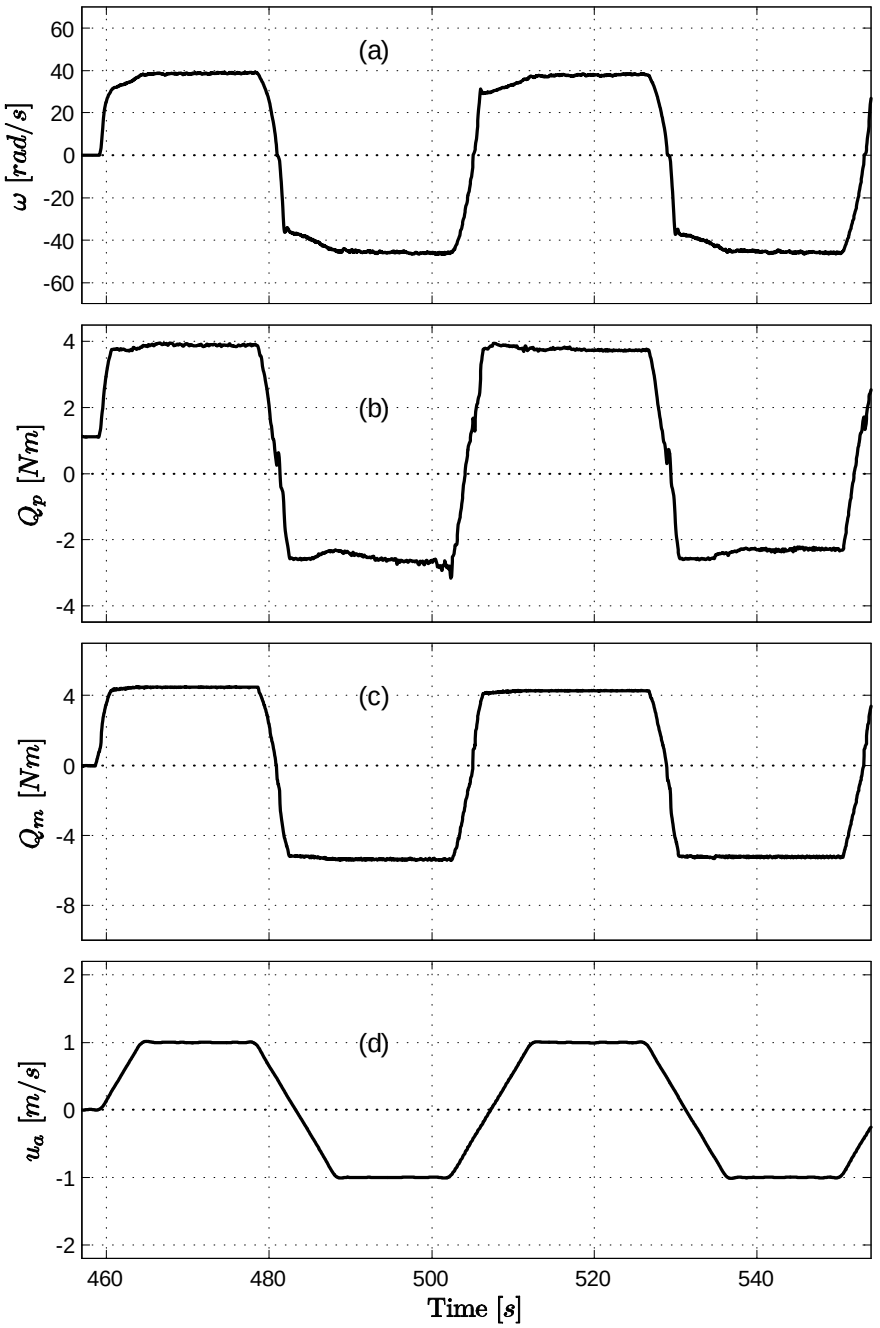

Figure 5.8: Performance of the conventional torque controller in open-water conditions with $T_d = \pm 80N$.

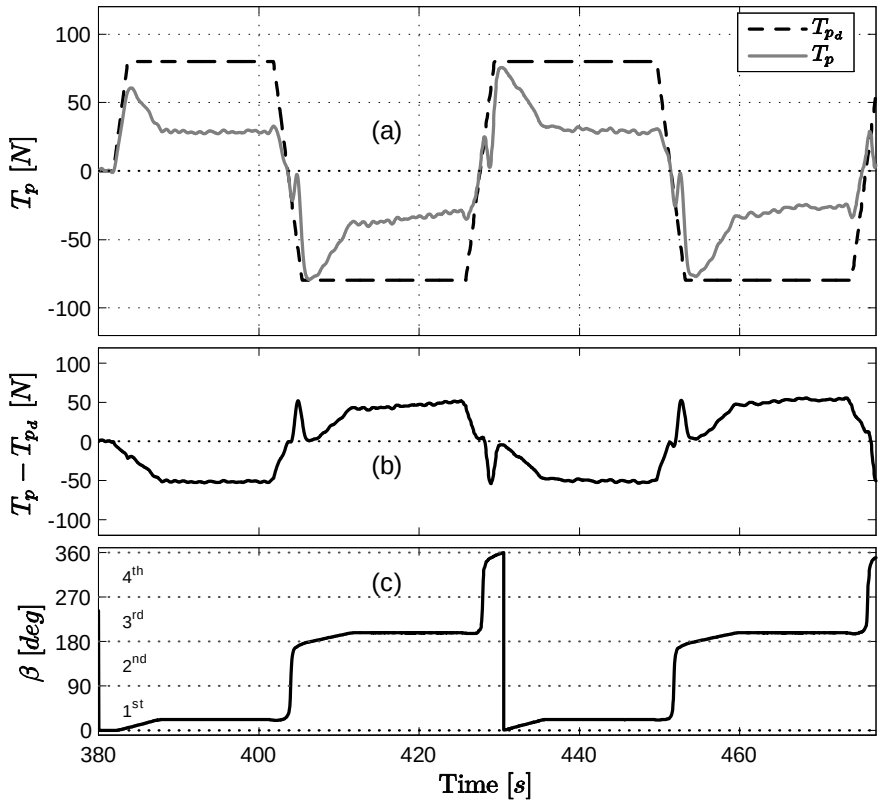

Figure 5.9: Performance of the conventional shaft speed controller in open-water conditions with $T_d = \pm 80N$.

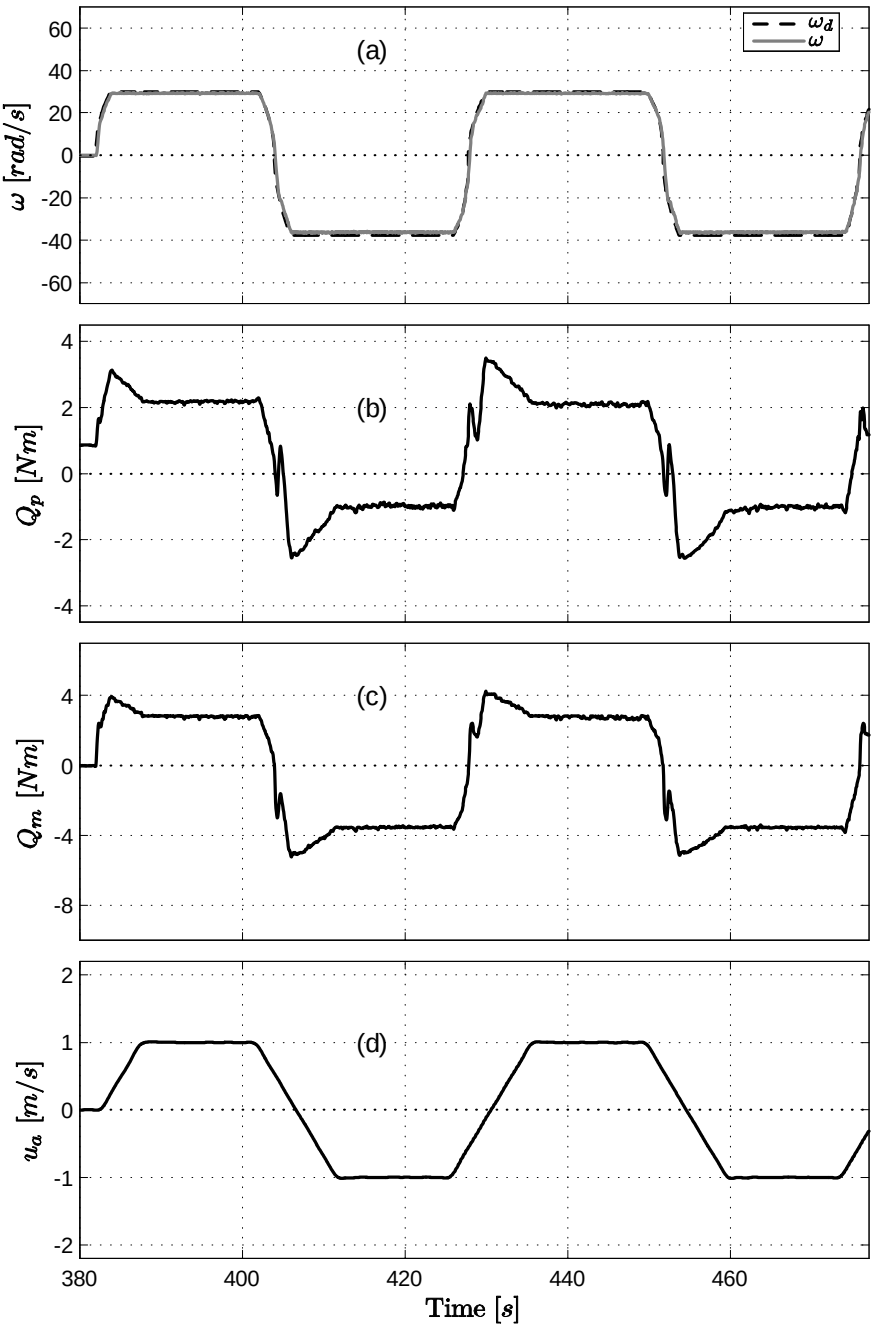

Figure 5.10: Performance of the conventional shaft speed controller in open-water conditions with $T_d = \pm 80N$.

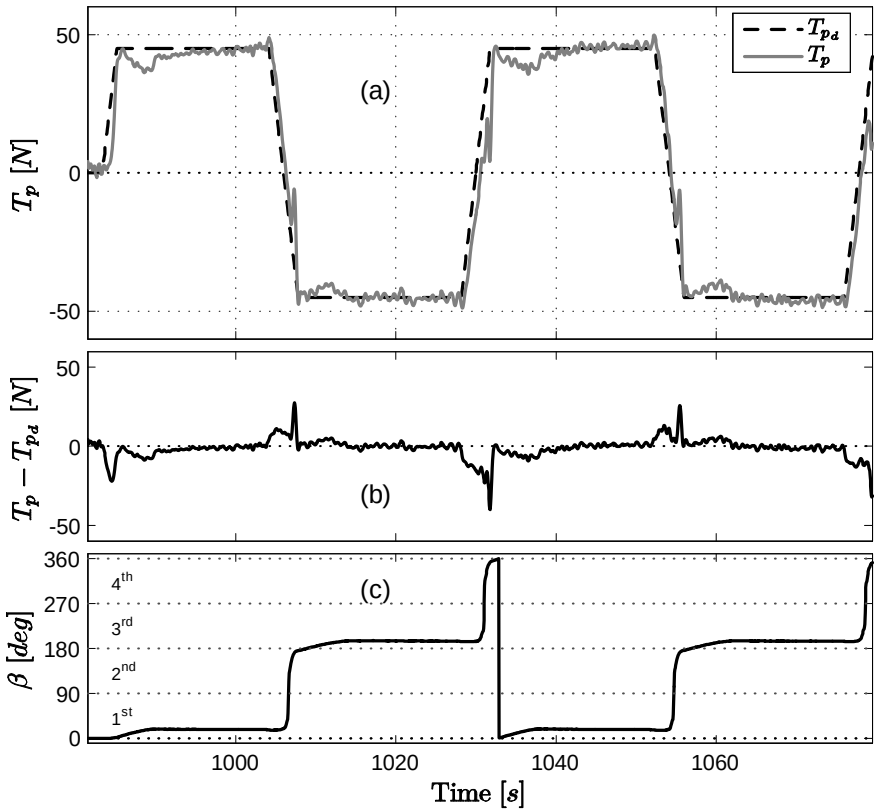

Figure 5.11: Performance of the thrust controller in open-water conditions with $T_d = \pm 45N$.

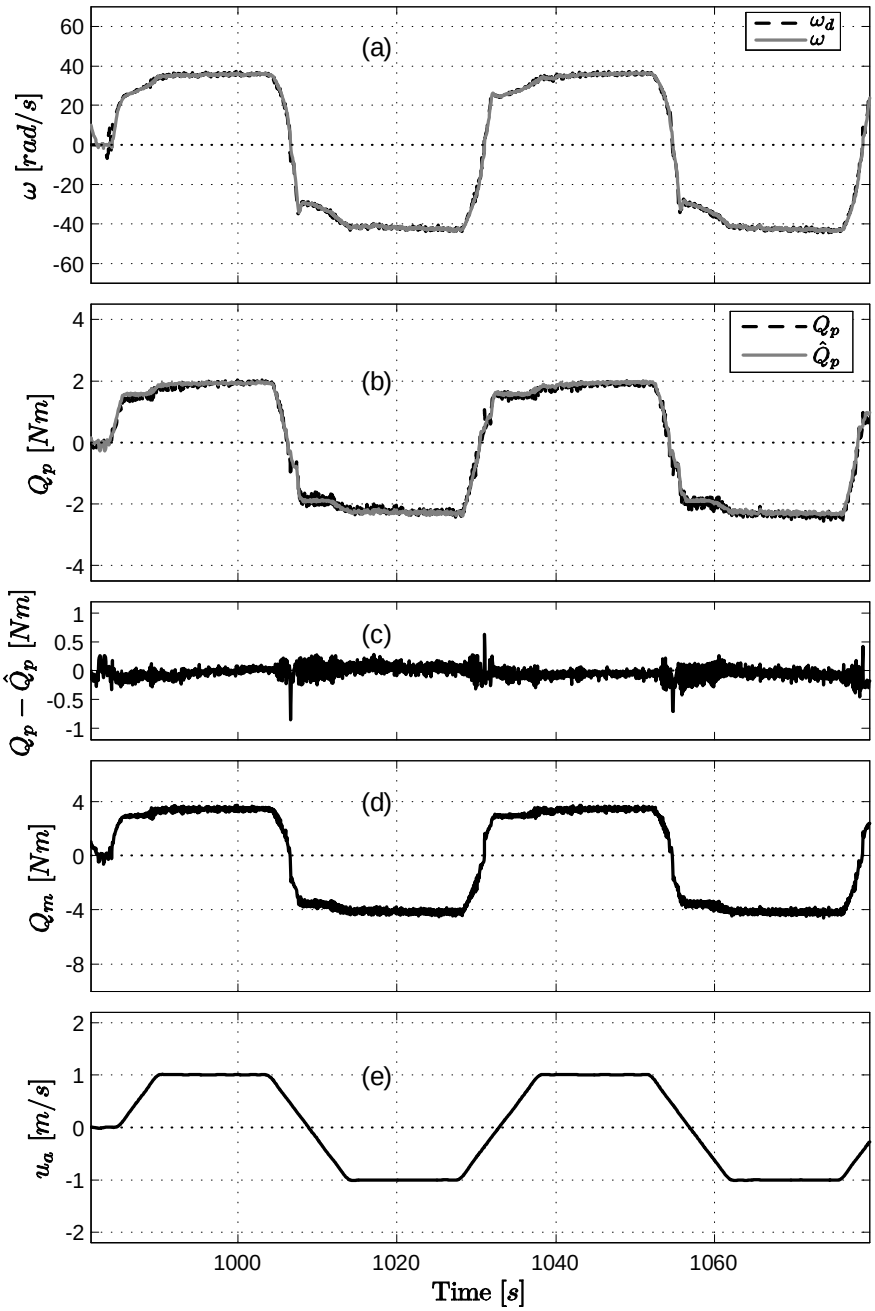

Figure 5.12: Performance of the thrust controller in open-water conditions with $T_d = \pm 45N$.

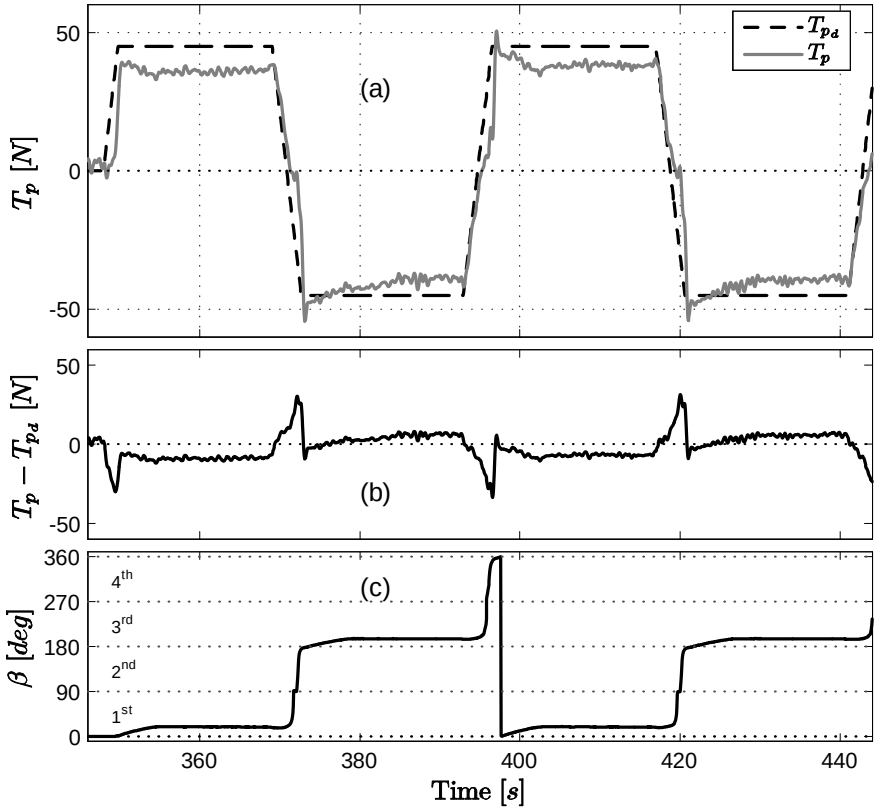

Figure 5.13: Performance of the conventional torque controller in open-water conditions with $T_d = \pm 45N$.

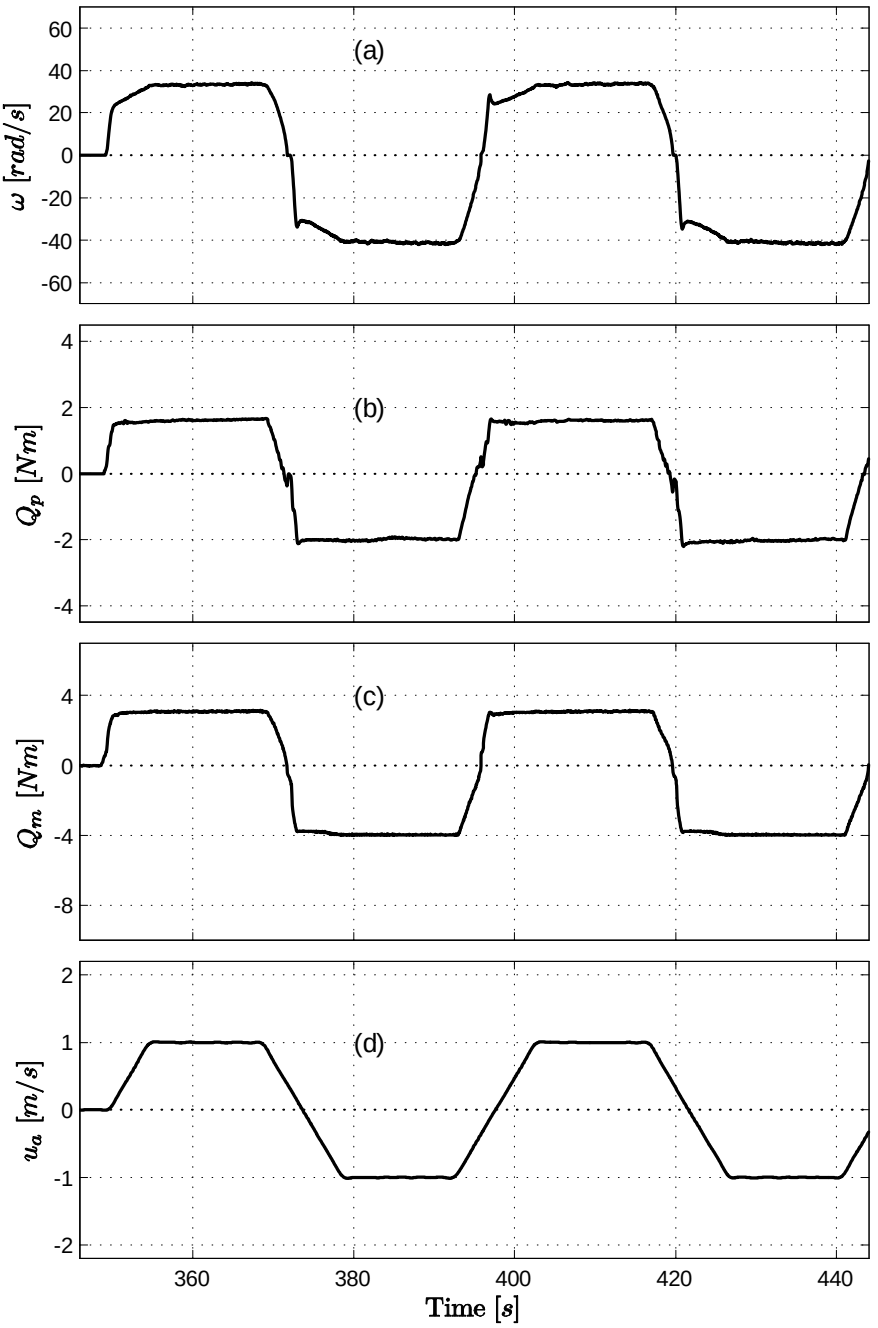

Figure 5.14: Performance of the conventional torque controller in open-water conditions with $T_d = \pm 45N$.

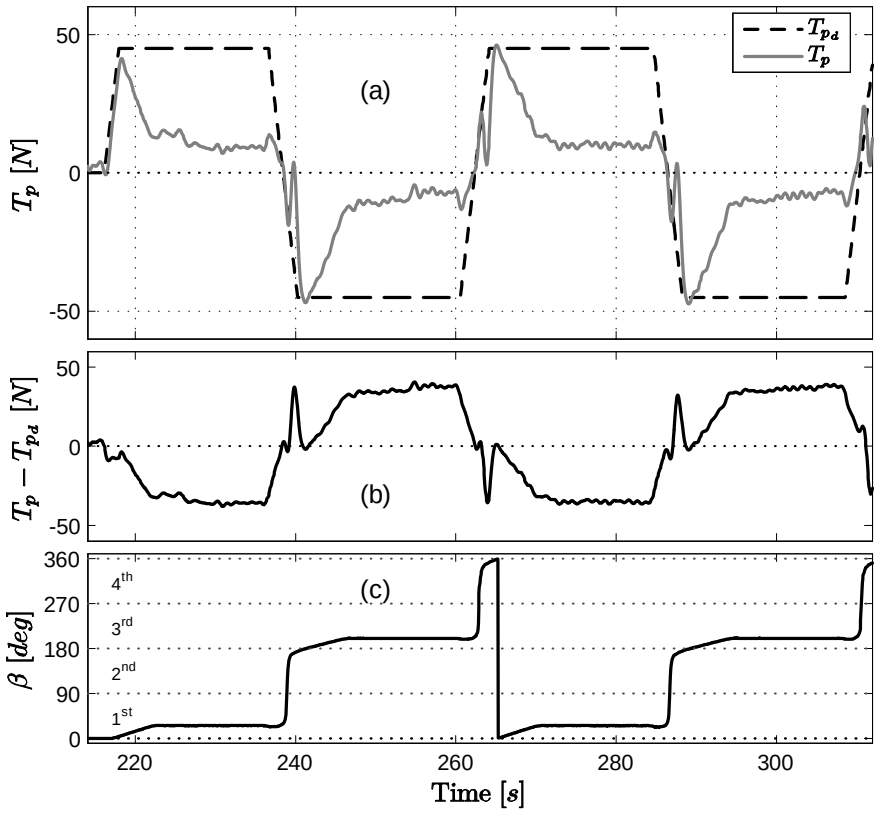

Figure 5.15: Performance of the conventional shaft speed controller in open-water conditions with $T_d = \pm 45N$.

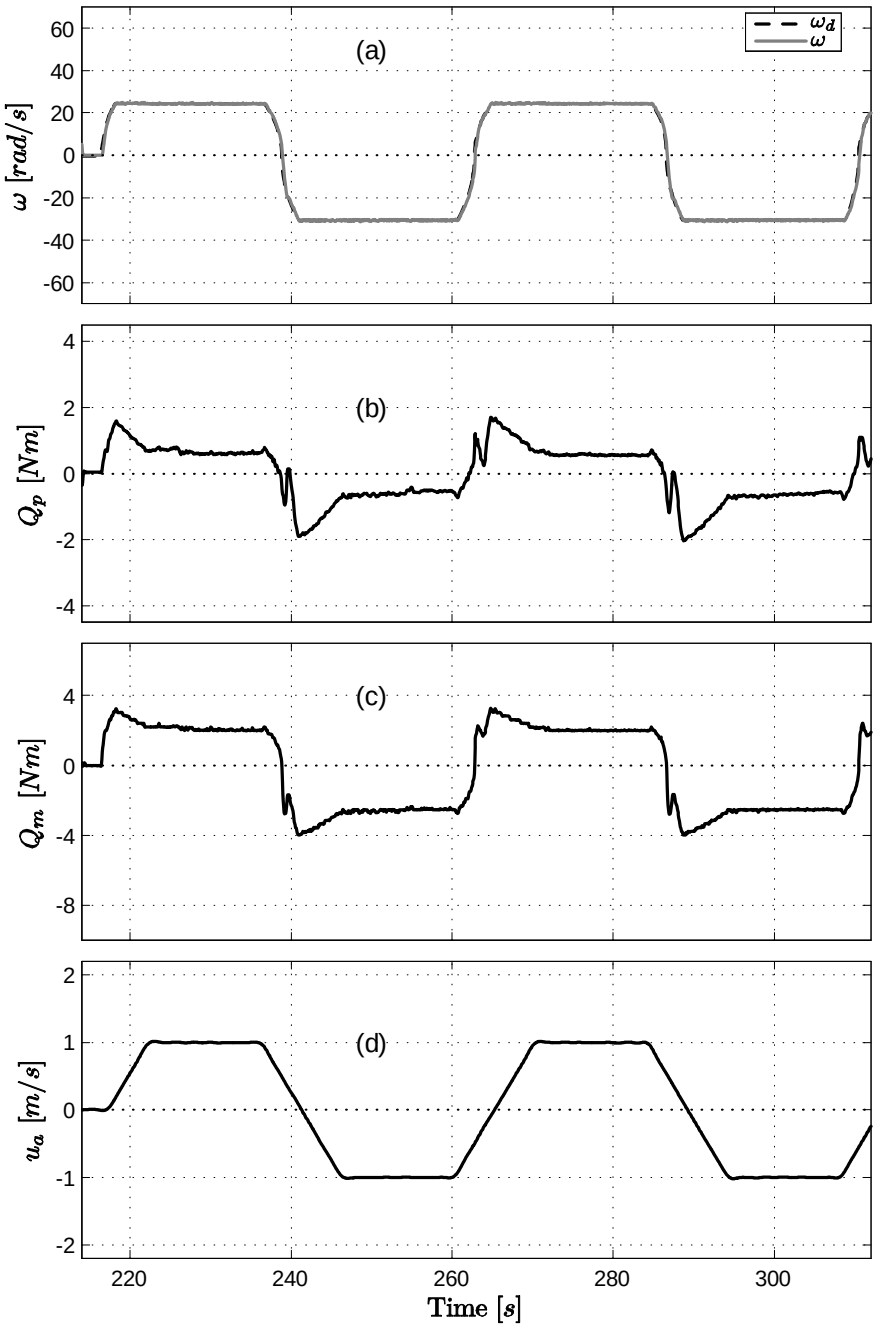

Figure 5.16: Performance of the conventional shaft speed controller in open-water conditions with $T_d = \pm 45N$.

5.5.3 Waves test

A series of tests were conducted in small amplitude waves with 12 cm peak-to-trough amplitude and 1.75 s period. This was done to validate the proposed controller scheme when the propeller is subject to fluctuating inflows, a typical situation that occurs for ships in transit. The desired thrust had a trapezoidal form with amplitude $T_{p_d} = \pm 120$ N. The towing carriage speed u_a, shown in part (e) of Figure 5.18, varied from 0 to ± 0.8 m/s. At constant shaft speed, waves create a fluctuating propeller inflow which induces oscillations in the propeller torque and thrust, as shown in the experiments described in Section 4.2.5. The thrust controller is able to reduce the thrust and torque oscillations by varying the shaft speed. The thrust, showed in part (a) of Figure 5.17, presented small oscillations but the tracking error, plotted in part (b) of the same figure, was however limited.

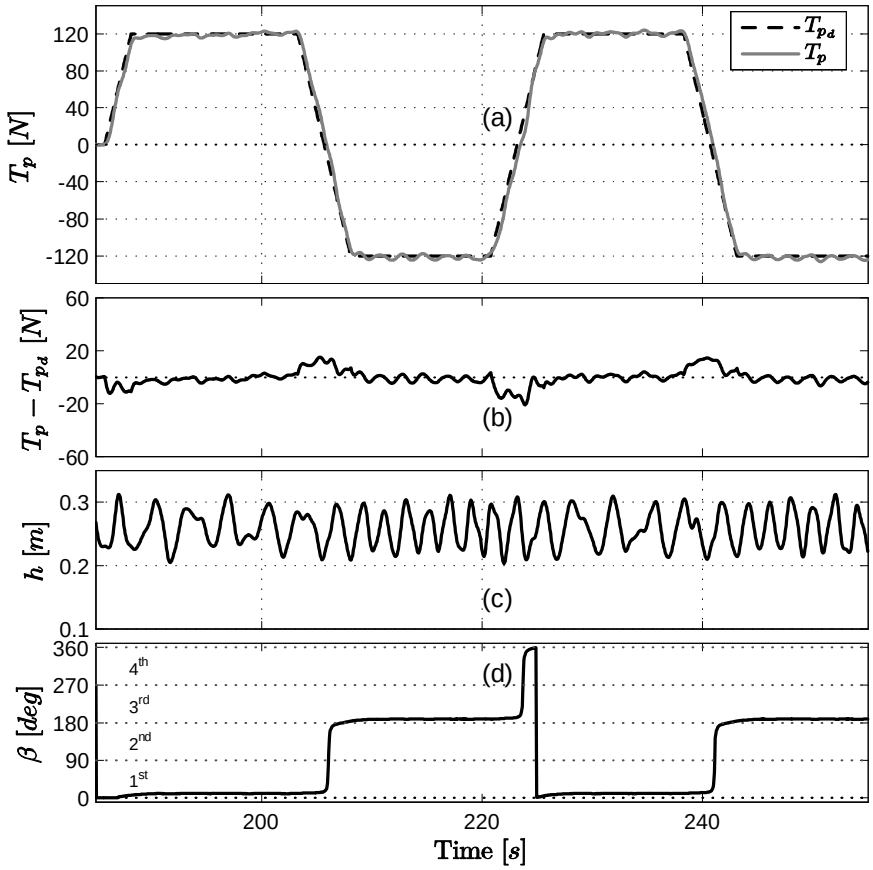

Figure 5.17: Performance of the thrust controller in small amplitude waves with $T_d = \pm 120N$.

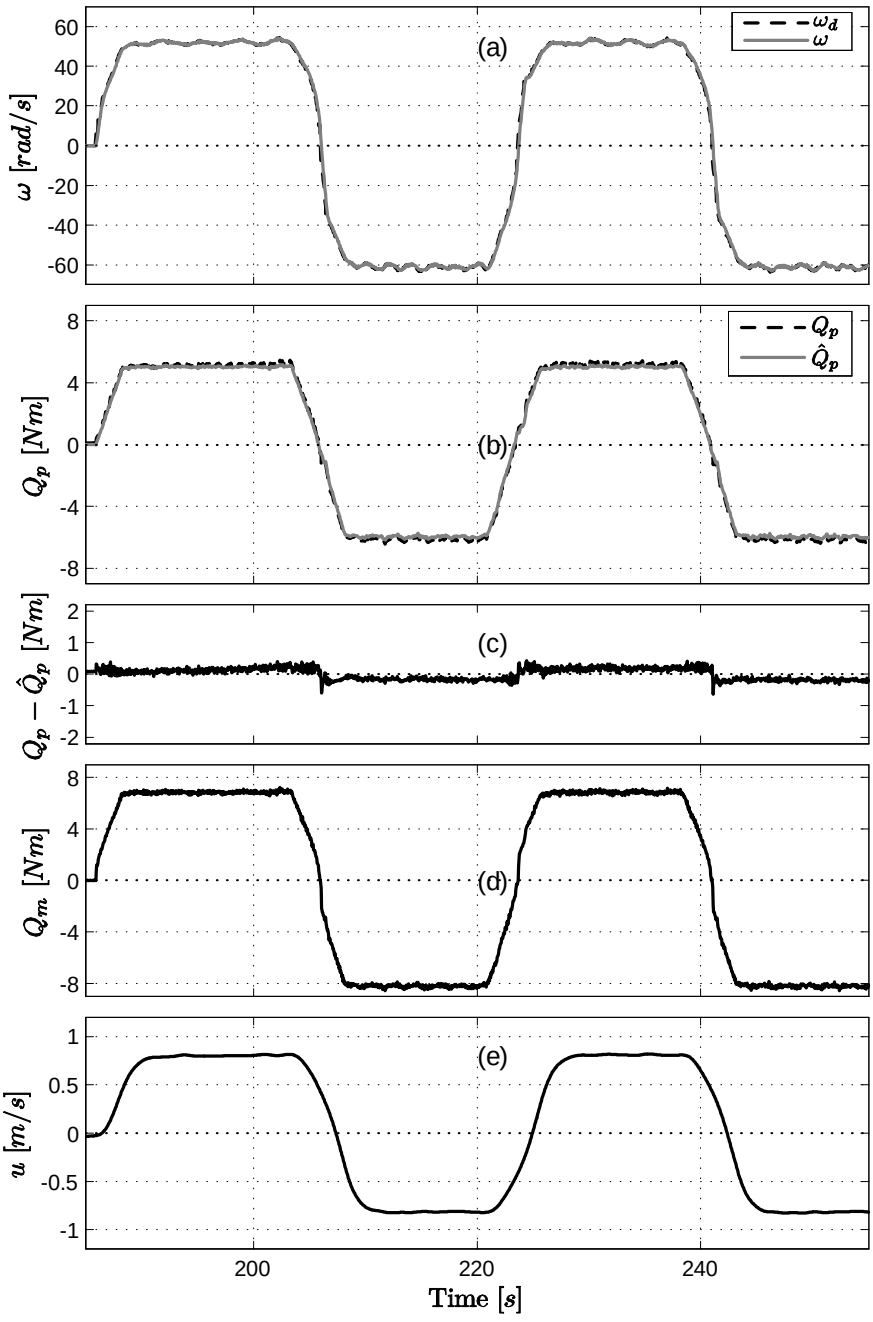

Figure 5.18: Performance of the thrust controller in small amplitude waves with $T_d = \pm 120N$.

5.5.4 Yawed flow test

These tests were carried out to validate the thrust controller in presence of varying yawed flows. Tests were performed by rotating the propeller housing along its vertical axis, as explained in Chapter 2. The results of two different experiments are presented. The first test was performed with a constant demanded thrust of amplitude 50 N while the second was performed with a sinusoidal demanded thrust.

Figures 5.19 and 5.20 show data from the first test where the propeller housing yaw angle ψ (see Figure 2.2) varied from -25 deg to $+25$ deg ($\psi = 0$ is the usual propeller position). When the propeller operated in the first quadrant, indicated in part (d) of Figure 5.19, the propeller thrust presented small oscillations, but it followed quite well the demanded one. The small thrust tracking error was due to the fact that the thrust/torque relationship, used to compute the shaft speed reference, did not account for cross flows but only for variations in the advance speed. When the propeller operated in the fourth quadrant, the thrust presented larger oscillations than in the first quadrant. This was due to the use of the first version of the thrust/torque gain $G_{QT}(\hat{J})$, plotted in Figures 4.2 and 4.3, that furnished a speed reference with high frequency content when the propeller operated in the second and fourth quadrants. Thrust oscillations were reduced when employing the second version of the shaft speed reference generator.

Similar results were obtained in the experiments with a sinusoidal demanded thrust. The data of this experiment are shown in Figures 5.21 and 5.22. When operating in the first quadrant, the thrust tracked quite well the demanded one. In the fourth quadrant, similarly to the previous test, the produced thrust presented some oscillations.

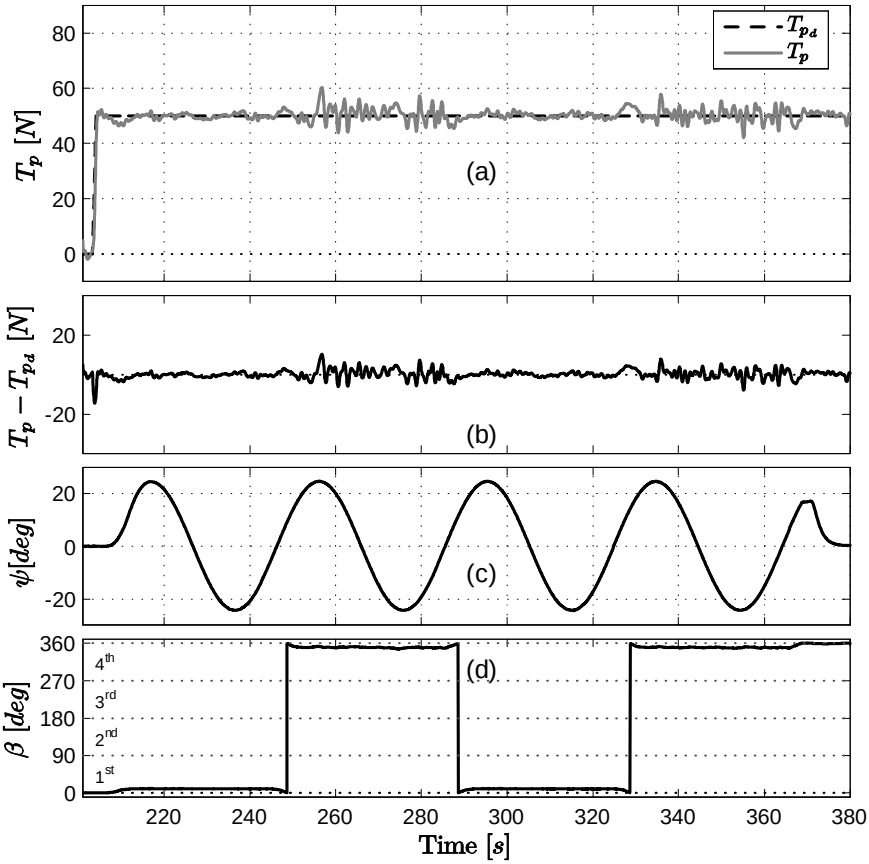

Figure 5.19: Performance of the thrust controller in presence of yawed flows with constant demanded thrust.

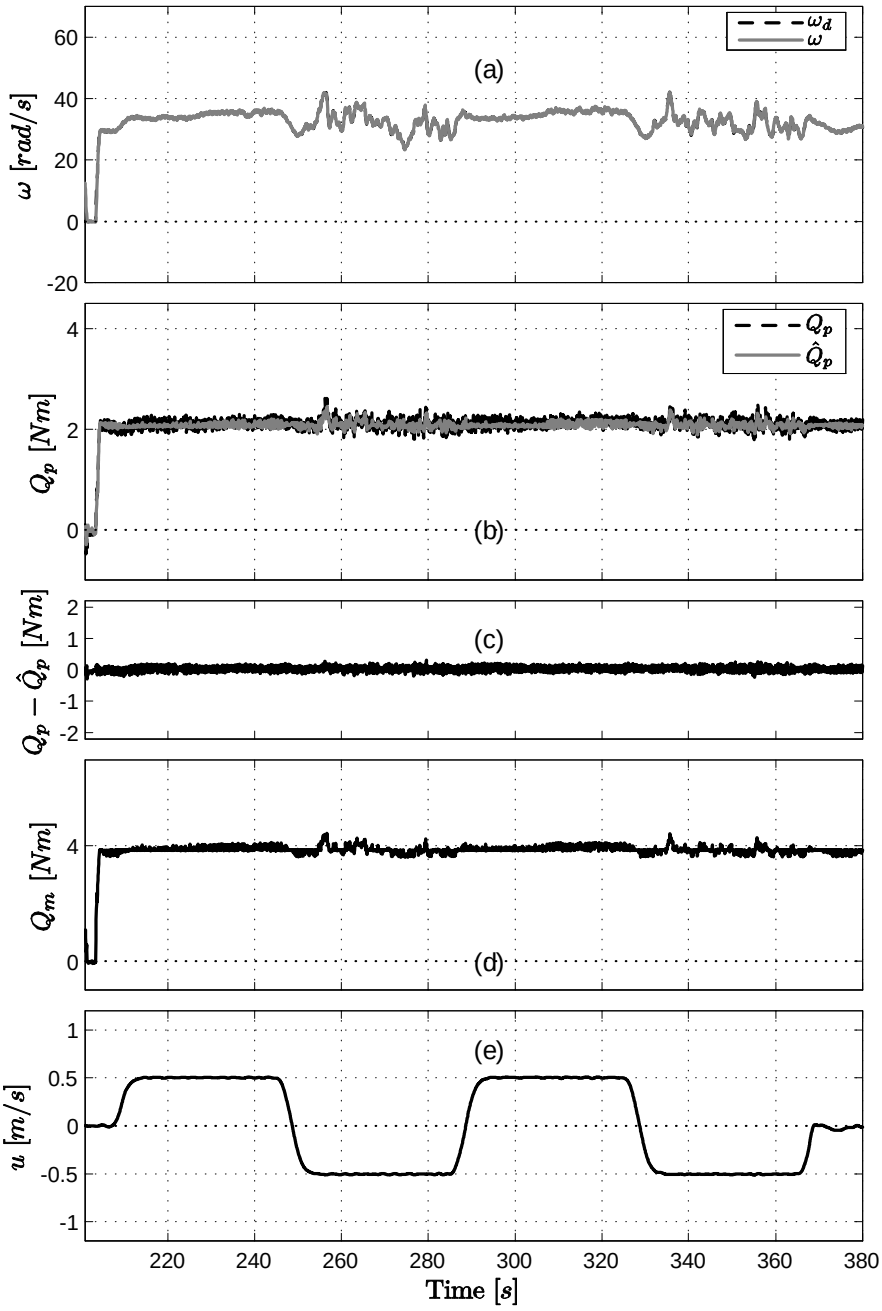

Figure 5.20: Performance of the thrust controller in presence of yawed flows with constant demanded thrust.

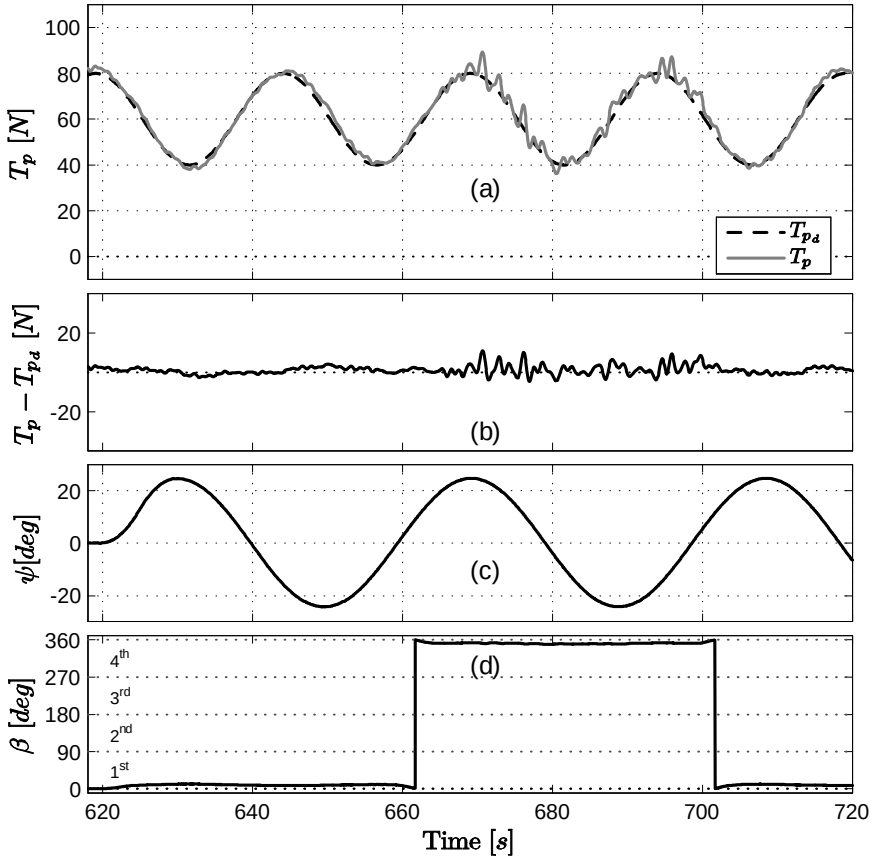

Figure 5.21: Performance of the thrust controller in presence of yawed flows with sinusoidal demanded thrust.

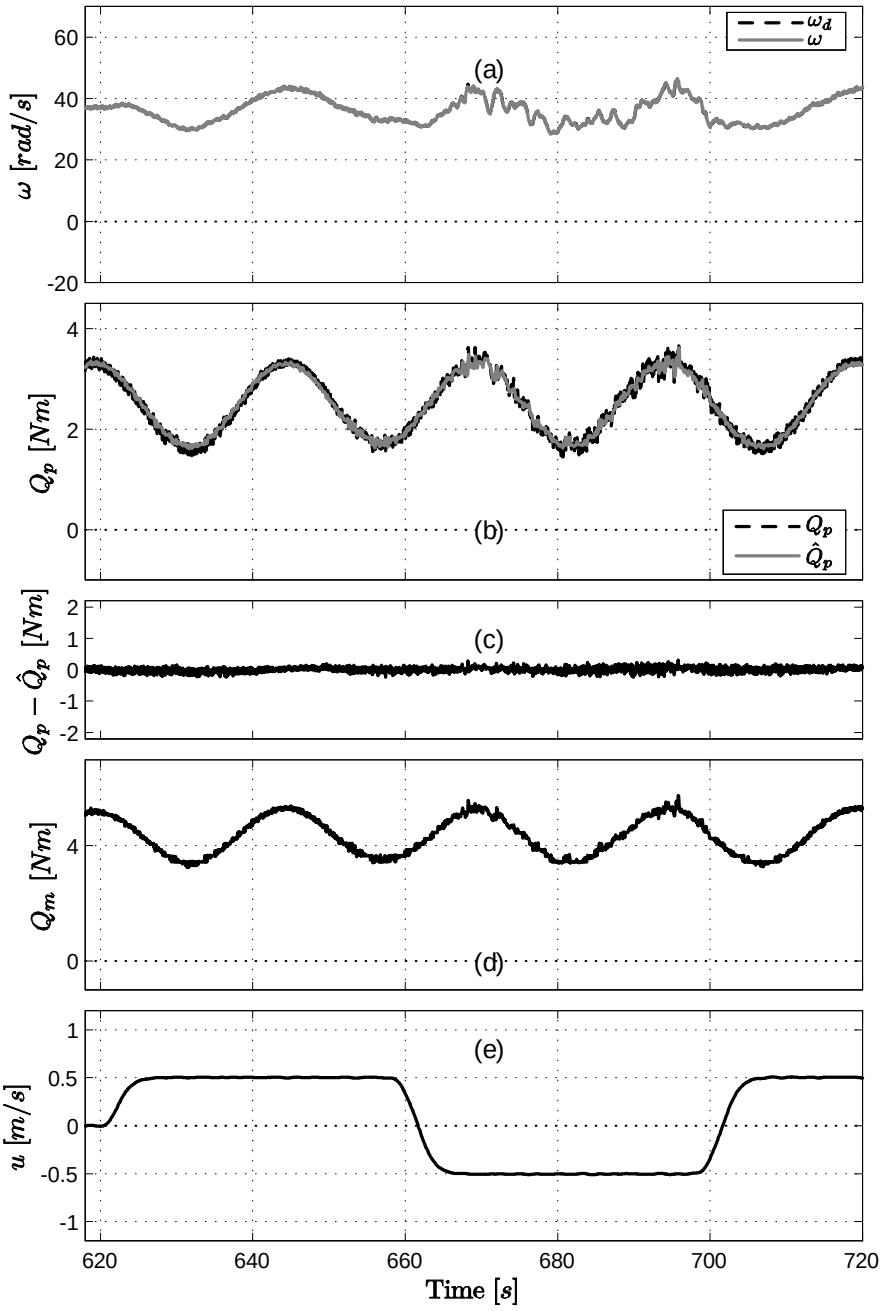

Figure 5.22: Performance of the thrust controller in presence of yawed flows with sinusoidal demanded thrust.

5.6 Alternative thrust control schemes

The thrust controller could have also been implemented in different ways that, for different reasons, did not appear to be as effective as the chosen one. Alternative schemes are presented below.

- The thrust control could have been achieved by employing the built-in motor torque controller. The desired motor torque could have been computed directly from the desired propeller torque Q_{p_d} (5.7) by adding the terms to compensate for the friction torque and the shaft moment of inertia:

$$Q_{m_d} = Q_{p_d} + Q_f(\omega) + J_m\dot{\omega}. \tag{5.14}$$

  In terms of thrust tracking capabilities, this approach would have probably furnished the same performance that has been obtained by controlling the shaft speed. However, it could have been less flexible in high and extreme sea state where the shaft speed needs to be controlled (see Chapter 7). In that case, a switching between the torque controller and a shaft speed controller would have been necessary.

- A thrust control could have been achieved by employing, in a feedback loop, the thrust estimated with the scheme proposed in Chapter 4. This controller was tested and furnished the same performance as the proposed controller but the employment of the shaft speed controller would have been necessary in harsh sea conditions.

- An alternative thrust controller scheme could have been implemented by computing the shaft speed reference in (5.12) with an estimate of $K_T(J)$ instead of K_T computed at $J = 0$. An estimate of $K_T(J)$ could have been obtained from the estimated value of $\hat{J}$ combined with the propeller characteristics. To avoid oscillations of the shaft speed reference for negative values of J, the estimated value of K_T should have been set to constant and the performance in the 2^{nd} and 4^{th} would have been worse than the proposed scheme. This because for $J < 0$, K_T varies more than $G_{QT}(J)$ and a constant value of K_T would introduce a larger error when computing $\bar{\omega}_d$.

- Other propeller controllers could be implemented as combinations of shaft speed, torque and power controller. These controllers were presented in Smogeli (2006), where smooth a switching among the different types of controllers was performed based on the magnitude of the shaft speed.

5.7 Conclusion and discussion

The experimental results presented in this chapter demonstrated the effectiveness of the thrust controller designed for fixed pitch marine propellers operating in calm and moderate sea conditions. The controller was compared to the conventional torque and shaft speed controllers in undisturbed water, showing improved performance in thrust tracking capability. The performance of the controller was also verified in tests with waves and with the propeller subject to yawed flows.

Remark 5.1 *In the case where the propeller shaft speed measurement is highly corrupted by noise, forcing the use of small control gains, the transient performance of the shaft speed controller could be improved by employing resetting procedures. See for example Bakkeheim* et al. *(2006) and Bakkeheim* et al. *(2007).*

Remark 5.2 *For a practical implementation of the proposed controller, safety limits should be included, e.g. motor torque and power limits. Fault monitoring and redundancy should be also considered in order to improve the system reliability. See Smogeli (2006), Blanke* et al. *(1998), Bray (2003) and references therein for examples.*

Remark 5.3 *For vessel traveling in waves, the vessel motion is often characterized by oscillations in all 6 DOF. This motion creates a continuous variation of the propeller inflow, causing fluctuations of the thrust and torque. The full compensation of these fluctuations would lead to unnecessary wear-and-tear of the thrusters and increase in fuel consumption. Only the wave components that cause the vehicle to drift should be compensated. This can be achieved by decreasing the torque loss observer gains in order to reduce the high frequency content of the torque loss estimate.*

Remark 5.4 *The thrust controller causes an increase of the power consumption with respect to the use of the conventional controllers. This is due to the fact that the controller compensates the losses sensed through the torque loss observer.*

Remark 5.5 *To achieve high control vehicle performance, it is also fundamental to know the thrust induced pressure force on the hull (which can be accounted for in the thrust deduction factor).*

The improvement obtained in thrust tracking accuracy employing the thrust controller, compared to the conventional propeller controllers, is

promising for improving the vehicle performance in terms of positioning and speed control. However, for high and extreme sea state, the designed controller would try to counteract the torque losses, resulting in large values and quick variations of the shaft speed. This could increase the wear-and-tear of the mechanical parts of the system and cause large peaks in the consumed power, which may not be tolerated by the power generators. To avoid this, an anti-spin strategy, presented in Chapter 7, is developed.

Chapter 6

Thrust controller applied to the surge speed control of underwater vehicles

A simulation study was performed in order to evaluate the performance of an underwater vehicle when employing the thrust controller proposed in Chapter 5. A comparison among the designed thrust controller and the conventional shaft speed and torque propeller controllers was carried out.

This chapter is organized as follows. Section 6.1 presents the underwater vehicle dynamic model and the adopted speed controller. The propeller system is described in Section 6.2. The simulation results are presented in Section 6.3 and conclusions are given in Section 6.4.

6.1 Vehicle speed controller

Without loss of generality, we have considered an underwater vehicle moving in surge equipped with one single fixed pitch propeller aft of the hull. If, as in Fossen (2002) and Smallwood and Whitcomb (2004), ocean currents are neglected, then the 1-dimensional vehicle surge dynamics is given by

$$m_u \dot{u} + d_l u + d_q u \left|u\right| = \left(1 - t_d\right) T_p, \tag{6.1}$$

where u is the vehicle speed, $m_u > 0$ is the vehicle mass including the hydrodynamic added mass, $d_l > 0$ and $d_q > 0$ are the linear and quadratic hydrodynamic damping coefficients and $0 < t_d < 1$ is the thrust deduction number. We designed a control law for the vehicle to track a desired speed

reference u_d, with u_d and $\dot{u}_d$ being continuous and bounded. At this stage we have assumed that the propeller was able to produce the desired thrust $T_p = T_{p_d}(u_d, \dot{u}_d, u)$ instantaneously and later we have considered the effect of the propeller dynamics. We employed the following control law including a feed-forward part, a proportional action and an integral action to ensure convergence in presence of constant disturbances:

$$\begin{aligned} T_{p_d} = & \frac{1}{(1-t_d)} \left[m_u \dot{u}_d + d_l u_d - (k_I + \gamma k_P)\, e_1 - k_P e_2 \right. \\ & \left. + d_q \left(-\gamma e_1 + u_d\right) \left|-\gamma e_1 + u_d\right| \right], \end{aligned} \tag{6.2}$$

where $e_1 = \int_0^t (u(\tau) - u_d(\tau)) d\tau$ and $e_2 = u - u_d$ are the control error variables for position and velocity, respectively.

Using (6.2), the error dynamics can be written as

$$\begin{aligned} \dot{e}_1 &= e_2 \\ \dot{e}_2 &= -\frac{d_l}{m_u} e_2 - \frac{d_q}{m_u} \left(e_2 + u_d\right) \left|e_2 + u_d\right| - \frac{k_P}{m_u} e_2 \\ & \quad - \frac{(k_I + \gamma k_P)}{m_u} e_1 + \frac{d_q}{m_u} \left(-\gamma e_1 + u_d\right) \left|-\gamma e_1 + u_d\right|. \end{aligned} \tag{6.3}$$

Proposition 6.1 *If the gains γ, k_I and k_P are chosen such that*

A1 $\gamma > 0$,

A2 $k_P > 0$, $k_P > m_u \gamma - d_l$,

A3 $k_I > 0$, $k_I > -m_u \gamma^2 + d_l \gamma$,

then the control error dynamics (6.3) is uniformly globally exponentially stable (UGES).

Proof. The proof is given in Appendix A.4. ■

6.2 Propeller system

We have considered a fixed pitch propeller attached to a shaft driven by an electric servo motor, where the motor torque Q_m is controlled by the motor drive based on the reference Q_{m_d}. This is the most common solution adopted for underwater vehicles. A block diagram of the propeller system is presented in Figure 3.1. For the simulation, we employed a propeller with the same geometrical parameters and open-water characteristics of the propeller P1362; see Chapters 2 and 3.

The shaft dynamics was governed by (3.1), where the gear-box ratio R_{gb} was chosen to be equal 1. The friction torque, which included a Coulomb and a linear viscous effect, was modeled by

$$Q_f(\omega) = k_{f_1} \frac{2}{\pi} \arctan\left(\frac{\omega}{\epsilon}\right) + k_{f_2}\omega. \tag{6.4}$$

The simulated model of the friction torque did not include the nonlinear viscous effect, which was found in the experiments; see Chapter 3. The inclusion of that effect would not have changed significantly the results of the simulations. The propeller thrust and torque were computed with the four-quadrant propeller characteristics C_T and C_Q, shown in Figure 3.8, where the advance speed u_a was computed with (3.11) from the vehicle speed u and the wake fraction number w_f. For negative vehicle speed we assumed that the vehicle body did not disturb the inlet water to the propeller; therefore, w_f was considered equal to zero. For positive vehicle speed, we have chosen $w_f = 0.1$.

The propeller thrust controller was implemented employing the nonlinear observer (5.4), the shaft speed reference generator described in Section 5.3 and the control law (5.10).

6.3 Simulation results

A simulation was performed with the parameters given in Table 6.1. White noise was added to the shaft speed measurement signal. The vehicle dynamics (6.1) was simulated employing the thrust produced by the propeller. The thrust reference was computed from (6.2). The vehicle speed was assumed to be measured with a Doppler velocity log (DVL) measurement with 10 Hz of updating frequency. A speed measurement error was added by considering a 1200 Hz DVL unit with a total error standard deviation equal to $\pm 0.5\% + 0.01$ m/s.

The proposed controller, defined as the thrust controller, was compared to the conventional shaft speed and torque controllers. Figures 6.1, 6.2, and 6.3 present the simulation results obtained employing the three propeller controllers. The desired vehicle speed was a sinusoidal signal of 2 m/s amplitude, and the vehicle initial speed was set equal to 1 m/s. The thrust reference, plotted in part (c) in all figures, does not correspond to the actual T_{p_d} but it was obtained from (6.2) in the ideal case where the propeller was able to produce the required thrust instantaneously. It is possible to see that the thrust produced using the thrust controller was the closest to the ideal case compared to the conventional controllers. Consequently, the vehicle speed followed more accurately the reference. The traditional shaft speed controller provided the worst result with regard to the thrust production,

resulting in a large vehicle speed error. The torque controller performed more accurately than the classical shaft speed controller.

Remark 6.1 *The vehicle performance is also influenced by the choice of controller gains in (6.2). If the vehicle speed measurement is not very noisy, the use of high gains will lead to an improvement of the control performance with all the propeller controllers.*

Remark 6.2 *A vehicle with hydrodynamic damping coefficients larger than the ones used in the simulation (larger drag), would require larger thrust at the same vehicle speed, resulting in greater shaft speeds. The propeller would work at lower values of J and, hence, near to the nominal condition $J = 0$, where the three propeller controllers perform equally well. This is demonstrated by the results of a second simulation, shown in Figures 6.4, 6.5 and 6.6, carried out with $d_l = 130$ and $d_q = 100$.*

Table 6.1: Simulation parameters.

Parameter	Value	Parameter	Value	Parameter	Value
m_u[Kg]	200	J_m [kg·m^2]	0.09	n_P	0.5
d_l[Kg/s]	50	k_{f1} $\left[\frac{\text{s·N}}{\text{m·rad}}\right]$	0.3	n_I	0.1
d_q[Kg/m]	30	k_{f_2} $\left[\frac{\text{s·N}}{\text{m·rad}}\right]$	0.09	α	0.1
t_d	0.1	ϵ	$1 \cdot 10^{-3}$	ω_c [rad/s]	44
k_I	5	τ_2[s]	10	ξ	1
k_P	2	l_1	3		
γ	0.1	l_2	-80		

6.4 Conclusion

The presented simulation confirmed the results obtained in the experiments presented in Chapter 5. The improved capability in thrust tracking obtained with the thrust controller, compared to the employment of the conventional propeller controllers, leaded to better vehicle performance in terms of speed control.

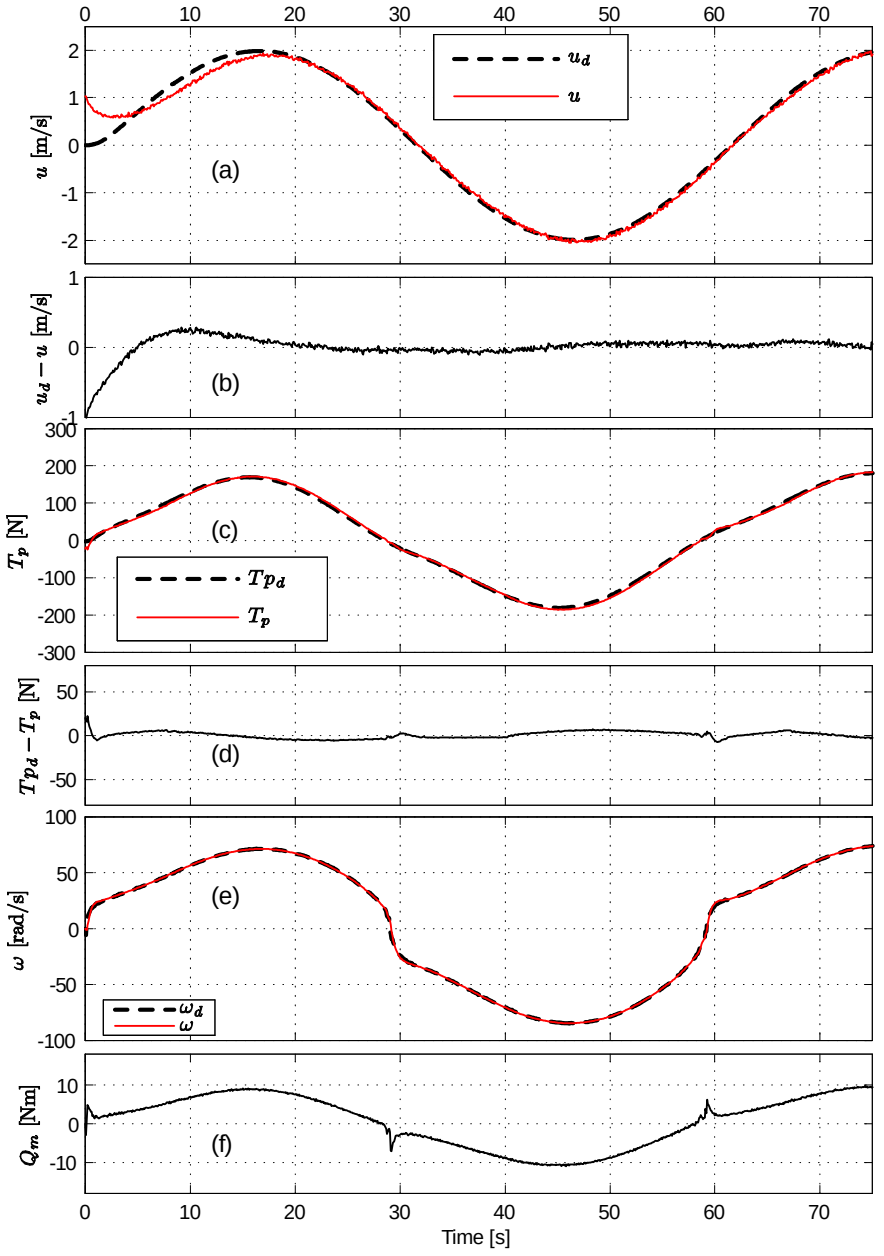

Figure 6.1: Propeller thrust controller: desired and actual vehicle speed (a), vehicle speed error (b), desired and actual thrust (c), thrust error (d), desired and actual shaft speed (e) and commanded motor torque (f).

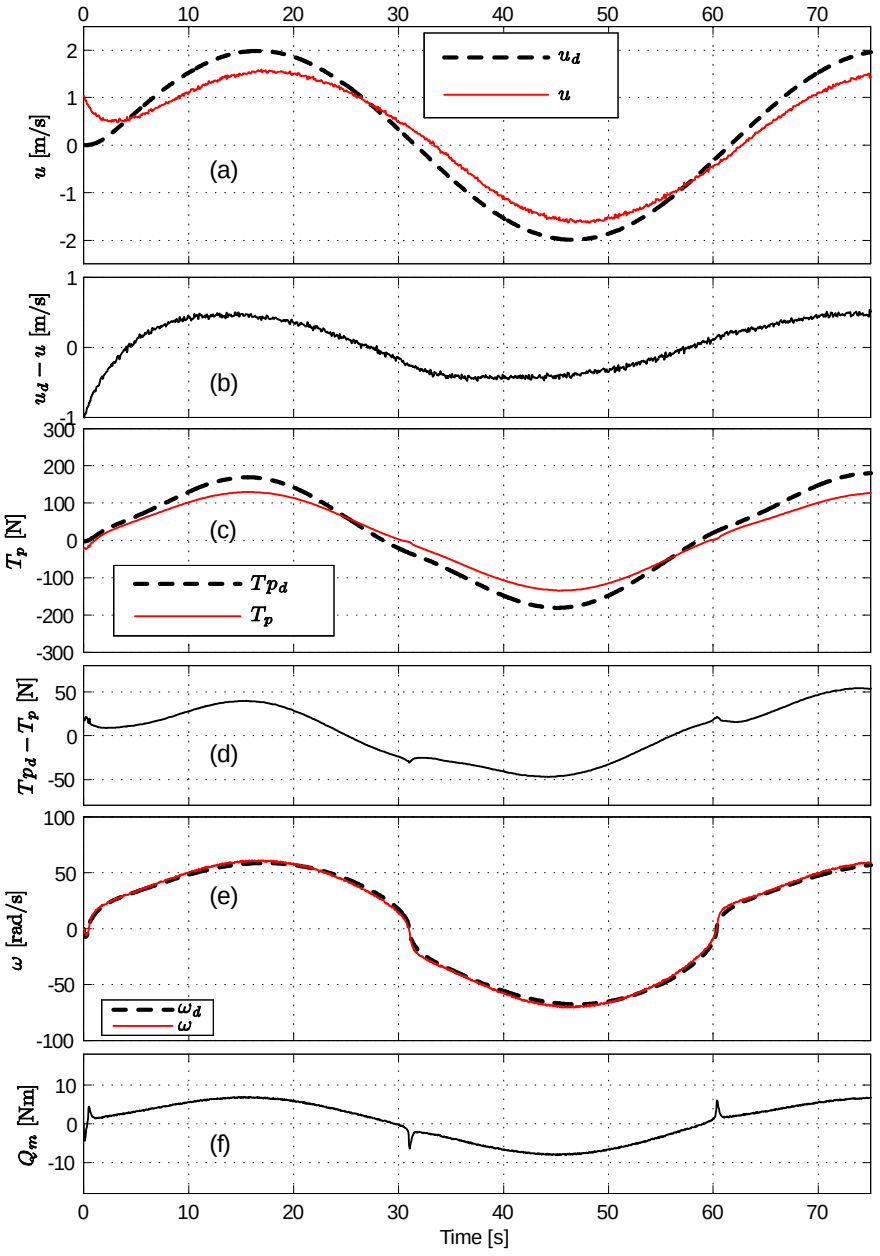

Figure 6.2: Shaft speed controller: desired and actual vehicle speed (a), vehicle speed error (b), desired and actual thrust (c), thrust error (d), desired and actual shaft speed (e) and commanded motor torque (f).

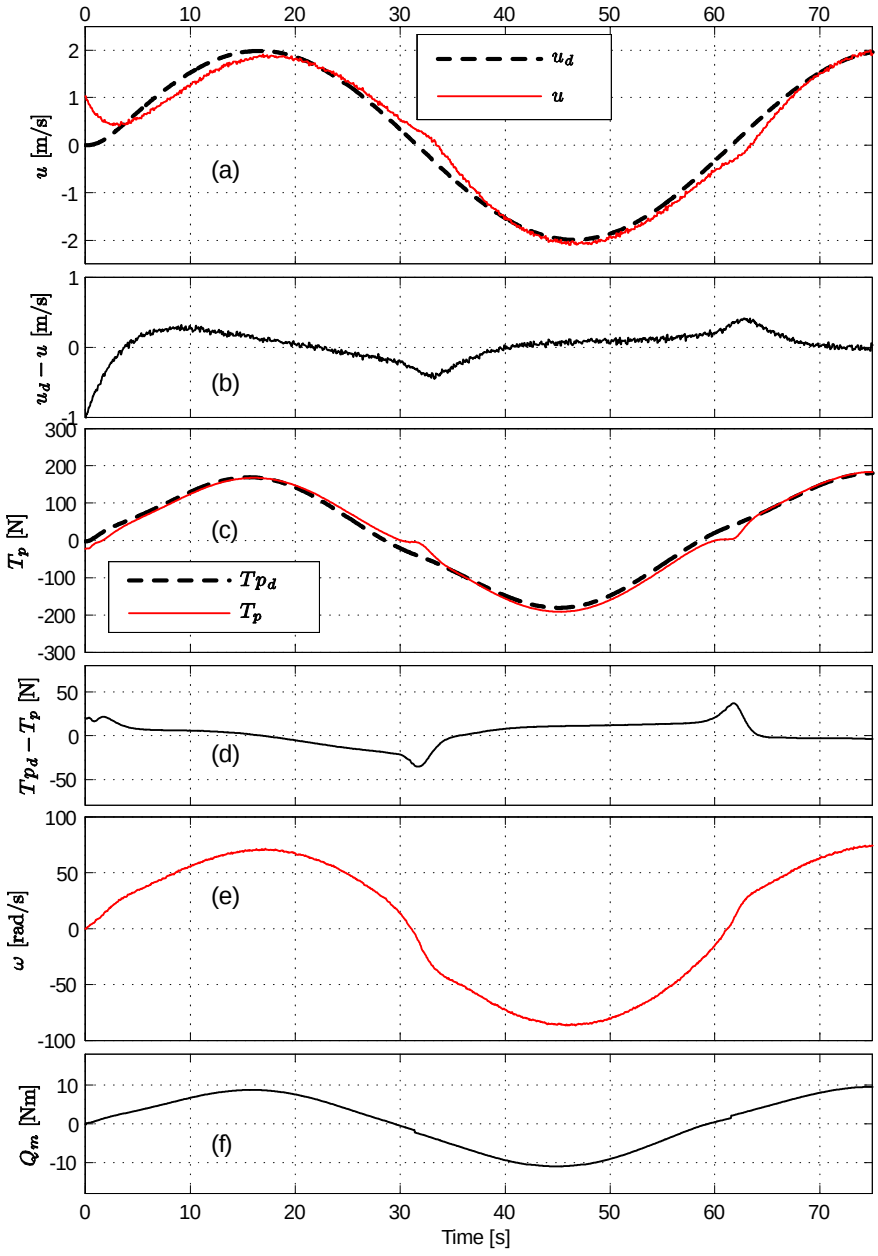

Figure 6.3: Torque controller: desired and actual vehicle speed (a), vehicle speed error (b), desired and actual thrust (c), thrust error (d), shaft speed (e) and commanded motor torque (f).

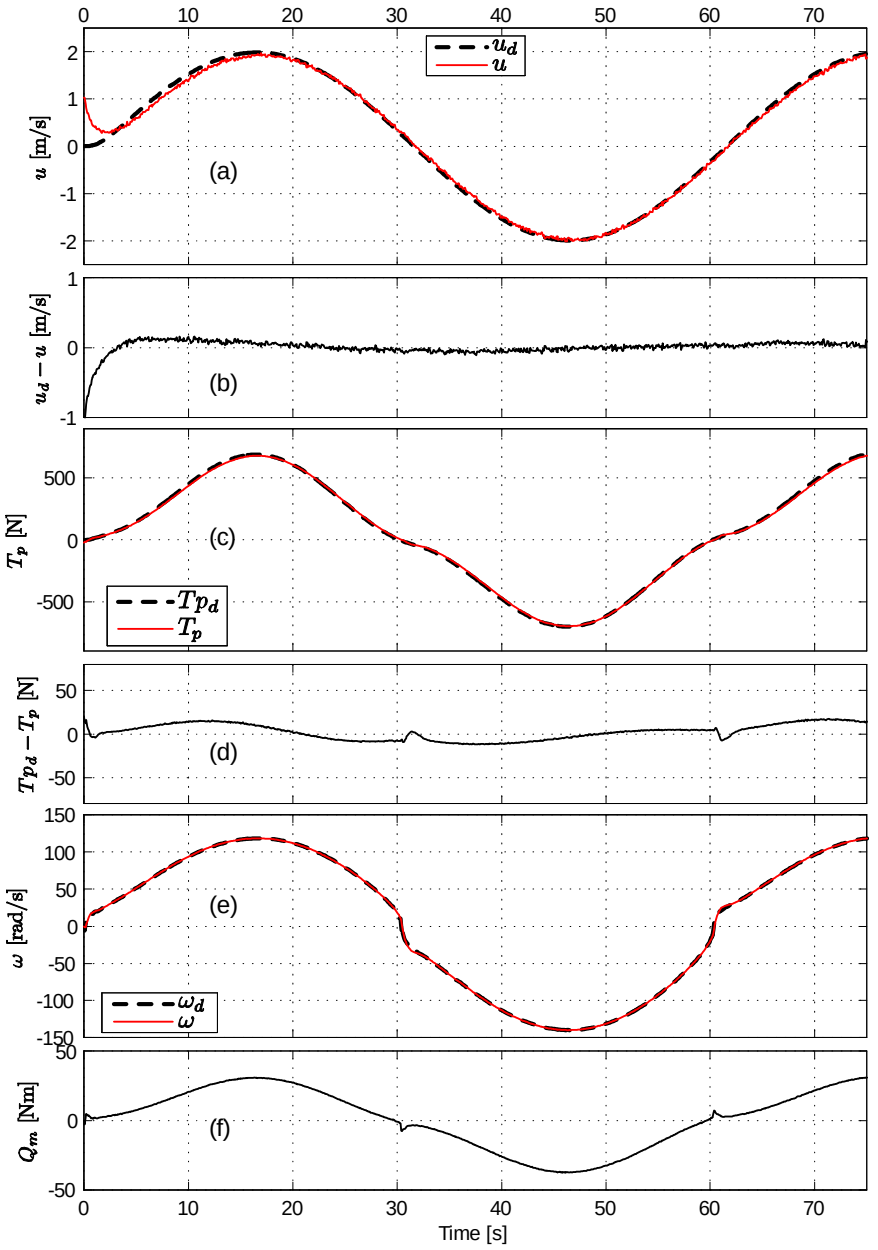

Figure 6.4: Simulation with a large vehicle drag employing the thrust controller: desired and actual vehicle speed (a), vehicle speed error (b), desired and actual thrust (c), thrust error (d), desired and actual shaft speed (e) and commanded motor torque (f).

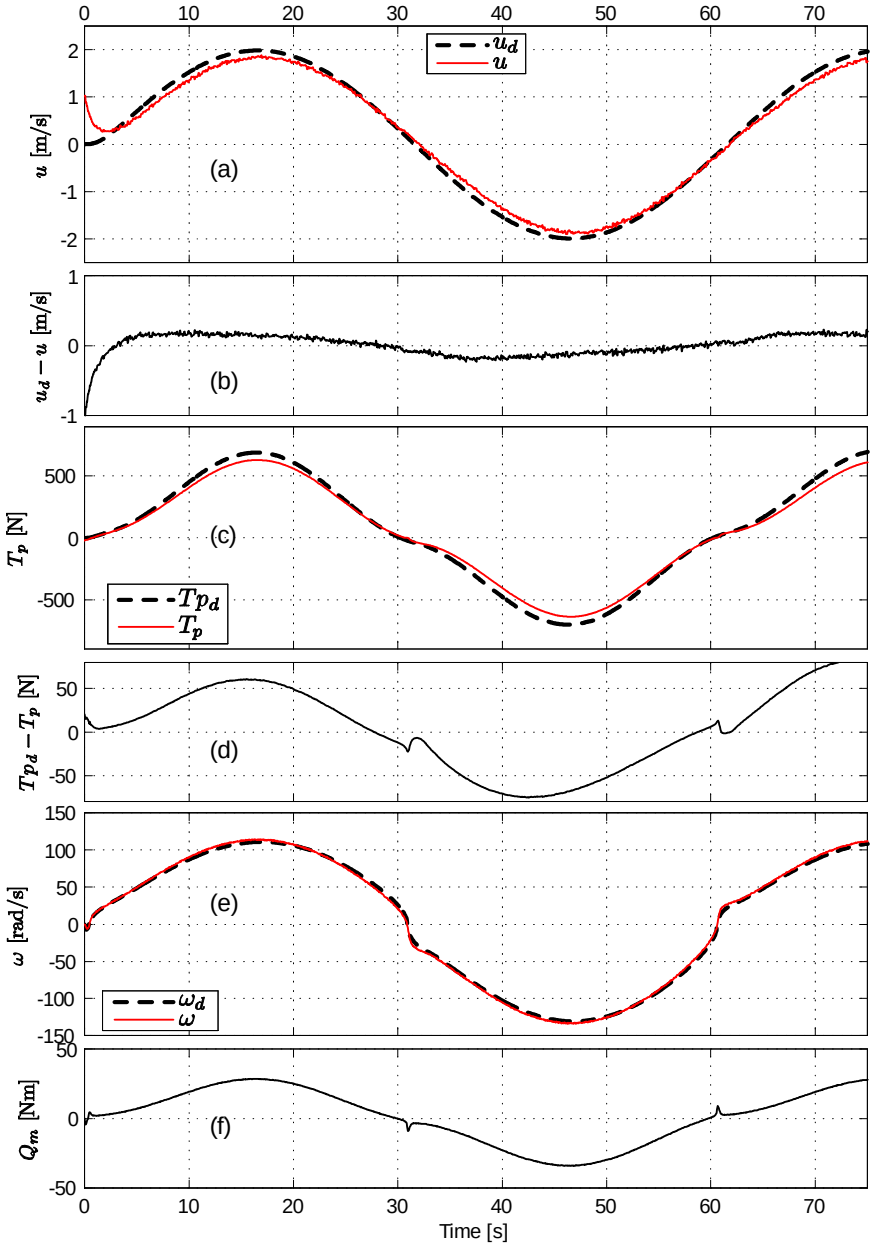

Figure 6.5: Simulation with a large vehicle drag employing the shaft speed controller: desired and actual vehicle speed (a), vehicle speed error (b), desired and actual thrust (c), thrust error (d), desired and actual shaft speed (e) and commanded motor torque (f).

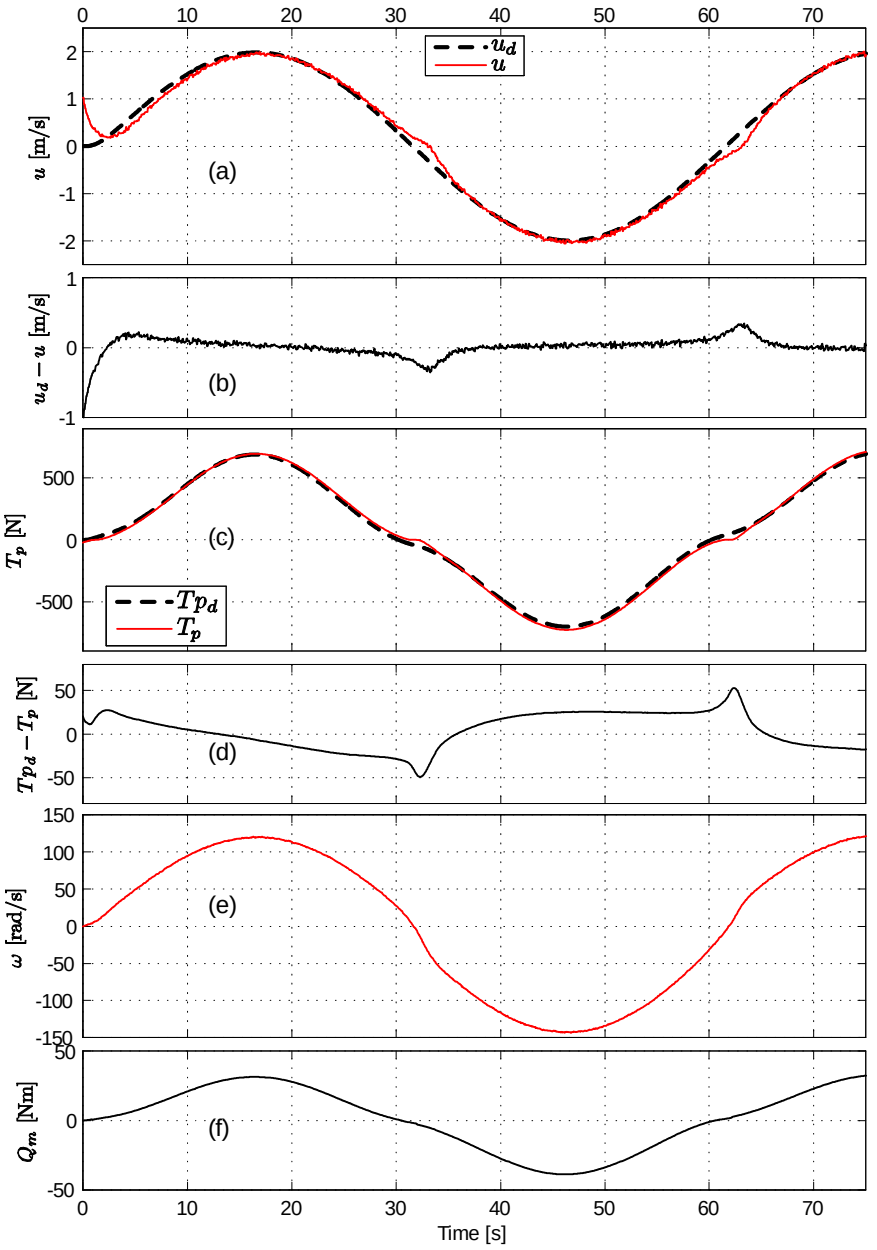

Figure 6.6: Simulation with a large vehicle drag employing the torque controller: desired and actual vehicle speed (a), vehicle speed error (b), desired and actual thrust (c), thrust error (d), shaft speed (e) and commanded motor torque (f).

Chapter 7

Thrust control in extreme sea condition

In extreme sea conditions, due to the motion of the vessel induced by waves, propellers are often subject to ventilation and in-and-out of water effect that cause large losses in the thrust and torque. Ventilation occurs when surface air or exhaust gases are drawn into the propeller blades due to a decrease of pressure. This phenomenon is particularly common for heavily loaded propellers that operate close to the water surface. The effect of ventilation can result in thrust loss up to 80%. Moreover, there have been cases of mechanical failure of power transmission components, which were related to ventilation. In-and-out of water effect results in sudden drop of thrust following a hysteresis pattern; see Sørensen *et al.* (1997). These phenomena have been studied extensively since 1934 when, in Kempf (1934), the effects of ventilation on the thrust and torque for different propeller shaft speed and immersion ratios was investigated. Later, in Shiba (1953), the effect of different propeller parameters on the ventilation phenomena was examined. Other studies on in-and-out of water effect and ventilation, with respect to the vessel operational performance, were carried out in Faltinsen *et al.* (1980), Minsaas *et al.* (1983), Minsaas *et al.* (1987), Karlsen *et al.* (1986) and Lehn (1992). More recently, the dynamic blade loading of a propeller subject to ventilation was analyzed in Koushan (2004), Koushan (2006*b*), Koushan (2006*a*) and Koushan (2007). In these latter works, experiments were carried out to understand the dynamics of the propeller blade forces that, in turn, may lead to improved design of mechanical components for realistic loads and possibly avoid the most harmful operational conditions. In Smogeli (2006), losses of thrust and torque due to ventilation

were analyzed from the control point of view. An anti-spin algorithm for propellers in extreme sea conditions was developed to optimize the thrust production and to reduce power peaks and mechanical wear-and-tear when ventilation occurs.

In extreme sea conditions, the conventional shaft speed controller is generally preferred over the conventional torque controller. When employing the torque controller, large variations in the propeller loads give rise to significant oscillations in the shaft speed that may cause wear-and-tear of the propulsion system. The use of torque controller causes also excessive fluctuations in the consumed power that may not be tolerated by the power generators. The employment of the propeller power controller, due to the fact that its main scope is to keep the power constant, is also not recommended because it would also lead to large shaft speed variations.

When the propeller is subject to large losses, similarly to the torque controller, the thrust controller presented in Chapter 5 and developed for calm and moderate seas may increase the shaft speed to large values in order to counteract the losses. When large losses occur, an increase of the shaft speed does not always correspond to an increase of thrust and it might not be possible to fulfill the thrust requirements, even at the maximum shaft speed available. In fact, in Smogeli *et al.* (2003), it was experimentally demonstrated that, during ventilation, a reduction of the shaft speed to an optimal value may increase the propeller thrust, especially for ducted propellers. This, together with the need of avoiding excessive mechanical wear-and-tear and power peaks, motivated the use of an anti-spin strategy that limits the shaft speed when high thrust losses are detected.

An anti-spin algorithm for marine propellers, motivated by control strategies in car anti-spin and ABS systems, was first introduced in Smogeli *et al.* (2003) and further developed in Smogeli *et al.* (2004*b*) and Smogeli (2006). The cited anti-spin controllers were designed for DP operations where the vessel speed usually does not exceed 1 m/s. The anti-spin algorithm presented in this thesis is based on the cited works. Improvements were introduced in order to exploit the anti-spin strategy also for maneuvering and transit operations, where the vehicle speed is larger than in DP operations.

This chapter is organized as follows. The Anti-Spin strategy is described in Section 7.1. The experimental results are presented in Section 7.2. Conclusions are given in Section 7.3.

7.1 Anti-Spin strategy

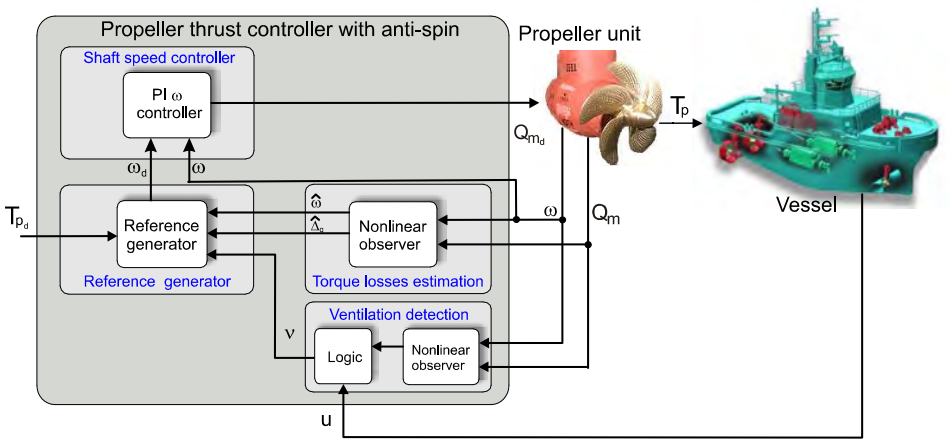

Figure 7.1: Block diagram of the thrust controller with anti-spin.

A block diagram of the overall thrust control system is depicted in Figure 7.1. As introduced above, the main idea of the anti-spin algorithm is to avoid excessive power peaks and mechanical wear-and-tear. This is achieved by setting the speed reference to a constant value when high torque losses are detected. The ventilation detection procedure is based on an estimated value of the torque loss. When the loss situation is considered over, the desired shaft speed is set to the normal value computed by the shaft speed reference developed for calm and moderate sea conditions; see Section 5.3.

An exhaustive description of the anti-spin concept and its impact on the propeller performance in extreme sea conditions are described in Smogeli (2006).

Four-quadrant ventilation detection

The ventilation incident is detected by monitoring the ratio between the estimated propeller torque $\hat{Q}_p$ and the nominal torque Q_{p_n} computed from the K_Q coefficient through (3.9). The torque estimate is obtained either with the observer proposed in Section 4.1.1 or with the one presented in Section 5.2. The observer for the ventilation detection was implemented independently from the observer used to derive the torque loss in the shaft

speed reference generator of the thrust controller. Since the ventilation incident can happen suddenly, it is very important to detect it quickly. Therefore, the gains employed in the observer for the anti-spin procedure should be larger than the one used in the observer for the shaft speed reference generator.

The ratio between the estimated propeller torque and the nominal torque, often termed as the torque reduction coefficient, is written as

$$\hat{\beta}_Q = \alpha(\omega) + (1 - \alpha(\omega)) \frac{\hat{Q}_p}{Q_{p_n}}, \tag{7.1}$$

where

$$\alpha(\omega) = e^{-k_1 |\omega|^{p_1}} \tag{7.2}$$

and

$$Q_{p_n} = K_Q \frac{\rho \, |\omega| \, \omega D^5}{4\pi^2}. \tag{7.3}$$

The weighting function $\alpha(\omega)$ with positive tuning gains k_1 and p_1 is used to avoid the singularity of $\hat{Q}_p/Q_{p_n}$at $\omega = 0$. The nominal value of K_Q in (7.3) is derived from the K_Q propeller characteristic using the nominal value of J computed from (3.10), where the the value of the advance speed u_a is obtained from (3.11) employing the vessel speed and the wake fraction number.

The ventilation is detected when the value of $\hat{\beta}_Q$ becomes smaller than a threshold value $\beta_{v,on}$ and it is considered terminated when the value of $\hat{\beta}_Q$ becomes larger than $\beta_{v,off}$. The ventilation state, described by the variable ν, is defined as follows:

$$\begin{aligned}
\hat{\beta}_Q \geq \beta_{v,on} \quad &\Rightarrow \quad \nu = 0, \text{ no ventilation} \\
\hat{\beta}_Q < \beta_{v,on} \quad &\Rightarrow \quad \nu = 1, \text{ ventilation on} \\
\hat{\beta}_Q \geq \beta_{v,off} \quad &\Rightarrow \quad \nu = 0, \text{ ventilation off}
\end{aligned}$$

The hysteresis is included in order to increase the robustness of the ventilation detection procedure with respect to measurement noise that could affect the $\hat{\beta}_Q$ estimate. When the propeller works in the 2$^{\text{nd}}$ or 4$^{\text{th}}$ quadrant of the plane (u_a, ω), the nominal torque model (7.3) may be inaccurate, as shown in Chapter 4, leading to jumps in the ventilation state. For this reason a ventilation detection is held on for a minimum time $\mathrm{T_{hold}}$. Moreover, since the nominal torque Q_{p_n} accounts only for variations in the advance speed and does not include any term that represents the effect of other losses, if the thresholds are not chosen carefully, a ventilation could be detected even if the propeller does not actually ventilates.

Anti-spin action

When the ventilation is detected, the desired shaft speed $\bar{\omega}_d$, computed in (5.8), is redefined as:

$$\bar{\omega}_d = \omega_{v_{opt}} \qquad \text{if } \nu = 1 \text{ and } \bar{\omega}_d \geq \omega_{v_{opt}}. \tag{7.4}$$

The value of $\omega_{v_{opt}}$ may be chosen such that the thrust produced by the propeller at $\omega_{v_{opt}}$ is equal to or larger than the thrust produced at higher shaft speeds. It may also be chosen according to an optimization criterion based on the estimate of the torque loss. An optimal solution for the power generators would be to chose $\bar{\omega}_d(t)$ in order to reduce the oscillations in the consumed power. In that case, during ventilation, the shaft speed will not be constant. Other criteria may include power peaks and torque oscillations. This could be addressed in the future.

7.2 Experimental results

This section presents the result of a test carried out to compare the performance of the thrust controller designed for calm and moderate sea conditions with and without the anti-spin algorithm enabled. The anti-spin algorithm was validated with various tests carried out at different advance speeds, propeller immersion rates, propeller submergences and shaft speeds.

To simulate the motion that a propeller may experience in extreme sea states, the tests were performed by moving the propeller along its vertical axis with a sinusoidal motion. This test did not reproduce entirely extreme sea conditions, but it was executed to validate the performance of the proposed anti-spin algorithm with large torque losses. In order to simulate a realistic scenario, the towing carriage speed was positive when the thrust was positive and became negative when the thrust was reversed.

The thrust controller was implemented with the gains and parameters presented in Table 5.1. As described above, an observer faster than the one used in the shaft speed reference generator in the thrust controller was employed for the ventilation detection procedure. The estimate of the propeller torque, used in (7.1), was obtained with the observer presented in Section 5.2 with gains $l_1 = 3$ and $l_2 = 140$ and with the time constant $\tau_2 = 10$.

Figure 7.2 shows data from the test with the anti-spin algorithm enabled. Due to the propeller asymmetry, the value of $\omega_{v_{opt}}$ in (7.4) was set equal to 45 rad/s for positive ω and 54 rad/s for negative ω. These values

were chosen to obtain at $\omega_{v_{opt}}$ approximately the same thrust that would have been obtained at larger shaft speeds. In Figure 7.2 (a) the measured propeller torque and its estimate are plotted showing good agreement. Part (b) of the same figure shows the torque loss reduction used for the ventilation detection. The ventilation state ν is plotted in Figure 7.2 (c) together with the propeller submergence h. The ventilation incident was detected when the propeller moved toward the water surface causing a drop in the propeller torque. In Figure 7.2 (e), we can notice that before the ventilation detection, the controller increased the shaft speed to compensate for the torque loss. When the ventilation was detected, the desired speed was set to the $\omega_{v_{opt}}$ value. Also in this situation, despite the shaft load variation, the shaft speed controller provided very good performance.

The data of a test performed under similar conditions, but with the anti-spin disabled, are shown in Figure 7.3. During the ventilation incident, the shaft speed increased quickly to the maximum value which was set to 75 rad/s. Without the anti-spin, when the propeller rotated close to the water surface, the thrust presented larger fluctuations. Moreover, even if the shaft speed was almost double, the produced thrust was practically equal to the one obtained when the anti-spin was enabled.

Figure 7.4 shows the measured motor power P_m for the two tests. Without the anti-spin, large power peaks were experienced. They may not be tolerated by the power system and increase the possibility of blackouts. Table 7.1 presents the mean values of the propeller thrust $\bar{T}_p$, the consumed power $\bar{P}_m$, and the propulsion efficiency $\bar{\eta}_p$. The average thrust, produced without the anti-spin strategy, was slightly larger than the one produced with the anti-spin. This was due to the thrust spikes that occurred when the ventilation incident was terminating, when the shaft speed was at the maximum value and the propeller submergence increased toward deeply submerged values. The average propulsion efficiency was computed taking the mean of (3.16) with $t_d = 0$, $w_f = 0$, $\eta_m = 0$, $\eta_R = 0$. The controller that employed the anti-spin algorithm increased the average propulsion efficiency of about 20% with respect to the case where the anti-spin was not employed. For a vessel traveling in waves, the efficiency gained from using the anti-spin algorithm would be slightly less than 20% since the average thrust produced with the anti-spin was smaller than the one obtained without the anti-spin. This would cause a smaller vessel speed and, in turn, a smaller advance speed u_a, resulting in a reduced efficiency.

Table 7.1: Mean values of thrust, motor power, and propulsion efficiency.

Controller	$\bar{T}_p$ $[N]$	$\bar{P}_m$ $[W]$	$\bar{\eta}_p$
Anti-spin	79.2	290	0.151
No anti-spin	89.1	378	0.123

7.3 Conclusion

This chapter demonstrated the utility of an anti-spin strategy for the controller designed for calm and moderate sea conditions, which was presented in Chapter 5. When enabled, the anti-spin strategy allowed the reduction of power peaks and the increase of the propeller efficiency. As reported also in Smogeli (2006), the use of anti-spin can reduce the mechanical wear-and-tear of the propulsion system.

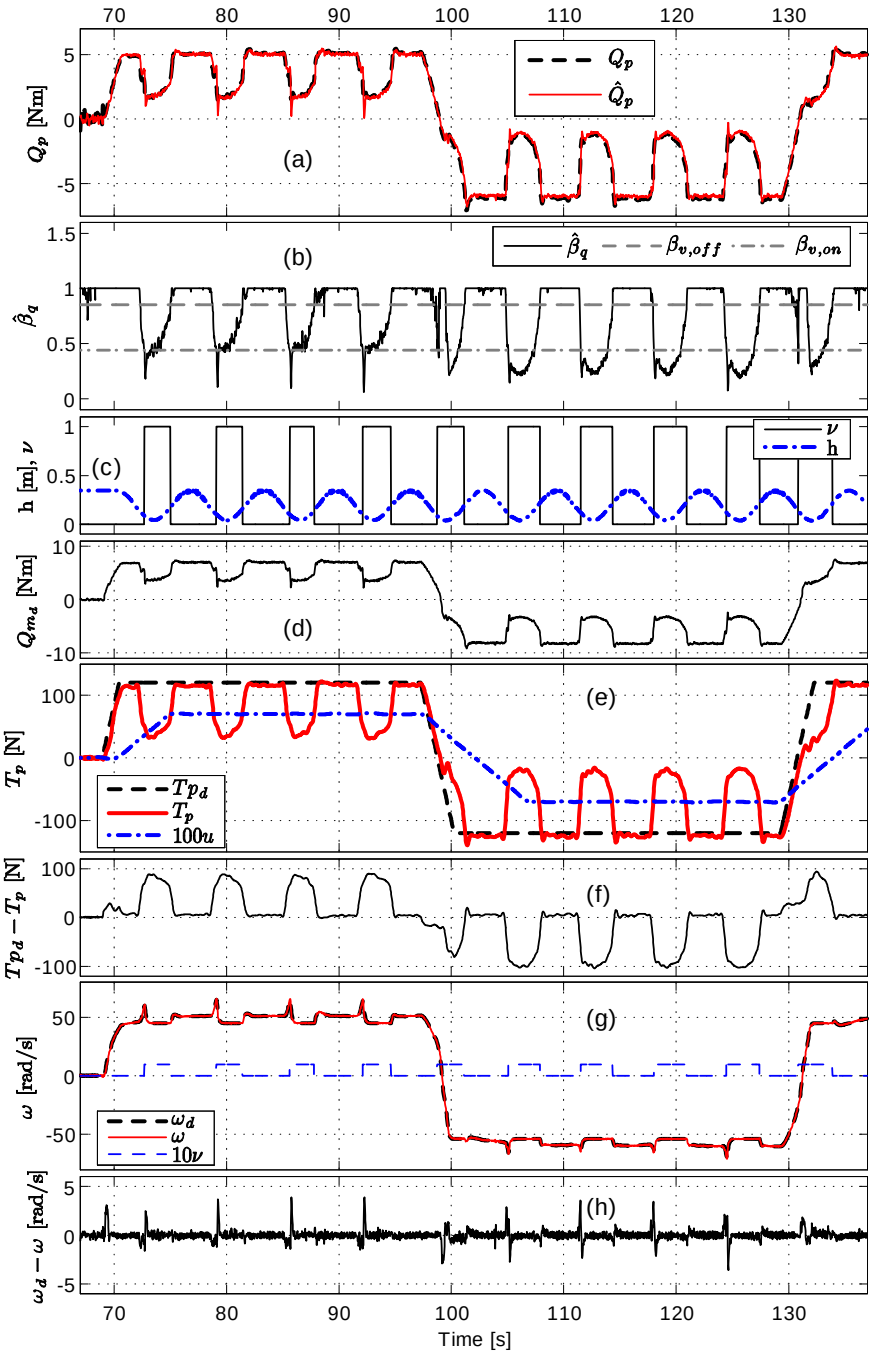

Figure 7.2: Test with anti-spin enabled.

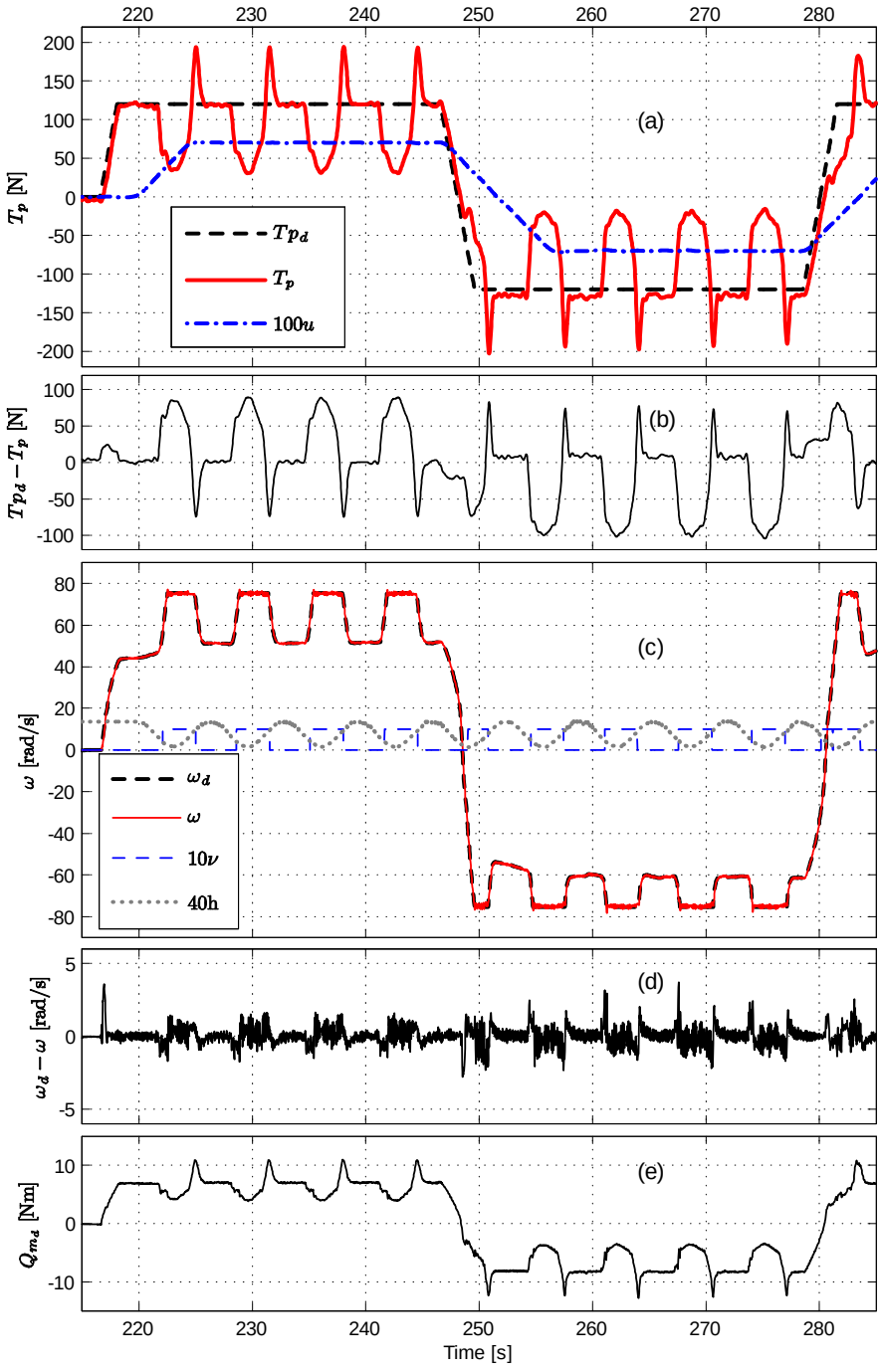

Figure 7.3: Test with anti-spin disabled.

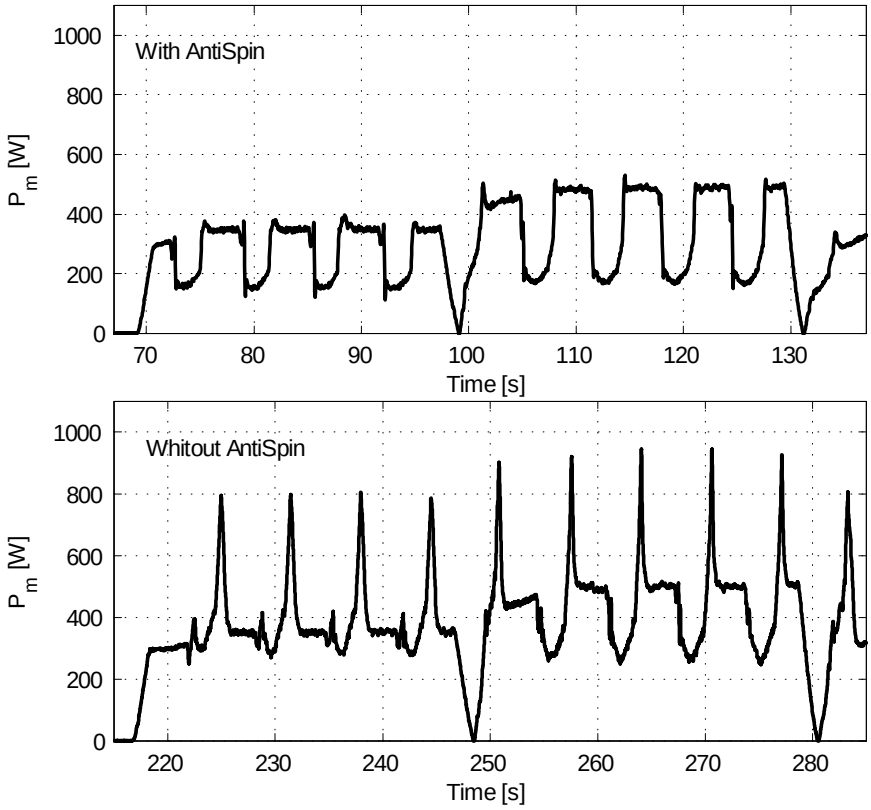

Figure 7.4: Motor power with and without the anti-spin algorithm enabled.

Chapter 8

An efficiency optimizing shaft speed controller

For ships on passage, waves create load fluctuations in the shaft of the main propellers due to variations in inflow velocity to the propeller. When a propeller rotates at constant speed, variations in inflow velocity give rise to variations of the advance number and, hence, in the propeller efficiency, as known from the open-water propeller characteristics. The topic of this chapter is to determine whether periodic variation in the inflow velocity could be utilized actively to obtain higher average propulsion efficiency with respect to the use of conventional propeller controllers.

This chapter will scrutinize the properties of propellers subjected to periodic wave induced velocity. A quasi steady-state model of a propeller with varying inflow is revisited and a proposition is made about possible enhancements in the overall propulsion efficiency in waves. Experimental results from model tests are analyzed and are used to show that quasi-steady state model assumptions are valid for a propeller in moderate sea. Subsequently, the efficiency optimization under periodic wave induced velocity is formulated as a nonlinear optimization problem and a numerical solution is presented. The results are discussed in view of impact on fuel economy and in view of feasibility of implementation. A simulation study is performed in order to demonstrate the properties of the efficiency optimizing controller.

This chapter is organized as follows. A propulsion model for moderate sea is introduced in Section 8.1. Experiments carried out in moderate waves are described in Section 8.2. The optimization problem is formulated in Section 8.3. In the same section, a numerical solution of the optimization problem is proposed and a simulation is presented. Conclusions are given

in Section 8.4.

8.1 Quasi steady-state propulsion model

For simplicity, we consider a vessel that cruises at positive speed with one single propeller aft of the hull. The propeller shaft speed dynamics, introduced in Section 3.2, is rewritten here for the sake of clarity:

$$J_m\dot{\omega} = R_{gb}Q_m - Q_p - Q_f. \tag{8.1}$$

When performing operations at positive shaft and advance speeds, lift theory results in bilinear thrust and torque relations for the propeller (Blanke *et al.*, 2000):

$$T_p = t_{nn}\omega^2 + t_{nu}\omega u_a, \tag{8.2}$$

$$Q_p = q_{nn}\omega^2 + q_{nu}\omega u_a, \tag{8.3}$$

where t_{nn}, t_{nu}, q_{nn} and q_{nu} are constant parameters. These parameters can be identified by linearizing the standard propeller characteristics in the first quadrant. The advance speed u_a can be written as the sum of the nominal advance speed U_a and the term u_w representing wave induced inflow, such that

$$u_a = U_a + u_w. \tag{8.4}$$

The nominal advance speed U_a is computed from (3.11) employing the vessel speed and the wake fraction number. The balance between the propeller thrust and vessel hull resistance $R(u)$ determines the surge velocity u through

$$m\dot{u} = R(u) + (1 - t_d)\, T_p, \tag{8.5}$$

where $(1 - t_d)$ is the thrust deduction introduced in Section 3.4.

The energetic performance of the propeller is analyzed by considering the total propulsion efficiency η_p, given by (3.16), where the mechanical efficiency η_m and the relative rotative efficiency η_R are assumed to be equal to 0.97 and 1, respectively. These values are commonly employed for ships. Since, due to waves, the actual advance speed u_a cannot be computed from the vessel speed and the wake fraction number as in (3.11), the total propulsion η_p must be written explicitly with the vessel speed as

$$\eta_p = \frac{T_p(1 - t_d)u}{\omega\,(Q_p + Q_f)}\eta_m\eta_R. \tag{8.6}$$

Using (8.2) and (8.3), the total propulsion efficiency is rewritten as

$$\eta_p = \frac{(1-t_d)\left(t_{nn}\omega^2 + t_{nu}\omega u_a\right)u}{\left(q_{nn}\omega^2 + q_{nu}\omega u_a + Q_f\right)\omega}\eta_m\eta_R. \tag{8.7}$$

Periodic wave disturbance

The wave induced velocity in (8.4) is assumed to be periodic such that

$$u_w(t+\tau_w) = u_w(t). \tag{8.8}$$

This is true in regular waves, where the wave induced velocity can be approximate with

$$u_w(t) = u_{wo}\sin\left(\frac{2\pi}{\tau_w}t\right), \tag{8.9}$$

where u_{wo} is the induced water speed amplitude and τ_w is the wave period. Considering regular waves is clearly an approximation, but in many cases the bandwidth of the wave frequency spectrum is not particularly wide. The average propulsion efficiency during one cycle of the wave induced velocity period is

$$\bar{\eta}_p = \frac{1-t_d}{\tau_w}\eta_m\eta_R\int_0^{\tau_w}\frac{T_p(t)u(t)}{\left(Q_p(t)+Q_f(t)\right)\omega(t)}dt \tag{8.10}$$

where the thrust and the torque are computed from (8.2) and (8.3).

8.2 Propeller in waves

Experiments for the study of the propeller behavior in moderate waves were performed at the MCLab. In order to avoid losses due to ventilation, the nominal propeller submergence h/R was set equal to 2.68, where R is the propeller radius. The tests were performed on the propeller P1362, described in Chapter 2, with regular waves of 4 cm amplitude (peak-to-trough) and 1.75 s period. The standard open-water propeller characteristics K_T and K_Q for positive shaft and advance speeds are depicted in Figure 8.1 (a).

In order to simulate a real scenario, the towing carriage was moved according to the measured thrust produced by the propeller and the vessel dynamics (8.5). The hull resistance $R(u)$ included a linear and quadratic drag term, the main drag effects in the surge dynamics for a vessel traveling ahead:

$$R(u) = -d_l u - d_q u\left|u\right|. \tag{8.11}$$

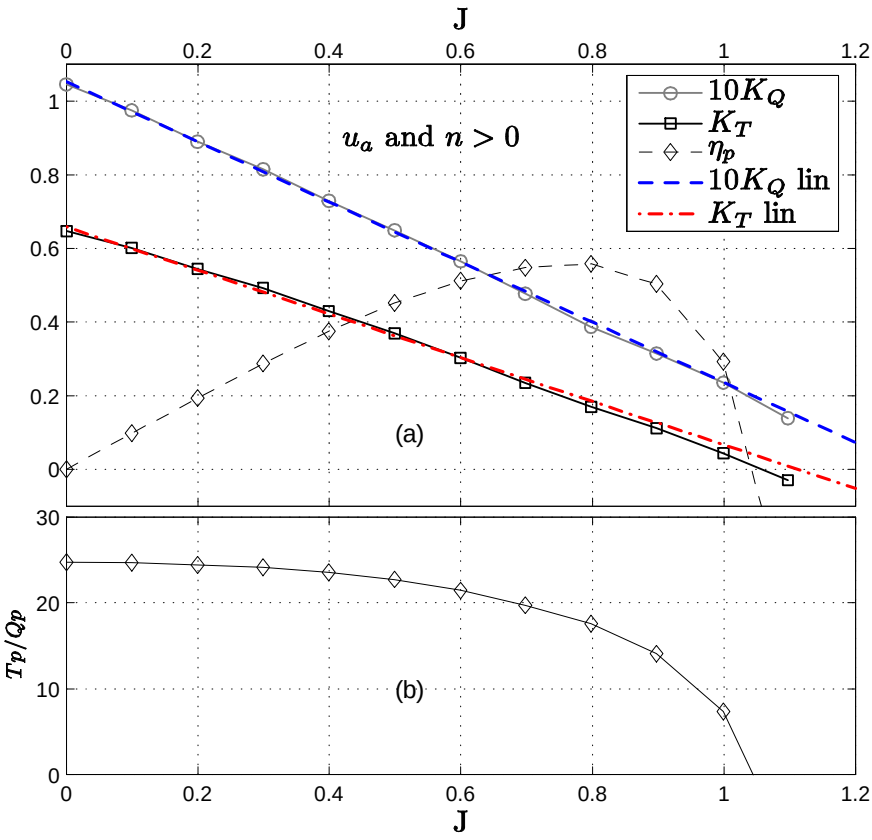

Figure 8.1: Propeller P1362 standard characteristics (a) and thrust torque ratio (b).

The vessel dynamics was simulated with $m = 200\ kg$, $d_l = 30$ and $d_q = 20$. These values were chosen in order to obtain a vehicle with limited inertia, due to the small length of the towing tank, and, at the same time, to avoid that the vehicle speed was too sensitive with respect to the thrust oscillations induced by waves. The measured propeller thrust was fed into the model (8.5) and the resulting vehicle speed was used as a reference for the towing carriage velocity. In our setup, the nominal advance speed U_a was considered equal to the towing carriage speed since the propeller housing did not create a significant wake. For the same reason, the thrust deduction number t_d was neglected ($t_d = 0$). The shaft friction torque was given by (3.2), employing the parameters of Table 3.1.

Figure 8.2 presents data of a test performed at constant shaft speed of about 37 rad/s. The waves propagated in the same direction of the vessel speed (following sea). The shaft speed is depicted in Figure 8.2 (a). The measured propeller thrust is plotted in Figure 8.2 (b). The same plot presents also the thrust computed with the bilinear relation (8.2), where J was computed with (3.10), using the nominal value of the advance speed U_a, the best guess of the actual advance speed. We can notice that the thrust computed from the propeller characteristics did not reproduce accurately the measurements, suggesting that U_a was not a good measure of the actual advance speed. This explained also the discrepancy between the measured propeller torque and the one computed from the propeller characteristics, shown in Figure 8.2 (c).

Figure 8.2 (e) shows the nominal value of the advance speed and the actual one, computed from (8.3) employing the torque measurement:

$$u_a = \frac{Q_p - q_{nn}\omega^2}{q_{nu}\omega}, \tag{8.12}$$

The obtained value of the advance speed may be considered as the average inflow velocity at the propeller disc. Since the propeller torque is not usually available in a real vessel, an estimate $\hat{Q}_p$ was obtained employing the nonlinear observer presented in Chapter 4. The estimate reproduced well the measurement and it was used to derive $\hat{u}_a$, an estimate of the advance speed, through (8.12). The estimate $\hat{u}_a$ is shown in Figure 8.2 (e). It is interesting to note the correlation between the advance speed u_a and the propeller submergence h, plotted in Figure 8.2 (f). The magnitude of the advance speed was larger when the propeller was closer to the water surface. This was due to the horizontal water speed induced by the waves that, according to the classical wave theory, was greater close to the surface.

Figure 8.2 (g) shows J_n and J_m, the nominal and the measured value of the advance number J, respectively. J_n was obtained from (3.10), using U_a instead of the actual advance speed u_a, employed to compute J_m. Figure 8.2 (h) shows the nominal and measured open-water propeller efficiency η_{0_n} and η_{0_m}, and the nominal and measured total propulsion efficiency η_{p_n} and η_{p_m}. The total propulsion efficiency was smaller than the open-water propeller efficiency since it accounts for the shaft friction torque, quite significant in our system. The open-water propeller efficiency was computed from the corresponding value of J combined with the efficiency curve in Figure 8.1 (a). The nominal value of total propulsion efficiency η_{p_n} was computed with (8.7) using U_a, while η_{p_m} was computed with the actual value of u_a. It is important to notice the opposite behaviors of η_{0_m} and η_{p_m}

with respect to the advance speed. When u_a decreased, since the shaft speed was constant, J decreased producing a reduction of the open-water propeller efficiency. At the same time, the thrust torque ratio increased due to the reduction of the value of J, as shown in Figure 8.1 (b). This leaded to an increase of the total propulsion efficiency, since the vessel speed did not change considerably. For increasing value of u_a, the opposite behaviour was observed.

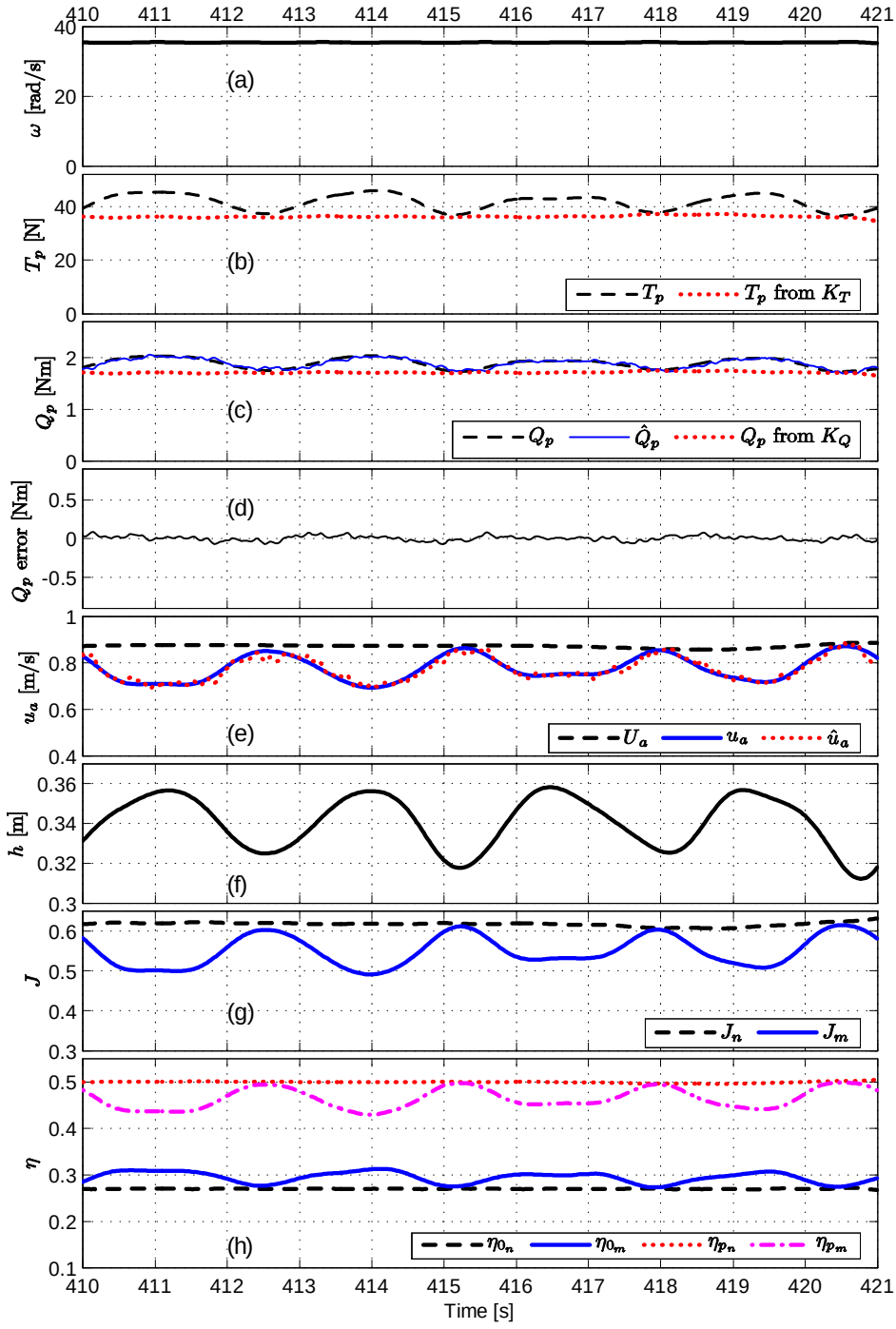

Figure 8.2: Experimental data from a simulated moderate sea test.

8.3 Efficiency optimization

The oscillations experienced in the total propulsion efficiency may be exploited in order to reduce the average power consumption without reducing the vessel speed.

Problem 8.1 *The optimal control problem can be formulated as*

$$\max_{\omega(t)} \bar{\eta}_p = \max_{\omega(t)} \frac{1-t_d}{T} \eta_m \eta_R \int_0^T \frac{T_p(t)u(t)}{(Q_p(t)+Q_f(t))\,\omega(t)} dt, \tag{8.13}$$

with $t \subset [0, T]$ *where* $T = k\tau_w$, k *being an integer, subject to*

$$\frac{1}{T}\int_0^T T_p(\tau)d\tau = T_{0,} \tag{8.14}$$

$$|T_p(t) - T_0| \leq T_M, \tag{8.15}$$

where T_p *and* Q_p *are given by (8.2) and (8.3).*

The first constraint (8.14) is needed to maintain a constant average vessel speed. The second constraint (8.15) is used to limit the thrust oscillations in order to reduce wear-and-tear of engine and other mechanical parts.

8.3.1 Numerical solution of the optimization problem

A numerical solution of the optimization problem, defined as offline efficiency optimizer controller**,** was computed in order to evaluate a possible increase of the total propulsion efficiency with respect to the employment of the conventional shaft speed and torque controllers, introduced in Chapter 5. The average vessel speed was set equal to 0.86 m/s. The wave induced inflow velocity u_w was a sinusoidal signal of 0.2 m/s amplitude and 3 s period. At this stage the shaft moment of inertia was neglected, thus considering the propeller able to spin at the desired shaft speed instantaneously. The inclusion of the shaft moment of inertia will be considered in a future work. The wake fraction number and the thrust deduction number were assumed to be 0.1. The friction torque was modeled as a Coulomb plus a linear viscous effect as in (6.4). The speed of the vessel and the advance speed were assumed to be available. The vessel speed is usually measured, while the advance speed could be estimated, as presented in Section 8.2.

With the same parameters of vessel dynamics employed in the experiments, the average propeller thrust T_0 was equal to 45 N, corresponding to an average shaft speed of 37.7 rad/s at the given vessel speed. The value of T_M in (8.3) was chosen equal to ± 7 N in order to obtain thrust oscillations smaller than the ones obtained using the conventional shaft speed controller. The solution was computed in the Matlab® environment by solving the problem (8.13) in three wave periods with the constraints (8.14) and (8.15); see Becerra (2004) for example.

Figure 8.4 shows the result of a simulation. The vessel speed, equal to the nominal advance speed in this case, is depicted in the subplot (a). The torque controller produced the least oscillatory vessel speed due to the smallest variations of the propeller thrust around its mean values, as shown in the subplot (c). The vessel speed obtained with the optimizing controller and conventional shaft speed controllers presented approximately the same variation around the average. The shaft speed is shown in the subplot (d). The optimizing controller produced the largest shaft speed variations, but the thrust showed smaller oscillations compared to the conventional shaft speed controller. The propeller torque is shown in the subplot (e) while the load torque Q, computed as $Q = Q_p + Q_f$, is depicted in the subplot (f). The open-water and total propeller efficiency are depicted in subplots (g) and (h). It is interesting to note that the shaft speed, obtained as a solution of the optimizing problem, presented the largest values when the total efficiency was larger and vice versa.

Remark 8.1 *The offline computation of the optimal solution was computed for regular waves, i.e. the wave induced inflow preserved the same amplitude and frequency all time. The computed solution may not be optimal for wave induced inflow with different characteristics. This will be addressed in future works.*

For a practical implementation, a static mapping was identified from the advance speed u_a to the shaft speed ω. Defining the variations of u_a and ω around their average values with Δu_a and $\Delta\omega$, we have

$$\Delta\omega = f_{opt}(\Delta u_a). \tag{8.16}$$

The average value of ω corresponds to the shaft speed reference required from the conventional shaft speed controller. The optimal solution is obtained by adding $\Delta\omega$ to the reference shaft speed. The value of $\Delta\omega$ is computed from (8.16), where Δu_a is obtained from an estimate of u_a by subtracting its average values (computed using a low pass filter for example).

Figure 8.5 (b) shows the static mapping f_{opt} identified as a series of tansig functions, where the tansig function is defined as

$$\text{tansig}(x) = \frac{2}{1 + e^{-2x}} - 1.$$

See for example Narendra and Parthasarathy (1990). Figure 8.5 (a) shows Δu_a, $\Delta\omega$ and its approximation $\Delta\omega_{nn}$ obtained with (8.16). Figure 8.3 shows the controller block diagram.

Fast variations in the advance speed give quick variations in the shaft speed that may increase the wear-and-tear of the mechanical part of the system. This can be avoided by decreasing the propeller torque observer gains, reducing the high frequency content in the advance speed estimate. Moreover, for diesel engines, the performances may be reduced due to the motor torque limitation that does not allow fast changes in the shaft speed.

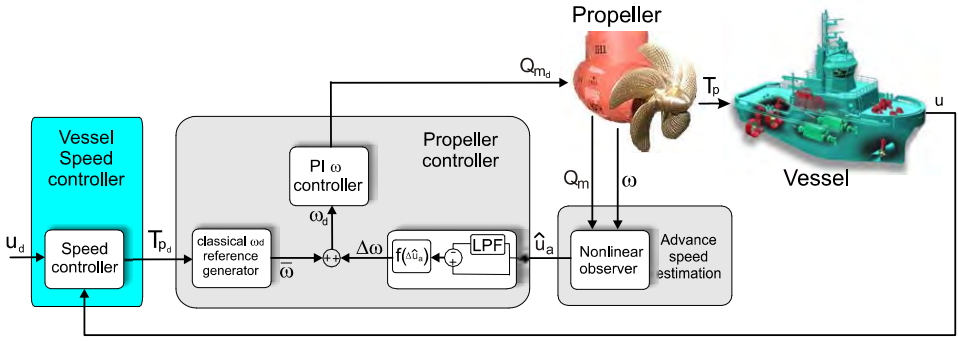

Figure 8.3: Block diagram of the efficiency optimizing controller.

Table 8.1: Average efficiency employing different controllers.

Controller	η_p	η_0
shaft speed	0.394	0.429
Torque	0.399	0.435
Offline η optimizing	0.406	0.445

Table 8.1 shows the average values of the total and open-water propeller efficiency. The offline η optimizing controller produced an increase of the total efficiency of about 3% with respect to the conventional shaft speed controller. The total efficiency increased about 1.7% compared with the torque controller. The improvement may look tiny, but for ships in ocean

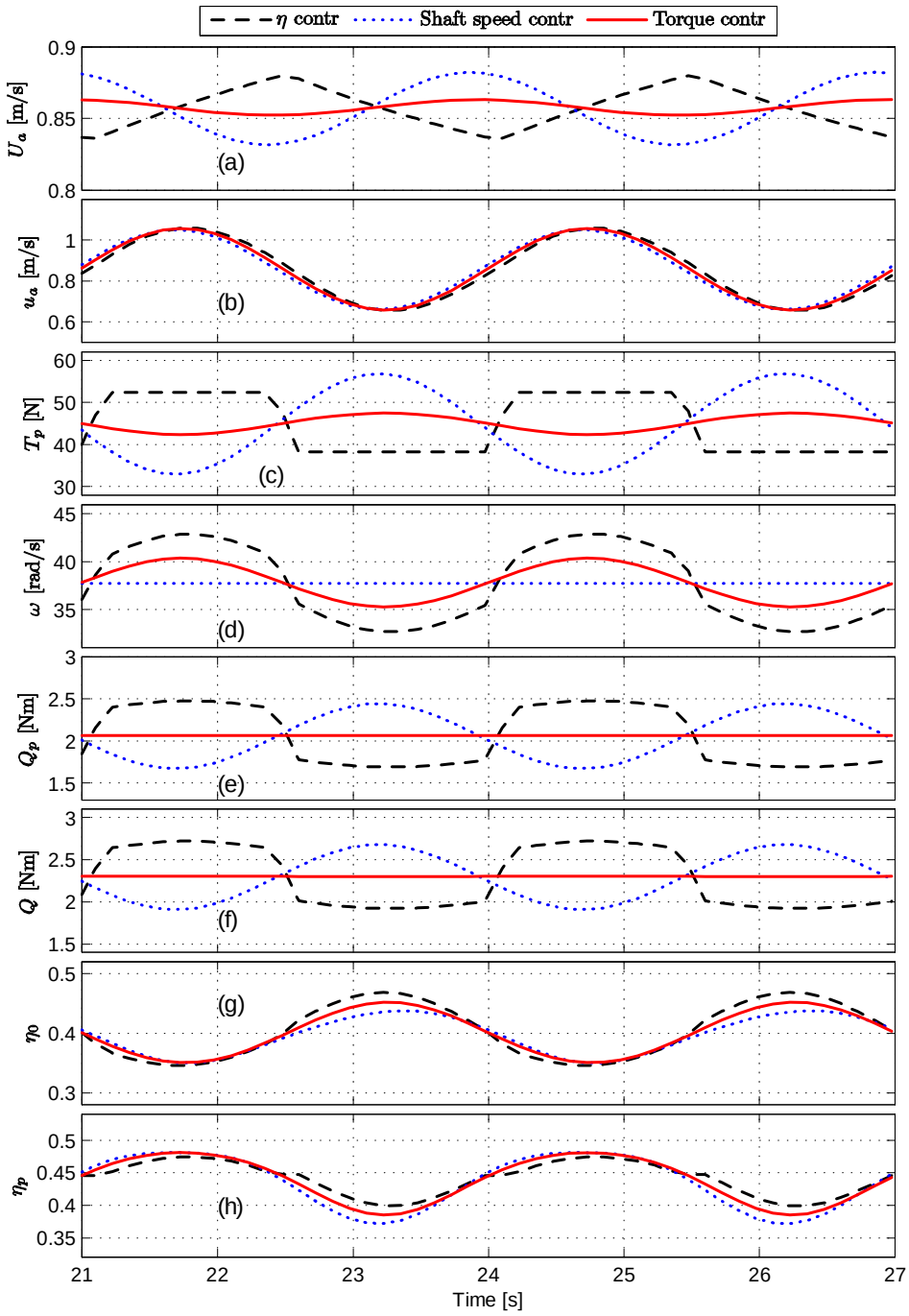

Figure 8.4: Comparison among the η optimizing, shaft speed and torque controllers.

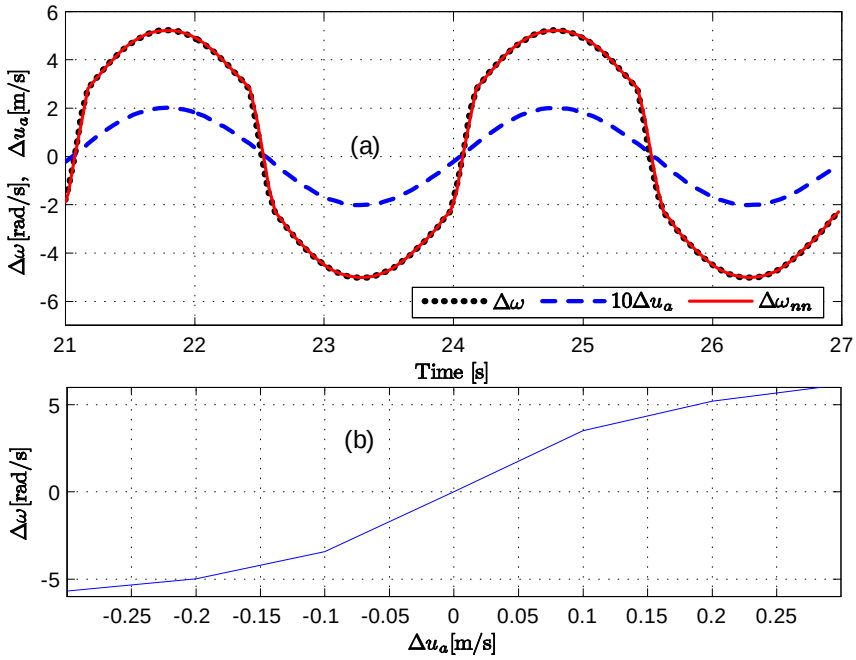

Figure 8.5: Online optimal solution: Δu_a, $\Delta\omega$ and its approximation $\Delta\omega_{nn}$ (a); f_{opt} (b)

passage, the increase of the propulsion efficiency could result in essential savings. Also, the reduction of fuel consumption may contribute to the reduction of CO_2 and other emissions.

8.4 Conclusion

In this chapter, a novel control scheme for marine propellers operating in moderate sea conditions was presented. By exploiting the variation of the propeller inflow due to waves, it was shown that it is possible to increase the total propulsion efficiency with respect to the conventional propeller controllers. The shaft speed reference was computed as a solution of a nonlinear optimizing problem with constraints where regular waves were considered. Results were presented in simulations where the employed model was derived from experimental tests. These results were obtained at experimental conditions with wave with 4 cm amplitude (peak to trough) and propeller

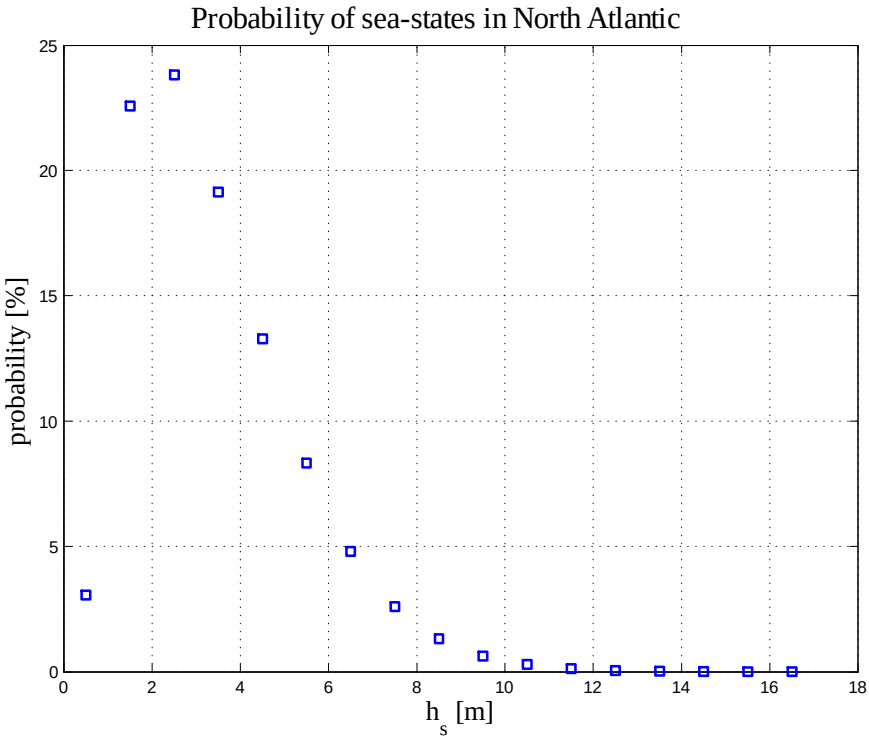

Figure 8.6: Probability of sea-states in the North Atlantic as function of significant wave height. (Source: IACS recommendation REC34)

diameter equal to 25 cm. Experiments conducted subsequently showed that the phenomena described in the experiments are valid up to at least three times the wave height used here, i.e. up to a wave height of 12 cm. This is equivalent approximately to wave amplitude of 2.8 m for a containership with 6 m diameter propeller. It is difficult to anticipate how the proposed controller scheme will be effective in irregular waves. However, by looking at the statistic of the sea state in the North Atlantic, depicted in Figure 8.6, if the increase in the propulsion efficiency is possible, this could results in substantial reduction of the fuel consumption.

Chapter 9

Conclusion

This thesis focused on the development of thrust estimation schemes and new strategies for the *low-level thruster control* in order to improve the thrust control performance with respect to the conventional thruster controllers. The accuracy in the thrust control was one of the performance criteria adopted, but also the mechanical wear-and-tear, the power consumption and the efficiency of the propulsion system have been considered, especially for moderate and rough sea conditions. The work presented in the thesis can be applied to fixed pitch propellers. Particular attention was given to four-quadrant operations, in which the propeller shaft speed and the propeller inflow velocity assume values in the whole plane. For example, for station-keeping-operations and low speed maneuvering, it is important to obtain accurate performance in all quadrants since they may be equally explored in certain sea and weather conditions. For transit operations, however, only the first quadrant is usually explored, therefore the accuracy required in the other quadrants is not particularly high. Unless few exceptions, only positive shaft speed and advance speed were traditionally considered in the literature.

The topic of propeller modeling, in the prospective of simulation and control, was treated in Chapter 3. It was shown that the inclusion of the axial flow velocity dynamics in the propeller model could improve the model accuracy. This, unfortunately, requires the use of fragile equipment that may not be suitable for the marine environment. Moreover, the identified model appeared to be quite complex for its use in control systems.

Marine vehicles are not usually equipped with thrust sensors, therefore the development of accurate thrust estimations schemes may lead to improved overall vehicle performance. Motivated by this, a new four-quadrant

thrust estimation scheme was presented in Chapter 4, extending previous results valid for propeller operating in two quadrants. Based on shaft speed and motor torque measurements, usually available on marine vehicles, the scheme involved a nonlinear observer for the propeller torque that showed stability and robustness with respect to modeling and measurement errors. The propeller thrust was computed as a static function of the propeller torque involving the estimation of the advance number. Good results were obtained in experimental tests conducted in open-water, with varying cross flows, in waves to simulate moderate and extreme sea state. Moreover the estimation scheme showed improved accuracy in thrust prediction with respect to the use of the four-quadrant propeller characteristics. To obtain accurate results, the open-water propeller characteristics need to be precise. For the application of the estimation scheme to full-scale vessels, if the propeller characteristics are obtained from model scale tests, they must be corrected for scale effects. This may represent a difficult task.

In Chapter 5, a nonlinear observer for the torque loss estimation, similar to the one implemented in the thrust estimation scheme, was included in a new four-quadrant nonlinear thrust controller designed for calm and moderate sea conditions. The control strategy was based on a shaft speed controller where the desired velocity was computed based on the desired propeller thrust and on the torque losses. The thrust controller was tested in open-water conditions, in moderate regular waves and cross flows showing good performance in tracking the demanded propeller thrust. Experiments were also conducted in order to compare the presented controller with the conventional shaft speed and torque controllers. These experiments, conducted in open-water conditions, showed that the compensation of the thrust loss due to changes in the advance speed leaded to improved accuracy in thrust tracking with respect to the use of the conventional controllers. These improvements were more significant when the propeller operated at high values of the advance number J, where losses due the advance speed are larger. At low values of J the performances of the three controllers, in terms of produced thrust, were practically equal.

The price to pay for the improvements in thrust control performance is the increase of consumed power. Moreover, to avoid unnecessary mechanical wear-and-tear of the propulsion unit, the torque loss observer gains should not be chosen too large. The performance of the thrust controller could deteriorate in case of slow propeller dynamics due to slew rate and rise time limits. This problem affects also the performance of the conventional controllers. For underwater vehicles, where the propeller dynamics

is usually very fast, the thrust controller can be fully exploited. As for the thrust estimation scheme, the performance of the thrust controller is influenced by the accuracy of the propeller characteristics.

In Chapter 6, the four-quadrant nonlinear thrust controller, presented in Chapter 5, was applied to the velocity control of an underwater vehicle. A simulation study was performed in order to compare the performance of the underwater vehicle when employing the new thrust controller with respect to the use of the conventional shaft speed and torque propeller controllers. It was shown that the improved capability in thrust tracking, obtained with the new thrust controller, leaded to better vehicle performance in terms of speed control. Two underwater vehicles, with different hydrodynamic drags, were simulated. In the first case, a low drag vehicle was employed and the use of the new thrust controller leaded to an improvement of the speed tracking error (root mean square error) of about 10% and 30% with respect to the use of the conventional torque and shaft speed controller. The improvement in the second simulation, performed with vehicle with a larger drag, was about 5.4% and 10.6%, respectively. This showed, as reported above, that the new propeller control strategy is more effective when the propeller works at high values of J (greater than about 0.35 in this case).

The thrust controller, designed for calm and moderate sea conditions, was subsequently improved in Chapter 7, by including an anti-spin strategy to reduce power peaks and wear-and-tear in extreme sea conditions. The anti-spin algorithm was derived from the work of Smogeli et al. (Smogeli *et al.* (2004*b*), Smogeli (2006)), where anti-spin controllers were designed for DP operations. The presented controller can operate also for maneuvering and transit operations, in which the vehicle speed is larger than in DP operations. Experimental tests showed the effectiveness of the anti-spin strategy that allowed the reduction of power peaks and fluctuations, and the increase of the propulsion efficiency with respect to the case where the anti-spin was not employed. The power peaks were reduced of about 40% and the propulsion efficiency increased of about 20%. For a vessel traveling in waves, the propulsion efficiency gained from using the anti-spin algorithm would be slightly less than 20% since the average thrust with the anti-spin enabled was smaller than the one obtained without anti-spin. This would cause a smaller vessel speed and, in turn, a smaller advance speed u_a, resulting in a reduced efficiency.

Motivated by environmental issues and the need of reduced CO_2 emissions, a novel control scheme for improving the propulsion efficiency in

moderate sea was presented in Chapter 8. The main idea was to exploit the variation in the advance speed due to waves to increase the average propulsion efficiency without reducing the vessel speed. A nonlinear controller was proposed showing that, theoretically, it is possible to increase the propulsion efficiency with respect to conventional thruster controllers. Model tests were carried out to determine the dynamic characteristics of propellers in waves and a simulation was employed to validate the novel control scheme. In a simulation carried out in regular waves, the novel optimizing controller produced an increase of the propulsion efficiency of about 3% with respect to the conventional shaft speed controller. The propulsion efficiency increased of about 1.7% with respect to the torque controller.

9.1 Recommendations for future work

- The thrust estimation scheme was thoroughly tested in the laboratory. Self propulsion tests, where a model scale vessel is pushed by the propeller, may be the next step for the validation of the estimation scheme. In this case, the propeller would operate in flows with characteristics more similar to full scale experiments than in open-water conditions. Eventually, full-scale experiments may represent the ultimate step.

- The natural next step for the new thrust control scheme with anti-spin is also represented by self propulsion and full-scale experiments. The thrust control strategy needs be tested when included in the overall vehicle control system. This would give a better understanding of the effective potential of the new controller compared to the conventional thrust controllers in terms of positioning and speed control performance. As discussed in Chapter 4, safety limits should be included. Also, the anti-spin strategy could be developed further. Fixed values for the optimal shaft speed during ventilation may not be the most effective solution.

- The new efficiency optimizing thruster control strategy needs to be addressed in future works. The optimal solution, computed for regular waves, may not be the optimum for irregular waves. Simulations of full-scale or model scale vessels should be performed considering different wave spectra. The impact of the new control strategy on the mechanical wear-and-tear of the propulsion system should also be ex-

amined. More work needs to be done also in the implementation side. Eventually, experiments should be performed to better understand the potential of the new approach.

Bibliography

Alonge, F., F. D'Ippolito and F. M. Raimondi (2001). Trajectory tracking of underactuated underwater vehicles. In: *Proceedings of the 40th IEEE Conference on Decision and Control, Orlando, Florida, USA*. Vol. 5. pp. 4421 – 4426.

Andersen, T.E. (1974). On dynamics of large ship diesel engines. Master's thesis. Technical University of Denmark.

Bachmayer, R. and L. L. Whitcomb (2001). An open loop nonlinear model based thrust controller for marine thrusters. In: *IEEE/RSJ International Conference on Intelligent Robots and Systems, Oct. 29- Nov. 03*. Maui, Hawaii, USA. pp. 1817–1823.

Bachmayer, R., L. L. Whitcomb and M. A. Grosenbaugh (2000). An accurate four-quadrant nonlinear dynamical model for marine thrusters: Theory and experimental validation. *IEEE Journal of Oceanic Engineering* **25**(1), 146–159.

Bakkeheim, J., L. Pivano, T.A. Johansen and Ø.N. Smogeli (2007). Integrator reset anti-spin for marine thrusters operating in four-quadrants and extreme sea conditions. In: *IFAC Conference on Control Applications in Marine Systems (CAMS 2007)*. Bol, Croatia.

Bakkeheim, J., Ø. N. Smogeli, T. A. Johansen and A. J. Sørensen (2006). Improved Transient Performance by Lyapunov-based Integrator Reset of PI Thruster Control in Extreme Seas. In: *45th IEEE Conference on Decision and Control*. San Diego, CA, USA.

Balchen, J. G., N. A. Jenssen and S. Sælid (1976). Dynamic Positioning Using Kalman Filtering and Optimal Control Theory. In: *IFAC/IFIP Symposium on Automation in Offshore Oil Field Operation*. Bergen, Norway. pp. 183–186.

Becerra, V. M. (2004). Solving optimal control problems with state constraints using nonlinear programming and simulation tools. *IEEE Transactions on Education* **47**(3), 377 – 384.

Berge, S. P. and T. I. Fossen (1997). Robust control allocation of overactuated ships; experiments with a model ship. In: *In Preprints of IFAC Conference on Maneuvering and Control of Marine Craft*. Brijuni, Croatia.

Blanke, M. (1981). Ship Propulsion Losses Related to Automatic Steering and Prime Mover Control.. PhD thesis. Technical University of Denmark.

Blanke, M. and P. Busk Nielsen (1990). The Marine Engine Governor. In: *2nd Int. Conf. on Maritime Communications and Control*. London, UK. pp. 11–20.

Blanke, M., K. Lindegaard and T. I. Fossen (2000). Dynamic model for thrust generation of marine propellers. In: *5th IFAC Conference of Manoeuvring and Control of Marine craft (MCMC)*. Aalborg, Denmark. pp. 363–368.

Blanke, M., L. Pivano and T.I. Johansen (2007). An efficiency optimizing propeller speed control for ships in moderate seas - model experiments and simulation. In: *IFAC Conference on Control Applications in Marine Systems (CAMS 2007)*. Bol, Croatia.

Blanke, M., R. Izadi-Zamanabadi and T. F. Lootsma (1998). Fault monitoring and reconfigurable control for ships propulsion plant. *Journal of Adaptive Control and Signal Processing* **12**, 671–688.

Bray, David (2003). *Dynamic Positioning*. Oilfield Seamanship Series, Vol. 9. Oilfield Publications, Incorporated.

Breslin, J. P. and P. Andersen (1994). *Hydrodynamics of Ship Propellers*. Cambridge University Press.

Børhaug, E. and K. Y. Pettersen (2005). Cross-track control for underactuated autonomous vehicles. In: *44th IEEE Conference on Decision and Control, and 2005 European Control Conference, CDC-ECC '05*. Seville, Spain. pp. 602 – 608.

Børhaug, E., L. Pivano, K.Y. Pettersen and T.A. Johansen (2007). A model-based ocean current observer for 6dof underwater vehicles. In:

IFAC Conference on Control Applications in Marine Systems (CAMS 2007). Bol, Croatia.

Carlton, J. S. (1994). *Marine Propellers and Propulsion*. Oxford, U.K.: Butterworth-Heinemann Ltd.

Domachowski, Z., W. Prochnicki and Z. Puhaczewski (1997). The investigation of the influence of the disturbances caused by the ship propeller on the dynamic processes of the ship propulsion system. *Marine Technology II* pp. 237–246.

Encarnação, P., A. Pascoal and M. Arcak (2000). Path following for autonomous marine craft. In: *Proceedings of the 5th IFAC Conference on Manoeuvring and Control of Marine Craft (MCMC)*. Aalborg, Denmark. pp. 117–122.

Faltinsen, O.M., K.J. Minsaas, N. Liapis and S.O. Skjørdal (1980). Prediction of resistance and propulsion of a ship in a seaway. In: *Proceedings of 13th Symposium on Naval Hydrodynamics*. Tokyo, Japan.

Fossen, T. I. (1991). Nonlinear Modeling and Control of Underwater Vehicles. PhD thesis. Department of Engineering Cybernetics, Norwegian University of Science and Technology. Trondheim.

Fossen, T. I. (2002). *Marine Control Systems - Guidance, Navigation, and Control of Ships, Rigs and Underwater Vehicles*. Marine Cybernetics, Trondheim, Norway.

Fossen, T. I. and M. Blanke (2000). Nonlinear output feedback control of underwater vehicle propellers using feedback from estimated axial flow velocity. *IEEE Journal of Oceanic Engineering* **25**(2), 241–255.

Fossen, T. I. and O. E. Fjellstad (1995). Robust Adaptive Control of Underwater Vehicles: A Comparative Study. In: *IFAC Workshop on Control Applications in Marine Systems (CAMS'95)*. Trondheim, Norway. pp. 66–74.

Gill, P.E., W. Murray and M.H. Wright (1981). *Practical Optimization*. London, Academic Press.

Guibert, C., E. Foulon, N. Aït-Ahmed and L. Loron (2005). Thrust control of electric marine thrusters. In: *31nd Annual Conference of IEEE Industrial Electronics Society. IECON 2005*. Raleigh, North Carolina, USA.

Healey, A. J. and D. B. Marco (1992*a*). Slow Speed Flight Control of Autonomous Underwater Vehicles: Experimental Results with the NPS AUV II. In: *Proceedings of the 2nd International Offshore and Polar Engineering Conference (ISOPE)*. San Francisco, CA, USA. pp. 523–532.

Healey, A. J. and D. Lienard (1993). Multivariable Sliding Mode Control for Autonomous Diving and Steering of Unmanned Underwater Vehicles. *IEEE Journal of Ocean Engineering* **18**(3), 327–339.

Healey, A. J., S. M. Rock, S. Cody, D. Miles and J. P. Brown (1995). Toward an improved understanding of thruster dynamics for underwater vehicles. *IEEE Journal of Oceanic Engineering* **20**(4), 354–61.

Healey, A.J. and D.B. Marco (1992*b*). Experimental verification of mission planning by autonomous mission execution and data visualization using the nps auv II. In: *Proceedings of the 1992 Symposium on Autonomous Underwater Vehicle Technology, AUV '92*. Washington D.C, USA. pp. 65 – 72.

ITTC (1999). *Recommended Procedures - Performance, Propulsion 1978 ITTC Performance Prediction Method - 7.5-02-03-01.4*. International Towing Tank Conference.

ITTC (2002*a*). *ITTC - Recommended Procedures - Testing and Extrapolation Methods. Propulsion, Performance Propulsion Test - 7.5-02-03-01.1*. ITTC.

ITTC (2002*b*). *Recommended Procedures - Testing and Extrapolation Methods. Propulsion, Propulsor, Open Water Test*. International Towing Tank Conference.

Jessup, S., C. Chesnakas, D. Fry, M. Donnelly, S. Black and J. Park (2004). Propeller performance at extreme off design conditions. In: *25th Symposium on Naval Hydrodynamics*. St. Johns, Newfoundland and Labrador, Canada. pp. 270–292.

Johansen, T. A., T. I. Fossen and S. P. Berge (2004). Constrained nonlinear control allocation with singularity avoidance using sequential quadratic programming. *IEEE Transactions on Control Systems Technology* **12**, 211–216.

Johansen, T. A., T. P. Fuglseth, P. Tøndel and T. I. Fossen (2008). Optimal constrained control allocation in marine surface vessels with rudders. *To appear in Control Engineering Practise*.

Joon, L. Sang, P. Bu Geun, Y. Jong Hwan and L. Choung Mook (2004). Three-component velocity field measurements of propeller wake using a stereoscopic piv technique. *Experiments in Fluids* **36**(4), 575–585.

Jung, M. and K. Glover (2006). Calibratable linear parameter-varying control of a turbocharged diesel engine. *IEEE Transactions on Control Systems Technology* **14**(1), 45 – 62.

Karlsen, S., K. Martinussen and K.J. Minsaas (1986). Towing performance and effectiveness of bow thrusters in waves and current. In: *9th International Tug Convention*.

Kempf, G. (1934). The influence of viscosity on thrust and torque of a propeller working near the surface. *Transactions of the institution of naval architects* **LXXVI**, 321–326.

Khalil, H. K. (2000). *Nonlinear Systems*. third ed.. Prentice Hall.

Kim, J. and W. K. Chung (2006). Accurate and practical thruster modeling for underwater vehicles. *IEEE Journal of Ocean Engineering* **33**(5-6), 566–586.

Kim, J., W. H. Shon, H.-G. Lee and W. K. Chung (n.d.). Preliminary thruster control experiments for underwater vehicle positioning. In: *IEEE International Conference on Robotics and Automation, ICRA 2006.*. Orlando, Florida. pp. 3233 – 3237.

Koushan, K. (2004). Environmental and interaction effects on propulsion systems used in dynamic positioning, an overview. In: *9th Int. Symp. Practical Design of Ships and Other Floating Structures (PRADSŠ04)*. Lübeck-Travemünde, Germany.. pp. 1013–1020.

Koushan, K. (2006*a*). Dynamics of propeller blade and duct loadings on ventilated ducted thrusters operating at zero speed. In: *T-POD06 - 2nd International Conference on Technological Advances in Podded Propulsion*. Brest, France.

Koushan, K. (2006*b*). Dynamics of ventilated propeller blade loading on thrusters. In: *World Maritime Technology Conference*. London, UK.

Koushan, K. (2007). Dynamics of propeller blade and duct loadings on ventilated thrusters in dynamic positioning mode. In: *Dynamic positioning conference*. Houston, USA.

Kristensen, J. and K. Vestgard (1998). Hugin - an untethered underwater vehicle system for cost effective seabed surveying in deep waters. In: *OCEANS '98 Conference*. Vol. 1. Nice, France. pp. 118–123.

Lehn, E. (1992). Fps-2000 mooring and positioning, part 1.6 dynamic positioning - thrust efficiency: Practical methods for estimation of thrust losses. Technical Report 513003.00.06. Marintek, Sintef, Norway.

Leonard, W. (2001). *Control of Electrical Drivers*. 3rd ed.. Springer.

Lewis, E. V. (1988). *Principles of Naval Architecture Vol II: Resistance, Propulsion and Vibration*. 3rd ed.. Society of Naval Architects and Marine Engineers. New York.

Lindegaard, K.-P. and T.I. Fossen (2003). Fuel efficient control allocation for surface vessels with active rudder usage: Experiments with a model ship. *IEEE Transactions on Control Systems Technology* **11**, 850–862.

Lindfors, I. (1993). Thrust allocation methods for the dynamic positioning system. In: *10th international ship control symposium*. Ottawa, Canada. pp. 3.93–3.106.

Lootsma, T. F. (2001). Observer-based faut detection and isolation for nonlinear systems. PhD thesis. Aalborg University, Denmark.

Makartchouk, A. (2002). *Diesel Engine Engineering: Thermodynamics, Dynamics, Design, and Control*. CRC Press.

Martin, S.C., L.L. Whitcomb, D. Yoerger and H. Singh (2006). A mission controller for high level control of autonomous and semi-autonomous underwater vehicles. In: *MTS/IEEE OCEANS '06*. Boston, USA. pp. 1 – 6.

Martínez-Calle, J., L. Balbona-Calvo, J. González-Pérez and E. Blanco-Marigorta (2002). An open water numerical model for a marine propeller: A comparison with experimental data. In: *ASME FEDSM Joint US-European Fluids Engineering Summer Conference*. Montreal, Canada.

Minsaas, K.J., H.J. Thon and W. Kauczynski (1987). Estimation of required thruster capacity for operation of offshore vessels under severe weather conditions. In: 3^{rd} *Int. symp. Practical Design of Ships and Mobile Units (PRADS '87)*. Trondheim, Norway. pp. 411–427.

Minsaas, K.J., O. M. Faltinsen and B. Persson (1983). On the importance of added resistance, propeller immersion and ventilation for large ships in a seaway. In: 2^{nd} *Int. Symp. on practical Design in Shipbuilding, Tokyo and Seoul (PRADS '83)*. Tokyo, Japan. pp. 149–159.

Narendra, K. S. and K. Parthasarathy (1990). Identification and control of dynamical systems using neural networks. *IEEE Transactions on Neural Networks* **1**(1), 4–27.

Parsons, M.G. and W.S. Vorus (1981). Added mass and damping estimates for vibrating propellers. In: *SNAME Propellers '81 Symposium*. Virginia beach, Virginia, USA. pp. 273–301.

Pascoal, A., P. Oliveira, C. Silvestre, A. Bjerrum, A. Ishoy, J.-P. Pignon and G. Ayela amd C. Petzelt (1997). Marius: an autonomous underwater vehicle for coastal oceanography. *IEEE Robotics & Automation Magazine* **4**, 46–59.

Pivano, L., J. Bakkeheim, T. A. Johansen and O. N. Smogeli (2008*a*). A four-quadrant thrust controller for marine propellers with loss estimation and anti-spin. *To appear at the 17th IFAC World Congress, Seoul, Korea.*

Pivano, L., L. L. Whitcomb, T.A. Johansen and T.I. fossen (2007*a*). Preliminary simulation studies of a new four-quadrant propeller thrust controller applied to underwater vehicles. In: *IFAC Conference on Control Applications in Marine Systems (CAMS 2007)*. Bol, Croatia.

Pivano, L., Ø. N. Smogeli, T. A. Johansen and T. I. Fossen (2006*a*). Experimental Validation of a Marine Propeller Thrust Estimation Scheme. In: *7th IFAC Conference on Manoeuvring and Control of Marine Craft (MCMC)*. Lisbon, Portugal.

Pivano, L., Ø. N. Smogeli, T. A. Johansen and T. I. Fossen (2006*b*). Marine propeller thrust estimation in four-quadrant operations. In: *45th IEEE Conference on Decision and Control*. San Diego, CA, USA.

Pivano, L., T. A. Johansen and Ø. N. Smogeli (2008*b*). A four-quadrant thrust estimation scheme for marine propellers: Theory and experiments. *accepted for publication in IEEE Transactions on Control Systems Technology.*

Pivano, L., T. A. Johansen, Ø. N. Smogeli and T. I. Fossen (2007*b*). Nonlinear Thrust Controller for Marine Propellers in Four-Quadrant Operations. In: *26th American Control Conference (ACC07)*. New York, USA.

Pivano, L., T. I. Fossen and T. A. Johansen (2006*c*). Nonlinear model identification of a marine propeller over four-quadrant operations. In: *14th IFAC Symposium on System Identification, SYSID*. Newcastle, Australia.

Rajamani, Rajesh (2006). *Vehicle Dynamics and Control*. Springer New York.

Refsnes, J. E., A. J. Sorensen and K. Y. Pettersen (2007). Output feedback control of an auv with experimental results. In: *15th Mediterranean Conference on Control and Automation, MED'07*. Athens, Greece.

Refsnes, J. E., K.Y. Pettersen and A. J. Sorensen (2006). Control of slender body underactuated auvs with current estimation. In: *45th IEEE Conference on Decision and Control*. San Diego, USA. pp. 43 – 50.

Rhee, Shin Hyung and Shitalkumar Joshi (2005). Computational validation for flow around a marine propeller using unstructured mesh based navier-stokes solver. *JSME International Journal Series B* **48**(3), 562–570.

Shiba, H. (1953). Air-drawing of marine propellers.. Report of Transportation Technical Research Institute 9. The Unyu-Gijutsu Kenkyŕujo, Japan.

Smallwood, D. A. and L. L. Whitcomb (2003). Preliminary identification of a dynamical plant model for the jason 2 underwater robotic vehicle. In: *IEEE/MTS OCEANS*. Vol. 2. San Diego, CA, USA. pp. 688–695.

Smallwood, David A. and Louis L. Whitcomb (2004). Model Based Dynamic Positioning of Underwater Robotic Vehicles: Theory and Experiment. *IEEE Journal of Oceanic Engineering* **29**(1), 169–186.

Smogeli, Ø. N. (2006). Control of Marine Propellers: From Normal to Extreme Conditions. PhD thesis. Department of Marine Technology, Norwegian University of Science and Technology (NTNU). Trondheim, Norway.

Smogeli, Ø. N., A. J. Sørensen and T. I. Fossen (2004*a*). Design of a hybrid power/torque thruster controller with loss estimation. In: *IFAC Conference on Control Applications in Marine Systems (CAMS'04)*. Ancona, Italy.

Smogeli, Ø. N., E. Ruth and A. J. Sorensen (2005). Experimental validation of power and torque thruster control. In: *IEEE 13th Mediterranean Conference on Control and Automation (MED'05)*. Cyprus. pp. 1506–1511.

Smogeli, Ø. N., J. Hansen, A. J. Sørensen and T. A. Johansen (2004*b*). Anti-spin control for marine propulsion systems. In: *43rd IEEE Conference on Decision and Control*. Paradise Island, Bahamas.

Smogeli, Ø. N., L. Aarseth, E. S. Overå, A. J. Sørensen and K. J. Minsaas (2003). Anti-Spin Thruster Control in Extreme Seas. In: *6th IFAC Conf. on Manoeuvring and Cont. of Marine Craft (MCMCŠ03)*. Girona, Spain. p. 221Ű226.

Sørensen, A. J., A. K. Ådnanes, T. I. Fossen and J. P. Strand (1997). A new method of thruster control in positioning of ships based on power control. In: *4th IFAC Conference on Manoeuvring and Control of Marine Craft*. Brijuni, Croatia.

Stella, A., G. Guj and F. Di Felice (2000). Propeller wake flowfield analysis by means of ldv phase sampling techniques. *Experiments in Fluids* **28**(1), 1–10.

Stokey, R.P., A. Roup, C. von Alt, B. Allen, N. Forrester, T. Austin, R. Goldsborough, M. Purcell, F. Jaffre, G. Packard and A. Kukulya (2005). Development of the remus 600 autonomous underwater vehicle. In: *MTS/IEEE OCEANS '05*. Vol. 2. Washington, USA. pp. 1301–1304.

Strand, J. P. (1999). Nonlinear Position Control Systems Design for Marine Vessels. PhD thesis. Department of Engineering Cybernetics, Norwegian University of Science and Technology. Trondheim, Norway.

Sørdalen, O.J. (1997). Optimal thrust allocation for marine vessels. *Control Engineering Practice* **5**(9), 1223–1231.

Sørensen, A. J., S. I. Sagatun and T. I. Fossen (1996). Design of a dynamic positioning system using model-based control. *Control Engineering Practice* **4**(3), 359–368.

Tjønnås, J. and T. A. Johansen (2007). On optimizing nonlinear adaptive control allocation with actuator dynamics. In: *7th IFAC Symposium on Nonlinear Control Systems*. Pretoria, South Africa.

Vysohlid, M. and K. Mahesh (2004). Large-eddy simulation of propeller crashback. In: *57th Annual Meeting of the Division of Fluid Dynamics*. Seattle, Washington.

Wereldsma, R. (1965). Dynamic behaviour of ship propeller. *International Periodieke Pers, Rotterdam*.

Whitcomb, L. L. and D. Yoerger (1999). Developement, comparison, and preliminary experimental validation of nonlinear dynamic thruster models. *IEEE Journal of Oceanic Engineering* **24**(4), 481–494.

Xiros, Nikolaos (2002). *Robust Control of Diesel Ship Propulsion*. Springer-Verlag London Ltd.

Yoerger, D. R., John G. Cooke and Jean-Jacques E. Slotine (1990). The influence of thruster dynamics on underwater vehicle behavior and their incorporation into control system design. *IEEE Journal of Oceanic Engineering* **15**(3), 167–178.

Zhinkin, V. B. (1989). Determination of the screw propeller thrust when the torque or shaft power is known. In: *Fourth international symposium on practical design of ships and mobile units*. Bulgaria.

Appendix A

Appendix

A.1 Proof of Proposition 4.1

First we consider the input δ, defined in (4.4), equal to zero $\forall t$ and later we investigate its effect on the error dynamics. Taking the Lyapunov function candidate $V := \frac{1}{2}\tilde{e}^T P_1 \tilde{e}$, where $P_1 = P_1^T > 0$ and

$$P_1 = \begin{bmatrix} p_{11} & p_{12} \\ p_{12} & p_{22} \end{bmatrix}, \tag{A.1}$$

we can compute its time derivative along the trajectory of (4.5) obtaining

$$\begin{aligned} \dot{V} = \quad & -\left[\frac{1}{J_m} p_{11} \left(k_{f_2} + l_1\right) - p_{12} l_2\right] \tilde{e}_1^2 - \left[\frac{p_{22}}{\tau_1} + \frac{p_{12}}{J_m}\right] \tilde{e}_2^2 \\ & -\left[\frac{p_{12}}{J_m} \left(k_{f_2} + l_1\right) + \frac{p_{12}}{\tau_1} + \frac{p_{11}}{J_m} - p_{22} l_2\right] \tilde{e}_1 \tilde{e}_2 \\ & -p_{12} \psi(\tilde{e}_1, \hat{\omega}) \tilde{e}_2 - p_{11} \psi(\tilde{e}_1, \hat{\omega}) \tilde{e}_1. \end{aligned} \tag{A.2}$$

From the nonlinearity $\psi(\tilde{e}_1, \hat{\omega})$ we can subtract the linear function $\alpha \tilde{e}_1$, where α is constant and satisfies A1, such that

$$g_1(\tilde{e}_1, \hat{\omega}) = \psi(\tilde{e}_1, \hat{\omega}) - \alpha \tilde{e}_1. \tag{A.3}$$

Since the graph of $\psi(\tilde{e}_1, \hat{\omega})$ belongs to the sector $[0, \alpha]$, the graph of $g(\tilde{e}_1, \hat{\omega})$ belongs to the sector $[-\alpha \ \alpha]$, i.e.

$$\forall \tilde{e}_1, \forall \hat{\omega} : [g(\tilde{e}_1, \hat{\omega})]^2 < \alpha^2 \tilde{e}_1^2. \tag{A.4}$$

Substituting (A.3) in (A.2) and recalling that, since $p_{11} > 0$, $p_{11}\psi(\tilde{e}_1, \hat{\omega})\tilde{e}_1 > 0$ we get

$$\begin{aligned} \dot{V} \leq \quad & -\left[\tfrac{1}{J_m} p_{11} \left(k_{f_2} + l_1\right) - p_{12} l_2\right] \tilde{e}_1^2 - \left[\tfrac{p_{22}}{\tau_1} + \tfrac{p_{12}}{J_m}\right] \tilde{e}_2^2 \\ & -\left[\tfrac{p_{12}}{J_m} \left(k_{f_2} + l_1\right) + \tfrac{p_{12}}{\tau_1} + \tfrac{p_{11}}{J_m} - p_{22} l_2 + p_{12}\alpha\right] \tilde{e}_1 \tilde{e}_2 \\ & -p_{12} g_1(\tilde{e}_1, \hat{\omega}) \tilde{e}_2. \end{aligned} \tag{A.5}$$

Choosing $p_{12} > 0$, we can use Young's inequality

$$-2xy \leq \mu x^2 + \frac{1}{\mu} y^2 \quad \forall \mu > 0, \tag{A.6}$$

on the last term of (A.5) obtaining

$$\begin{aligned} -p_{12} g_1(\tilde{e}_1, \hat{\omega}) \tilde{e}_2 \quad & \leq \mu \tfrac{p_{12}}{2} \tilde{e}_2^2 + \tfrac{p_{12}}{2\mu} \left[g_1(\tilde{e}_1, \hat{\omega})\right]^2 \\ & \leq \mu \tfrac{p_{12}}{2} \tilde{e}_2^2 + \tfrac{p_{12}}{2\mu} \alpha^2 \tilde{e}_1^2. \end{aligned} \tag{A.7}$$

Using (A.7) in (A.5), we attain

$$\begin{aligned} \dot{V} \leq \quad & -\left[\tfrac{1}{J_m} p_{11} \left(k_{f_2} + l_1\right) - p_{12} l_2 - \tfrac{p_{12}}{2\mu} \alpha^2\right] \tilde{e}_1^2 \\ & -\left[\tfrac{p_{12}}{J_m} \left(k_{f_2} + l_1\right) + \tfrac{p_{12}}{\tau_1} + \tfrac{p_{11}}{J_m} - p_{22} l_2 + p_{12}\alpha\right] \tilde{e}_1 \tilde{e}_2 \\ & -\left[\tfrac{p_{22}}{\tau_1} + \tfrac{p_{12}}{J_m} - \mu \tfrac{p_{12}}{2}\right] \tilde{e}_2^2. \end{aligned} \tag{A.8}$$

Selecting $l_2 > 0$ and p_{22} such that

$$p_{22} = \frac{1}{l_2} \left[\frac{p_{12}}{J_m} \left(k_{f_2} + l_1\right) + \frac{p_{12}}{\tau_1} + \frac{p_{11}}{J_m} + p_{12}\alpha\right], \tag{A.9}$$

the cross-term in (A.8) is cancelled. To obtain a negative definite $\dot{V}$, the following are needed:

$$\frac{1}{J_m} p_{11} \left(k_{f_2} + l_1\right) - p_{12} l_2 - \frac{p_{12}}{2\mu} \alpha^2 > 0, \tag{A.10}$$

$$\frac{p_{22}}{\tau_1} + p_{12} \left(\frac{1}{J_m} - \frac{\mu}{2}\right) > 0. \tag{A.11}$$

Choosing $p_{11} = p_{12} \alpha^2 \kappa J_m$ with $\kappa > 0$, the inequality (A.10) is satisfied for

$$l_1 > -k_{f_2} + \frac{l_2}{\alpha^2 \kappa} + \frac{1}{2\mu\kappa}. \tag{A.12}$$

With this choice of l_1, we observe from (A.9) that $p_{22} > 0$ and the inequality (A.11) certainly holds if

$$\mu < \frac{2}{J_m}. \tag{A.13}$$

Combining (A.12) and (A.9), we get $p_{22} > \frac{p_{11}}{l_2 J_m}$. This yields

$$P_1 > \begin{bmatrix} p_{11} & \frac{p_{11}}{\alpha^2 \kappa J_m} \\ \frac{p_{11}}{\alpha^2 \kappa J_m} & \frac{p_{11}}{l_2 J_m} \end{bmatrix}. \tag{A.14}$$

If $l_2 < \alpha^4 \kappa^2 J_m$ then P_1 is positive definite. Choosing the observer gains according to A4 and A5 of Proposition 4.1, the derivative of the Lyapunov function candidate is negative definite since

$$\dot{V} \leq \quad -\min\{q_1, q_2\} \left\|\tilde{e}\right\|_2^2, \tag{A.15}$$

where

$$q_1 = \frac{1}{J_m} p_{11} \left(k_{f_2} + l_1\right) - p_{12} l_2 - \frac{p_{12}}{2\mu} \alpha^2, \tag{A.16}$$

$$q_2 = \frac{p_{22}}{\tau_1} + p_{12} \left(\frac{1}{J_m} - \frac{\mu}{2}\right). \tag{A.17}$$

The observer error dynamics, with $\delta = 0 \ \forall t$, is thus globally exponentially stable (GES). When the input δ is different from zero for some t, the term $2\tilde{e}^T P_1 B_1 \delta$ must be added to the derivative of the Lyapunov function in (A.15):

$$\begin{aligned} \dot{V} &\leq -\min\{q_1, q_2\} \left\|\tilde{e}\right\|_2^2 + 2\tilde{e}^T P_1 B_1 \delta \\ &\leq -\min\{q_1, q_2\} \left\|\tilde{e}\right\|_2^2 + 2 \left\|\tilde{e}^T P_1 B_1 \delta\right\|_2 \\ &\leq -\min\{q_1, q_2\} \left\|\tilde{e}\right\|_2^2 + 2 \left\|\tilde{e}^T\right\|_2 \left\|P_1\right\|_2 \left\|B_1\right\|_2 \left\|\delta\right\|_2. \end{aligned} \tag{A.18}$$

With $0 < \theta < 1$, we obtain

$$\begin{aligned} \dot{V} &\leq -\min\{q_1, q_2\} \left\|\tilde{e}\right\|_2^2 + \left\|P_1\right\|_2 \left\|B_1\right\|_2 \left\|\tilde{e}\right\|_2 \left\|\delta\right\|_2 \\ &\leq -(1-\theta) \min\{q_1, q_2\} \left\|\tilde{e}\right\|_2^2 - \theta \min\{q_1, q_2\} \left\|\tilde{e}\right\|_2^2 \\ &\quad + \left\|P_1\right\|_2 \left\|B_1\right\|_2 \left\|\tilde{e}\right\|_2 \left\|\delta\right\|_2. \end{aligned} \tag{A.19}$$

For any $\left\|\tilde{e}\right\|_2$ such that

$$\left\|\tilde{e}\right\|_2 \geq \rho(\left\|\delta\right\|_2), \tag{A.20}$$

where

$$\rho(\left\|\delta\right\|_2) = \frac{\left\|P_1\right\|_2 \left\|B_1\right\|_2}{\theta \min\{q_1, q_2\}} \left\|\delta\right\|_2 \tag{A.21}$$

is a (linear) class $\mathcal{K}$ function, we obtain

$$\dot{V} \leq -(1-\theta)\min\{q_1, q_2\}\left\|\tilde{e}\right\|_2^2 \leq 0. \tag{A.22}$$

Since V is positive definite and radially unbounded, from Theorem 4.19 in Khalil (2000), the system (4.5) is ISS. Furthermore, the observer error is uniformly ultimately bounded (UUB) by $\rho\left(\sup_{t>t_0}\left(\left\|\delta\right\|_2\right)\right)$.

A.2 Proof of Proposition 5.1

Taking the Lyapunov function candidate $V_o(\tilde{\omega}, \tilde{\Delta}_q) := \frac{1}{2}a_{11}\tilde{\omega}^2 + \frac{1}{2}a_{22}\tilde{\Delta}_q^2$, we can compute its time derivative along the trajectory of the observer error dynamics in (5.5) obtaining:

$$\begin{aligned}\dot{V}_o = \quad & -\tfrac{a_{11}k_{f_2}}{J_m}\tilde{\omega}^2 - \tfrac{a_{11}l_1}{J_m}\tilde{\omega}^2 - \tfrac{a_{22}}{\tau_2}\tilde{\Delta}_q^2 - \tfrac{a_{11}}{J_m}\tilde{\omega}\tilde{\Delta}_q \\ & +a_{22}w_2\tilde{\Delta}_q - \tfrac{a_{11}}{J_m}\left[\psi(\omega) - \psi(\hat{\omega})\right]\tilde{\omega} + l_2 a_{22}\tilde{\omega}\tilde{\Delta}_q.\end{aligned} \tag{A.23}$$

Since the function $\psi(\cdot)$ belongs to the sector $[0, \infty]$ and is not decreasing, we have $\forall\omega, \hat{\omega} : \left[\psi(\omega) - \psi(\hat{\omega})\right](\omega - \hat{\omega}) \geq 0$. Using this property, (A.23) becomes

$$\begin{aligned}\dot{V}_o &\leq -\frac{a_{11}\left(k_{f_2} + l_1\right)}{J_m}\tilde{\omega}^2 - \frac{a_{22}}{\tau_2}\tilde{\Delta}_q^2 - \left(\frac{a_{11}}{J_m} - a_{22}l_2\right)\tilde{\omega}\tilde{\Delta}_q \\ &\quad +a_{22}\tilde{\Delta}_q w_2 \\ &\leq -\tilde{e}_o^T Q_1 \tilde{e}_o + a_{22}\tilde{\Delta}_q w_2,\end{aligned} \tag{A.24}$$

where $\tilde{e}_o = [\tilde{\omega} \;\; \tilde{\Delta}_q]^T$ and

$$Q_1 = \begin{bmatrix} \frac{a_{11}\left(k_{f_2}+l_1\right)}{J_m} & \frac{1}{2}\left(\frac{a_{11}}{J_m} - a_{22}l_2\right) \\ \frac{1}{2}\left(\frac{a_{11}}{J_m} - a_{22}l_2\right) & \frac{a_{22}}{\tau_2} \end{bmatrix}. \tag{A.25}$$

If the assumptions A1 and A2 hold, then Q_1 is positive definite and the origin of (5.5), with $w_2 = 0 \;\forall t$, is uniformly globally exponentially stable (UGES) since:

$$\dot{V}_o \leq -\lambda_{\min}\{Q_1\}\left\|\tilde{e}_o\right\|^2. \tag{A.26}$$

When $w_2 \neq 0$ for some t, (A.24) can be written as follows:

$$\begin{aligned}\dot{V}_o &\leq -\lambda_{\min}\{Q_1\}\left\|\tilde{e}_o\right\|^2 + a_{22}\left|w_2\right|\left\|\tilde{e}_o\right\| \\ &\leq -(1-\theta)\lambda_{\min}\{Q_1\}\left\|\tilde{e}_o\right\|^2 - \theta\lambda_{\min}\{Q_1\}\left\|\tilde{e}_o\right\|^2 \\ &\quad +a_{22}\left|w_2\right|\left\|\tilde{e}_o\right\|,\end{aligned} \tag{A.27}$$

where $0 < \theta < 1$. For any $\|\tilde{e}_o\|$ such that

$$\|\tilde{e}_o\| \geq \frac{a_{22}}{\theta \lambda_{\min}\{Q_1\}} |w_2| := \rho_1(|w_2|), \tag{A.28}$$

where $\rho_1(\cdot)$ is a (linear) class $\mathcal{K}$ function, we obtain:

$$\dot{V}_o \leq -(1-\theta)\lambda_{\min}\{Q_1\} \|\tilde{e}_o\|^2 \leq 0. \tag{A.29}$$

From Theorem 4.19 of Khalil (2000), the system of (5.5) is ISS with respect to w_2.

A.3 Proof of Proposition 5.2

Proof. First we consider $\tilde{\Delta}_q = 0$, and later we investigate its effect on the control error dynamics (5.11). Let the Lyapunov function candidate be

$$V = \frac{1}{2} e^T P e, \tag{A.30}$$

where $e = [e_1 \ e_2]^T$ and

$$P = \begin{bmatrix} p_{11} + p_{22}\gamma^2 & \gamma p_{22} \\ \gamma p_{22} & p_{22} \end{bmatrix}, \tag{A.31}$$

is positive definite. This implies $p_{11} > 0$ and $p_{22} > 0$. Taking its time derivative along the trajectory of the error dynamics (5.11), we obtain

$$\begin{aligned} \dot{V} = \quad & -\tfrac{p_{22}}{J_m}\gamma \left(k_I + \gamma k_P\right) e_1^2 \\ & + \left(p_{11} - p_{22}\left(-\gamma^2 + \tfrac{k_{f_2}}{J_m}\gamma + 2\gamma\tfrac{k_P}{J_m} + \tfrac{k_I}{J_m}\right)\right) e_1 e_2 \\ & - p_{22}\left(-\gamma + \tfrac{k_{f_2}}{J_m} + \tfrac{k_P}{J_m}\right) e_2^2 \\ & - p_{22}\tfrac{1}{J_m}\left[\psi(\omega) - \psi(-\gamma e_1 + \omega_d)\right]\left(\gamma e_1 + e_2\right), \end{aligned} \tag{A.32}$$

Since $\psi(\cdot)$ belongs to the sector $[0, \infty]$ and is not decreasing, the last term in (A.32) is always negative since

$$\begin{aligned} \forall \omega, e_1, \omega_d, \quad & \left[\psi(\omega) - \psi(-\gamma e_1 + \omega_d)\right]\left(\gamma e_1 + e_2\right) \\ & = \left[g\left(a\right) - g\left(b\right)\right]\left(a - b\right) \geq 0, \end{aligned} \tag{A.33}$$

where $g = \psi$, $a = \omega$, $b = -\gamma e_1 + \omega_d$. Choosing

$$p_{11} = p_{22}\left(-\gamma^2 + \frac{k_{f_2}}{J_m}\gamma + 2\gamma\frac{k_P}{J_m} + \frac{k_I}{J_m}\right), \tag{A.34}$$

we cancel the cross term in (A.32). This is possible because, due to the assumptions B2 and B3 of Proposition 5.2, the term inside the parenthesis in (A.34) is positive. Using (A.33) and (A.34), (A.32) becomes

$$\begin{aligned} \dot{V} &\leq -e^T Q_2 e, \\ &\leq -\lambda_{\min}\{Q_2\}\|e\|^2, \end{aligned} \tag{A.35}$$

where

$$Q_2 = \begin{bmatrix} \frac{p_{22}}{J_m}\gamma\left(k_I + \gamma k_P\right) & 0 \\ 0 & p_{22}\left(-\gamma + \frac{k_{f_2}}{J_m} + \frac{k_P}{J_m}\right) \end{bmatrix} \tag{A.36}$$

is positive definite if assumptions B1, B2 and B3 of Proposition 5.2 are satisfied. The error dynamics (5.11), with $\tilde{\Delta}_q = 0\ \forall t$, is thus UGES.

When $\tilde{\Delta}_q \neq 0$ for some t, (A.35) can be written as follows:

$$\begin{aligned} \dot{V} &\leq -\lambda_{\min}\{Q_2\}\|e\|^2 - \frac{p_{22}}{J_m}\tilde{\Delta}_q\left(\gamma e_1 + e_2\right) \\ &\leq -(1-\theta)\lambda_{\min}\{Q_2\}\|e\|^2 - \theta\lambda_{\min}\{Q_1\}\|e\|^2 \\ &\quad + \frac{p_{22}}{J_m}\left|\tilde{\Delta}_q\right|\sqrt{1+\gamma^2}\|e\|, \end{aligned} \tag{A.37}$$

where $0 < \theta < 1$. For any $\|e\|$ such that

$$\|e\| \geq \frac{p_{22}\sqrt{1+\gamma^2}}{\theta J_m \lambda_{\min}\{Q_2\}}\left|\tilde{\Delta}_q\right| := \rho_2\left(\left|\tilde{\Delta}_q\right|\right), \tag{A.38}$$

where $\rho_2(\cdot)$ is a (linear) class $\mathcal{K}$ function, we obtain:

$$\dot{V} \leq -(1-\theta)\lambda_{\min}\{Q_2\}\|e\|^2 \leq 0. \tag{A.39}$$

From Theorem 4.19 of Khalil (2000), the control error dynamics (5.11) is ISS with respect to $\tilde{\Delta}_q$ and the control error is uniformly ultimately bounded by $\rho_2\left(\sup_{t>t_0}\left(\left|\tilde{\Delta}_q\right|\right)\right)$.

The observer/controller error dynamics can be considered as a cascaded system where the observer error $\tilde{\Delta}_q$ drives the control error dynamics. The observer error dynamics $\tilde{\Delta}_q$ is bounded and ISS with respect to w_2, implying that the control error dynamics e is bounded. Due to the boundness of T_{p_d} and from the relation (5.7) between thrust and torque, also Q_{p_d} is bounded. The torque loss estimation $\hat{\Delta}_q$ is also bounded due to the property of the observer, therefore the desired shaft speed $\bar{\omega}_d$ and thus ω_d are bounded. This last condition implies boundness of the shaft speed ω since e is confined. The propeller thrust is thus bounded and converges to a ball around the desired thrust. ■

A.4 Proof of Proposition 6.1

Proof. Let the Lyapunov function candidate be $V_1 = \frac{1}{2}e^T P e$, where $e = [e_1 \; e_2]^T$ and P is positive definite such that

$$P = \begin{bmatrix} p_{11} + p_{22}\gamma^2 & \gamma p_{22} \\ \gamma p_{22} & p_{22} \end{bmatrix}. \tag{A.40}$$

This implies $p_{11} > 0$ and $p_{22} > 0$. Taking the time derivative of V_1 along the trajectory of the system (6.3), we obtain

$$\begin{aligned} \dot{V}_1 = & -\tfrac{p_{22}}{m_u}\gamma\left(k_I + \gamma k_P\right) e_1^2 \\ & + \left(p_{11} - p_{22}\left(-\gamma^2 + \tfrac{\gamma d_l}{m_u} + \tfrac{2\gamma k_P}{m_u} + \tfrac{k_I}{m_u}\right)\right) e_1 e_2 \\ & - p_{22}\left(-\gamma + \tfrac{d_l}{m_u} + \tfrac{k_P}{m_u}\right) e_2^2 \\ & - \tfrac{p_{22} d_q}{m_u}\Gamma(e_1, e_2, u_d)\left(\gamma e_1 + e_2\right), \end{aligned} \tag{A.41}$$

where

$$\begin{aligned} \Gamma(e_1, e_2, u_d) = & \left(e_2 + u_d\right)\left|e_2 + u_d\right| \\ & - \left(-\gamma e_1 + u_d\right)\left|-\gamma e_1 + u_d\right|. \end{aligned} \tag{A.42}$$

The last term in (A.41) is always non positive since

$$\Gamma(e_1, e_2, u_d)\left(\gamma e_1 + e_2\right) = \left[g\left(a\right) - g\left(b\right)\right]\left(a - b\right), \tag{A.43}$$

where $a = e_2 + u_d$, $b = -\gamma e_1 + u_d$ and $g(r) = r\left|r\right|$ is a non decreasing function. Choosing

$$p_{11} = p_{22}\left(-\gamma^2 + \frac{\gamma d_l}{m_u} + 2\frac{\gamma k_P}{m_u} + \frac{k_I}{m_u}\right), \tag{A.44}$$

we cancel the cross term in (A.41). This is possible because, due to the assumptions A2 and A3, the term inside the parenthesis is positive. Using (A.43) and (A.44), (A.41) becomes

$$\dot{V}_1 \leq -e^T Q e, \tag{A.45}$$

where

$$Q_1 = \begin{bmatrix} \frac{p_{22}}{m_u}\gamma\left(k_I + \gamma k_P\right) & 0 \\ 0 & p_{22}\left(-\gamma + \frac{d_l}{m_u} + \frac{k_P}{m_u}\right) \end{bmatrix} \tag{A.46}$$

is positive definite due to assumptions A1 and A2 of Proposition 6.1. ■

A.5 Scaling factors

To predict full-scale quantities from model-scale measurements, scaling laws are employed in combination with appropriate correction methods. Corrections are applied in order to take into account the finite validity of scaling laws. Three laws of similitude should be considered: geometrical, kinematic and dynamic. The geometrical similarity ensures that all linear dimensions (L) of the model scale structure have the same scale ratio:

$$\lambda = \frac{L_{FS}}{L_{MS}}, \tag{A.47}$$

where λ is the geometrical scale factor and the subscripts FS and MS mean full scale and model scale.

The kinematic similarity ensures that the flow will have geometrically similar motion in model and full scale. For example velocities in the horizontal plane must have the same ratio, such that a circular motion in full scale corresponds to a circular motion in model scale. For a propeller, the ratio between propeller tip speed and advance speed must be the same in model and full scale. This implies that

$$J_{FS} = \frac{u_{a_{FS}}}{n_{FS} D_{FS}} = \frac{u_{a_{MS}}}{n_{MS} D_{MS}} = J_{MS}, \tag{A.48}$$

where u_a is the advance speed, J the advance number, n the shaft speed (in rotations per second) and D the propeller diameter.

The dynamic similarity is needed to obtain the same ratios between different forces acting on the model and full scale. The following force contributions are considered to be important: inertial forces, viscous forces, gravitational forces, pressure forces, elastic forces in the fluid and surface forces. The relationship between inertial and gravitational forces is defined by the Froude number Fn as:

$$Fn = \frac{V}{\sqrt{gL}}, \tag{A.49}$$

where V is a linear velocity, g the acceleration of gravity, and L a characteristic length. For propellers, applying $V = nD$, the Froude's number is written a

$$Fn = n\sqrt{\frac{D}{g}} \tag{A.50}$$

When applying Froude scaling, the advance speed and the shaft speed will be computed as $u_{a_{FS}} = u_{a_{MS}}\sqrt{\lambda}$ and $n_{FS} = n_{MS}/\sqrt{\lambda}$.

The relationship between inertial and viscous forces is defined by the Reynolds' number Re:

$$Re = \frac{VL}{\nu}, \tag{A.51}$$

where ν is the kinematic viscosity of water. For a propeller, the Reynolds' number is computed as

$$Re = \frac{V_\infty c}{\nu}, \tag{A.52}$$

where V_∞ is the velocity seen by the propeller blade at radius $0.7R$, c is the chord length of the propeller blade at radius $0.7R$. The same Reynolds' number, in model and full scale tests, ensures that viscous forces are correctly scaled. Another important coefficient is the Weber's number, defined as the ratio between the inertial and surface tension forces. For a propeller, it is written as:

$$W = nD\sqrt{\frac{\rho}{\sigma}D}, \tag{A.53}$$

where ρ is the water density and σ is the surface tension. For some applications, it is important to predict correctly cavitation phenomena in full scale, therefore similarity on cavitation number should be maintained. The cavitation number is computed as:

$$\sigma_c = \frac{p_{static} - p_{cav}}{0.5\rho V_\infty^2}, \tag{A.54}$$

where p_{static} is the static water pressure at a given submergence, and p_{cav} is the pressure in the cavity. Another important parameter that influences the propeller performance, and needs to be scaled, is the relative propeller submergence h/R.

If the geometrical and kinematic similarity are satisfied, the application of the Reynolds and Weber scaling would lead to too large velocities in model scale tests. Tests of model scale propellers are typically executed considering Froude scaling. Open-water tests are usually performed with submergence h/R larger than $0.625D$ and at Reynolds numbers larger than the critical one; see ITTC (2002*b*) and ITTC (2002*a*). Typically it is recommended that $Re > 2 \cdot 10^5$. The measured propeller characteristics must to be corrected to account for scaling effects. This can be performed, for example, by using the empirical methods described in ITTC (1999).